Universitat Autònoma de Barcelona

A theoretical study on some exotic quantum phase transitions

by

Abel Vicenç Yuste Roca

under the supervision of

Dr. Anna Sanpera Trigueros

A thesis submitted in partial fulfillment for the
degree of Doctor of Philosophy

in

Unitat de Física Teòrica: Informació i Fenòmens Quàntics
Departament de Física
Facultat de Ciències

Bellaterra, September, 2018

"How little we know of what there is to know (...) I'd like to be an old man to really know. I wonder if you keep on learning or if there is only a certain amount each man can understand. I thought I knew so many things that I know nothing of. I wish there was more time."

Ernest Hemingway,
For Whom the Bells Tolls

Abstract

My Ph.D. is devoted to the analysis of some exotic quantum phase transitions arising in strongly correlated systems described by spin Hamiltonians. On the one hand, my studies have focused on quantum phase transitions occurring close to multicritical points. These points are particularly pathological since several quantum phases coexist in a narrow range of Hamiltonian parameters. This fact, as I will discuss in this thesis, has strong effects on the properties displayed by the strongly correlated system. On the other hand, I have also analyzed quantum phase transitions leading to quantum spin liquids which are novel phases of matter occurring in some frustrated systems. These phases are at the forefront of condensed matter research since their characterization remains very elusive both experimentally and theoretically.

The research presented here can be split into three different parts. The first part deals with the unusual behavior of bipartite entanglement in some quantum spin chains. The role of quantum fluctuations is enhanced in low dimensions, and thus 1D systems offer a plethora of possibilities to analyze the role of quantum fluctuations in quantum phase transitions. Some studies have been carried out for spin-1/2 models, while others have been realized for spin-1 systems. The second part of my thesis covers disordered frustrated quantum systems and, in particular, the presence of quantum spin liquids. Frustration reflects the impossibility of fulfilling simultaneously all constraints posed by some Hamiltonians. It is an inherent property of some strongly correlated systems, e.g., classical spin ice models or 2D quantum antiferromagnets. Such incompatibility often translates into a severe problem of energy minimization when finding the ground state of the system. Many frustrated systems order at zero or low temperatures but there also states that do not order and lay beyond the Landau theory of phase transitions presenting a fascinating underlying structure. Quantum spin liquids belong to this last type. My approach to address their study has been to develop a new numerical method using engineered boundary conditions. Such approach has allowed me to obtain some unambiguous signatures about the nature of some quantum spin liquids. The last part of my thesis is devoted to describe and analyze frustrated quantum spin models by means of modified spin wave theory. The use of such analytical tool has allowed me to asses the performance and validity of the numerical approach I have developed as well as to deepen my understanding of quantum spin liquids.

Finally, I would like to mention that the first and third part of my thesis were mostly developed during the months I spent as a Ph.D. research visitor

at Queen's University of Belfast (UK) on the group of Dr. G. de Chiara in 2016, and at the Universität Heidelberg (Germany) in the group of Junior Prof. P. Hauke in 2018 respectively.

Resum

El meu doctorat està dedicat a analitzar transicions de fases quàntiques de naturalesa exòtica en sistemes fortament correlacionats descrits per Hamiltonians de spin. D'una banda, m'he centrat en l'estudi de transicions de fase quàntiques localitzades a prop de punts multicrítics. Aquests punts són particularment patològics ja que diverses fases quàntiques coexisteixen en una petita regió de paràmetres del Hamiltonià. Aquest fet, tal i com argumentaré al llarg de la tesis, condiciona palesament les propietats mostrades pel sistema fortament correlacionat. De l'altre, també he investigat transicions de fase quàntiques cap a líquids de spin quàntics que són fases exòtiques de la matèria que apareixen en alguns sistemes frustrats. Aquestes fases es situen a l'avantguarda de la recerca en matèria condensada ja que són, teòrica i experimentalment, molt difícils de caracteritzar.

La recerca presentada es pot dividir en tres parts. La primera part tracta sobre comportaments insòlits que pateix l'entrellaçament quàntic, més conegut com a *entanglement*, en algunes cadenes de spin. La rellevància de les fluctuacions quàntiques creix en baixes dimensions i per tant els sistemes unidimensionals ofereixen un bon ventall de possibilitats per analitzar el paper de les fluctuacions quàntiques en transicions de fase quàntiques. Alguns càlculs han estat realitzats en models de spin-1/2 i d'altres en sistemes de spin-1. La segona part de la meva tesis tracta de sistemes quàntics frustrats i, particularment, de la presència de líquids de spin. La frustració reflecteix la impossibilitat de satisfer simultàniament totes les restriccions imposades per alguns Hamiltonians. És una propietat intrínseca d'alguns sistemes fortament correlacionats, com ara els gels clàssic de spins o models quàntics antiferromagnètics en 2D. Aquesta incompatibilitat fa que sovint sigui molt difícil minimitzar-ne l'energia per a trobar l'estat fonamental. Molts sistemes frustrats s'ordenen a baixes, o inclús zero, temperatures però també hi ha estats que no s'ordenen i que queden fora de la teoria de les transicions de fase de Landau, presentant així una estructura subjacent extraordinària. Els líquids de spin pertanyen a aquest segon tipus. El meu enfocament per a estudiar-los ha consistit en desenvolupar un nou mètode numèric fent servir unes condicions de contorn degudament dissenyades. Això m'ha permès detectar-ne inequívocament algunes de les empremtes característiques de la seva naturalesa. L'última part de la meva recerca l'he dedicada a descriure i analitzar models frustrats de spin quàntics mitjançant una tècnica anomenada *modified spin wave theory*. L'ús d'aquesta tècnica analítica m'ha permès contrastar l'aplicació i validesa de l'enfocament numèric que he desenvolupat i també m'ha permès aprofundir en l'estudi dels líquids de spin.

Finalment, voldria mencionar que la primera i tercera part de la meva tesis va ser principalment duta a terme durant els mesos que vaig passar com a investigador predoctoral visitant a la *Queen's University of Belfast* (Regne Unit) en el grup del Dr. G. de Chiara al 2016 i a la *Universität Heidelberg* (Alemanya) en el grup del Junior Prof. P. Hauke l'any 2018 respectivament.

Resumen

Mi doctorado está dedicado a analizar transiciones de fase cuánticas de naturaleza exótica en sistemas fuertemente correlacionados descritos por Hamiltonianos de espines. Por un lado, me he centrado en el estudio de transiciones de fase cuánticas localizadas cerca de puntos multicríticos. Dichos puntos son particularmente patológicos ya que diferentes fases cuánticas coexisten en una pequeña región de parámetros del Hamiltoniano. Este hecho, tal y como voy a argumentar a lo largo de la tesis, condiciona notablemente las propiedades mostradas por sistemas fuertemente correlacionados. Por otro lado, también he investigado transiciones de fase cuánticas hacia líquidos de espín que son fases exóticas de la materia que aparecen en algunos sistemas frustrados. Dichas fases se sitúan en la vanguardia de la investigación en materia condensada ya que son, teórica y experimentalmente, muy difíciles de caracterizar.

La investigación presentada se puede dividir en tres partes. La primera parte trata sobre comportamientos insólitos que sufre el entrelazamiento cuántico, más conocido como *entanglement*, en algunas cadenas de espines. La relevancia de las fluctuaciones cuánticas crece en bajas dimensiones y por lo tanto los sistemas unidimensionales ofrecen un amplio repertorio de posibilidades para analizar el papel de las fluctuaciones cuánticas en transiciones de fase cuánticas. Algunos cálculos han estado realizados en sistemas de espín 1/2 y otros en sistemas de espín 1. La segunda parte de mi doctorado trata con sistemas cuánticos frustrados y, particularmente, con la presencia de líquidos de espines. La frustración es un reflejo de la imposibilidad de satisfacer simultáneamente todas las restricciones impuestas por algunos Hamiltonianos. Es una propiedad intrínseca de algunos sistemas fuertemente correlacionados como pueden ser los hielos clásicos de espín o modelos cuánticos antiferromagnéticos en 2D. Dicha incompatibilidad hace que a menudo sea muy difícil minimizar la energía para hallar el estado fundamental. Muchos sistemas frustrados se ordenan a bajas, o incluso cero, temperaturas, pero también hay estados que no se ordenan y que quedan fuera de la teoría de las transiciones de fase de Landau, presentando así una estructura subyacente extraordinaria. Los líquidos de espín pertenecen a este segundo tipo. Mi enfoque para estudiarlos ha consistido en desarrollar un nuevo método numérico usando unas condiciones de contorno debidamente diseñadas. Esto me ha permitido detectar inequívocamente algunas de las huellas características de su naturaleza. La última parte de mi tesis la he dedicado a describir y analizar modelos frustrados de espín cuánticos mediante una técnica llamada *modified spin wave theory*. El uso de dicha técnica me ha permitido profun-

dizar en el estudio de los líquidos de espín.

Finalmente, me gustaría mencionar que la primera y tercera parte de mi tesis fue realizada principalmente durante los meses que estuve como investigador predoctoral visitante en la *Queen's University of Belfast* (Reino Unido) en el grupo del Dr. G. de Chiara en el 2016 y en la *Universität Heidelberg* (Alemania) en el grupo del Junior Prof. P. Hauke el año 2018 respectivamente.

Agraïments

Escribiendo estas lineas de agradecimiento, termino con 23 (uff!!) cursos como estudiante. Es por este motivo que me gustaría empezar por agradecer a todo y cada uno de los profesores y profesoras que he tenido a lo largo de tantos y tantos cursos de enseñanza pública, de todos he aprendido alguna cosa u otra, muchas gracias.

Cal començar amb la meva última "professora", Anna moltes gràcies per dedicar el teu temps en aquest últims 4 anys tant complicats per a tu. Ens vam entossudir en seguir una línia de recerca que quedava apartada de la resta del grup, cosa que va fer que fossis la meva única referència acadèmica dins del nostre GIQ. Per tant és evident que si he aconseguit tirar endavant una tesis doctoral és gràcies a la teva dedicació i paciència. Sembla ser que la meva vida com a científic té una aturada indefinida, però si algun dia tinc èxit professional o científicament serà també gràcies a tu.

Seguint temporalment endarrere, vull agrair en Bruno Juliá-Díaz, en Miguel Ángel García March i especialment a l'Artur Polls per confiar en mi aquell estiu del 2013 a la UB, just acabat de graduar, introduint-me per primer cop en recerca i guiant-me durant el Màster. Sense vosaltres no hagués fet mai el pas per a entrar a un doctorat en física teòrica, gràcies.

Seguim! Vull agrair a la facultat de física de l'UB per 5 anys de formació d'excel·lència. A l'Università della Calabria per quelli mesi bellissimi in una bella terra con gente maravigliosa e per regalarmi per sempre questa bella lingua. Al Institut Milà i Fontanals per formar-me en l'edat més complicada i a l'escola Mas i Perera per fer-me sortir de l'ou.

Gabriele, ti voglio reingraziare per avermi ospitato 3 mesi nella carissima e soleggiata Belfast. Thanks Christine, you know that a piece of this thesis is also yours. Grazie a vuoi e a il resto del gruppo italiano-irish-british della QUB per questi tre mesi di accoglienza.

Philipp, vielen Dank dafür, dass du mich während meiner Zeit in Deutschland bei dir aufgenommen hast! Ein ebenfalls großer Dank auch an Julius, Kevin, Jan und Ricardo, die mir den Büroalltag als fantastische Arbeitskollegen stets erheitert haben! Außerdem gilt auch ein Dank Marius und Philipp dafür, dass sie super Mitbewohner waren! Ihr alle habt dafür gesorgt, dass meine Zeit in Heidelberg meine Erwartungen übertroffen hat und ich auch ein wenig eure hartäckige Sprache lernen konnte.

Thanks to all the GIQas and GIQos, despite that I will periodically have nightmares related to some strange definition of the entropy, I will miss working in our headquarters. Sorry for not being able to attend to most of your night events. En especial, gràcies John per tanta paciència sent el meu ”jefe”en l'assignatura de MQ, el fet de donar classes a tanta gent ha sigut un aprenentatge brutal.

I would like also to thanks Verònica Aufingher, Román Orús, Simone Paganelli and Alessio Celi for agreeing to be member of my Ph.D. tribunal.

Finalment vull agrair a tothom pertanyent a l'altre formació que he tingut al llarg de la vida: Mama, Papa, Juncal, Mireia, Sergi, Iaia, cosins, cosines, tiets, tietes, avis, àvies, amigues i amics. Tot i no entendre ni un borrall a partir d'aquest pàgina, us reconfortarà pensar que també heu contribuït a escriure aquesta tesis.

Contents

Preface

The Ph.D. thesis presented here is formed by the original research articles resulting from my Ph.D. work (Part II). It is preceded by a broad introduction which presents the main concepts used along the thesis together with the original motivations of my work and the most important results that I have obtained (Part I).

The thesis is structured as follows. In Chapter 1, I present the motivations and open questions which inspired my research. This chapter also provides a general view of each article with their main results. In Chapter 2, the phenomena on strongly correlated systems which are relevant along the thesis are detailed. Chapter 3 contains different aspects on entanglement and correlations in strongly correlated systems. The spin models under study in my thesis are introduced in Chapter 4. The numerical methods which have been used to solve non-integrable spin models are explained in Chapter 5. In particular, in Sec. 5.2, I detail the novel method I have developed based on exact diagonalization with random boundary conditions, clarifying aspects of the algorithm which are not reported in the articles. I conclude Part I by summarizing the results obtained and providing some open questions and future perspectives in Chapter 6.

In Part II, the original research articles resulting from my Ph.D. are attached in their printed journal version (Articles 1 and 2). Notice as well that Article 3 is presently, at the time of the Ph.D. thesis handing, still in editorial process. As a consequence, I attach the last version, before editorial corrections. Finally, the publication of the last part of my research, covering the study of 2D frustrated spin systems by means of modified spin wave theory, is still being prepared at the time of this thesis handing. Consequently, the motivations, results and conclusions belonging to this research line are just

presented in Part I.

Finally, three appendixes are also provided. Appendix A contains a technical comparison between different modified spin wave theory approaches present in the literature. It also includes some open questions which need still to be elucidated in order to fully comprehend this approach in the triangular lattice. In Appendix B the most important MATLAB codes which I have written along the Ph.D. are provided. Finally, in Appendix C I include also the articles that have resulted from my research during my Master thesis after the graduation. Although these articles do not form part of my Ph.D. thesis defense, I include them here for completeness.

List of publications

1. A.Yuste, M. Moreno-Cardoner, and A. Sanpera. Using random boundary conditions to simulate disordered quantum spin models in two-dimensional systems. *Phys. Rev. B* **95**, 195167 (2017)

2. A. Yuste, C. Cartwright, G. D. Chiara, and A. Sanpera. Entanglement scaling at first order quantum phase transitions. *New Journal of Physics* **20**, 043006 (2018)

3. A. Yuste, D. Castells-Graells, and A. Sanpera. Signatures of quantum spin liquids in small lattices. *Phys. Rev. B*. **In editorial processing.** arxiV:1806.06542 (2018)

4.* A. Yuste, P. Hauke and A. Sanpera. A MSWT study on the anisotropic $J_1 - J_2$ model in the triangular lattice. *: **In preparation.**

Other publications

5. A.Yuste, B. Julià-Díaz, E. Torrentegui, J. Martorell, J. G. Muga, and A. Polls. Shortcut to adiabaticity in internal bosonic Josephson junctions. *Phys. Rev. A* **88**, 043647 (2013)

6. M.A. García-March, A.Yuste, B. Julià-Díaz, and A. Polls. Mesoscopic superpositions of Tonks-Girardeau states and the Bose-Fermi mapping. *Phys. Rev. A* **92**, 033621 (2015)

List of abbreviations

1QPT	First order quantum phase transition
2QPT	Second order quantum phase transition
AF	Antiferromagnetic
CPT	Classical phase transition
CSL	Chiral spin liquid
DM	Dyson-Maleev transformation
DMRG	Density matrix renormalization group
ED	Exact diagonalization
FSS	Finite size scaling
HP	Holstein-Primakov transformation
LOCC	Local operations and classical communication
LSWT	Linear spin wave theory
MERA	Multi-scale entanglement renormalization ansatz
MPS	Matrix product states
MSWT	Modified spin-wave theory
NN	Nearest-neighbors
NNN	Next-to-nearest neighbors
OBC	Open boundary conditions
PBC	Periodic boundary conditions
PEPS	Projected entangled pair states
QI	Quantum information
QM	Quantum mechanics
QMC	Quantum Monte Carlo
QPT	Quantum phase transition
QSL	Quantum spin liquid
RBC	Random boundary conditions
RG	Renormalization group
SATL	Spatially anisotropic triangular lattice
SCATL	Spatially completely anisotropic triangular lattice
TBC	Twisted boundary conditions

Part I

Condensed matter physics and quantum information. A startling interface

Motivations and main results

I landed in the group of Quantum Information and Phenomena at the Universitat Autònoma of Barcelona with a background in the theoretical and numerical study on ultracold atoms systems, the subject of my undergraduate and master thesis (see Appendix C). My interest rapidly moved onto the use of quantum information (QI) and, in particular, in the study and use of entanglement to characterize some features of strongly correlated systems. During my Ph.D., I have focused in the analysis of exotic quantum phase transitions in spin models, where quantum correlations are particularly relevant. My Ph.D. can be split into three different topics which I motivate and briefly summarize in what it follows.

The first topic I have addressed, enclosed in Article 1, is the pathological behavior of first order quantum phase transitions (1QPT) occurring in the vicinity of a second order quantum phase transition (2QPT). As it is well known, a classical phase transition (CPT) occurs as the consequence of a broken symmetry. A phase transition is crossed when an infinitesimal change on one of the parameters describing the system results into a dramatic change of the system and its order. This is the so-called Ginzburg-Landau theory of phase transitions and can also be applied to a vast majority of quantum phase transitions (QPT). In analogy to CPT, QPT can also be cataloged by their order. A QPT is called of first (or second) order, if the first (or second) derivative of the ground state energy with respect to the parameter of interest has a singular behavior. In 2002, the seminal works of Osterloh and collaborators [1] and Osborne and Nielsen [2] show that QPT can
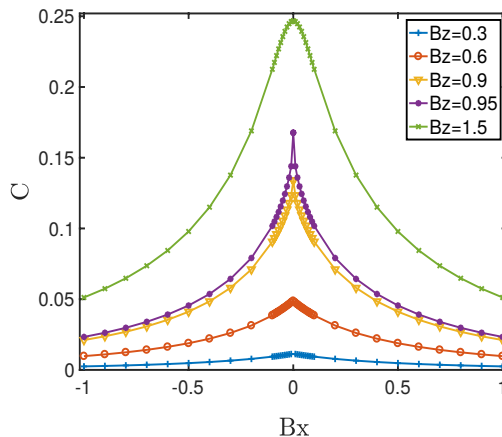
Figure 1.1: Spike in the concurrence in the spin-1/2 Ising chain with longitudinal field at $B_x = 0$ (1QPT critical point) for different values of the transverse magnetic field B_z (for more details see Article 1). This apparently controversial results was the starting point of our research.

also be understood by means of singularities of their entanglement content. Since then, many works have studied the behavior of entanglement close to a QPT. Nevertheless, we realized that the vast majority of entanglement studies were devoted to second order (also called continuous) QPT, while first order (discontinuous) QPT were much less studied. Our initial motivation was to determine whether it was always feasible to distinguish a 1QPT from a 2QPT in a spin model by means of measures of entanglement. We used as benchmark 1D spin systems, since the ground state properties can be obtained with high accuracy for reasonable large systems using density matrix renormalization group (DMRG). Naively, it would seem that a 1QPT should be easily identified by a discontinuity on a proper chosen measure of entanglement. However, we found a first counterintuitive result, illustrated in Fig. 1.1. There, the concurrence, which is a measure of bipartite entanglement between two spin-1/2 particles, shows a spike at the 1QPT critical point instead of a discontinuity. The model studied is the quantum Ising chain with transverse and longitudinal fields (see Sec. 4.2.1). As a matter of fact, such behavior apparently contradicts the theorem stated in [3] which states that for local Hamiltonians $H = \sum h_i$, where h_i is a k-body interacting Hamiltonian, the order of the QPT is indicated by the order of the singularity of the derivatives of k-entanglement measures. Further analysis brought us to understand that the expected discontinuous behavior of a 1QPT occurring in the neighborhood of a 2QPT becomes smoother due to the diverging correlation length associated to the later. To deal with such feature, a finite size

scaling (FSS) for 1QPT had been recently proposed [4], though it had never been applied to any measure of entanglement. We successfully applied the FSS to the concurrence recovering the correct thermodynamic limit. Later, in order to extend our work, we studied a spin-1 model (see Sec. 4.2.2), which has a richer phase diagram with several multicritical points and critical phases. We could identify all the 1QPT present in the model by means of the negativity, which is another measure of bipartite entanglement, and by using, again, the FSS for 1QPT. The main part of this work was done in collaboration with the group of Dr. G. de Chiara, where I spent several months at the Queen's University of Belfast.

The second part of my research, resulting in Articles 2 and 3, has focused on the study of 2D frustrated spin models. In a quantum system, frustration i.e., the impossibility of simultaneously minimizing all local energy constrains, together with quantum fluctuations may lead to non trivial disordered phases of matter. In particular we have been interested in quantum spin liquids (QSL) phases, (see Sec. 2.3), which are present in some spin models like for instance the Heisenberg model in the anisotropic antiferromagnetic (AF) triangular lattice with nearest-neighbors (NN) interactions. Motivated by the calculations performed to simulate the Fermi-Hubbard model on a square lattice using random boundary conditions (RBC) [5], we realized that a similar scheme could be implemented for detecting quantum spin liquids. In Ref. [5], the quantities of interest were calculated by performing an average over all random configurations, a technique that strongly mitigates finite size effects. Our initial idea was to apply in a similar way RBC to the triangular lattice to mitigate finite size effects and obtain significant results in small lattices. As a benchmark we studied Heisenberg models in the spatially anisotropic triangular lattice, a model also known as SATL (see Sec.4.3), where previous works using variational methods pointed towards the existence of a gaped QSL phase. In the first results obtained, we were considering an average over all the random boundaries. However, the results were not very promising. Then, we realized that when doing the average there were random configurations which lead to the wrong order. That is because every diagonalization in a small lattice imposes extra symmetries which may lead to an erroneous ground state. The following reflection was made. On the one hand, in the ordered phases, such configurations lead to an increase of the energy with respect to the ones which do recover the correct order. On the other hand, in quantum disordered phases, where no symmetries are broken, many of the random boundary configurations may lead to an energy close to the minimal one. With this idea in mind, we decided to count how many ground states generated with random boundary conditions
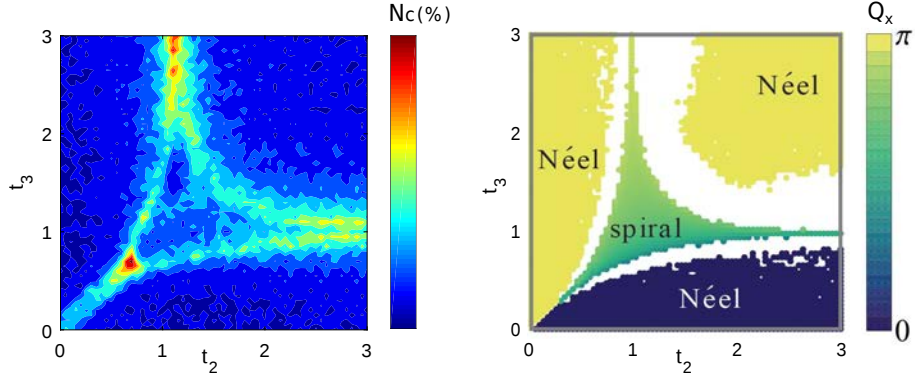
Figure 1.2: Left, number of configurations, N_c, with a normalized energy below a bias for the SCATL model with XY interactions with lattice geometry 4x3 (for more details see Article 3). Right, phase diagram of the SCATL as obtained with MSWT taken from Ref [6]. The maxima in N_c are located in the anisotropy values where the MSWT study signal gaped QSL phases (white colored region).

could lead to the correct ground state energy of the system. We considered that quantity, denoted as N_c (number of "degenerate" ground state configurations), as a figure of merit, since it could provide an important hint on the real degeneracy of the ground state of a QSL. The comparison between N_c and a proper study of the quantum phase diagram of the model is depicted in Fig. 1.2. In the areas of the phase diagram where a QSL is predicted in the literature, the number of configurations with an energy close to the minimal one is substantially larger as our intuitive argument suggested. We decided then, to post-select such configurations to do the average over the quantities of interest. In Article 2, the study of the SATL model with our method was provided and the quantum phase diagram of the model obtained. Remarkable enough, such quantum phase diagram is pretty close to the ones previously derived in the literature by means of much more sophisticated methods. In Article 3, I successfully extended my method to two other more complex models in the triangular lattice: the SCATL and the $J_1 - J_2$ model, which contains next-to-nearest neighbors (NNN) interactions (see Sec. 4.3). Furthermore, this second article contained also an study on entanglement whose results were in accordance of what we could expect for a QSL. In the putative QSL phases it is observed both, an increase of the geometrical measure of entanglement and large fluctuations of the arrangement of bipartite entanglement among different configurations. These features are also in accordance with the properties of QSL. To the best of my knowledge, our method is the first one able to find QSL signatures in 2D quantum frustrated
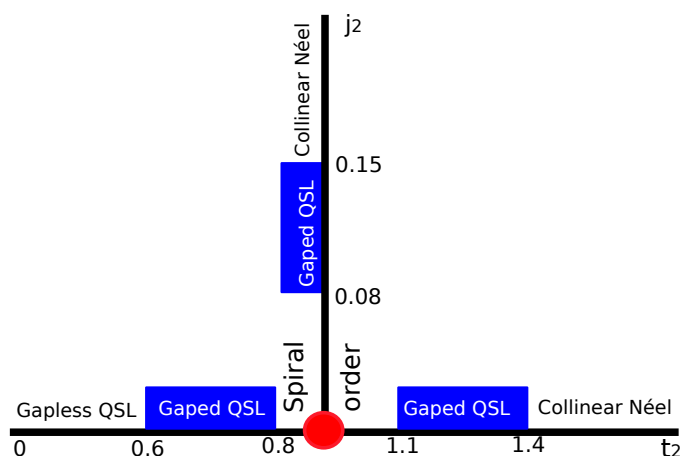
Figure 1.3: Scheme of the original idea consisting of connecting the gaped QSL phases present in both the SATL (horizontal phase diagram) and $J_1 - J_2$ models (vertical phase diagram). The red dot signals the intersection of both models, the isotropic triangular lattice with NN interactions, which contains spiral long-range order.

models for such small lattices.

Finally, during the last part of my research, I studied 2D frustrated spin models by using modified spin wave theory (MSWT). This analytic semiclassical tool consists of a mean field approach where quantum fluctuations only slightly peruturb the long-range ordered state of the classical model, (see Sec. 5.4). It was firstly developed for the AF square lattice by Takahashi, [7] and has been recently applied on the triangular lattice by P. Hauke and co-authors, [8], whom I visited and joined his group for a few months in 2018. The initial motivation was twofold. First, we wanted to rigorously extend the derivation of MSWT in the triangular lattice for the Heisenberg model as it was done for the XY model [9]. As a matter of fact, we realized that the original work using MSWT to solve the Heisenberg model in the triangular lattice, [10], presented some caveats which we wanted to address. The second motivation was to apply, for the first time, MSWT on the $J_1 - J_2$ model which we had previously studied in Article 3. For this model, in contraposition to the SATL, all recent numerical works converge into a gapped QSL between commensurate spiral and collinear Néel orders. However, our calculations with MSWT could not signal any intermediate phase. Despite we cannot formally prove it yet, our preliminary results indicated that MSWT cannot detect a QSL phase which is located between two commensurate orders. A possible way we found to check for such a conjecture was to invent a hybrid

model which could smoothly connect the apparently different QSL phases as schematically shown in Fig. 1.3. Our premises were that in the isotropic NN case, the addition of anistropy (SATL model) leads to a QSL phase between non-commensurate spiral order and collinear Néel order which can be detected by means of MSWT [8]. We wondered whether it was possible to connect continuously the QSL present in both phase diagrams. We called this new hybrid model the anisotropic $J_1 - J_2$ triangular lattice. We studied it using both MSWT and RBC leading to a positive answer to the above question. Since the manuscript corresponding to this last part of my research is not ready in the time of the thesis handing, I provide some of the results in Sec. 4.3.3, which is devoted to the above mentioned hybrid model.

In what it follows, I provide the basic tools, techniques and concepts I have used along my P.h.D. thesis. Chapter 2 summarizes some basic concepts of physics in strongly correlated systems. In particular, I define first the basic notions of QPT. Then, I focus on quantum frustrated Hamiltonians providing a brief report of what is up to now understood by quantum spin liquids. In Chapter 3, I present the main tools I have used to quantify and detect entanglement in 1D and 2D spin models, both for spin-1/2 as well as for spin-1 models. Chapter 4 and 5 constitute the main body of my Ph.D. thesis and therefore are significantly more extended. Chapter 4 deals with the spin models I have considered along the thesis, and explains the open questions I have addressed and the solutions I have provided. Chapter 5 gives a detailed explanation of the numerical approaches I have developed along my Ph.D. thesis to address and solve the questions that puzzled me regarding the exact nature of some exotic quantum phase transitions. Finally, in Chapter 6 I present the conclusions of my research as well as the open questions that need still to be addressed in the path to understand how matter organizes itself under strong correlations. These chapters contextualize the research done in the articles presented in Part II and provide some of the most relevant literature on the field.

CHAPTER 2

Strongly correlated systems

During my Ph.D., I have focused on several phenomena in strongly correlated systems. In this chapter, I give a brief introduction to these topics providing the most relevant features and literature. In Sec. 2.1 I introduce the concept of a quantum phase transition. Sec. 2.2 is devoted to the phenomenon of frustration in quantum systems. I conclude this chapter by providing an introduction to quantum spin liquids in Sec. 2.3.

2.1 Classical and quantum phase transitions

In a classical system, thermal fluctuations may induce sudden changes on physical quantities, such as e.g., the density, upon a variation of its thermodynamic propierties. Classical phase transitions can be understood within the Landau-Ginzburg theory, which associates the spontaneous breaking of a symmetry with the change of one of the parameters describing the system [11, 12]. The competition between the energy and the entropy of the thermal fluctuations is the responsible for this sudden reorganization of the particles. In a CPT, one finds singular behaviour in the thermodynamic functions. First (second) order CPT display singular behaviour in the first (second) derivative of the partition function $\mathcal{Z}$. For second order (or continuous) CPT this critical phenomena is well understood within the renormalization group (RG) theory [13]. The critical behavior of the physical quantities can be described by a few universal critical exponents which do not depend on the details of the physical system but only on its dimension or on the range

of the interactions, (see e.g.,[14, 15]). For first order (or discontinuous) CPT finite size effects have also been studied [16–18].

As the temperature is lowered, thermal fluctuations, and therefore the entropy related to them, become less relevant. For sufficiently small temperature, T, any CPT is suppressed and in the limit of $T = 0$ any degree of freedom is frozen. In a quantum system the situation changes due to quantum fluctuations. Even at T=0, a system may change its properties by the change of some external parameter, λ, of the Hamiltonian,

$$H = H_0 + \lambda H_1, \tag{2.1}$$

where $[H_0, H_1] \neq 0$. Quantum phase transitions [19] describe abrupt changes in the ground state of a quantum system at a certain critical value λ_c. Note that since the transitions occurs at zero temperature, the system is always in the ground state and the transition is exclusively driven by quantum fluctuations and not by thermal ones. Some QPT can also be classified as first/second order when they show singular behavior on the first/second derivative of the ground state energy respectively. These QPT can also be associated to a symmetry breaking which leads to a change of an order parameter. This allows to apply similar finite size scaling ansatz as in the CPT case. However, in quantum system there are other kinds of order, e.g., topological order [20, 21] which cannot be associated to a symmetry breaking. In such cases, the classical Landau-Ginzburg theory falls and new kinds of order, associated to rich patterns of many-body entanglement arise [22]. The phenomena of QPT (which fall or not inside the Landau-Ginzburg theory), has been reinterpreted by studying entanglement close to critical points, see the seminal works [1, 2]. Since then, a large amount of work has been devoted to deepen the connections between quantum information and QPT, see for instance [23–33] and Article 1.
Finally, it is imperative to mention that QPT can also occur at non zero temperature [19]. These cases, which are studied by means of quantum thermodynamics theory [34, 35], are out of the scope of this thesis.

2.2   Frustration

Often, the Hamiltonians representing strongly correlated systems are local (short range) and can be written as,

$$H = \sum_i h_i. \tag{2.2}$$
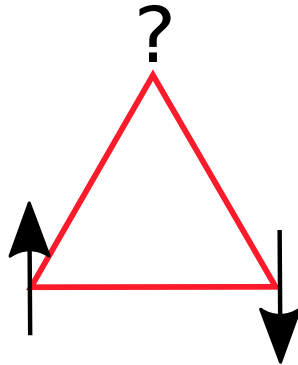
Figure 2.1: Frustration in the AF triangular lattice. All the spins cannot be simultaneously anti-parallel.

Frustration arises when all the local Hamiltonians cannot be simultaneously in their ground state [36]. To determine whether a Hamiltonian is frustration-free is a NP-Hard problem [37]. A paradigmatic example are 2D antiferromagnetic spin models (e.g.,[38–40]). An illustration of frustration induced by the geometry of the triangular lattice can be seen in Fig. 2.1. It can also take place in simple structures (e.g., a 2D square lattice), if some interactions are ferromagnetic while others are AF or, for instance, there are second neighbors terms. The study of frustrations is also relevant in the framework of high-T_c superconductivity [41, 42], and in spin glasses, which are phases appearing in frustrated disordered systems [43].

Frustration may lead to a degeneracy in the ground state and to a non-trivial arrangement of the spins which can even suppress long-range order at zero temperature leading to exotic phases of matter [44].

2.3   Quantum spin liquids

Quantum spin liquids are quantum disordered nonmagnetic phases that do not spontaneously break the spin rotation and discrete translational symmetry of the spin Hamiltonian [45–47]. This lack of order, which survives even at zero temperature, is originated by strong quantum fluctuations on the spin orientations and prevents their characterization by means of local order parameters. They are characterized by a massive degenerated ground state which is highly entangled. They display unique physical features such as exotic non-local excitations [47] and topological propierties [48, 49]. Recently, they have been proven to be the ground state of some Hamiltonians [39, 50] and QSL candidates have been experimentally discovered in a vast

range of materials [51–61].

QSL are often caricatured as a liquid of singlets which are formed between nearby spins and which strongly fluctuate from one configuration to another. Due to such fluctuations, the ground state of the system is far from a product state, implying that entanglement in QSL plays a crucial role. Ground states of local spin Hamiltonians are normally short range entangled, as evidenced by the fact that the entanglement entropy, $\mathcal{S}$, of any bipartite cut of the system follows an area law,

$$\mathcal{S}(L) \sim L^{D-1}, \tag{2.3}$$

where D is the dimension of the system and L the linear size of the boundary separating both regions. Corrections to this law appear, for instance, in critical gapless quantum phases or in topologically ordered states. In 2D, the later fulfill $\mathcal{S}(L) \sim L + b_0 \gamma$, where γ is a universal correction, called topological entanglement entropy, which is independent of the lattice size and signals topological order [62–64]. In the following, I briefly describe the main characteristics of both topological and critical QSL. For an extense comparision I refer to Ref. [44].

Topological spin liquids

Topological QSL are characterized by a ground state degeneracy which depends on the topology of the system. They are locally indistinguishable meaning that they cannot be detected or distinguished using local measurements which makes them a promising candidate for quantum storage memories. Indeed, they are thought to play a key role in topological quantum computation, [65]. They are gaped and can hold exotic delocalized excitations, as the so-called spinons, which are neutral in charge and have spin 1/2, and can be seen as free delocalized spins which do not form any singlet. Topological QSL can be classified according to their topological order [49]. For a detailed list on all the possible quantum topological phases of matter known up to now see Ref. [21].

Critical spin liquids

Critical QSL, also denoted as algebraic QSL, have gapless bulk excitations. They have decaying power law correlations but no true long range order. They are usually pictured as valence bonds between pair of spins separated by arbitrary distances. The spinons, in contraposition in topological spin-liquids, interact with this valence bond background and cannot be

considered as free particles. A prominent example of a critical QSL is the ground state of the spin-1/2 AF Heisenberg chain which can be analytically solved by Bethe ansatz [66].

CHAPTER 3

Entanglement in many-body systems

In this chapter, I briefly present the measures of entanglement which I use along the thesis. First, in Sec. 3.1, I motivate the chapter by providing a brief introduction to entanglement and its relevance within quantum mechanics (QM). Then, in Sec. 3.2, I define the measures of bipartite entanglement (for pure and mixed states) and multipartite entanglement. I conclude in Sec. 3.3 with an overview of the entanglement area law and some of its consequences.

3.1 Introduction

Quantum mechanics is inherently non local [67]. Entanglement, which is the expression of this non local nature, has played a central role in the comprehension and development of quantum physics. This "spooky action at a distance" was initially seen, indeed, as the quantum effect which most in contradiction got with the classical physics intuition [68]. It was after Bell's seminal work [69, 70] and specially after the experimental verification of his inequalities [71] when entanglement became also a quantitative measure of quantum correlations. During the 1990's, with the birth and development of quantum information [72], entanglement was reinterpreted as a resource capable of realizing tasks which go beyond classical physics, e.g., teleportation [73], quantum cryptography [74] or quantum computation algorithms [75]. The study of entangled many-body systems lies at the interface between QI theory, condensed matter physics and quantum field theory. For a review on entanglement in many-body systems see Refs. [76–78]. A

paradigmatic example is the development of tensor networks [79–82], a very efficient numerical descriptions of many-body states which has been developed with QI tools.

What is entanglement?

The state of a quantum system which is composed of N subsystems given by $\rho_{1,2,...,N} \in \mathcal{H}_1 \otimes \mathcal{H}_2 \otimes ... \otimes \mathcal{H}_\mathcal{N}$ is separable when it can be written as,

$$\rho_{1,2,...,N} = \sum_i p_i(\rho_i^1 \otimes \rho_i^2 \otimes ... \otimes \rho_i^N). \tag{3.1}$$

Otherwise, it is said that the state is *entangled*.

3.2 Measures of entanglement

In general, to establish whether a system is entangled or not is, by no means, an easy task. In addition, apart from certifying the presence of entanglement, one is interested in quantifying it. A measure of entanglement, $\mathcal{E}(\rho)$, quantifies the amount of entanglement in a quantum state ρ. Defining proper measures of entanglement is a field of research itself [83, 84]. Some properties which a measure of entanglement must fulfill are:

- For a separable state, $\mathcal{E}(\rho) = 0$.

- $\mathcal{E}$ does not increase under local operations and classical communication (LOCC), i.e., if Λ is a LOCC map, $\mathcal{E}(\Lambda(\rho)) \leq \mathcal{E}(\rho)$

Other properties such as convexity, additivity and continuity can also be required, [85, 86]. In what it follows I define some of the most relevant measures of bipartite and multipartite entanglement which I have considered along my research.

3.2.1 Bipartite entanglement: Schmidt decomposition and entanglement entropy

Consider a bipartite state, $|\psi\rangle_{AB}$, acting on $\mathcal{H}_A \otimes \mathcal{H}_B$. Any measure of bipartite entanglement, $\mathcal{E}$, is lower and upper bounded by two measures which are conceptually very important [86]. The lower bound measure, called entanglement of distillation $\mathcal{E}_D$, is defined as the optimal rate of maximally entangled states (e.g., singlets in spin-1/2 systems) which can be distilled from $|\psi\rangle_{AB}$ by means of LOCC. The upper bound is the entanglement cost,

$\mathcal{E}_C$, and it is defined as the rate of maximally entangled states needed to create $|\psi\rangle_{AB}$ using LOCC. Both quantities are defined in the asymptotic limit and are not, indeed, very practical since they require an optimization over the LOCC set.

It is always possible to write $|\psi\rangle_{AB}$ as the so called Schmidt decomposition,

$$|\psi\rangle_{AB} = \sum_{i=1}^{M} \sqrt{\lambda_i}(|e_i\rangle \otimes |f_i\rangle)). \tag{3.2}$$

Here, $|e_i\rangle$ and $|f_i\rangle$ form an orthonormal basis in $\mathcal{H}_{\mathcal{A}}$ and $\mathcal{H}_{\mathcal{B}}$ respectively. λ_i are the Schmidt eigenvalues which are positive, real and $\sum_{i=1}^{M} \lambda_i = 1$. The Schmidt decomposition of a pure uncorrelated (entangled) state has one (more than one) Schmidt eigenvalue.

As a measure of bipartite entanglement for a pure states, it is often used the Von Neumann entropy,

$$S(\rho_A) = -\operatorname{Tr} \rho_A \log_2 \rho_A = S(\rho_B). \tag{3.3}$$

Using the Schmidt decomposition, it can be written as $S(\rho_A) = -\sum_i \lambda_i \log(\lambda_i)$. This quantity is often also called entropy of entanglement. For pure states, the Von Neumann entropy coincides with the entanglement of distillation and the entanglement cost [87].

3.2.2 Pairwise entanglement in spin-1/2 mixed states: Concurrence

All the measures of bipartite entanglement for pure states are function of the eigenvalues of the reduced density matrix with respect to the chosen partition and all of them are in one to one correspondence [88]. For mixed states, such correspondence only occurs for spin-1/2 systems. It is customary to choose the concurrence, $\mathcal{C}$ [89], as the measure of bipartite entanglement which is defined for any two spin-1/2 i, j in the mixed state $\rho_{ij} = \operatorname{Tr}_{k\neq ij}(|\psi_p\rangle \langle\psi_p|)$. It is defined as,

$$\mathcal{C}_{ij} = \max(0, \mu_1 - \mu_2 - \mu_3 - \mu_4), \tag{3.4}$$

where μ_k are the eigenvalues in decreasing order of the matrix $R_{ij} = (\rho_{ij}\rho'_{ij})^{1/2}$ and $\rho'_{ij} = (\sigma^y \otimes \sigma^y)\rho^*_{ij}(\sigma^y \otimes \sigma^y)$. Here σ refers to the usual Pauli matrices.

3.2.3 Bipartite entanglement in mixed states: Negativity

The negativity [90, 91], $\mathcal{N}$, is a bipartite measure of entanglement for mixed states beyond spin-1/2. It is based on the partial transpose of the density

matrix of the whole system with respect to one of the two subsystems. It is defined as,

$$\mathcal{N}(\rho) = \frac{||\rho^{T_B}||_1 - 1}{2},$$ (3.5)

where the operation T_B is the partial transpose defined now on the reduced density matrix of two spins, ρ^{ij}, and $||...||_1$ is the sum of the absolute value of all singular values. Notice that the negativity is a lower bound to entanglement.

3.2.4   Multipartite entanglement: Geometrical entanglement

Quantifying multipartite entanglement is even a more challenging task. One of the most used measure of multipartite entanglement is the geometrical entanglement. It "measures" the distance of a state to its closest separable one

$$\Lambda_{\max} = \max_{|\phi_{\mathrm{prod}}\rangle} |\langle \psi_p | \phi_{\mathrm{prod}} \rangle|,$$ (3.6)

where $|\phi_{\mathrm{prod}}\rangle = \otimes_{i=1}^N |\phi_i\rangle$ and the maximization is performed over the set of all separable (non entangled) states. The larger $\Lambda_{\max}$ is, the lower the entanglement of $|\psi_p\rangle$ is since it is closer to a product state. It makes sense to define the geometric entanglement [92] as:

$$E_G = 1 - \Lambda_{\max}.$$ (3.7)

Geometrical entanglement considers all type of possible multipartite entanglement and clearly goes beyond bipartite entanglement.

3.3   The area law

In black hole physics, it was already seen that the entanglement entropy of the ground state of a free scalar bosonic field obeys the area law [93, 94],

$$S(\rho_A) = aL^{d-1} + ...$$ (3.8)

where a is a constant and d is the dimension of the system. Such behaviour is also found in condensed matter physics, where non critical ground states which have a finite correlation lenght also fulfill that the bipartite entanglement between the two parts of a system after an arbitrary cut depend on the boundary between them and not the volume [95, 96]. Indeed, entanglement is bounded for the ground states of gapped 1D quantum systems. On

the contrary, critical 1D systems described by conformal field theory (CFT) exhibit a logarithmic violation of the area law, [95]. Corrections to the area law for higher dimensions have been reviewed in [97].

Density matrix renormalization group (see Sec. 5.3) is a numerical algorithm which is very efficient for systems which contains a small amount of entanglement, [98]. This is so because they generate a very particular class of states, the matrix-product state (MPS) [99], whose efficiency in describing ground states of many-body quantum systems is deeply coupled to their entanglement scaling [100]. This makes MPS (and in extension DMRG), a very suitable tool to study 1D gapped quantum systems. The 2D version of MPS, called projected entangled pair state (PEPS), represents 2D states which strictly fulfill the area law [101]. PEPS can efficiently describe 2D gapped spin systems and even also critical and topological ones. Finally, it is worth mentioning that other approaches have been considered to study critical states. One example is the multi-scale entanglement renormalization ansatz (MERA), proposed by Vidal [102].

CHAPTER 4

Spin models under study

In this chapter, I briefly introduce the spin models under discussion during my Ph.D. providing their main relevant characteristics and quantum phase diagram. I start by a general introduction to spin models in Sec. 4.1. Then, in Sec. 4.2, I introduce the spin chain models which are under study in Article 1: the spin-1/2 Ising chain with longitudinal field (4.2.1) and the spin-1 XXZ chain with uniaxial single-ion anisotropy (4.2.2). Finally, Sec. 4.3 is devoted to the spin systems in the AF triangular lattice which are under study in Articles 2 and 3. In concrete, the spatially anisotropic triangular lattice (4.3.1), the $J_1 - J_2$ model (4.3.2) and a hybrid model merging both of them (4.3.3).

4.1   Introduction to spin models

In the 1920s, statistical mechanics models, as the well known Ising model, were studied in order to unveil the phase transitions present in ferromagnetism. Contemporaneously, the birth of quantum mechanics introduced the quantization of angular momentum and the concept of a spin, i.e., the intrinsic angular momentum of elementary particles. In 1926, Heisenberg and Dirac independently discovered the exchange interaction which is a quantum effect that rules the interaction among spins. Consequently, the study of ferromagnetism was necessarily coupled to quantum mechanics. Since the first proposed model, the so called Heisenberg model, quantum spin systems have been a vast field of research providing a benchmark to mathematicians,

theoretical and experimental physicists.

For the sake of concreteness, the quantum spin systems considered here have N spin-S particles with $2S+1$ internal degrees of freedom in a D-dimensional lattice. The most general Hamiltonian considered in the thesis can be written as,

$$H = \sum_{\substack{i,j;i\neq j \\ \alpha=x,y,z}} J_{ij}^{\alpha} S_i^{\alpha} S_j^{\alpha} + H_{ext} \qquad (4.1)$$

where i and j run over all the lattice sites. The lattices under consideration along this thesis are 1D lattices, the so called spin chains, and the 2D triangular lattice. The S_i^{α} are spin operators on lattice site i which fulfill the usual angular momentum relations,

$$[S_j^{\alpha}, S_j^{\beta}] = i \sum_{\gamma} \epsilon_{\alpha\beta\gamma} S_j^{\gamma} \qquad (4.2)$$

and commute when they are not on the same lattice site. The coefficients J_{ij}^{α} quantify the exchange interaction among spins which may be positive (negative) for antiferromagnetic (ferromagnetic) interactions. Finally H_{ext} accounts for any Hamiltonian term aside of spin-spin interactions, as for instance, external magnetic fields interacting with all the spins. The spin models which I introduce below can all be obtained from the Hamiltonian above.

4.2   Spin chains

Numerical studies on 1D quantum spin systems, or quantum spin chains, are a very suitable benchmark for the study of QPT. With the development of DMRG, it is possible to obtain the ground state of non integrable 1D models with very high accuracy. I briefly describe in this section the two models considered in Article 1 and provide their quantum phase diagram.

4.2.1   Spin-1/2 Ising chain with longitudinal field

The spin-1/2 Ising chain with transverse field at zero temperature is a well known integrable model which has a 2QPT between the ferromagnetic and the paramagnetic phases,

$$H = -J \sum_{i=1}^{N-1} S_i^x S_{i+1}^x - B_z \sum_{i=1}^{L} S_i^z \qquad (4.3)$$
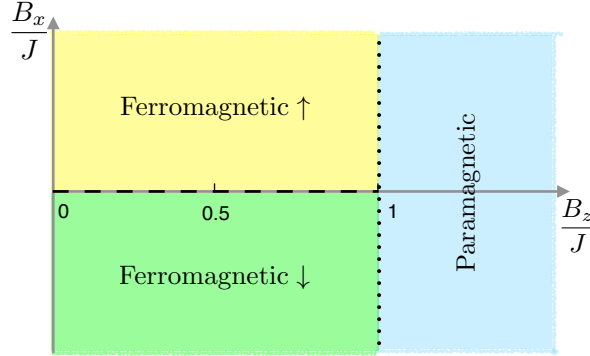
Figure 4.1: Phase diagram for the spin-1/2 Ising chain with a longitudinal and a transverse field. The dashed line (- - -) depicts the 1QPT while the dotted line (...) the 2QPT.

where S_i^α are the Pauli matrices for spin-1/2 on site i. Without losing generality, it is settled $J = 1$ and $B_z \geq 0$. The ground state of the model can be found by means of a Jordan-Wigner transformation plus a Bogoliuvov transformation. Adding a longitudinal field to the Ising chain removes the integrability of the model,

$$H = -J \sum_{i=1}^{N-1} S_i^x S_{i+1}^x - B_z \sum_{i=1}^{N} S_i^z - B_x \sum_{i=1}^{N} S_i^x. \tag{4.4}$$

Nonetheless, the phase diagram remains quite simple, see Fig. 4.1. For $B_x = 0$, where the system reduces to the integrable Ising model, there is a 2QPT at $B_z = 1$ between the ferromagnetic $(B_z < 1)$ and paramagnetic phases $(B_z > 1)$. When the system is in the ferromagnetic phase, a 1QPT takes place at $B_x = 0$ between the two ferromagnetic ground states, ferromagnetic ↑ and ferromagnetic ↓. This transition can be detected by a discontinuity in the magnetization, $M_x = \sum_i \langle S_i^x \rangle$, which passes from positive to negative values.

4.2.2 Spin-1 XXZ chain with uniaxial single-ion anisotropy

The second model considered is the spin-1 XXZ chain with uniaxial single-ion anisotropy,

$$H = \sum_{i=1}^{N-1} \left[J S_i^x S_{i+1}^x + J S_i^y S_{i+1}^y + J_z S_i^z S_{i+1}^z \right] + D \sum_{i=1}^{N} (S_i^z)^2, \tag{4.5}$$

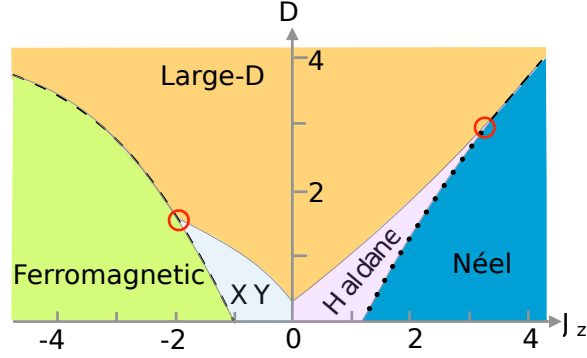Figure 4.2: Phase diagram for the spin-1 model in Eq. (4.5) with $D > 0$. The dashed lines depict 1QPT. The black dotted line depicts the 2QPT between Haldane and Néel phases. The red circles signal the tri-critical points present in the phase diagram.

where S_i^α are the spin-1 matrices for spin i and D is the uniaxial single-ion anisotropy which is taken as positive. It is also settled $J = 1$ and used as the unit of energy. This model has a rich phase diagram [103], schematically shown in Fig. 4.2, with several 1QPT which are depicted with dashed lines. Aside from the two "classical" phases: ferromagnetic (all spins aligned along one direction) and antiferromagnetic Néel order (spins orientated up-down along one direction) the system presents several quantum phases which cannot be found in spin-1/2 systems: a large D-phase (all spins in the component $S_z = 0$ of spin 1), a Haldane phase (which is topological) and the XY phase (ferromagnetic in the XY plane).

4.3   The spin-1/2 antiferromagnetic triangular lattice

The magnetic properties of spin-1/2 systems interacting in an AF triangular lattice with NN Heisenberg interactions have been under study for several decades. The present frustration in the triangular lattice geometry makes the nature of the ground state a very subtle feature. In 1973, a spin-liquid ground state was conjectured by Anderson in the form of a resonating valence bound state [104]. However, many years later several numerical works suggested a long range Néel ordered state [105–107], which was finally ratified in [108, 109]. Nonetheless, these studies also pointed that the model could be close to a quantum critical point towards a gaped QSL phase merging with Anderson's original idea. In what it follows I consider three models in the triangular lattice where the enhancement of frustration leads to QSL phases.
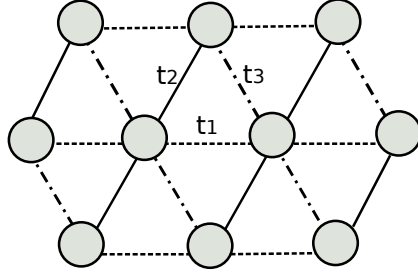
Figure 4.3: Scheme of the spatially completely anisotropic triangular lattice. The different line styles depict the anisotropy present in the model.

4.3.1 Anisotropy in the triangular lattice, SATL and SCATL

One possible way to further enhance the frustration of the model is by adding anisotropy in the direction bounds. The Hamiltonian reads,

$$H = \sum_{<i,j>} t_{ij} \left(S_i^x S_j^x + S_i^y S_j^y + \lambda S_i^z S_j^z \right), \tag{4.6}$$

where $\langle i, j \rangle$ are NN in the triangular lattice. The parameter λ is introduced to consider both the case of XY interactions ($\lambda = 0$) and Heisenberg interactions ($\lambda = 1$). The anisotropy of the model is given by the different interaction strengths (t_1, t_2, t_3) along the lattice directions (see Fig.4.3). Without loosing generality, it is settled $t_1 = 1$ and t_2, t_3 can be considered as free parameters. This model is known as the spatially completely anisotropic triangular lattice (SCATL). Up to my knowledge, it has only been studied by means of MSWT [6] and in Article 3. The case $t_2 = t_3$, known as spatially anisotropic triangular lattice (SATL), has been, on the contrary, extensively studied [8, 110–114]. This model has also been experimentally used to describe some materials as Cs_2CuCl_4 [61] or $\kappa-(ET)_2Cu_2[N(CN)_2]Cl$ [54].

Classical phase diagram

A better understanding of the quantum phases can be obtained by previously analyzing the classical phase diagram of the model. This helps to identify "classical" orderings appearing also in the quantum case. The spins are substituted by classical unit vectors and therefore angular momentum commutation relations are not fulfilled. Concretely, the spin operators in Eq.4.6 are replaced by the classical rotor: $\vec{S}_i = (\cos(\vec{Q}^{cl} \cdot \vec{r}_i), \sin(\vec{Q}^{cl} \cdot \vec{r}_i))$,

where $\vec{Q}^{cl}$ corresponds to the classical ordering vector. The energy per site is

$$H = \cos Q_x^{cl} + t_2 \cos(Q_x^{cl}/2 + \sqrt{3}Q_y^{cl}/2) + t_3 \cos(Q_x^{cl}/2 - \sqrt{3}Q_y^{cl}/2). \quad (4.7)$$

Note that this expression is independent of λ and therefore the classical phase diagram is the same for both Heisenberg and XY interactions. Minimizing over the ordering vector, i.e., $\dfrac{\partial H}{\partial Q_x^{cl}} = \dfrac{\partial H}{\partial Q_y^{cl}} = 0$, leads to a region in the phase diagram with continuously varying $\vec{Q}^{cl}$, described by the following equations:

$$
\begin{aligned}
Q_x^{cl} &= \ \pm \arccos\left[\frac{t_2 t_3}{2} - \frac{t_2^2 + t_3^2}{2t_2 t_3}\right] \quad if \quad \frac{t_2 t_3}{2} - \frac{t_2^2 + t_3^2}{2t_2 t_3} \leq 1 \\
Q_y^{cl} &= \ \pm\frac{2}{\sqrt{3}} \arccos\left[\mp\left(\frac{t_2 + t_3}{2t_2 t_3}\right)\sqrt{t_2 t_3 + 2 - \frac{t_2^2 + t_3^2}{t_2 t_3}}\right],
\end{aligned}
\quad (4.8)
$$

where the argument of Q_y^{cl} is negative if the corresponding Q_x^{cl} satisfies $|Q_x^{cl}| \leq \pi$, and positive otherwise. The classical phase diagram is depicted in Fig. 4.4, together with the representative spin structure factor of each phase which is defined as,

$$S(\vec{k}) = \frac{1}{N}\sum_{i \neq j} e^{-i\vec{k}\cdot(\vec{r}_i - \vec{r}_j)}\langle S_i S_j \rangle. \quad (4.9)$$

First, I describe the 1D lattice limit corresponding to (1) $t_2 = t_3 = 0$; (2) $t_2 \to \infty, t_3 = 1$; and (3) $t_3 \to \infty, t_2 = 1$ as shown in Fig. 4.4. For these cases, the lattice becomes a system of uncorrelated chains and the corresponding phases are 1D Néel ordered along the dominant lattice coupling and uncorrelated along the other two. This is clearly shown in the corresponding static spin structure factors which are constant along the direction perpendicular to the correlated chains. At the isotropic point ($t_2 = t_3 = 1$), indicated by (4) in Fig. 4.4, the system has spiral order (Néel 120°) with maxima in the structure factor at all the vertices of the reciprocal lattice cell. This phase extends as incommensurate spiral order smoothly merging with the classical 2D Néel phases corresponding to $t_i = t_j >> t_k$, where the lattice deforms into diamond lattices along the two dominant directions, indicated by (5,6,7). This completes the classical phase diagram of the model. Finally, a symbolic sketch of the spin orientations for each phase is also provided.
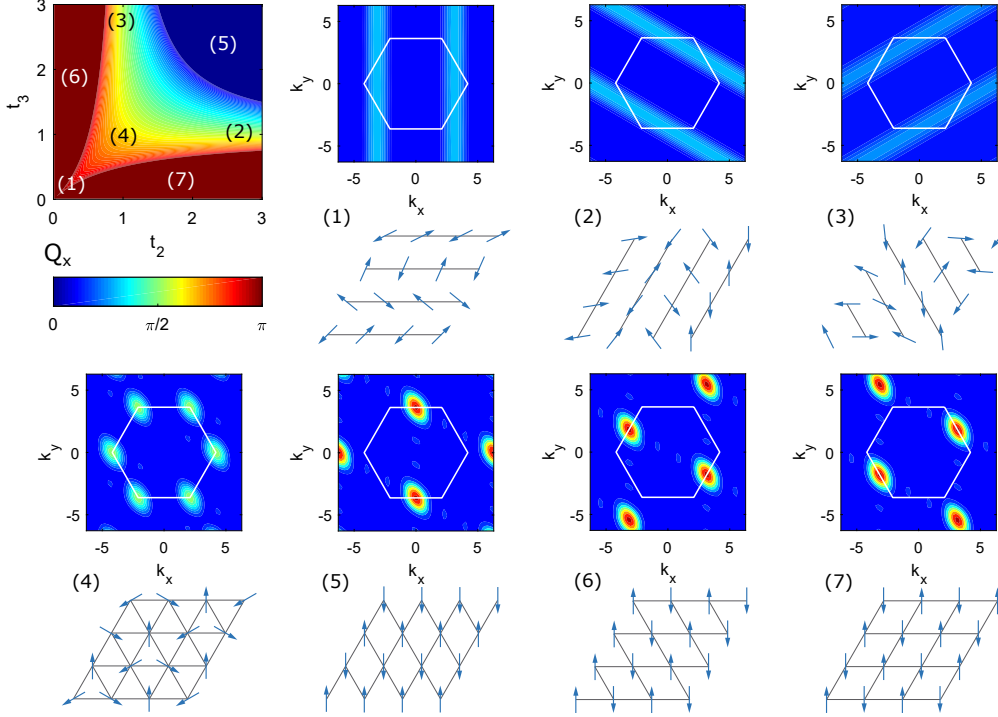
Figure 4.4: Classical phase diagram for the SCATL for both XY ($\lambda = 0$) and Heisenberg ($\lambda = 1$) interactions, obtained by plotting Q_x in Eq. (4.8) as a function of the anisotropy (top left). The other panels show the spin structure factor and a sketch of the spin order for each classical phase.

Quantum phase diagram

The main features of the SATL quantum phase diagram have been extensively studied using several methods. For instance, by means of variational quantum Monte Carlo (QMC) in [110], using tensor networks (PEPS) in [112], using MSWT in [8] and also by us in Article 2 by means of RBC. Note that, although the classical phase diagram is the same for both Heisenberg and XY interactions, they may differ in the quantum case. In Fig. 4.5 (a), the phase diagram for XY interactions obtained with RBC is provided. The addition of spatial anisotropy enhances quantum fluctuations which favors 2D-Néel order beyond the classical value $t_2 = 2$. Around $1.4 \lesssim t_2 \lesssim 1.6$ ($1.15 \lesssim t_2 \lesssim 1.3$) for XY (Heisenberg) interactions magnetic order is suppressed and a gapped QSL is predicted. The incommensurate spiral phase is shrunk in comparison with the classical case, specially for Heisenberg interactions. A second gapped QSL phase is found around $0.5 \lesssim t_2 \lesssim 0.7$
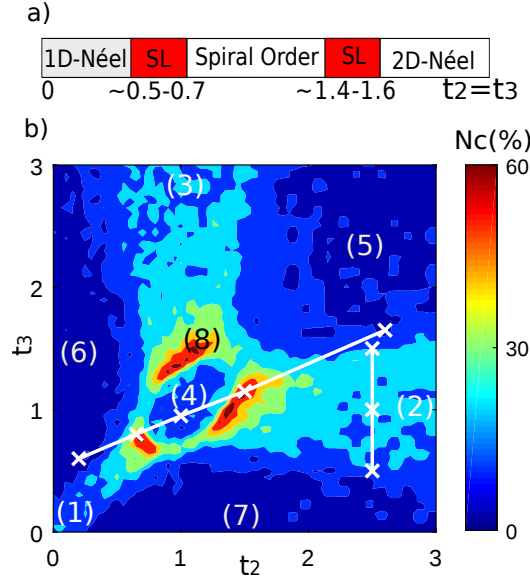
Figure 4.5: Panel a), quantum phase diagram for the SATL model ($t_2 = t_3$) with XY interactions extrapolated from the computation of N_c (for details see Article 2). Panel b), extension to the SCATL model with the explicit calculation of N_c. The labels depict all the phases present in the quantum phase diagram of the SCATL (see text).

($0.6 \lesssim t_2 \lesssim 0.8$) between the spiral phase and a gapless QSL. This gapless phase, which is located in the region $t_2 \lesssim 0.5$ ($t_2 \lesssim 0.6$), contains correlations decaying algebraically [112] and corresponds to the limit of 1D uncoupled chains.

The quantum phase diagram of the SCATL, as I obtained using RBC, is shown in Fig. 4.5 (b). The figure of merit is N_c, for more details see Sec. 5.2 and Article 3. Furthermore, the understanding of the different quantum phases appearing in the figure has been realized by analyzing the spin structure factor, which unambiguously determines the way the spins orientate among themselves. In accordance to the classical phase diagram, spiral orderer (labeled by (4) in Fig. 4.5) occurs around the isotropic point $t_3 = t_2 = 1$ and its extension is much reduced as compared to the classical case, in particular with Heisenberg interactions. Surrounding the spiral phase, a region absent in the classical phase diagram is observed, which is highlighted by a large N_c (labeled by (8)). In Article 3, we identify this region as a gaped QSL. Continuously connected to this phase, there are three regions labeled by (1,2,3). These regions lay between two 2D Néel ordered phases (5,6,7) that span around $t_i = t_j >> t_k$, and are connected to the respective classi-

cal 1D limit of uncoupled chains: $t_i \to \infty$, $t_j = t_k$. The regions (1,2,3) are commonly referred in the literature as gapless QSL and despite not being particularly enhanced in Fig. 4.5, they can be detected by other quantities. This completes the whole quantum phase diagram of the system. The numerical result depicted in Fig.4.5, is obtained using XY interactions. Nevertheless, the general behavior is similar for Heisenberg interactions, the only difference being the stronger shrinkage of the spiral phase.

4.3.2 Second neighbors model, $J_1 - J_2$, in the triangular lattice

As stated previously, the frustration present in the AF Heisenberg model in the triangular lattice makes it a perfect candidate for displaying a QSL phase. Nevertheless, the model with isotropic NN interactions exhibits long range spiral order [105–109]. Another natural way to further enhance the frustration present in the triangular lattice is by adding NNN terms,

$$H_{J_1-J_2} = J_1 \sum_{\langle i,j \rangle} \vec{S}_i \vec{S}_j + J_2 \sum_{\langle\langle i,j \rangle\rangle} \vec{S}_i \vec{S}_j, \tag{4.10}$$

where it is fixed $J_1 = 1$ leaving J_2 as the free parameter and the sums run over all NN and NNN pairs respectively. This model has been in the last years a focus of interest since a QSL phase has been found in the region $0.08 \lesssim J_2 \lesssim 0.16$ [115–120].

Classical phase diagram

The classical phase diagram of this system is well known [121]. For $J_2 < 1/8$, there is a three-sublattice 120° Néel ordered ground state (commensurate spiral order). For $1/8 < J_2 < 1$ the classical phase diagram is degenerate with the three different collinear 2D Néel orders and a tetrahedral noncoplanar state. However, an order-by-disorder mechanism selects the 2D Néel orders when quantum fluctuations are taken into account [121, 122]. For $J_2 > 1$, there is non-commensurate spiral order.

Quantum phase diagram

Recent studies have analyzed the quantum phase diagram of the model with special attention in the surroundings of the classical phase transition point, at $J_2 = 1/8$, with 2D DMRG [116, 117], variational quantum Monte Carlo [118], exact diagonalization [119] and Schwinger-boson mean-field [120]. A consensus has been reached in identifying a QSL phase for $0.08 \lesssim J_2 \lesssim$
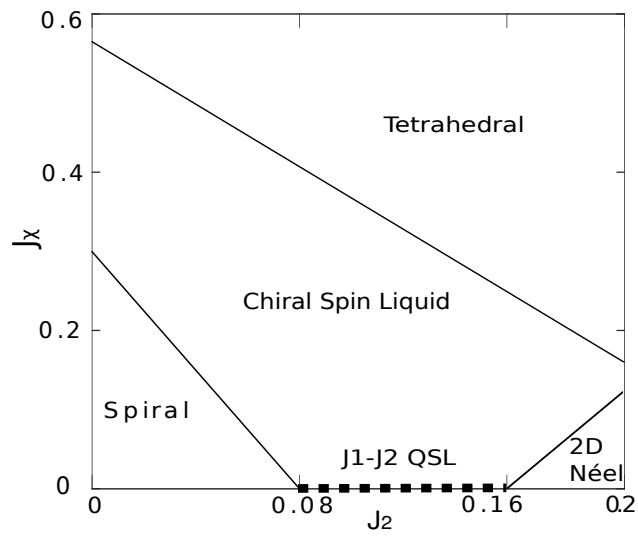
Figure 4.6: Sketch of the quantum phase diagram for the $J_1 - J_2$ model with chiral interactions.
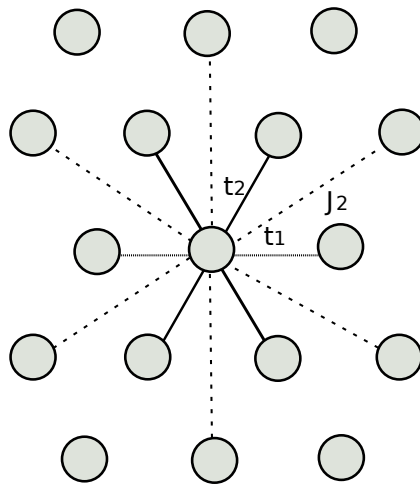

Figure 4.7: Sketch of the anisotropy of the model in Eq. (4.12) which is given by t_1, t_2 (NN) and J_2 (NNN) . For clarity, only the bounds of the central spin are depicted.

0.16. The nature of this phase, though, is still under debate. To shed more light on the issue, an extra chiral term in the Hamiltonian has been proposed [117, 119, 123–125],

$$H_\chi = H_{J_1-J_2} + J_\chi \sum_{i,j,k \in \Delta} \vec{S}_i(\vec{S}_j \times \vec{S}_k), \tag{4.11}$$

where the sum runs to all the up and down triangles of the lattice clockwisely. In Fig. 4.6, a sketch of the quantum phase diagram taken from Refs. [119, 123, 126] and from our results in Article 3 is shown. For $J_\chi = 0$, the $J_1 - J_2$ model is recovered. As J_χ is turned on, there is a phase transition from the QSL under debate towards a topological chiral spin liquid (CSL) which lies between the spiral, the collinear (2D Néel) and the tetrahedral phases.

4.3.3 A hybrid model, the anisotropic $J_1 - J_2$ triangular lattice

As it has been motivated in Chapter 1, it is interesting to explore the Hamiltonian which connects the above SATL and $J_1 - J_2$ models. The intersection of both models corresponds to the the NN isotropic triangular lattice, whose ground state displays commensurate Néel order. The Hamiltonian of the proposed model reads,

$$H = t_1 \sum_{\langle i,j \rangle'} (S_i^x S_j^x + S_i^y S_j^y + \lambda \, S_i^z S_j^z)$$

$$+ t_2 \sum_{\langle i,j \rangle''} (S_i^x S_j^x + S_i^y S_j^y + \lambda \, S_i^z S_j^z)$$

$$+ J_2 \sum_{\langle\langle i,j \rangle\rangle} (S_i^x S_j^x + S_i^y S_j^y + \lambda \, S_i^z S_j^z). \tag{4.12}$$

The first two sums run over NN couplings with the anisotropy given by the SATL model and the last sum over NNN without anisotropy. A sketch of the model interactions is given in Fig. 4.7. In the following it is settled $t_1 = 1$ and $t_2 \geq 1$ and $J_2 > 0$ are left as free parameters. The value $\lambda = 1$ (0) corresponds to Heisenberg (XY) interactions.

Classical phase diagram

The classical phase diagram can be obtained by minimizing the energy once the spin operators of the above Hamiltonian are replaced by classical rotors: $\vec{S}_i = (\cos(\vec{Q}^{cl} \cdot \vec{r}_i), \sin(\vec{Q}^{cl} \cdot \vec{r}_i))$, where $\vec{Q}^{cl}$ is the classical ordering
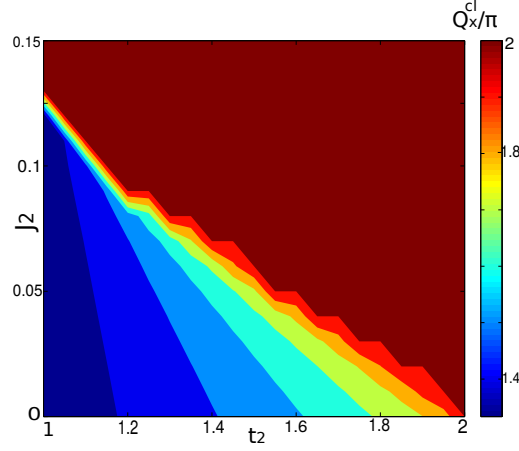
Figure 4.8: Classical phase diagram of the anisotropic $J_1 - J_2$ model obtained by a numerical plot of Q_x^{cl}. Collinear Néel order corresponds to the region $Q_x^{cl}/\pi = 2$ and it is connected to non-commensurate (commensurate, $Q_x^{cl}/\pi = 4/3$) spiral order for $t_2 > 1$ ($t_2 = 1$).

vector. In Fig. 4.8 a numerical plot of Q_x^{cl} in the region $t_2 > 1$ is shown. The classical model contains two phases, collinear Néel and non-commensurate (commensurate) spiral order $t_2 > 1$ ($t_2 = 1$).

Quantum phase diagram

The quantum phase diagram has been explored by means of both MSWT and RBC. The results are summarized in Fig. 4.9 for both Heisenberg and XY interactions. In the following, the region $t_2 \geq 1$ is described. The spiral order phase is substantially shrunken with respect to the classical phase diagram and collinear order is found beyond the classical value. The expected signatures of gaped QSL phases consists of large values of N_c and non-convergence of MSWT respectively. Both RBC and MSWT find signatures of a gaped QSL phase between both classical orders. This gaped QSL connects the ones present in the phase diagram of the limiting cases (SATL and $J_1 - J_2$). However, MSWT cannot find the expected gaped QSL region between commensurate spiral and collinear orders. In Chap. 6, it is conjectured that MSWT cannot detect a quantum disordered phases which lies between two commensurate orders. However, an analytical proof of the above statement has not still been found.
The numerical analysis for RBC is extended also to the region $t_2 < 1$, see Fig. 4.10, and also shows that the $J_1 - J_2$ QSL phase can be continuously connected to the QSL present in the SATL for $t_1 < 1$.
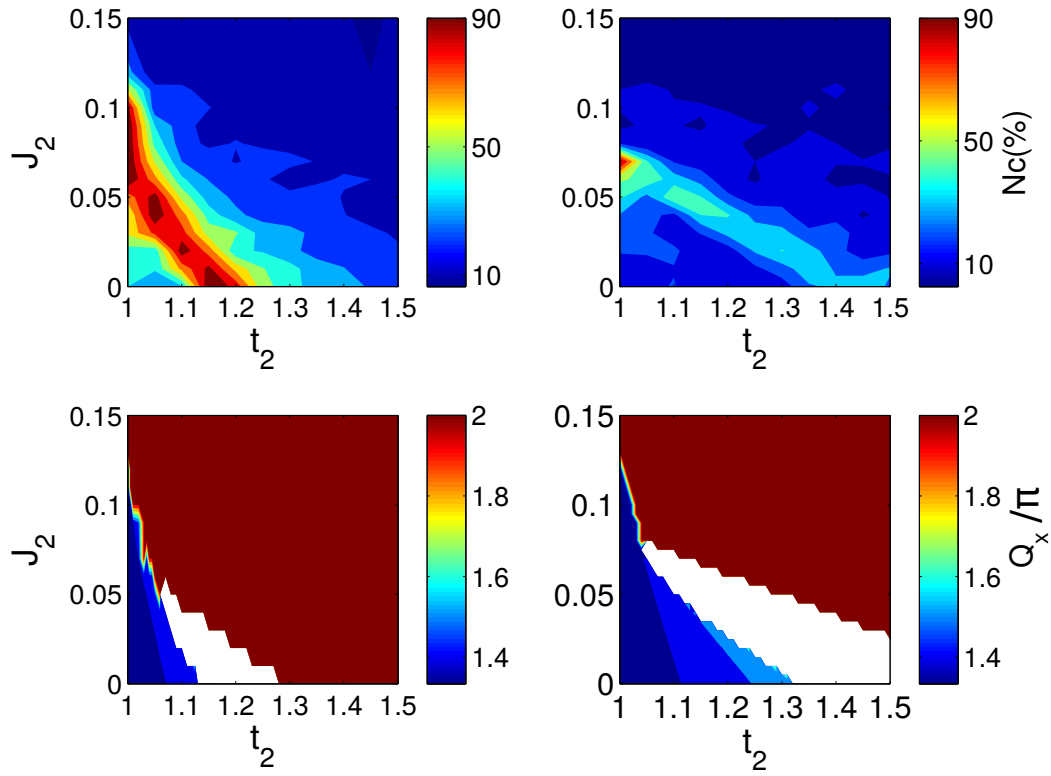
Figure 4.9: Numerical analysis on the quantum phase diagram of the anisotropic $J_1 - J_2$ model with Heisenberg (left panels) and XY (right panels) interactions by means of RBC (top panels) and MSWT (bottom panels). The large value of N_c and the non-convergence (in white) of the MSWT algorithm are the signatures of gaped QSL phases respectively.
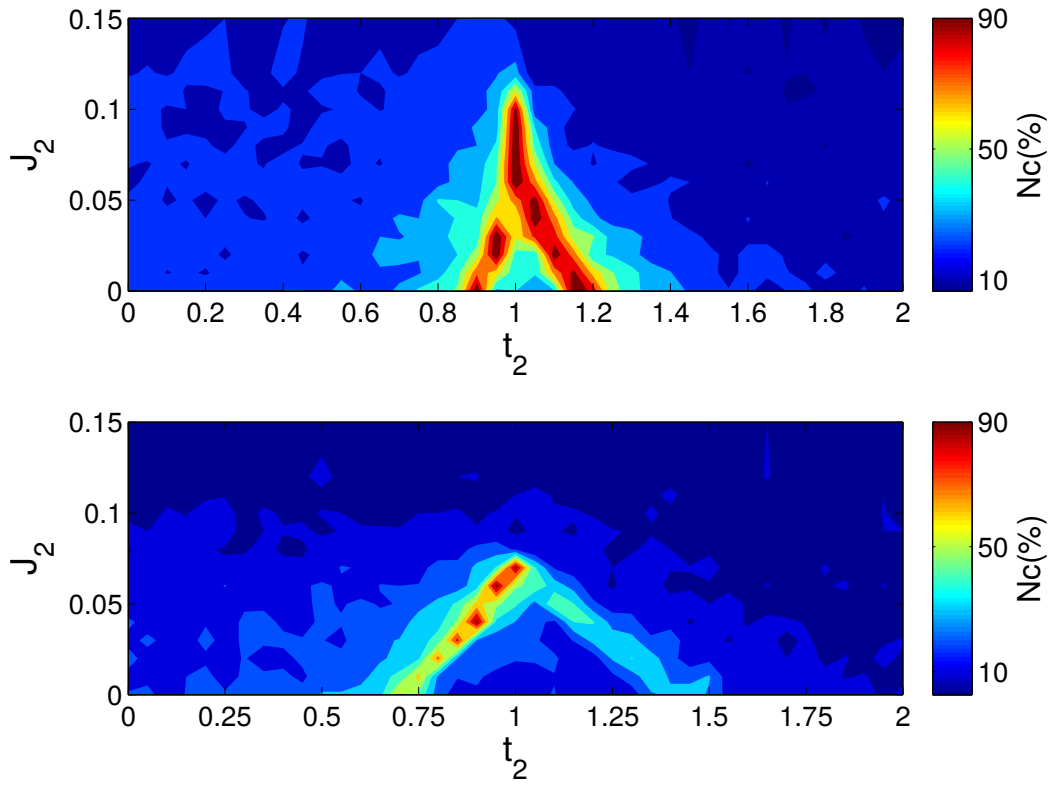
Figure 4.10: Numerical analysis on the quantum phase diagram of the anisotropic $J_1 - J_2$ by means of RBC considering also the region $t_2 < 1$. Top (bottom) panel corresponds to Heisenberg (XY) interactions.

Simulating strongly correlated systems

In this Chapter, I briefly describe the numerical methods I have used and developed along my Ph.D. to study different spin models. In Sec. 5.1, I provide general remarks concerning the difficulty to use numerical methods to simulate many-body quantum systems. In Sec. 5.2, I introduce exact diagonalization (ED) with random boundary conditions, an extension of ED methods to calculate ground states of many-body Hamiltonians. This is a tool which I have developed along the last years to address the study of QSL (Article 2 and 3). In Sec. 5.3, I move to DMRG, which is the technique for 1D systems I have used to study some QPT (Article 1). Finally, in Sec. 5.4 I introduce modified spin wave theory, which has been used to unveil properties of the anisotropic $J_1 - J_2$ model introduced in Sec.4.3.3.

5.1   Introduction

Quantum Mechanics theory was born to give answer to some phenomena which could not be explained by means of classical theories, for instance the Sodium doublet or the photoelectric effect. Based on first principles, which it is not at all the aim of this section to introduce them, a new theory together with a new mathematical structure came out, grounded from just a few postulates. The way QM is built up is puzzling simple and elegant if compared, for instance, to general relativity. Despite this apparent mathematical simplicity, when a physicist uses quantum mechanics to compute quantities of interest, as could be the angle of a water molecule or the ionization energy of

an atom, faces with two relevant challenges. The first one arises directly from the fact that an individual quantum systems with d degrees of freedom is described by a vector in a Hilbert space of dimension $\mathbb{C}^d$, and, by extension, the description of an N-body quantum system lies in the tensor product Hilbert space $(\mathbb{C}^d)^N$ of dimension d^N. In general, this exponential growth makes impossible to simulate many-body systems in classical (or even quantum) computers if their size is larger than some tens of particles. The second challenge, comes from the fact that the Schrödinger equation has analytical solution just for very few physical systems. When dealing with many-body interacting systems, mean-field approaches are often used in order to solve the Schrödinger equation. A mean-field approach reduces the N-body problem to a single particle problem with an effective potential. However, for most of the strongly correlated many-body systems a mean-field approach is not appropriated. In addition, only many-body systems whose conserved quantities are larger than the system's degrees of freedom, are analytically solvable (integrable). The vast majority of strongly correlated systems are not integrable, and therefore require a numerical solution. The numerical methods used to diagonalize the corresponding Hamiltonian are often variational methods around a mean-field approach or purely quantum methods like e.g. Tensor Networks algorithms.

5.2   Exact diagonalization with random twisted boundary conditions

Solving the Schrödinger equation of a given system, is equivalent to diagonalize its Hamiltonian,

$$H \ket{\psi_i} = E_i \ket{\psi_i} \tag{5.1}$$

so the first strategy which naturally turns up is to compute H, diagonalize it $H = \sum_i E_i \ket{\psi_i} \bra{\psi_i}$ and obtain the quantities of interest. This ED can be analytic in just a very few cases and, in full generality, the numerical computation is feasible just for small systems. Even quantum computers could not support a computation of some hundreds of qubits, since the Hilbert space of the system would be already larger than the number of atoms in the universe. Nevertheless, if one still wants use ED, current computers can diagonalize up to $N \sim 20$ qubits or $N \sim 14$ quitrits, using the Lanczos algorithm [127] to obtain the lower energy eigenstates. However, most of the quantum models contain symmetries in the Hamiltonian which allow to
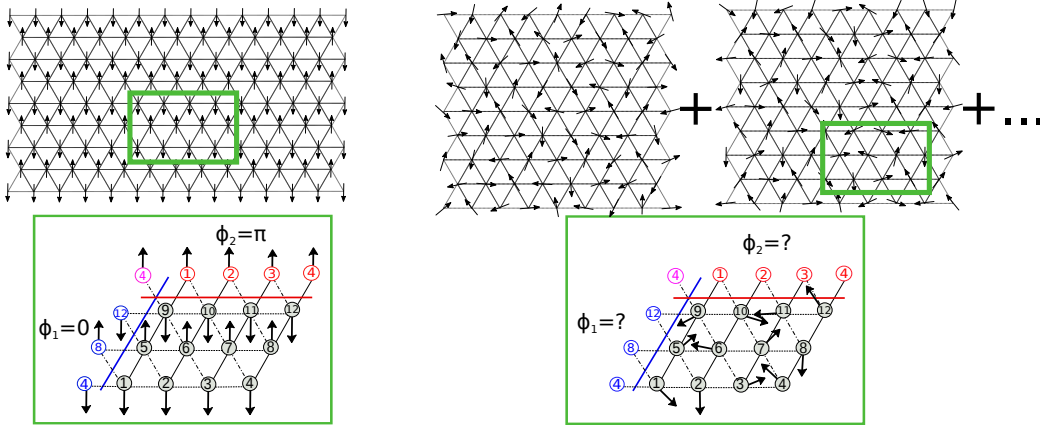
Figure 5.1: Upper panels: sketch representation of a quantum ordered Néel phase (left) and a QSL phase (right) in a large lattice. Lower panels: sketch of twisted boundary conditions in a 4×3 triangular lattice with anisotropic nearest-neighbor interactions. Boundary spins in blue are twisted in the XY plane by an angle ϕ_1, while red colored boundary spins are twisted by a phase ϕ_2. The pink colored boundary spin (top-left corner) is twisted by an angle $\phi = \phi_1 + \phi_2$. For the Néel phase (bottom left) the phases which reproduce the order are $\phi_1 = 0$ and $\phi_2 = \pi$. For the QSL (bottom right) such a set of phases cannot be defined.

perform the calculations in a reduced subspace. For example, in [128] the spin-1/2 AF honeycomb lattice is diagonalized up to $N = 42$ and in [129] a spin-1 chain up to $N = 18$. In particular, we are interested in the 2D spin-1/2 frustrated models, described in Chapter 4. For such models, ED can be currently performed up to 36 particles with PBC using translational and spin reflection symmetries. The larger is the diagonalized system the fewer are the finite size effects and calculations with $N = 36$ already lead to very accurate predictions of the thermodynamical limit by means of a finite size scaling [107, 111, 130, 131] or by a tower of states analysis [119, 132].

The approach proposed here has, nonetheless, a completely different philosophy. Our goal is finding signatures of QSL phases in small lattices at a low computational cost. In other words, instead of going to larger lattices to mitigate the finite size effects, we keep on small lattices, $N = 12, 16$ or 24 and exploit some of the properties of QSL by means of engineering the boundary conditions.

5.2.1   Basic concepts and figures of merit

Twisted boundary conditions (TBC) were introduced in the seminal contributions of [133, 134], and can be thought as PBC under a lattice twist. Since then, they have been often used to calculate properties of quantum magnets, as they provide better access to momentum space and help to mitigate finite size effects, see e.g. [5, 53, 135–137]. However, here we use TBC in a conceptually different approach. In Fig. 5.1, we sketch our philosophy. Consider a generic AF Heisenberg model in the triangular lattice. For the ordered phases of the Hamiltonian, the relative orientation of the spins is fixed due to a broken symmetry, as depicted for example in the cartoon of a 2D Néel phase in Fig. 5.1 (top left). If the lattice is large, the bulk spins dominate over the boundary ones imposing the order expected in the thermodynamic limit, independently of the chosen boundaries. However, for small lattices this is not anymore the case. The boundaries must be properly chosen –in accordance to the lattice geometry– to recover the underlying symmetries of the ordered phase, Fig. 5.1 (bottom left). For quantum disordered phases that are not associated to a symmetry breaking, we expect the ground state of the system to be spanned over a large superposition of states, as schematically shown in Fig. 5.1. presumably, for small lattices different boundary configurations should be compatible with the ground states of the system in the thermodynamic limit. We cannot predict a priory which are the right boundaries configurations since there is not an underlying local symmetry in the phase. This feature is illustrated with the symbols "?" in Fig. 5.1 (bottom right). Nevertheless, we can count how many random TBC lead to the same ground state energy and post-select only those to calculate physical quantities of interest. This post-selection is the key point to engineer our boundary conditions in Articles 2 and 3.

Specifically, for 2D spin-1/2 AF Heisenberg models, the spins lay in the XY plane and TBC correspond to adding a phase in the spins i, j interacting through the boundaries:

$$
\begin{aligned}
S_i^+ S_j^- &\to S_i^+ S_j^- e^{-i\phi}, \\
S_i^- S_j^+ &\to S_i^- S_j^+ e^{+i\phi}.
\end{aligned}
\tag{5.2}
$$

To twist the lattice simultaneously in two directions requires two different phases ϕ_1 (ϕ_2), for left-right (top-bottom) boundaries, as depicted in the bottom panels of Fig. 5.1. The spins of the lattice laying at both boundaries acquire a phase $\phi = \phi_1 + \phi_2$. Notice that conventional PBC favor order commensurate with the lattice dimensions, $N = L \times W$, since in the reciprocal lattice, momentum is selected at $k_1 = 2\pi n_1/L$ and $k_2 = 2\pi n_2/W$ for $n_i \in \mathbb{N}$.

In contrast, TBC allow to test all possible momenta in the first Brillouin zone [133, 134, 137]

$$
\begin{aligned}
k_1 &= \frac{2\pi n_1}{L} \pm \frac{\phi_1}{L}, \\
k_2 &= \frac{2\pi n_2}{W} \pm \frac{\phi_2}{W}.
\end{aligned}
\tag{5.3}
$$

The method is carried out as follows. First, we fix the lattice size, N, and geometry. Then, we generate a set p of two randomly chosen phases, $\{\phi_1, \phi_2\}_p$, with $\phi_i \in [0, 2\pi)$ and $p = 1, 2, \ldots, 200$. For each configuration, we diagonalize the Hamiltonian, generating a ground state $|\psi_p\rangle$ with energy E_p, and denote by $|\psi_0\rangle$ the ground state with the lowest energy, E_0. We post-select those configurations whose ground state energy fulfills: $\epsilon_p = (E_p - E_0)/E_0 < \alpha$. The election of the energy bias, α, is somehow arbitrary as it depends on the lattice size and the ratio between bulk and boundary interactions. Nevertheless, our results are independent of it, if the set p is sufficiently large. Notice, however, that for small lattices the bias cannot be vanishingly small.

Consequently, one relevant figure of merit is the number of configurations, N_c, laying in the interval $0 \le \epsilon_p < \alpha$. Typically, we choose $\alpha = 0.01$ meaning that only configurations whose ground state energies are less than 1% than E_0 are retained. Actually, for ordered phases just very few random TBC accommodate the symmetry of the phase, and the ones which do not, correspond to large E_p and are automatically discarded in our approach. In contrast, we find regions in the Hamiltonian parameters where N_c increases dramatically. The corresponding ground states, $|\psi_p\rangle$, strongly differ one from each other, as observed by computing the overlap with the configuration with the lowest energy, i.e., $O_p = |\langle \psi_p | \psi_0 \rangle|$. Finally, as it is standard in disordered systems, we calculate the quantities of interest for each post-selected configuration and perform afterwards the corresponding average which we denote by $\langle ... \rangle_d$. The average washes out the spurious symmetries introduced by TBC.

5.2.2 Technical implementation of the algorithm

In the following, the steps to build up from the scratch a code which implements the random twisted boundary conditions are detailed. In Appendix B, the corresponding MATLAB codes are provided. The model implemented is the AF spin-1/2 spin system with XY/Heisenberg interactions in the SCATL

(see Sec. 4.3). Its Hamiltonian reads,

$$H = \sum_{\langle i,j \rangle} t_{ij} \left(S_i^x S_j^x + S_i^y S_j^y + \lambda S_i^z S_j^z \right), \qquad (5.4)$$

where $\langle i,j \rangle$ run over all the first neighbors couplings and the S_i^α are the spin-1/2 Pauli matrices at site i. The anisotropy of the model is given by the different interaction strengths (t_1, t_2, t_3) along the lattice directions (see Fig.5.1 (bottom)). The model conserves the z-component of the total spin, $S_z = 1/N \sum_i S_i^z$, and the ground state lies in the $S_z = 0$ subblock. Hence, it is sufficient to diagonalize in the subspace of $S_z = 0$ which substantially reduces the number of coefficients and computational time. For instance, the size of the whole Hilbert space for $N = 24$ is already of 16.777.216 which is not feasible for current computers. The $S_z = 0$ subspace has 2.704.156 coefficients and diagonalization of sparse matrices can be performed by a reasonable powerful computer [138] using $\sim$15GB of RAM memory in a time ~ 300s. Using the spin creation and annihilation operators, $S_j^+ = S_j^x + iS_j^y$; $S_j^- = S_j^x - iS_j^y$, the above equation can be rewritten as,

$$\begin{aligned}
H = &\frac{1}{2} \sum_{\langle i,j \rangle \in bulk} t_{ij} \left(S_i^+ S_j^- + S_i^- S_j^+ \right) + \frac{1}{2} \sum_{\langle i,j \rangle \in twist1} t_{ij} \left(S_i^+ S_j^- e^{+i\phi_1} + S_i^- S_j^+ e^{-i\phi_1} \right) \\
&+ \frac{1}{2} \sum_{\langle i,j \rangle \in twist2} t_{ij} \left(S_i^+ S_j^- e^{+i\phi_2} + S_i^- S_j^+ e^{-i\phi_2} \right) \\
&+ \frac{1}{2} \sum_{\langle i,j \rangle \in twist3} t_{ij} \left(S_i^+ S_j^- e^{+i(\phi_1+\phi_2)} + S_i^- S_j^+ e^{-i(\phi_1+\phi_2)} \right) + \lambda \sum_{\langle i,j \rangle} t_{ij} S_i^z S_j^z,
\end{aligned}$$
$$(5.5)$$

where the Hamiltonian is split into bulk and TBC terms which have a complex phase as described in Eq. (5.2). The sum over $twist1$, $twist2$ and $twist3$ run over the bounds depicted in Fig. 5.1 in blue, red and pink respectively. The terms with $S_z^i S_z^j$ are not affected by the complex phases and are written together. In fact, every term in the above expression is split into three terms, one for each anisotropy value. In this way, the anisotropy can be taken out of the sum and the matrices belonging to each sum have to be computed just once. In the following I describe the steps to numerically build up the above Hamiltonian. For the sake of concreteness, I refer in to a $N = 12$, 4x3 lattice as the one in Fig. 5.1.

- The spin-1/2 Fock basis is defined with $2^{12} = 4096$ elements,

$$|1\rangle = |000000000000\rangle$$
$$|2\rangle = |000000000001\rangle$$
$$|3\rangle = |000000000010\rangle$$
$$|4\rangle = |000000000011\rangle \tag{5.6}$$
$$...$$
$$|4096\rangle = |111111111111\rangle$$

where 0 (1) means a spin up (down) in each lattice site. With this basis, an element can easily by identified by the binary position, i.e, $|000000000011\rangle = |2^1 + 2^0\rangle = |4\rangle$.

- It is just considered the subspace with $S_z = 0$,

$$|1'\rangle = |64\rangle = |000000111111\rangle$$
$$|2'\rangle = |96\rangle = |000001011111\rangle$$
$$|3'\rangle = |112\rangle = |000001101111\rangle \tag{5.7}$$
$$...$$
$$|924'\rangle = |4033\rangle = |111111000000\rangle$$

the ' is the label denoting the $S_z = 0$ subspace basis.

- In the original basis, the Hamiltonian terms can be built using its binary structure. The term $S_i^+ S_j^-$ acting on a state of the reduced basis $|in'\rangle$ consists of a flip of a 1 in site j for a 0 in site i. Thus, the output of $S_i^+ S_j^- |in\rangle$ is $|out\rangle = |in + 2^{N-i} - 2^{N-j}\rangle$ if $|in\rangle$ has a 1 in site j and a 0 in site i or is 0 otherwise. Running over all the reduced basis vectors, three sparse matrix (one per anisotropy) are built up for each term in Eq. (5.5). For example,

$$| \underbrace{3'}_{112=96+2^5-2^4} \rangle = S_7^+ S_8^- |\underbrace{2'}_{96}\rangle. \tag{5.8}$$

This term corresponds to the interaction between site 7 and 8 which is in the "bulk" sum with anisotropy t_1. Therefore the matrix corresponding to that sum and anisotropy has a 1 in the position (3,2) and (2,3) for hermiticity.

- The last term in Eq.5.5, is diagonal and is computed as,

$$\langle j'| S_i^z |j'\rangle = \pm 1/2, \tag{5.9}$$

where the + (-) sign corresponds to a 1 (0) of the position i in the state $|j'\rangle$.

- All the sparse matrices are stored in the hard disk memory. For $N = 24$ the hard memory required is $\sim$ 500MB. These matrices need to be computed just once for every lattice size and geometry.

The main program starts by loading the matrices belonging to every sum in Eq.(5.5). The Hamiltonian is computed adding the anisotropy and random complex phases. Then, H is diagonalized using the Lanczos method [127]. The ground state of the system ψ_0 and its energy E_0 are stored in the hard disk and erased from the CPU memory (dragging all of them during the computation may collapse the RAM memory of the computer). The procedure is repeated around $\sim$ 200 times with different random complex phases, which requires a hard disk memory of $\sim 1GB$ for every anisotropy value. As every diagonalization does not depend on the others, the process can be done parallelizing the computation to reduce the total time cost. The quantities of interest (see Articles 2 and 3) are computed a posteriori with the stored eigenvectors with the energy post selection protocol explained above.
In our articles we have also used this technique with NNN and chiral interaction terms. The procedure is quite similar to the explained above, but it requires some small modifications which are explained in the appendix of Article 3.

5.3   Density matrix renormalization group

The density matrix renormalization group is a variational technique to obtain the low-energy physics of 1D quantum systems. As mentioned above, the numerical study of quantum many-body systems is restricted by the structure of the Hilbert space. However, for 1D systems the number of parameters needed to describe the ground state of the system is very reduced [139, 140]. The strategy of DMRG is looking for this small relevant subset of the Hilbert space to efficiently describe the ground state of the system with much less parameters. DMRG was introduced by White[141, 142], based on Wilson's renormalization group idea [143]. In the last 25 years it has been *the* method for numerical studies of one-dimensional quantum systems. However, it was soon realized that it was not specially efficient for higher dimensional systems [144–148]. Nevertheless, the 2D version of DMRG, has provided remarkable results as the location of QSL in the triangular [116–118, 124, 126, 149] and kagomé lattices [150–154]. Some years after its first implementation, DMRG was reinterpreted in the framework of matrix product states and tensor networks [99, 155]. For a review on the vast topic of TN I refer to [156, 157] and for the connection between DMRG and MPS

to [158]. At this point, it was evidenced that QI and, in particular, entanglement play a crucial role in the efficiency of simulating quantum many-body systems [79, 80, 159]. In particular, efficient simulations are possible given that the entanglement of a subsystem with respect to the whole is bounded or grows logarithmically with the system size. This is always the case for 1D systems but not for higher dimensional ones [139, 140], since entanglement obeys the well known area laws(see Sec. 3.3). In the TN framework, the ground state of a DMRG calculation (even though it is applied to a higher dimensional system) is an MPS which is a representation of a 1D state defined as a contraction of local tensors aligned in a chain. The 2D extension of an MPS is called PEPS [160, 161] and consist of a 2D plain of tensors. PEPS can construct 2D quantum states which fulfill the area law of entanglement entropy, in contraposition to DMRG. This makes them a promising tool to study critical topological and gapped states in 2D systems. A broad view on PEPS can be found in [156, 157].

The aim of this section is not cover the whole literature and technical details of DMRG but to explain the basic idea behind the algorithm I have used in Article 1. An extensive review of the method can be found in [98, 162].

5.3.1 Algorithm

Even a brief introduction on the physical idea and technical implementation of DMRG can be quite extensive and it is out of the scope of this thesis. For a concise introductory work to DMRG algorithm I refer to [163]. The basic idea comes from the real space blocking renormalization group [143], where firstly the computation is upon a small portion of a system, called block, with a certain length L in a $m-$dimensional Hilbert space. Then, a system of 2 identical blocks (with new size of $2L$ and dimension m^2) which are interacting is solved in the subspace of the m lowest energy eigenstates. In this way the initial block is enlarged iteratively. The truncation avoids the exponential growth of the Hilbert space and it allows to study systems of very large sizes with a small number of parameters. Nevertheless, this approximation fails in most of the models. DMRG proposes also the union of 2 identical blocks, but the enlargement at every interaction step is of only one site. The rest of the new block, serves as environment to the new added site and it is afterwards removed from the computation by doing the partial trace over the original block plus the new site.

The DMRG calculations performed in Article 1 are done with an open source program [164], and for system size up to $N = 500$ ($N = 150$) for spin-1/2 (1) systems. We use the static DMRG algorithm for a finite system with open boundary conditions. Following the idea above, the steps of the algorithm
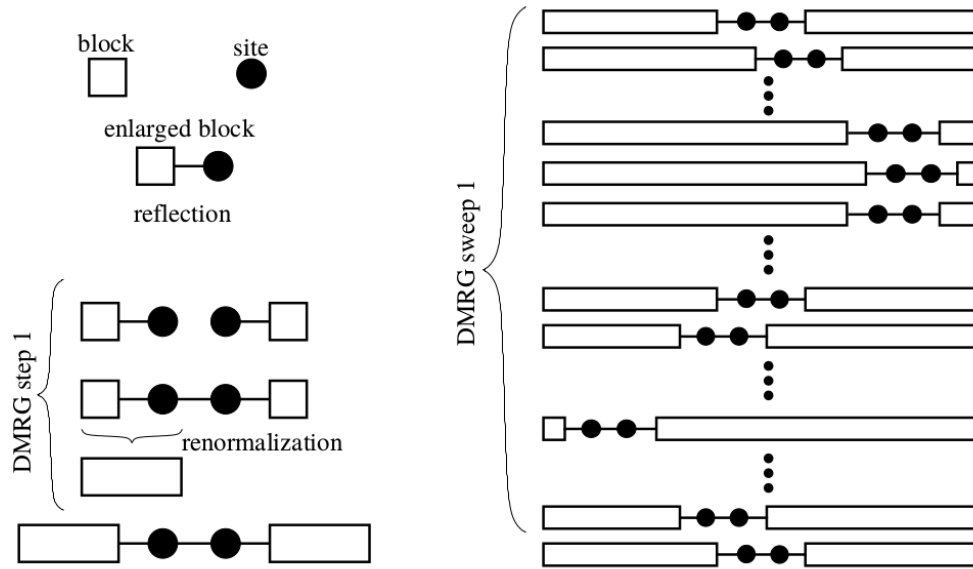
Figure 5.2: Sketch of the steps of the finite system DMRG with OBC algorithm (see text). The figure is extracted from Ref. [163].

are as following (see Fig. 5.2),

- The starting point is a block of size L and dimension m, which is called left block.

- The block is enlarged by one site on the right.

- The block is reflected to create a second block: the right block.

- The left and right blocks are merged creating a super-block.

- The super-block is diagonalized with a Lanczos or Davidson diagonalization [165].

- The eigenstates of the reduced density matrix, ρ_{L+1} of the left block plus the new site are computed. The truncation is done selecting the m_{max} eigenstates with largest eigenvalue, where m_{max} is a parameter which is fixed at the beginning of the computation. This step is the core of the DMRG algorithm and the linkage with entanglement and QI.

- At every step, the desired operators are also renormalized with the new truncated basis.

- The above steps are iteratively repeated until the desired size L_{max}.

- By a "sweep" procedure (see Fig.5.2 (right)), the system is divided in two blocks and enlarge one while shrinking the other, in a similar way than in the previous steps. Here, the total length of the system is kept and normally with 3 full sweeps steps the quantities converge.

5.4   Spin wave theories in the AF triangular lattice

Spin-waves, firstly introduced by Block [166], provide a very suitable semi-classical tool for the study of the properties of quantum magnets and anti-ferromagnets [167, 168]. For a broad introduction on spin-wave theories see e.g., Ref. [169]. The idea behind it is quite simple: as a reference state, one chooses the state derived from the classical limit, which contains long-range order given by the ordering vector Q^{cl}, and associates it to the vacuum state $|0\rangle$. Then, quantum fluctuations are taken into account and induce coherently delocalized spin-flips, usually named spin-waves or magnons. A state with one magnon of momentum λ is defined as,

$$|n_\lambda = 1\rangle = \frac{1}{\sqrt{2S}} S_\lambda^+ |0\rangle, \qquad (5.10)$$

where S_λ^+ is the Fourier transform of the spin raising operator,

$$S_\lambda^+ = \frac{1}{\sqrt{N}} \sum_i e^{-ir_i\lambda} S_i^+, \qquad (5.11)$$

S the spin quantum number and N the number of spins. At sufficiently low temperature, the magnons are elementary excitations and the system can be regarded as a dilute gas of weakly interacting spin-waves, providing a mean field approach which can reproduce in many cases the physical properties of quantum magnets and antiferromagnets. In the following we describe how to apply a spin-wave theory at zero temperature for a 2D antiferromagnet in a triangular lattice with Hamiltonian,

$$H = \sum_{\langle i,j \rangle} t_{ij} (S_i^x S_j^x + S_i^y S_j^y + \lambda S_i^z S_j^z), \qquad (5.12)$$

where $\langle i, j \rangle$ and $t_{ij} > 0$ depend on the model and the parameter $\lambda = 1, (0)$ corresponds to Heisenberg (XY) interactions.
The first step consists of a global rotation of the spin operators, $\vec{S} = (S^x, S^y, S^z)$, in order to have a new set of spin operators, $\vec{S} = (S^\nu, S^\varsigma, S^\xi)$, which point

towards the same direction as the classical spins. In the classical limit of the above Hamiltonian, for both Heisenberg and XY interactions, the spins lie in the xy-plane and the rotation reads [10],

$$
\begin{aligned}
S_i^x &\to -\sin(Q^{cl} \cdot r_i)S_i^\nu + \cos(Q^{cl} \cdot r_i)S_i^\zeta \\
S_i^y &\to +\cos(Q^{cl} \cdot r_i)S_i^\nu + \sin(Q^{cl} \cdot r_i)S_i^\zeta \\
S_i^z &\to -S_i^\xi.
\end{aligned}
\tag{5.13}
$$

S_i^ζ is taken as the quantization axis. The above Hamiltonian is rewritten as,

$$
H = \sum_{\langle i,j \rangle} t_{ij}[c_{ij}(S_i^\nu S_j^\nu + S_i^\zeta S_j^\zeta) + \lambda S_i^\xi S_j^\xi],
\tag{5.14}
$$

where $c_{ij} \equiv \cos(Q^{cl} \cdot r_{ij})$, and $r_{ij} \equiv r_j - r_i$. The second step consists of a spin-boson mapping. Usually, a Holstein-Primakov (HP) transformation [170] is used,

$$
\begin{aligned}
S_i^- &\to \sqrt{2S}\sqrt{1 - \frac{a_i^\dagger a_i}{2S}}a_i \\
S_i^+ &\to \sqrt{2S}a_i^\dagger\sqrt{1 - \frac{a_i^\dagger a_i}{2S}} \\
S_i^\zeta &\to -S + a_i^\dagger a_i.
\end{aligned}
\tag{5.15}
$$

Where $S_i^+ \equiv S_i^\xi + iS_j^\nu$ and $S_i^- \equiv S_i^\xi - iS_j^\nu$. The physical intuition of this transformation is as follows. Now, instead of having a spin on each site i, we have an harmonic oscillator with creation and annihilation operators $a_i^\dagger$, a_i. Every excitation of these harmonic oscillators corresponds to a 'quanta of vibration' of the spins around their classical position. Therefore, as pointed out above, spin-waves theories let quantum fluctuations perturb the classical order by means of magnons in order to reproduce quantum features.

Linear Spin Wave Theory

The square roots of the HP are somehow problematic, since they are imaginary when there are more than 2S bosons in one site and also because they do not lead to an analytic diagonalization of the Hamiltonian. It is very common to make an expansion of the square roots, $\langle a_i^\dagger a_i \rangle/(2S) << 1$ to the first order in $1/S$. This assumption makes sense if the classical order is only "slighlty" perturbed. This approach, called linear spin wave theory (LSWT),

has been extensively used, see e.g., [167, 168, 171, 172]. After first order expansion in the HP transformation, the Hamiltonian in Eq. (5.14) reads,

$$
\begin{aligned}
H_{LSWT} = & \frac{1}{4} \sum_{\langle i,j \rangle} t_{ij} \{ (\lambda - c_{ij}) 2S(a_i^\dagger a_j^\dagger + a_i a_j) \\
& + (\lambda + c_{ij}) 2S(a_i^\dagger a_j + a_i a_j^\dagger) + 4c_{ij}[S^2 - S(a_i^\dagger a_i + a_j^\dagger a_j)] \}.
\end{aligned}
\tag{5.16}
$$

This Hamiltonian is quadratic in creation and annihilation operators and therefore can be diagonalized using a Bogoliubov-transformation,

$$
\begin{aligned}
\beta_k = & \cosh \theta_k b_k - \sinh \theta_k b_{-k}^\dagger \\
\beta_{-k} = & - \sinh \theta_k b_k - \cosh \theta_k b_{-k}^\dagger
\end{aligned}
\tag{5.17}
$$

where b_k are the bosonic operators in the Fourier space: $b_k = \frac{1}{\sqrt{N}} \sum_i a_i e^{-ik \cdot r_i}$. The diagonalization leads to,

$$
H_{LSWT} = \sum_k \omega_k^{LSWT} \beta_k^\dagger \beta_k
\tag{5.18}
$$

and the problem reduces to finding which θ_k fulfill this last equation, i.e., diagonalize H_{LSWT}. It can be shown [173] that the result can be written as,

$$
\begin{aligned}
\sinh 2\theta_k = & \frac{-A_k}{\omega_k^{LSWT}} \\
\cosh 2\theta_k = & \frac{B_k}{\omega_k^{LSWT}}.
\end{aligned}
\tag{5.19}
$$

The spin-wave dispersion relation is

$$
\omega_k^{LSWT} = S \sqrt{(\tilde{t}_{Q^{cl}} - \lambda \tilde{t}_k)[\tilde{t}_{Q^{cl}} - (\tilde{t}_{k+Q^{cl}} + \tilde{t}_{k-Q^{cl}})/2]},
\tag{5.20}
$$

where $\tilde{t}_q$ denotes the q-Fourier transform of t_{ij} and

$$
\begin{aligned}
A_k = & \frac{S}{N} \sum_{\langle i,j \rangle} t_{ij} [(\lambda - c_{ij}) \cos(k \cdot r_{ij})] \\
B_k = & \frac{S}{N} \sum_{\langle i,j \rangle} t_{ij} [(\lambda + c_{ij}) \cos(k \cdot r_{ij}) - 2S c_{ij}].
\end{aligned}
$$

With the spin-wave dispersion relation, A_k and B_k, it is possible to compute quantities as, for instance, the classical order parameter,

$$
M_{LSWT} \equiv \langle \frac{1}{N} \sum_i (-S_i^\zeta) \rangle = S - \frac{1}{2N} \sum_k \frac{B_k}{\omega_k^{LSWT}}.
\tag{5.21}
$$

As it is well known in some quantum disordered phases the spins arrange in a radically different way as in the classical limit,.e.g, topological or critical phases. In such cases, the approximation $\langle a_i^\dagger a_i \rangle/(2S) << 1$ is not a good approach and LSWT turns to be extremely inaccurate. Another limitation is that LSWT breaks down when using an ordering vector Q which is not the classical one. Therefore, other long-range ordered states beyond the classical limit cannot be normally explored. Finally, one last, but not least weak point in LSWT is the assumption of spontaneous symmetry breaking, since the spins are restricted to point into a certain direction. Therefore, the ground state obtained with LSWT does not exhibit the same symmetries of the initial Hamiltonian. In conclusion, it becomes clear that LSWT is not a good tool for the study of the 2D frustrated AF models described in Sec. 4.3. Nevertheless, we have provided the main steps of its derivation because they are illustrative to enhance the strong points of the so-called modified spin wave theory, a more sophisticated approach which is introduced in the next section. For an extense study of frustrated spin models in the triangular lattice by means of LSWT see Ref. [173].

5.4.1   Modified spin wave theory

Firstly developed for the AF square lattice by Takahashi [7] and contemporaneously by Hirsch and Tang [174–176], MSWT is a spin-wave theory which has been succesfully applied to frustrated square lattice models[177–179] and more recently to the honeycomb lattice [180]. It was early implemented in the isotropic triangular lattice with Heisenberg interactions by Xu and Ting [10]. Using a mapping with Xu's equations, Hauke and collaborators explored the SATL [8] and SCATL [6] models for both XY and Heisenberg interactions. A recent work of Celi and collaborators [9] rigorously derives MSWT for the SATL model with XY interactions from the scratch. The results obtained are close, though not equal, to the ones obtained by Hauke [8]. In the following I provide the main steps of the MSWT formalism for both Heisenberg and XY interactions. The derivation, although similar to the work of Hauke, leads to different final set of equations. The results derived here exactly match the ones obtained by Celi (XY interactions) but do not resemble the ones obtained by Xu (Heisenberg interactions). A paralell derivation as the one in [9] for Heisenberg interactions remains an open problem which I address in Appendix A together with the discrepancies among the different mentioned derivations.

MSWT formalism

The starting point is the Hamiltonian in Eq. 5.14. MSWT has the advantage that can consider an arbitrary ordering vector, Q, beyond the classical one Q^{cl}. Hence, it is redefined, $c_{ij} \equiv \cos(Q \cdot r_{ij})$. Instead of the usual HP, it uses a Dyson-Maleev (DM) transformation [181],

$$
\begin{aligned}
S_i^- &\to \frac{1}{\sqrt{2S}}(2S - a_i^\dagger a_i)a_i \\
S_i^+ &\to \sqrt{2S}a_i^\dagger \\
S_i^\zeta &\to -S + a_i^\dagger a_i.
\end{aligned}
\tag{5.22}
$$

Note that, in contrast with the HP transformation, now there is a one-to-one correspondence between the physical spin-wave state and the DM bosons space,

$$
\begin{aligned}
|n_\lambda\rangle_S &= \prod_\lambda \frac{1}{(2S)^{n_\lambda/2}\sqrt{n_\lambda}}(S_\lambda^+)^{n_\lambda} |0\rangle_S \\
|n_\lambda\rangle_{DM} &= \prod_\lambda \frac{1}{\sqrt{n_\lambda}}(b_\lambda^\dagger)^{n_\lambda} |0\rangle_{DM}
\end{aligned}
\tag{5.23}
$$

where $b_\lambda^\dagger$ is now the Fourier transform of the DM operator. DM coincides with HP transformation in the leading order and gets rid of the problematic square root. Rigorously, it should be included a kinematic constraint which restricts the DM-bosons density n to the physical subspace $n < 2S$. However, it is usually neglected under the assumption that the population of bosons is small. The Hamiltonian after the transformation reads,

$$
\begin{aligned}
H_{MSWT} =& \frac{1}{4}\sum_{\langle i,j\rangle} t_{ij}\{[2S(a_i^\dagger a_j + a_i a_j^\dagger) - a_i^\dagger a_j^\dagger a_j a_j - a_i^\dagger a_i a_i a_j^\dagger](\lambda + c_{ij})) \\
&+ [2S(a_i^\dagger a_j^\dagger + a_i a_j) - a_i a_j^\dagger a_j a_j - a_i^\dagger a_i a_i a_j](\lambda - c_{ij}) \\
&+ 4[S^2 - S(a_i^\dagger a_i + a_j^\dagger a_j) + a_i^\dagger a_i a_j^\dagger a_j]c_{ij}\},
\end{aligned}
\tag{5.24}
$$

where 6-bosons terms have been dropped as usual [9, 10]. Using Wicks' theorem [182], the mean energy is obtained as the expected value of the Hamiltonian,

$$
\begin{aligned}
E = \langle H_{MSWT}\rangle =& \sum_{\langle ij\rangle} t_{ij}\{(f(r_{ij})X - \frac{g(r_{ij})g(0)}{2})[\lambda + c_{ij}] \\
&+ (g(r_{ij})X - \frac{f(r_{ij})g(0)}{2})[\lambda - c_{ij}] \\
&+ (X^2 + g^2(r_{ij}) + f^2(r_{ij}))c_{ij}\}
\end{aligned}
\tag{5.25}
$$

where the mean field quantities are defined as:

$$
\begin{aligned}
\langle a_i^\dagger a_j \rangle &= f(r_{ij}) - \frac{1}{2}\delta_{ij} \\
\langle a_i a_j \rangle &= \langle a_i^\dagger a_j^\dagger \rangle = g(r_{ij}) \\
X &= S + 1/2 - f(0)
\end{aligned}
\tag{5.26}
$$

Eq. (5.25) differs from Hauke's work (see for instance Eq.A4 in Ref. [6]) and does not lead to Xu's [10] results for $\lambda = 1$. Nonetheless, for XY interactions it recovers Celi's energy (see Eq.17 in Ref [9]). In Appendix A, I provide a technical description of the subtleties and mismatches among the mentioned works, including the addition of the previously dropped six-boson terms.

As in the LSWT formalism, first one goes to the Fourier space of the bosonic operators $b_k = \frac{1}{\sqrt{N}}\sum_i a_i e^{-ik \cdot r_i}$ and then a Bogoliubov transformation (Eq. (5.17)) is performed. This leads to the definition,

$$
\begin{aligned}
f(r) &= \frac{1}{2N}\sum_k \cosh(2\theta_k)e^{-ik \cdot r} \\
g(r) &= \frac{1}{2N}\sum_k \sinh(2\theta_k)e^{-ik \cdot r}.
\end{aligned}
\tag{5.27}
$$

Instead of a diagonalization, MSWT performs an energy minimization under the so-called Takahashi constraint of zero magnetization,

$$
\langle S_i^\zeta \rangle = -S + \langle a_i^\dagger a_i \rangle = -X = 0.
\tag{5.28}
$$

This restores the reflection symmetry of the ground state with respect to the quantization axis, (which was broken in the LSWT approach). The energy minimization yields to,

$$
\tanh 2\theta_k = \frac{A_k}{B_k}
\tag{5.29}
$$

$$
\omega_k = \sqrt{B_k^2 - A_k^2},
\tag{5.30}
$$

where,

$$
\begin{aligned}
A_k =& \frac{1}{2} \sum_{\langle ij \rangle} t_{ij} \{ [g(r_{ij}) + f(r_{ij})]\lambda + [g(r_{ij}) - f(r_{ij})]c_{ij} \\
& + \cos{(k \cdot r_{ij})}[g(0)\lambda + (g(0) - 4g(r_{ij}))c_{ij}] \} \\
B_k =& \sum_{\langle ij \rangle} t_{ij} \{ \frac{1}{2}[f(r_{ij}) + g(r_{ij}) + 2g(0)]\lambda \\
& + \frac{1}{2}[-5f(r_{ij}) - 3g(r_{ij})]c_{ij} \\
& + \cos(k \cdot r_{ij})[\frac{-g(0)}{2}\lambda + (\frac{g(0)}{2} + 2f(r_{ij}))c_{ij}] \}
\end{aligned}
\tag{5.31}
$$

The definitions of A_k and B_k, as mentioned before, match the ones obtained by Celi [9] setting $\lambda = 0$. However, for Heisenberg interactions, these equations lead to controversial numerical results and we use, for the numerical studies presented in the thesis, the ones obtained by Xu [10],

$$
\begin{aligned}
A_k =& \sum_{\langle ij \rangle} t_{ij}[1 - c_{ij}]g(r_{ij}) \cos(k \cdot r_{ij}) \\
B_k =& \sum_{\langle ij \rangle} t_{ij} \{ [1 - c_{ij}]g(r_{ij}) - [1 + c_{ij}]f(r_{ij})(1 - \cos(k \cdot r_{ij})) \}.
\end{aligned}
\tag{5.32}
$$

The quantities A_k, B_k are computed self-iteratively with $g(r_{ij})$ and $f(r_{ij})$ using,

$$
\begin{aligned}
f(r_{ij}) &= M_0 + \frac{1}{2N} \sum_{k \neq 0} \frac{B_k}{\omega_k} \cos(k \cdot r_{ij}) \\
g(r_{ij}) &= M_0 + \frac{1}{2N} \sum_{k \neq 0} \frac{A_k}{\omega_k} \cos(k \cdot r_{ij}).
\end{aligned}
\tag{5.33}
$$

Where the occupation of the zero mode $M_0 \equiv \langle b^\dagger_{k=0} b_{k=0} \rangle/N = \langle b_{k=0} b_{k=0} \rangle/N$ is removed from the sum. M_0 is the Bose condensation of DM bosons in the zero mode and it corresponds to the magnetic order parameter. Finally, the Takahashi constrain is rewritten as,

$$
S + \frac{1}{2} = M_0 + \frac{1}{2N} \sum_{k \neq 0} \frac{B_k}{\omega_k}
\tag{5.34}
$$

Algorithm

In the following, the steps to build up the MSWT algorithm are briefly detailed. The system is considered in the infinite L limit, i.e., taking all the

sums over k as integrals. The numerical implementation of the algorithm written in MATLAB language can be found in Appendix B.

- As initial guess, it is standard to start with the LSWT A_k and B_k (see Eq. 5.21) and therefore $Q = Q^{cl}$.

- Then, $f(r_{ij})$ and $g(r_{ij})$ are computed using Eq. (5.33).

- The energy is computed (Eq. (5.25)) with the new values of $f(r_{ij})$ and $g(r_{ij})$ and it becomes a function of the ordering vector, $E = E(Q)$.

- A numerical energy minimization is performed in order to find the optimal Q.

- The last step consists of updating the values of A_k and B_k with Eq. 5.31 for XY and Eq. 5.32 for Heisenberg interactions.

- The process is repeated until the difference between previous and updated A_k and B_k are below a certain bias.

- When convergence is reached, both Q and M_0 (Eq. (5.34)) are taken as figures of merit.

- If the initial LSWT guess does not lead to a stable minimum, the iteration is restarted with the corresponding A_k and B_k from nearby converged MSWT.

- If both LSWT and nearby MSWT initial guesses do not lead to a stable solution, it is suggested that the model may hold a phase with no long-range order as it could be a topological QSL or a critical phase.

CHAPTER 6

Conclusions and future perspectives

Along my Ph.D. thesis I have dealt with complex quantum many-body systems acquiring knowledge, tools and competences in quantum information science and condensed matter physics. I have contributed to the field of strongly correlated systems with 3 (+1) research articles, including a novel numerical technique to find signatures of quantum disordered phases in 2D frustrated spin systems and providing a novel hybrid quantum spin model that hosts different quantum spin liquids phases. I have given indications that these different quantum spin liquids have putatively the same origin as they can be smoothly connected one to another. To conclude this part of the thesis (Part I), I would like to provide some broad perspectives and open questions that have arisen along my research and which could serve as future potential lines of investigation.

In the first part of my research, Article 1, I have shown that measures of bipartite entanglement, such as the concurrence and negativity also fulfill a FSS for 1QPT in short range Hamiltonians. FSS is a tool to recover the thermodynamic limit in continuous transitions (2QPT) and its application to 1QPT is by no means trivial. This scaling, however, is needed to determine the order of the transition close to multicritical points in finite size systems. The two models under study in Article 1 contain 1QPT which had been found in previous works. However, there are other models, as for instance 2D frustrated systems, which contain QPT whose order is still a controversial issue. A question which remains to be answered is: 'Can a FSS be always applied to entanglement measures? Can such entanglement FSS unambiguously deter-

mine the order and nature of a quantum phase transition?' Another future line of research could be extending the work to multipartite measures of entanglement and to spin models with interaction terms involving more than two particles. For instance, is it possible to create a similar scaling which is fulfilled by the geometrical measure of entanglement? The answer is not straightforward since my work relies on the fact that both the concurrence and negativity depend only on the reduced density matrix of two spins, ρ^{ij}, which contains the non-analyticities of the ground state in a QPT. Although the study of QPT by means of measures of entanglement has been a vast focus of research during the last 15 years, I would still state that many more contributions to the field are about to come.

The second part of my Ph.D. work has been devoted to the study of quantum spin liquids (Articles 2, 3 and 4*). I have developed a new numerical technique to find signatures of QSL in spin models in the triangular lattice. The method provides a feasible tool for the detection of novel quantum disordered phases and it explicitly unveils some properties of QSL. A further line of investigation could be to engineer similar random boundary conditions to other frustrated geometries as the kagome lattice. This could give some new insight to the current open problems present in such models. It also seems to me feasible to engineer the boundary conditions in a way which preserves translational invariance. This symmetry, properly introduced in the algorithm, could allow to perform ED of larger systems which would further decrease the finite size effects of the results. Nonetheless, I have not put more effort on the issue because the results up to 24 sites were already quite stunning. I also attempted during the last months of my Ph.D., applying this RBC in the triangular lattice within a 2D DMRG algorithm. This would allow to substantially increase the lattice sizes used which could make feasible a finite size scaling in order to extract the results in the thermodynamic limit. This remains an open research line worth to pursuing. Finally, I still would like to mention that there are many relevant spin models in the triangular lattice with quantum disordered phases which could be studied with RBC. Examples of such models are the spin-1/2 XXZ or the spin-1 bilinear biquadratic models, (see Ref. [183]). Some of these models have still phases which are under debate and RBC could provide a new perspective to the issue.

In the last part of my research, I have used MSWT to extend my studies on 2D quantum antiferromagnets. In particular, I have obtained the quantum phase diagram of the anisotropic $J_1 - J_2$ model which continuously connects the gaped QSL phases present in the SATL and $J_1 - J_2$ models. The

results are qualitatively in agreement with RBC calculations. This linkage might provide a new insight to the open question about the nature of the QSL present in the $J_1 - J_2$ model. However, further studies with 2D DMRG, QMC or PEPS should be done in order to shed more light onto the issue.

A rigurous derivation of MSWT in the triangular lattice for the XY interactions has been perfomed by Celi and collaborators [9]. The final equations, though, are slightly different as the ones presented in the seminal work of Xu and Ting [10]. I have tried a similar derivation as the proposed by Celi for Heisenberg interactions with non-conclusive results (see Appendix A). This formal derivation remains and open problem.

Finally, the results obtained by means of MSWT, summarized in Fig. 4.9, suggest the following two conjectures:

- *Within the MSWT formalism, there is always a quantum disordered phase between commensurate and incommensurate orders which are connected by a 2QPT in the classical phase diagram.*

- *MSWT cannot detect a quantum disordered phase which lies between two commensurate orders connected in the classical limit by a 1QPT.*

The first conjecture was already suggested in [6] and is further supported by all my results, including those obtained by means of RBC. Indeed, in all the explored 2D frustrated models, the non-commensurate spiral order is always surrounded by putative gapped QSL phases. The second conjecture is exclusively formulated from the results in Fig. 4.9. In the limit of the $J_1 - J_2$ model, it is known that a gapped QSL phase is found between commensurate spiral and collinear orders. Nevertheless, the MSWT calculations detect a 1QPT between both orders without any intermediate phase. When NN anisotropy is added, the spiral order becomes non-commensurate and only then MSWT detects the expected signatures of an intermediate quantum disordered phase. Hence, it seems hinted that MSWT formalism is not appropriated for the detection of quantum disordered phases in such conditions.

To analytically proof these conjectures remains another interesting line of research as well as comprehending their implications beyond the MSWT formalism.

Part II

Articles

ARTICLE 1

Entanglement scaling at first order quantum phase transitions

Initial questions and motivations

The phenomena of QPT, which is introduced in Sec.2.1, is a paradigmatic example of how quantum information has given a completely new perspective to the subject. Many QPT fall inside the classical Ginzburg-Landau picture and can be studied with a very similar formalism as in the classical case. But it is well known that in QM there are QPT which have no classical analogous. It is precisely here where QI and entanglement might take a crucial role. In the last 15 years, several measures of entanglement have been used to study QPT. However, most of these works are focused in continuous or 2QPT whereas the discontinuous or 1QPT case has been less explored.

Our initial question was the following: 'Is it always possible to identify a 1QPT with just measures of entanglement?' And, furthermore: 'Is it always possible, in a finite system, to distinguish between a 1QPT and 2QPT by means of entanglement?' We show that this last question becomes particularly relevant in the vicinity of multicritical points where QPT of different orders are very close.

Main results

We have observed that for finite systems, in 1QPT which are close to a 2QPT, the measures of bipartite entanglement may have the apparent behavior of a 2QPT, i.e., they may be continuous with a non-analyticity in the first derivative. Under such conditions, we have successfully used, for the first time, a finite size scaling of different measures of bipartite entanglement in a 1QPT. It is thus the finite size scaling and not the order of the singularity which can correctly distinguish the order of the transition. We have successfully tested the finite size scaling for the spin-1/2 Ising model with longitudinal field, 4.2.1 and for the spin-1 XXZ model 4.2.2.

PAPER • OPEN ACCESS

Entanglement scaling at first order quantum phase transitions

To cite this article: A Yuste *et al* 2018 *New J. Phys.* **20** 043006

View the article online for updates and enhancements.

New Journal of Physics

The open access journal at the forefront of physics

PAPER

CrossMark

Entanglement scaling at first order quantum phase transitions

A Yuste[1], C Cartwright[2], G De Chiara[2] [iD] and A Sanpera[1,3]

1 Física Teòrica: Informació i Fenòmens Quàntics, Departament de Física, Universitat Autònoma de Barcelona, 08193 Bellaterra, Barcelona, Spain
2 Centre for Theoretical Atomic, Molecular, and Optical Physics, School of Mathematics and Physics, Queen's University Belfast, Belfast BT7 1NN, United Kingdom
3 ICREA, Pg. Lluís Companys 23, E-08010, Barcelona, Spain

E-mail: abel.yuste@uab.cat

Abstract

First order quantum phase transitions (1QPTs) are signalled, in the thermodynamic limit, by discontinuous changes in the ground state properties. These discontinuities affect expectation values of observables, including spatial correlations. When a 1QPT is crossed in the vicinity of a second order one, due to the correlation length divergence of the latter, the corresponding ground state is modified and it becomes increasingly difficult to determine the order of the transition when the size of the system is finite. Here we show that, in such situations, it is possible to apply finite size scaling (FSS) to entanglement measures, as it has recently been done for the order parameters and the energy gap, in order to recover the correct thermodynamic limit (Campostrini *et al* 2014 *Phys. Rev. Lett.* **113** 070402). Such a FSS can unambiguously discriminate between first and second order phase transitions in the vicinity of multicritical points even when the singularities displayed by entanglement measures lead to controversial results.

1. Introduction

Understanding how many-body interacting systems order into different quantum phases as well as the transitions between them remains one of the most challenging open problems in modern physics. Quantum phase transitions (QPTs) are associated with the non-analytical behavior of some observable and/or correlator which can be either local or non local. With the discovery of topological and new exotic phases [1], which fall outside Landau's symmetry breaking paradigm, the use of entanglement to describe quantum matter seems to be, by all means, necessary [2].

Here, we restrict ourselves to study entanglement behavior for a large class of QPTs which, in analogy to their classical counterparts, are signaled by singularities in the derivatives of the (free) energy [3]. In such cases, phase transitions are classified by the minimum order of the derivative of the ground state energy which is not continuous. Accordingly, first (1QPTs) and second (2QPTs) order QPTs show singular behavior on the first and second derivative of the ground state energy respectively. For 1QPTs, the singular behavior translates into abrupt discontinuities of some local observables while for 2QPTs the order parameters change continuously with a power law. In this last case, the thermodynamic limit can be recovered using finite size scaling (FSS) [4]. The scaling is characterized by the critical exponents allowing the classification of apparently different 2QPTs into the same universality class. With such definitions at hand it looks straightforward to distinguish if a given QPT is of first or second order. But this is not always the case when finite size effects are present. This question becomes especially relevant in the vicinity of multicritical points where several QPTs of different order coexist in a narrow range of Hamiltonian parameters.

First studies of the entanglement behavior close to a QPT were performed by analyzing bipartite entanglement in simple spin models like the quantum Ising spin-1/2 chain which exhibits a 2QPT. In [5, 6], the authors showed that, similarly to the ground state energy behavior, the bipartite entanglement between two adjacent spins, as measured by the concurrence, $\mathcal{C}$, has a derivative which diverges at the critical point in the thermodynamical limit.

Moreover, they showed that, for finite size systems, a FSS can be performed allowing the correct extraction of the critical exponents corresponding to the Ising transition. Since then, a large amount of work has been devoted to deepen the connections between quantum information and QPTs, see for instance [7–17].

In [18], the above results were generalized by using Kohn–Sham theorem which links ground state properties with reduced density matrices. For N-partite local Hamiltonians that contain at most k-body interactions, $\hat{H}(\lambda) = \sum_k \hat{H}_k(\lambda)$, where λ is a parameter in the Hamiltonian phase-space, such as the magnetization or an interaction strength. The energy of the ground state $|\Psi_0\rangle$ can be written as

$$E_0(\lambda) = \langle\Psi_0|\hat{H}|\Psi_0\rangle = \sum_k \mathrm{Tr}\ (\hat{H}_k\ \rho^k), \tag{1}$$

where ρ^k is the reduced density matrix acting on the local support of the corresponding local Hamiltonian $\hat{H}_k$. For the usual case of local Hamiltonians with just two-body interactions, $\hat{H}_k(\lambda) = \hat{H}_{ij}(\lambda)$, where the indexes i and j refer to two spins, it can be shown that $\partial_\lambda E_0 \sim (\partial_\lambda \hat{H}_{ij})\rho^{ij}$. If the local Hamiltonians are smooth functions of λ, then a one-to-one correspondence can be made between the singularities of $\partial_\lambda E_0(\lambda)$ arising in a 1QPT and the singularities of (the matrix elements of) ρ^{ij}. The above translates into discontinuous pairwise entanglement measures, which depend exclusively on ρ^{ij}. By the same reasoning, a singularity in $\partial_\lambda^2 E_0$, typical of a 2QPT, is associated to a singularity in the first derivative of the corresponding pairwise entanglement measure.

A theorem casting all the above results is stated in [18] claiming that, unless there exist accidental divergences, the order and properties of QPTs of local Hamiltonians are signalled by the entanglement measures associated to the corresponding reduced density matrix of the ground state. The theorem works in both directions, i.e. a discontinuity in a pairwise measure of entanglement in a 2-local Hamiltonian indicates a 1QPT while a discontinuity/divergence in its derivative signals a 2QPT. The above theorem has some known caveats. For instance, in the spin-1/2 XXZ chain, at the 1QPT between the ferromagnetic and critical phase, the concurrence is a function of the energy at the critical point and it remains continuous in the thermodynamic limit while its first derivative is discontinuous [19, 20]. For the same transition, it has been shown that a symmetry breaking in the ferromagnetic phase also modifies the origin of the non-analytic behavior of the concurrence [21]. In [22], a three-body local Hamiltonian model was presented in which the pairwise concurrence is non analytical in the absence of any QPT [22]. For 2D models even less is known.

Motivated by the above results, we analyze here scaling properties of pairwise entanglement measures for 2-local Hamiltonians near multicritical points. Although FSS is a tool to obtain the thermodynamical properties of the system for continuous (2QPT) phase transitions, here we show that such a tool can be employed also for entanglement measures for 1QPTs. Further, we demonstrate that when finite size effects are important, it is precisely the scaling of the entanglement measure and not the measure itself which determines the correct order of the transition. This fact is especially relevant for a 1QPT crossed in the vicinity of a 2QPT and it is in accordance with the recent results reported by Campostrini and coauthors [23] showing that the order parameter of a 1QPT can be continuous for finite systems and admits an appropriate FSS.
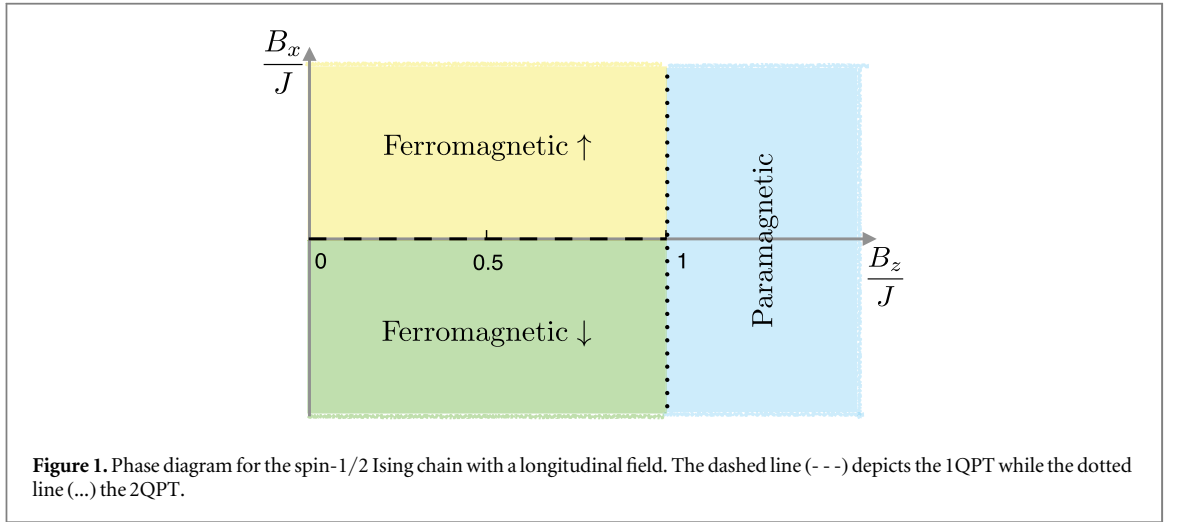
The paper is organized as follows. In section 2, we focus on the spin-1/2 Ising chain with longitudinal field and report how bipartite entanglement, as measured by e.g. the concurrence, scales in the 1QPT when is crossed near the multicritical point. This choice is motivated by the fact that this is an integrable model when the longitudinal field vanishes and serves as a playtool to analyze numerical results. In section 3, we move to a much more complex model, the spin-1 XXZ chain with uniaxial single-ion anisotropy. The phase diagram of the model is rich and has several QPTs whose boundaries are only known approximately. We focus on the 1QPT of the model and analyze by means of numerical techniques the behavior of bipartite entanglement in the vicinity of multicritical points. In section 4, we discuss the results and, finally, in section 5 we conclude.

2. Spin-1/2 Ising chain with longitudinal field

The first spin model we explore is the spin-1/2 Ising chain with a longitudinal field,

$$\hat{H} = -J\sum_{i=1}^{L-1} \hat{\sigma}_i^x \hat{\sigma}_{i+1}^x - B_z \sum_{i=1}^{L} \hat{\sigma}_i^z - B_x \sum_{i=1}^{L} \hat{\sigma}_i^x, \tag{2}$$

where L is the number of spins, $\hat{\sigma}_i^\alpha$ are the Pauli matrices for spin i and we set $J = 1$ and $B_z \geqslant 0$. In figure 1, we provide the phase diagram of the model. For $B_x = 0$, where the system reduces to the integrable Ising model, there is a 2QPT at $B_z = 1$ between the ferromagnetic ($B_z < 1$) and paramagnetic phases ($B_z > 1$). This 2QPT was the first one studied by means of bipartite entanglement [5]. When $B_x \neq 0$, the system is no longer integrable and we obtain the ground state of the system using both, the density matrix renormalization group (DMRG) with open boundary conditions (OBCs) [24–26] and exact diagonalization (ED) calculations. When the system is in the ferromagnetic phase, a 1QPT takes place at $B_x = 0$ between the two ferromagnetic ground states, ferromagnetic ↑ and ferromagnetic ↓. This transition can be detected by a discontinuity in the magnetization,

Figure 1. Phase diagram for the spin-1/2 Ising chain with a longitudinal field. The dashed line (- - -) depicts the 1QPT while the dotted line (...) the 2QPT.

$M_x = \sum_i \langle \hat{\sigma}_i^x \rangle$, which passes from positive to negative values. However, for finite systems, numerical calculations in a region sufficiently close to $B_x = 0$ show a smooth slope in M_x instead of a discontinuity. To deal with this effect, in [23] a FSS is proposed for first order quantum transitions in a chain of size L driven by a magnetic field h. There, on dimensional grounds, it is argued that around the critical point ($h = 0$), if there is scaling behavior, the relevant scaling variable, κ, should correspond to the ratio between the energy contribution of h, and the gap at the critical point, $\Delta_L = \Delta_L(L, h = 0)$,

$$\kappa \sim \frac{hL}{\Delta_L}. \tag{3}$$

As a result, heuristically when $hL \sim \Delta_L$, the ground state energy becomes effectively continuous along the transition and so does the order parameter. This feature becomes more relevant the closer the critical point is to a 2QPT, since the correlation length of the system (ξ) diverges, enhancing the nearby finite size effects. In [23], it is shown that across the 1QPT of the longitudinal Ising chain (equation (2)) occurring at $B_x = 0$, the first energy gap and the magnetization obey the following scaling ansatz:

$$\Delta(L, B_x) \approx \Delta_L f_\Delta(\kappa), \tag{4}$$

$$M_x(L, B_x) \approx m_0 f_M(\kappa), \tag{5}$$

where $f_\Delta(\kappa)$ and $f_M(\kappa)$ are continuous universal functions for all L and B_z. Since the model is integrable for $B_x = 0$, the scaling variable can be defined as [23]

$$\kappa_1 = \frac{2m_0 B_x L}{\Delta_L}, \tag{6}$$

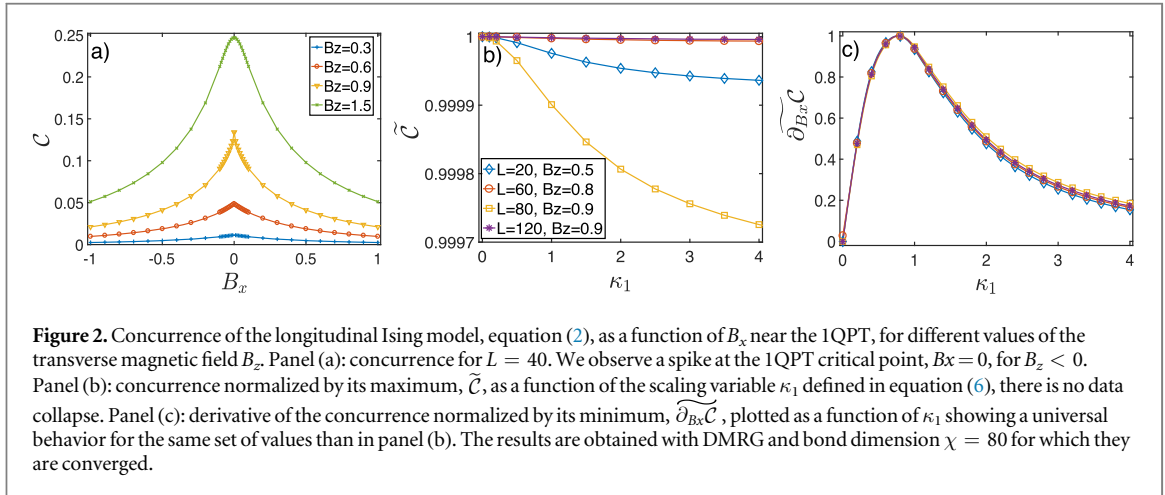where $\Delta_L = \Delta_{L, B_x=0} \approx 2(1 - B_z^2) B_z^L$, is the first gap at the critical point, $B_x = 0$ for OBC and

$$m_0 = \lim_{B_x \to 0^+} \lim_{L \to \infty} \langle \hat{\sigma}_x \rangle = (1 - B_z^2)^{1/8}. \tag{7}$$

Clearly, as one approaches the critical point, $B_x = 0$, in the nearby region of the 2QPT ($B_z = 1$), the gap closes and even at very small values of the driving parameter B_x around the critical point, the 1QPT transition looks continuous. Here, we apply the above scaling concepts to the entanglement across the 1QPT transition. Since the Hamiltonian is 2-local, discontinuities in entanglement measures have to be related to two-body (pairwise) entanglement of two nearest-neighbor spins (i, j) described by the reduced density matrix, ρ^{ij}. For pure states, all measures of bipartite entanglement are in one-to-one correspondence and are all a function of the eigenvalues of the reduced density matrix arising from the chosen partition. For mixed states, this is not the case anymore and the entanglement measure has to be calculated as the convex roof of the corresponding pure state measure. An exception for mixed states ρ of two spin-1/2 particles or qubits, is the concurrence [27] which is equivalent to the entanglement cost and has a closed analytical expression:

$$\mathcal{C}(\rho) = \max(0, \lambda_1 - \lambda_2 - \lambda_3 - \lambda_4), \tag{8}$$

where λ_i are the eigenvalues, in decreasing order, of the matrix $R = \sqrt{\sqrt{\rho} \, \tilde{\rho} \sqrt{\rho}}$ with $\tilde{\rho} = (\hat{\sigma}_y \otimes \hat{\sigma}_y) \rho^*(\hat{\sigma}_y \otimes \hat{\sigma}_y)$, where the product $\hat{\sigma}_y \otimes \hat{\sigma}_y$ is defined in the Hilbert space of the two spins and ρ^* is the complex conjugate of ρ. Since $\mathcal{C}$ is supposed to be discontinuous at the critical point for 1QPTs, naively we might expect that it will follow a similar scaling behavior as M_x, equation (5). In figure 2, we show $\mathcal{C}$ for the two central spins which, if border effects are neglected, will also hold for the rest of neighboring spin pairs. In the left panel, we observe that $\mathcal{C}$ is a continuous function with a spike at the critical point which signals a singularity in the first derivative, $\partial_{B_x} \mathcal{C}$. The

Figure 2. Concurrence of the longitudinal Ising model, equation (2), as a function of B_x near the 1QPT, for different values of the transverse magnetic field B_z. Panel (a): concurrence for $L = 40$. We observe a spike at the 1QPT critical point, $Bx = 0$, for $B_z < 0$. Panel (b): concurrence normalized by its maximum, $\widetilde{\mathcal{C}}$, as a function of the scaling variable κ_1 defined in equation (6), there is no data collapse. Panel (c): derivative of the concurrence normalized by its minimum, $\widetilde{\partial_{Bx}\mathcal{C}}$, plotted as a function of κ_1 showing a universal behavior for the same set of values than in panel (b). The results are obtained with DMRG and bond dimension $\chi = 80$ for which they are converged.

spike becomes more pronounced as the transition gets closer to the 2QPT at $B_z = 1$. It is worth pointing out that such a behavior bears strong similarities with the geometric entanglement, a collective measure of entanglement indicating how much the ground state differs from a separable state [14]. Notice that for $B_z > 1$, when the system is in the paramagnetic phase independently of the sign of the longitudinal field B_x, (as indicated in figure 2 for $B_z = 1.5$), the concurrence becomes a smooth function of B_x. In the central panel of figure 2, we plot the scaling of the concurrence normalized by its maximum value, $\widetilde{\mathcal{C}} = \mathcal{C}/\mathcal{C}_{\max}$, as a function of the scaling variable κ_1 to determine whether $\mathcal{C}$ fulfills a similar scaling relation as in equation (5). It is enough to investigate what happens for $\kappa_1 > 0$ because $\mathcal{C}(\kappa_1)$ has even parity, i.e. $\mathcal{C}(\kappa_1) = \mathcal{C}(-\kappa_1)$. This is a consequence of the Hamiltonian, and, therefore, the ground state, being invariant under the change $B_x \rightarrow -B_x$ and a local π-rotation of the spins around the z-axis. Finally, in panel c) we display the scaling of the derivative of the concurrence normalized by its minimum value $\widetilde{\partial_{Bx}\mathcal{C}} = \partial_{Bx}\mathcal{C}/[\partial_{Bx}\mathcal{C}]_{\min}$. Interestingly enough, the concurrence does not scale with the fitting parameter κ_1, but its derivative does. In the central panel, we can see that the data for different B_z and L do not collapse in a universal function, while, in the right panel, there is a good data collapse for different values of B_z and L. Thus, $\partial_{Bx}\mathcal{C}$ fulfills the scaling ansatz,

$$\partial_{Bx}\mathcal{C}(L, B_z) = [\partial_{Bx}\mathcal{C}]_{\min} g(\kappa_1), \tag{9}$$

where $g(\kappa_1)$ is a universal function for any L and B_z. We further discuss all these results in section 4.
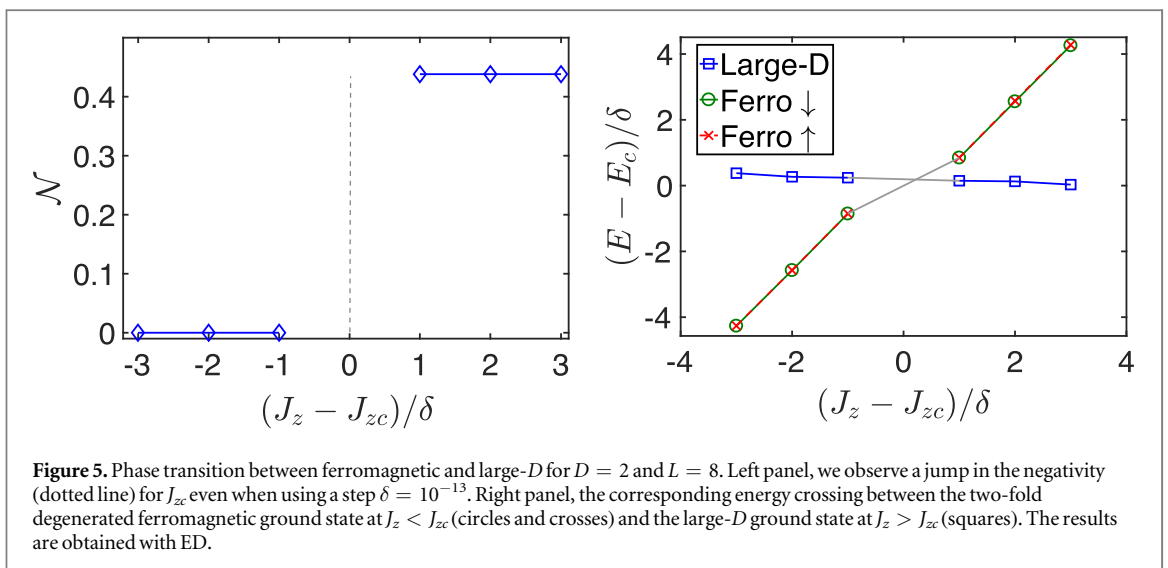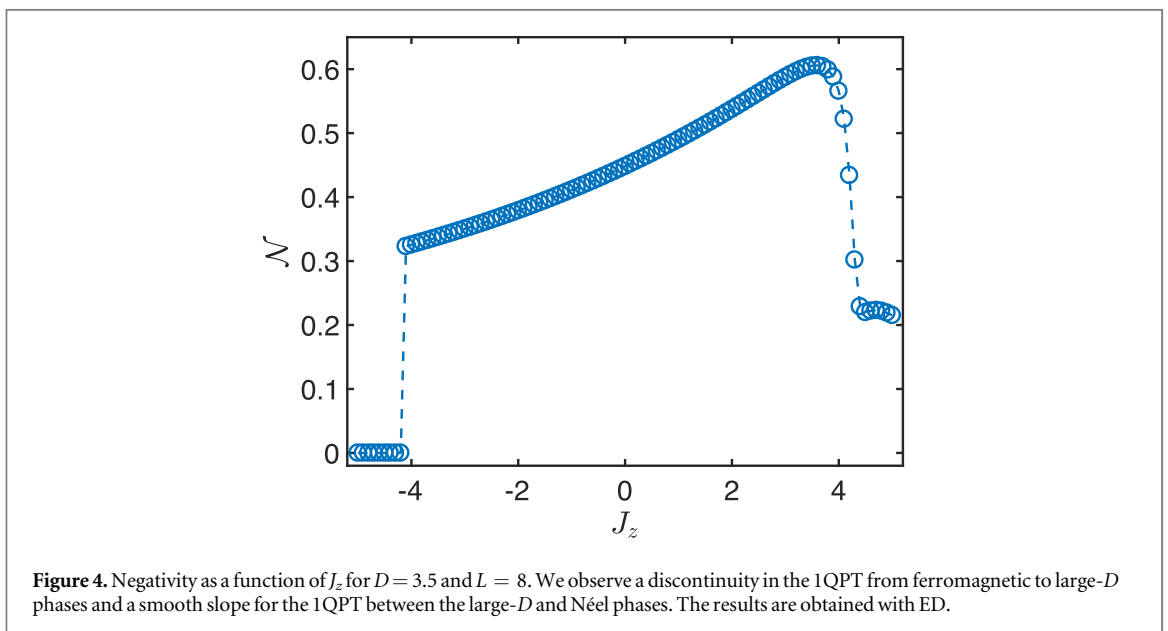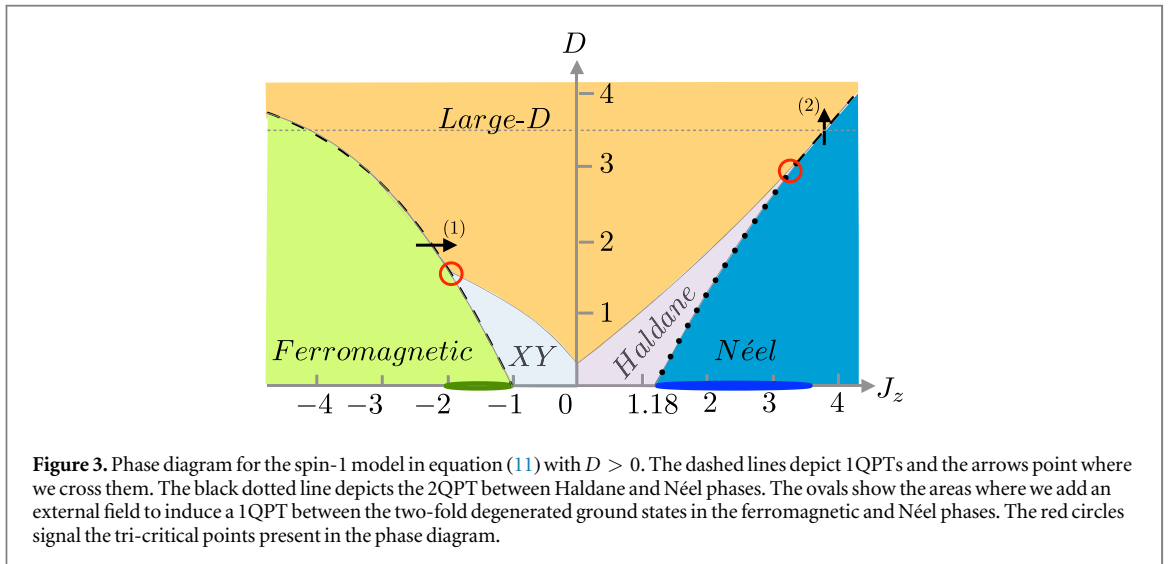
3. Spin-1 XXZ chain with uniaxial single-ion anisotropy

In this section, we extend the study of entanglement along 1QPTs to a spin-1 system. Since the concurrence, $\mathcal{C}$, can only be easily computed for the mixed states of qubits, in order to compute the entanglement between two spin-1 particles we use the negativity [28, 29]
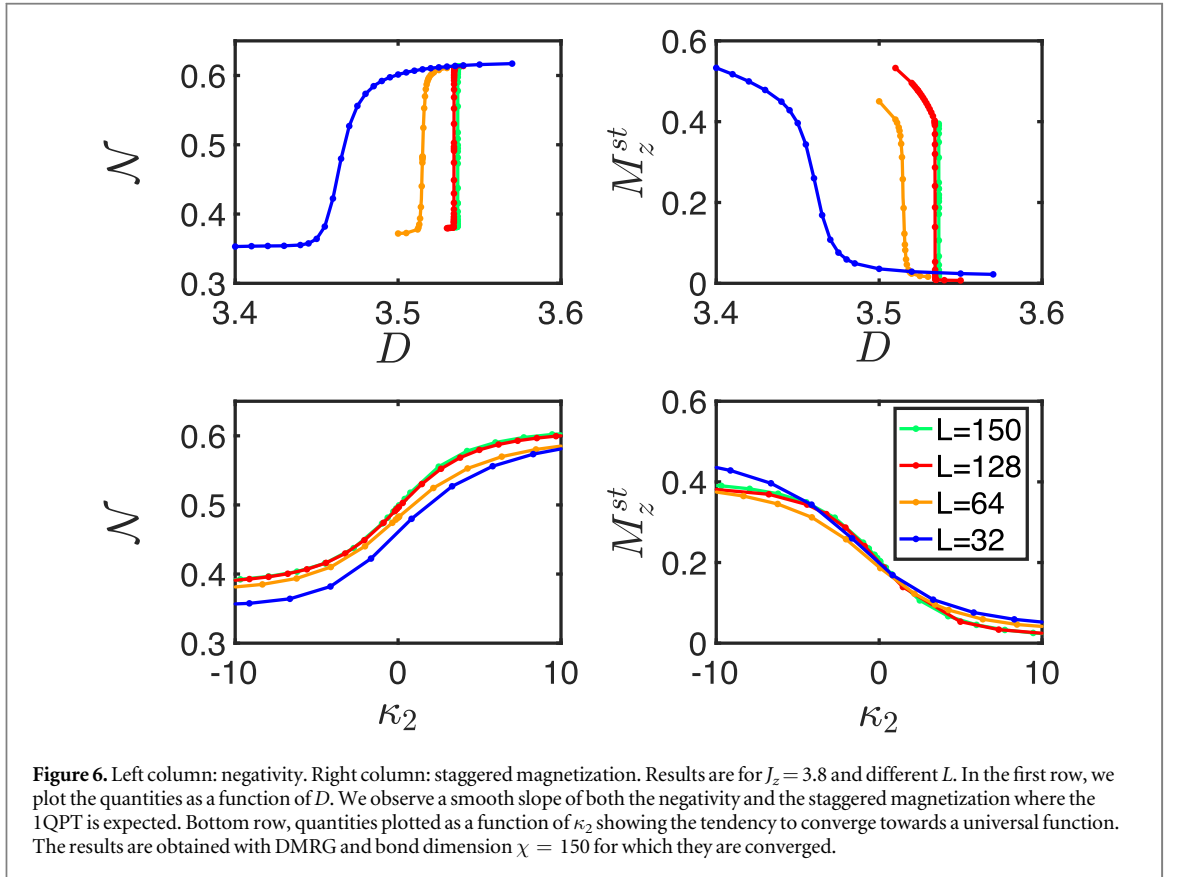
$$\mathcal{N}(\rho) = \frac{||\rho^{T_B}||_1 - 1}{2}, \tag{10}$$

where the operation T_B is the partial transpose defined now on the reduced density matrix of two nearest neighbors spins, ρ^{ij}, and $||...||_1$ is the sum of the absolute value of all singular values. Notice that negativity is a lower bound to entanglement. The model under scrutiny is the spin-1 XXZ chain with uniaxial single-ion anisotropy,

$$\hat{H} = \sum_{l=1}^{L-1} [J\hat{S}_l^x \hat{S}_{l+1}^x + J\hat{S}_l^y \hat{S}_{l+1}^y + J_z \hat{S}_l^z \hat{S}_{l+1}^z] + D \sum_{l=1}^{L} (\hat{S}_l^z)^2, \tag{11}$$

where $\hat{S}_l^{\alpha}$ are the spin-1 matrices for spin l and D is the uniaxial single-ion anisotropy which we take as positive. We set $J = 1$, and use it as the unit of energy. We choose this model because of the richness of its phase diagram [30], schematically shown in figure 3, with several 1QPTs which we depict with dashed lines. The behavior of $\mathcal{N}$ along the different 1QPTs present in the model is very different depending on their closeness to a multicritical point which also involves 2QPTs. We start by examining the negativity as a function of the J_z for a constant uniaxial field $D = 3.5$ and $L = 8$. Two 1QPTs are crossed at such value of D, as indicated in the phase diagram by a gray horizontal line (see figure 3). The first one corresponds to the transition from ferromagnetic order to the large-D phase, which is crossed approximately at $J_z = -4.2$. Another 1QPT appears between large-D/Néel at approximately $J_z = 3.8$. As clearly shown in figure 4, the former phase transition is clearly signalled by a discontinuity in $\mathcal{N}$, whereas the latter shows a smooth slope along the transition. In figure 5, we show in detail

Figure 3. Phase diagram for the spin-1 model in equation (11) with $D > 0$. The dashed lines depict 1QPTs and the arrows point where we cross them. The black dotted line depicts the 2QPT between Haldane and Néel phases. The ovals show the areas where we add an external field to induce a 1QPT between the two-fold degenerated ground states in the ferromagnetic and Néel phases. The red circles signal the tri-critical points present in the phase diagram.

Figure 4. Negativity as a function of J_z for $D = 3.5$ and $L = 8$. We observe a discontinuity in the 1QPT from ferromagnetic to large-D phases and a smooth slope for the 1QPT between the large-D and Néel phases. The results are obtained with ED.

Figure 5. Phase transition between ferromagnetic and large-D for $D = 2$ and $L = 8$. Left panel, we observe a jump in the negativity (dotted line) for J_{zc} even when using a step $\delta = 10^{-13}$. Right panel, the corresponding energy crossing between the two-fold degenerated ferromagnetic ground state at $J_z < J_{zc}$ (circles and crosses) and the large-D ground state at $J_z > J_{zc}$ (squares). The results are obtained with ED.

Figure 6. Left column: negativity. Right column: staggered magnetization. Results are for $J_z = 3.8$ and different L. In the first row, we plot the quantities as a function of D. We observe a smooth slope of both the negativity and the staggered magnetization where the 1QPT is expected. Bottom row, quantities plotted as a function of κ_2 showing the tendency to converge towards a universal function. The results are obtained with DMRG and bond dimension $\chi = 150$ for which they are converged.
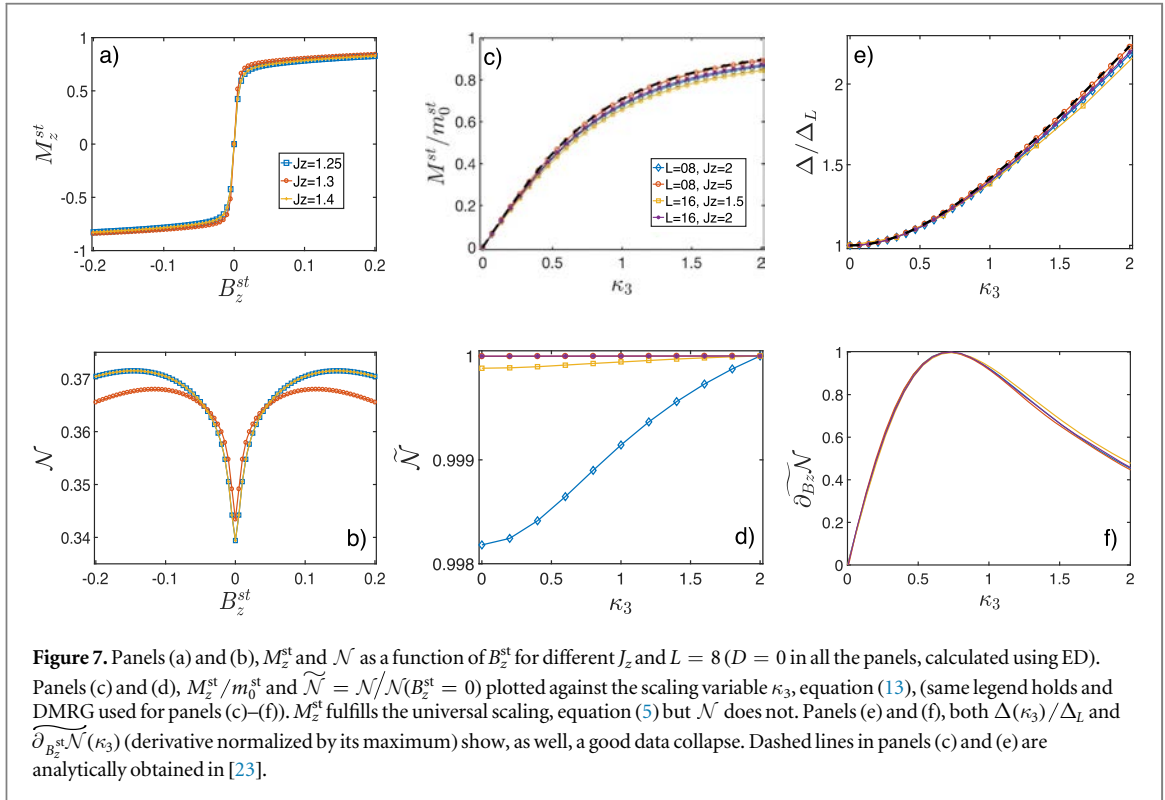
the generic behavior of $\mathcal{N}$ together with the corresponding level crossing along the ferromagnetic/large-D phase transition. We cross the transitions at a fixed value $D = 2$, as depicted by (1) in figure 3, in the nearby region of a critical point (depicted by a red circle). We observe that even for small steps of the parameter J_z driving the 1QPT, $\mathcal{N}$ is always discontinuous and a neat level crossing is shown between the two-fold degenerated ferromagnetic ground state, for $J_z < J_{zc}$, and the large-D ground state, for $J_z > J_{zc}$. This means that, at J_{zc}, there is a sudden change in the ground state which is detected by a discontinuity in $\mathcal{N}$. Therefore, in figure 5, we observe the expected discontinuous behavior for $\mathcal{N}$ along a 1QPT even for a system of just 8 spins without any finite size effects.

We focus now on to the large-D/Néel 1QPT. In figure 6 we display the negativity and the staggered magnetization for a fixed value $J_z = 3.8$ as a function of the anisotropy, D, around the critical point $D_{c,L}$ denoted by (2) in figure 3. We add the subindex L to indicate that this quantity now depends on the system size. In order to show the behavior for larger systems, we use DMRG calculations for $L = 32, 64, 128$ and 150. In the two top panels, we observe that both, $\mathcal{N}$ and the staggered magnetization, $M_z^{st} = \sum_{i=1}^{L} (-1)^i \langle \hat{S}_i^z \rangle$, change smoothly around the transition point. As L increases, the slope becomes more pronounced getting closer to a discontinuity and we need values of D closer to the critical point to observe the continuous slope. For instance, the necessary step in D to observe a continuous behavior is $\delta \sim 10^{-4}$ and $\delta \sim 10^{-6}$ for $L = 64$ and $L = 150$, respectively. Note that in this case, as in section 2, we are very close to a 2QPT. As we get further from the tricritical point, i.e. as we increase the value to $J_z \gg J_{crit} = 3.8$, this effect progressively becomes less important and both $\mathcal{N}$ and M_z^{st} are effectively discontinuous. Since the transition is known to be of first order, we propose a similar FSS as in the previous section, defining a relevant scaling variable, κ_2, as the ratio between the energy contribution of D along the transition and the gap at the critical point,

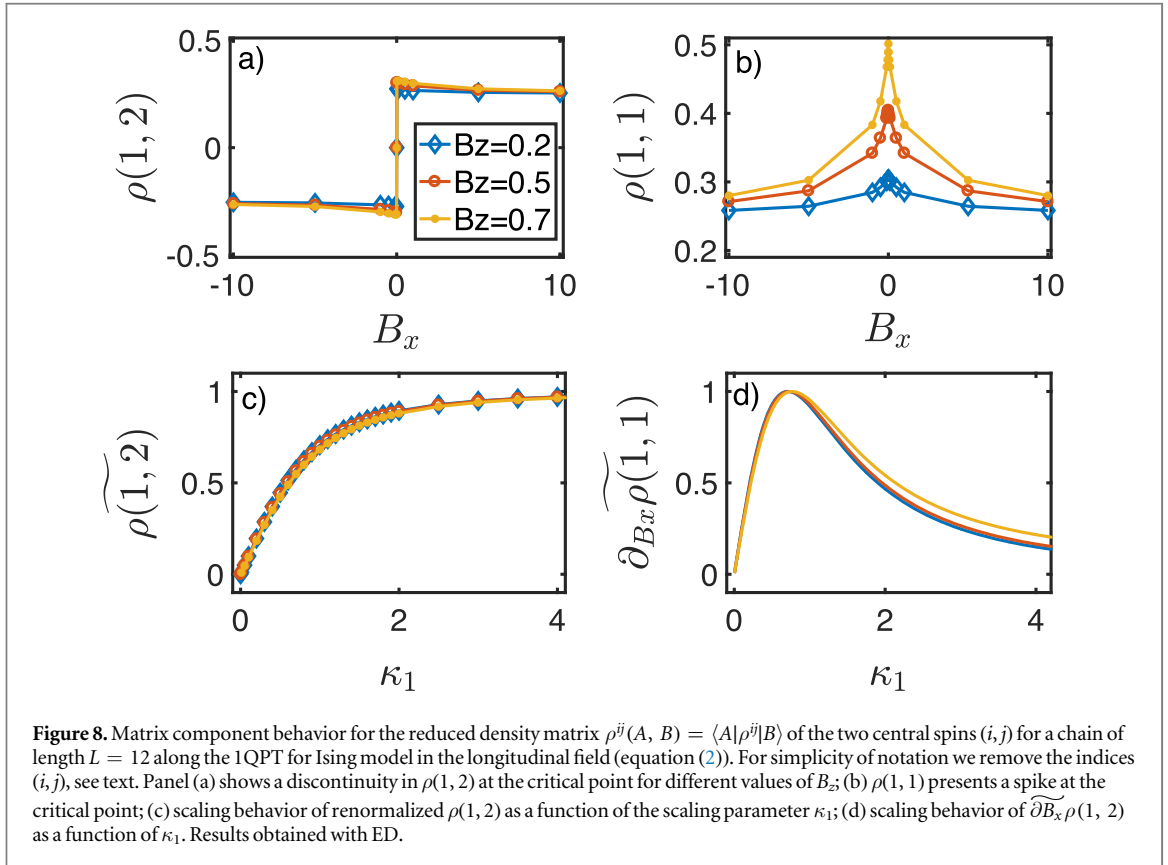$$\kappa_2 \sim \frac{(D - D_{c,L})L}{\Delta_L}. \tag{12}$$

Now, Δ_L is obtained numerically and $(D - D_{c,L})L$ is a bare estimation for the energy contribution of the parameter D. In the bottom panels, we plot $\mathcal{N}$ and M_z^{st} as a function of this scaling variable κ_2. As we can observe, both quantities seem to converge, though not perfectly, towards a universal scaling, as described by equation (5). It is worth mentioning that equation (12) is an approximation whereas, in the previous section we had analytic expressions for Δ_L and m_0 in equation (6). Actually, in [31], a similar FSS, with non-analytic expressions, is proposed for the Potts chain with a similar convergence. It seems reasonable, thus, to state that for this 1QPT, when we are close to the 2QPT, $\mathcal{N}$ is continuous due to finite size effects and that it obeys the scaling ansatz for 1QPT.

Figure 7. Panels (a) and (b), M_z^{st} and $\mathcal{N}$ as a function of B_z^{st} for different J_z and $L = 8$ ($D = 0$ in all the panels, calculated using ED). Panels (c) and (d), M_z^{st}/m_0^{st} and $\widetilde{\mathcal{N}} = \mathcal{N}/\mathcal{N}(B_z^{st} = 0)$ plotted against the scaling variable κ_3, equation (13), (same legend holds and DMRG used for panels (c)–(f)). M_z^{st} fulfills the universal scaling, equation (5) but $\mathcal{N}$ does not. Panels (e) and (f), both $\Delta(\kappa_3)/\Delta_L$ and $\widetilde{\partial_{B_z^{st}}\mathcal{N}}(\kappa_3)$ (derivative normalized by its maximum) show, as well, a good data collapse. Dashed lines in panels (c) and (e) are analytically obtained in [23].

Finally, we analyze the behavior of $\mathcal{N}$ when the 1QPT is due to a $\mathbb{Z}_2$ symmetry breaking of a two fold-degenerated ground state. To this aim we add an extra magnetic field, $B_z \sum_{i=1}^{L} \hat{S}_i^z$ (extra magnetic staggered field $B_z^{st} \sum_{i=1}^{L}(-1)^i \hat{S}_i^z$) in the ferromagnetic (Néel) phase of the XXZ spin-1 model in equation (11). These new terms lead to two new 1QPT between ferromagnetic ↑ / ferromagnetic ↓ (Néel/Anti Néel) phases, depicted graphically by ovals along $D = 0$ line in the phase diagram of the model (see figure 3). The corresponding order parameter for both transitions, the magnetization (M_z), and the staggered magnetization (M_z^{st}) respectively, are discontinuous in the thermodynamic limit. For the first induced QPT between the ferromagnetic phases, the entanglement remains always constant and zero. More interesting features appear in the Néel/Anti-Néel transition whose results are summarized in figure 7. These results are obtained using a mixture of ED (panels (a) and (b)) and DMRG (in the remaining panels). The bond dimension in DMRG was chosen in such a way that the results converged, which meant using a bond dimension of 100 or 150. In panels (a) and (b) we show, respectively, M_z^{st} and $\mathcal{N}$ as a function of the added staggered magnetic field B_z^{st}. While the order parameter, M_z^{st}, has the expected discontinuous behavior, the pairwise entanglement, $\mathcal{N}$, has a dip at the critical point, displaying a continuous $\mathcal{N}$ but a discontinuous derivative. In order to apply the proper FSS ansatz for the negativity, we start by defining first the relevant scaling variable (as we did in section 2):

$$\kappa_3 = \frac{2m_0^{st} B_z^{st} L}{\Delta_L}. \tag{13}$$

In full analogy with the results presented in section 2, and due to the fact that the 2QPT between Haldane/Néel phases belongs to the same universality class as the spin-1/2 Ising, we use the expression of m_0^{st} from equation (7) by substituting $B_z \rightarrow J_{zc}/J_z$, where $J_{zc} \approx 1.186$ corresponds the 2QPT critical point for $D = 0$ [32]. Our scaling results are summarized in panels (c) and (d) of figure 7, where we show, respectively, M_z^{st} and $\mathcal{N}$ as a function of κ_3. The scaling ansatz, equation (5), works properly for M_z^{st}, but, as it happens for the concurrence, $\mathcal{C}$, in the spin-1/2 Ising chain, the scaling also fails for the negativity $\mathcal{N}$ in this phase transition. Finally, in panels (e) and (f) we show how the gap, Δ_L, fulfills the scaling ansatz, equation (4), and how the derivative of the negativity, $\partial_{B_z^{st}} N$, also verifies the scaling ansatz, equation (9). This last behavior strongly resembles the behavior of the derivative on the concurrence for the spin longitudinal Ising spin 1/2 chain. To further ensure the correctness of our results, in figure 7 we also display the comparison between our numerical data, $M^{st}(\kappa_3)$ and $\Delta_L(\kappa_3)$, with the analytic expressions using an effective two level theory as derived in [23].

Figure 8. Matrix component behavior for the reduced density matrix $\rho^{ij}(A, B) = \langle A|\rho^{ij}|B\rangle$ of the two central spins (i, j) for a chain of length $L = 12$ along the 1QPT for Ising model in the longitudinal field (equation (2)). For simplicity of notation we remove the indices (i, j), see text. Panel (a) shows a discontinuity in $\rho(1, 2)$ at the critical point for different values of B_z; (b) $\rho(1, 1)$ presents a spike at the critical point; (c) scaling behavior of renormalized $\rho(1, 2)$ as a function of the scaling parameter κ_1; (d) scaling behavior of $\widetilde{\partial_{B_x}}\rho(1, 2)$ as a function of κ_1. Results obtained with ED.

4. Results discussion

Let us discuss here the origin of the concurrence's continuity together with its discontinuous first derivative across the the 1QPT in the spin-1/2 Ising model described in equation (2). A similar response is shown by the negativity in the spin-1 XXZ chain across the 1QPT between the Nèel/Anti-Néel phases. These transitions apparently contradict the expected behavior stated in [18] that links a singularity in the first derivative of the pairwise entanglement to a 2QPT, given that this singularity originates exclusively from the elements of ρ^{ij}, in equation (1). To determine the origin of this unusual behavior, we focus on the Ising longitudinal model and analyze the elements of the reduced density matrix of the two central spins (ij) that we denote by $\rho(A, B) \equiv \langle A|\rho^{ij}|B\rangle$ as a function of longitudinal field, B_x, for different values of the transverse magnetic field B_z. For simplicity of notation we remove from now on the super indices i, j. Given the symmetries of the Hamiltonian, it suffices to consider just two different matrix elements, $\rho(1, 1) = \langle \uparrow \uparrow |\rho^{ij}| \uparrow \uparrow\rangle$ and $\rho(1, 2) = \langle \uparrow \uparrow |\rho^{ij}| \downarrow \uparrow\rangle$, for analyzing the behavior of the concurrence. As plotted in the top panels of figure 8, $\rho(1, 2)$ is discontinuous along the 1QPT transition, while $\rho(1, 1)$ presents a spike signalling a singularity in its first derivative. In the bottom panels, we display our results regarding their scaling behavior as a function of the relevant scaling parameter κ_1 (see equation (6)). Interestingly enough, as shown in panel (c), the matrix element $\rho(1, 2)$ follows exactly the same scaling proposed for 1QPT [23], while it is derivative of the matrix element $\rho(1, 1)$ ($\partial_{B_x}\rho(1, 1)$) and not the matrix element itself which scales properly for different values of L and B_z. Furthermore, it can be shown that all the discontinuities present in elements such as $\rho(1, 2)$ cancel out when computing the concurrence. As a result, the concurrence $\mathcal{C}$ shows a singularity in the first derivative as it would happen in a 2QPT and it is precisely $\partial_{B_x}\mathcal{C}$ the quantity which fulfills the FSS and not $\mathcal{C}$ itself. The same analysis applies to the spin-1 XXZ chain with on-site anisotropy, where a dip in the negativity, $\mathcal{N}$, at the critical point appears. This behavior has the same origin as the previously reported spin-1/2 case and, therefore, it is the derivative of $\mathcal{N}$ and not the negativity itself which fulfills the FSS for 1QPTs. Hence, in these cases, a singularity in the first derivative of the concurrence/negativity (given and the concurrence/negativity are continuous functions), does not signal a 2QPT as it was conjectured in [18].

5. Conclusions

In conclusion, in this work we have analyzed pairwise entanglement behavior in diverse 1QPT transitions driven by 2-local Hamiltonians. We have shown the dramatic importance of finite size effects when 1QPT occur in the

nearby region of multicritical point containing also 2QPT. To illustrate this fact, we have shown examples of 1QPT in 2-body-Hamiltonians in which pairwise entanglement measures are continuous across the phase transition while their first derivatives are not. We have extended our results by using non integrable models in which the same behavior can be observed. A deeper analysis shows that the behavior is inherited from the two body reduced density matrix elements, which for 2-local Hamiltonians, are linked to the non-analyticities of the ground state energy. Our main result has been to demonstrate that for finite systems, the order of the QPT in symmetry broken phases is given by the scaling behavior of their bipartite entanglement and not by its non-analytical character. Our results should allow to better determine the order and boundaries of QPTs near multicritical points.

Acknowledgments

ORCID iDs

G De Chiara ⬤ https://orcid.org/0000-0003-3265-9021

References

[1]   Kosterlitz J M and Thouless D J 1973 *J. Phys. C: Solid State Phys.* **6** 1181
[2]   Amico L, Fazio R, Osterloh A and Vedral V 2008 *Rev. Mod. Phys.* **80** 517–76
[3]   Sachdev S 2001 *Quantum Phase Transitions* (Cambridge: Cambridge University Press)
[4]   Fisher M E and Barber M N 1972 *Phys. Rev. Lett.* **28** 1516–9
[5]   Osterloh A, Amico L, Falci G and Fazio R 2002 *Nature* **416** 608–10
[6]   Osborne T J and Nielsen M A 2002 *Phys. Rev. A* **66** 032110
[7]   Bose I and Chattopadhyay E 2002 *Phys. Rev. A* **66** 062320
[8]   Vidal G, Latorre J I, Rico E and Kitaev A 2003 *Phys. Rev. Lett.* **90** 227902
[9]   Latorre J I, Rico E and Vidal G 2004 *Quantum Inf. Comput.* **4** 48–92 (arXiv: quant-ph/0304098)
[10] Vidal J, Palacios G and Mosseri R 2004 *Phys. Rev. A* **69** 022107
[11] Alcaraz F C, Saguia A and Sarandy M S 2004 *Phys. Rev. A* **70** 032333
[12] Vidal J, Mosseri R and Dukelsky J 2004 *Phys. Rev. A* **69** 054101
[13] Barnum H, Knill E, Ortiz G, Somma R and Viola L 2004 *Phys. Rev. Lett.* **92** 107902
[14] Orús R and Wei T C 2010 *Phys. Rev. B* **82** 155120
[15] Gu S J, Lin H Q and Li Y Q 2003 *Phys. Rev. A* **68** 042330
[16] Stasińska J, Rogers B, Paternostro M, De Chiara G and Sanpera A 2014 *Phys. Rev. A* **89** 032330
[17] Hofmann M, Osterloh A and Gühne O 2014 *Phys. Rev. B* **89** 134101
[18] Wu L A, Sarandy M S and Lidar D A 2004 *Phys. Rev. Lett.* **93** 250404
[19] Gu S J, Lin H Q and Li Y Q 2003 *Phys. Rev. A* **68** 042330
[20] Syljuåsen O F 2003 *Phys. Rev. A* **68** 060301
[21] Pereira L J and de Oliveira T R 2016 *Front. Phys.* **4** 51
[22] Yang M F 2005 *Phys. Rev. A* **71** 030302
[23] Campostrini M, Nespolo J, Pelissetto A and Vicari E 2014 *Phys. Rev. Lett.* **113** 070402
[24] White S R 1992 *Phys. Rev. Lett.* **69** 2863–6
[25] White S R 1993 *Phys. Rev. B* **48** 10345–56
[26] De Chiara G, Rizzi M, Rossini D and Montangero S 2008 *J. Comput. Theor. Nanosci.* **5** 1277–88
[27] Hill S and Wootters W K 1997 *Phys. Rev. Lett.* **78** 5022–5
[28] Życzkowski K, Horodecki P, Sanpera A and Lewenstein M 1998 *Phys. Rev. A* **58** 883–92
[29] Vidal G and Werner R F 2002 *Phys. Rev. A* **65** 032314
[30] Chen W, Hida K and Sanctuary B C 2003 *Phys. Rev. B* **67** 104401
[31] Campostrini M, Nespolo J, Pelissetto A and Vicari E 2015 *Phys. Rev. E* **91** 052103
[32] Ejima S and Fehske H 2015 *Phys. Rev. B* **91** 045121

Using random boundary conditions to simulate disordered quantum spin models in two-dimensional systems

Initial questions and motivations

The study of QSL phases, which are introduced in 2.3, is currently a hot research topic within the condensed matter community. Due to its characteristics, a QSL phase is very elusive for both theoretical and experimental researchers. In the theoretical side, different numerical techniques have been recently used to tackle the issue, for instance Variational Quantum Monte Carlo, 2D-DMRG, or ED of up to 40 particles systems. In this article, we provide a different approach to study the issue. The details of the method, which consists of random boundary conditions, are extensively explained in Sec.5.2. It is well know that for small systems, as the ones we are restricted, the geometry of the lattice critically influences the results. A particular lattice geometry may not be suitable to reproduce the ordered phase expected in the thermodynamic limit and, thus, may give a different ground state in the finite lattice. The question arisen at this point is the following: 'In a QSL phase, where no symmetry is broken, has the lattice geometry a minor influence?' With random boundaries we can reproduce, in a small lattice, different geometries which can allow different ordering vectors to fit in the lattice. In an ordered phase, we expect that for a given lattice geometry, the set of random phases which favors the thermodynamic ordering vector will minimize the energy. The corresponding ground state will be the best guess which we can make of the thermodynamic one. As we get away from

this "optimal" set of random phases we will obtain a larger energy and a ground state which progressively gets away from this "optimal" one. But is this expected feature going to hold as well for a QSL phase? To check the validity of our intuitive idea we take as a model the XY spin model in the 2D SATL. In this model two QSL phases are expected though there is no totally consensus about their nature and exact extension.

Main results

In this article, we have successfully applied our novel method to the XY model in the SATL. We can identify the two conjectured QSL phases with several figures of merit which we report. Our work opens the door to use RBC to study some other systems where a QSL phase is expected. However, the limited size of the systems which can be diagonalized does not allow to determine with precision the boundaries of the QSL phases. A finite size scaling of our results has been discarded for the same reason.

Using random boundary conditions to simulate disordered quantum spin models in two-dimensional systems

A. Yuste,[1,*] M. Moreno-Cardoner,[1] and A. Sanpera[1,2]

[1]*Departament de Física, Universitat Autònoma de Barcelona, 08193 Bellaterra, Spain*
[2]*ICREA, Pg. Lluís Companys 23, 08010 Barcelona, Spain*

Disordered quantum antiferromagnets in two-dimensional compounds have been a focus of interest in the last years due to their exotic properties. However, with very few exceptions, the ground states of the corresponding Hamiltonians are notoriously difficult to simulate making their characterization and detection very elusive, both theoretically and experimentally. Here we propose a method to signal quantum disordered antiferromagnets by doing exact diagonalization in small lattices using random boundary conditions and averaging the observables of interest over the different disorder realizations. We apply our method to study the Heisenberg spin-1/2 model in an anisotropic triangular lattice. In this model, the competition between frustration and quantum fluctuations might lead to some spin-liquid phases as predicted from different methods ranging from spin-wave mean-field theory to 2D-DMRG or PEPS. Our method accurately reproduces the ordered phases expected of the model and signals quantum disordered phases by the presence of a large number of quasidegenerate ground states together with an undefined local order parameter. The method presents a weak dependence on finite-size effects.

I. INTRODUCTION

The characterization of disordered quantum antiferromagnets (AFs) is currently one of the open challenges in modern condensed matter [1]. Ground states of ordered phases in quantum spin systems manifest themselves by long-range order (LRO) accompanied by the presence of local order parameters. The situation is drastically different when disorder arises due to quantum fluctuations and frustration, i.e., the impossibility of simultaneously minimizing all local energy constrains. Such disordered spin systems are expected to lack LRO and do not have local order parameters associated with them. Their presence can, in some cases, be confirmed by the topological entanglement entropy, a subleading term in the entanglement entropy which is invariant with the size of the plaquette [2–4]. However, determining the topological entanglement requires the precise knowledge of the ground state wave function which is often impossible due to the nonintegrability of most AF frustrated models. The importance of these phases, often dubbed topological, is both of fundamental and practical importance. They are at the forefront of present knowledge of strongly correlated systems and possess several features that make them very appealing for possible technological applications. They also lead to a rich variety of exotica phenomena such as fractional excitations and non-Abelian statistics [5].

Spin-liquid (SL) phases are quantum disordered nonmagnetic phases that do not spontaneously break the spin rotation and discrete translational symmetry of the spin Hamiltonian [6]. Recently, they have been proven to be the ground state of some Hamiltonians [7,8] and SL candidates have been experimentally discovered in a vast range of materials [9–19]. Their existence seems to be intimately related to geometrical frustrated systems. A prototypes of frustrated spin models are antiferromagnetic Heisenberg Hamiltonians in the spatially anisotropic triangular lattice (SATL), where the anisotropy is due to the different spin couplings along the lattice directions. Recently, first attempts to understand such systems have been realized with ultracold bosonic atoms in optical lattices [20]. Despite the apparent simplicity of the model, there is presently a clear disagreement in the phase diagram of the system, in particular, in the existence, extension, and nature of the disordered phases. It has been conjectured that for such a model a quantum SL phase appears between commensurate and incommensurate order [21]. Such claim is controversial in the present literature. The AF Heisenberg model in the SATL has been theoretically approached with different techniques. These include, among others, mean-field methods such as modified spin-wave theory (MSWT) [21–23] or the cluster mean-field approach [24–26] and numerically variational methods such as 2D-DMRG in a cylinder [27–29], projected entangled pair states (PEPS) [30], and variational Monte Carlo [31–33]. Exact diagonalization (ED) in small plaquettes (see for instance [22,27,34–37]) have also been usually used to contrast results with the much more sophisticated techniques mentioned above.

Here, we present a different way to approach generic disordered quantum spin systems by using random boundary conditions in an otherwise ED method. As is customary in the treatment of disordered systems, for each realization of the disorder, i.e., for each set of random boundary conditions, we calculate the observables of interest and perform at the end an average. When performing ED, one of the observables of interest that can be easily computed is the static spin structure factor, $S(\vec{k})$, over the first Brillouin zone which is also a very relevant measurement in the experiments. In the ordered phases, $S(\vec{k})$ displays the relative orientation of the spins in the different lattice sites and its maxima straightforwardly translate into the ordered pattern that the spins acquire in the lattice. In the disordered phases, it is reasonable to expect that $S(\vec{k})$ will blur the well-defined peaks associated with ordered patterns substantially broadening the maxima over the first Brillouin

zone. Our approach, therefore, has a twofold purpose: first, to get rid of the rigidity imposed by periodic or open boundary conditions which forces the system to order depending on the size and geometry of the plaquette; second, to allow the possibility of a large degeneracy of ground states (each corresponding to different random boundary configurations) which, in turn, can translate into a broader $S(\vec{k})$ in the Brillouin zone obtained from the average of the different realizations. Our method is inspired by the work of Santos *et al.* [38] which used twisted random boundary conditions to study a Fermi-Hubbard model in a two-dimensional optical lattice. Their results for small lattices were in very good agreement with the ones obtained by quantum Monte Carlo with much larger lattices and did not present the sign problem inherent in this technique. Here we show that ED with random boundary conditions for really small clusters consisting of $N = 12$, 16, or 24 spins provides relatively independent cluster size results whereas the size and geometry of the cluster critically influence the open boundary condition (OBC) or periodic boundary condition (PBC) results. We focus here on the AF spin-1/2 XX model in the SATL, although the method we present is completely generic and can be adapted to study any other quantum spin model. The Heisenberg model in the SATL has been recently addressed in [37] using twisted boundary conditions but in a different spirit since the set of twisted boundaries has been used to select as the ground state the one that minimizes the energy (or the first excited state). Such a choice still depends strongly on the geometry and size of the plaquette and we will show that it might be insufficient to study disordered quantum phases.

Before proceeding further with the details of our research, we briefly outline our major results here. We analyze the quantum phase diagram of the XX model in the SATL using ED with random boundary conditions denoted generically by $\{\varphi_i\}$. For each boundary configuration we diagonalize the Hamiltonian and find the eigenstates and eigenvalues. First, in the ordered phases of the model we find that there is, in general, a single random configuration that leads to the lowest ground state energy, $E_{0,\min}$. Any other random configuration, $\{\varphi_l\}$, whose ground state energy $E_{0,l}$ is very close to $E_{0,\min}$ has a large fidelity with the latter (overlap) $F_{\min,l} = |\langle \Psi_{0,\min}|\Psi_{0,l}\rangle|^2 \simeq 1$. The expectation value of any observable, $\hat{O}$, obtained from such close states fulfills that $\mathrm{Tr}(\hat{O}\,|\Psi_{0,l}\rangle\langle\Psi_{0,l}|) \sim \mathrm{Tr}(\hat{O}\,|\Psi_{0,\min}\rangle\langle\Psi_{0,\min}|)$. We also find in some ordered phases configurations whose ground state energies $E_{0,l} \simeq E_{0,\min}$ and $F_{\min,l} = 0$. We observe that such configurations correspond to ground states whose spins are locally rotated but compatible with the given order, as happens with the different chirality of the spiral phase. Second, for some values of the lattice anisotropy, we observe that there are *many* random boundary configurations, $\{\varphi_s\}$, whose ground state energies $E_{0,s}$ are quasidegenerate with the configuration leading to lowest energy $E_{0,\min}$, but whose fidelity with the latter can take arbitrary values, i.e., $F_{\min,s} \in (0,1)$. Such energetically very close configurations can have very different expectation values of the same observable. The values of the lattice anisotropy for which such effects are present are in very close agreement with the predicted values for quantum SL using PEPS [30]. Third, the above features arise independently of the size/geometry of the cluster used to perform ED although finite-size effects are present.

The paper is organized as follows. In Sec. II, we introduce the AF spin-1/2 XX model in the SATL and describe the state of the art concerning its phase diagram. In Sec. III, we introduce our approach and explain in which way random boundaries are imposed. In Sec. IV, we present and discuss our results, and finally in Sec. V we conclude.

II. AF SPIN-1/2 XX MODEL IN THE SATL

The Bose-Hubbard Hamiltonian in the triangular lattice reads

$$\hat{H}_{BH} = \sum_{\langle i,j \rangle} \left(\frac{t_{ij}}{2} \hat{b}_i^\dagger \hat{b}_j + \mathrm{H.c.} \right) + \frac{U}{2} \sum_i \hat{n}_i (\hat{n}_i - 1), \quad (1)$$

where $\hat{b}_i^\dagger$ ($\hat{b}_i$) creates (annihilates) a boson on site i, $\hat{n}_i = \hat{b}_i^\dagger \hat{b}_i$ is the boson number operator, t_{ij} is the tunneling parameter on the link (i, j), and U is the on-site repulsive interaction. The anisotropy of the model is given by t_{ij} which translates into two different tunneling parameters: t_1 corresponding to tunneling along the horizontal links and t_2 for the diagonal ones, as sketched in Fig. 1. In the limit of hard-core bosons ($U \to \infty$), the model can be mapped onto a spin model using the Holstein-Primakov transformation,

$$\begin{aligned} \hat{b}_\alpha^\dagger &\longrightarrow S_\alpha^+ = S_\alpha^x + i S_\alpha^y, \\ \hat{b}_\alpha &\longrightarrow S_\alpha^- = S_\alpha^x - i S_\alpha^y, \end{aligned} \quad (2)$$

which maps creation and annihilation operators onto spin operators S_α and the Bose-Hubbard Hamiltonian becomes the spin-1/2 XX model,

$$\hat{H}_s = \sum_{\langle i,j \rangle} t_{ij} \left(\hat{S}_i^x \hat{S}_j^x + \hat{S}_i^y \hat{S}_j^y \right). \quad (3)$$

Although representations (1) and (3) are equivalent in the hard-core limit, in what follows we diagonalize directly (1). In this limit, the second term in Eq. (1) vanishes and the
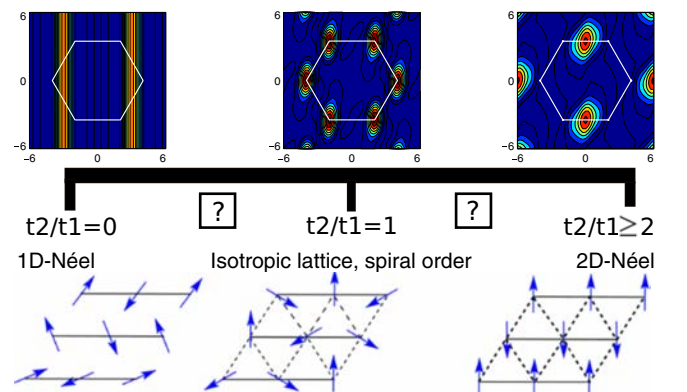

FIG. 1. Schematic phase diagram of the AF XX model in the SATL as a function of t_2/t_1, where t_2 (t_1) corresponds to the spin-spin interaction along the diagonal (horizontal) bonds. On the top, the static spin structure factor, $S(\vec{k})$, for the three known ordered phases of the system: Néel order in the 1D uncoupled chains ($t_2/t_1 = 0$), spiral order in the isotropic lattice ($t_2/t_1 = 1$), and Néel order between the different 1D chains for $t_2 \geqslant 2t_1$. On the bottom, schematic drawing of the spin directions in the above mentioned phases. The ? symbols mean that there is no consensus on the nature of these phases.

lattice filling factor is $\langle n_i \rangle = 1/2$. To extract the ordering of the different phases it is standard to analyze two-body correlations in momentum space,

$$n(\vec{k}) = \frac{1}{N} \sum_{i \neq j} e^{-i\vec{k}(\vec{r}_i - \vec{r}_j)} \langle \hat{b}_i^\dagger \hat{b}_j + \text{H.c.} \rangle, \qquad (4)$$

which in the experiments with ultracold gases is obtained by means of the time-of-flight technique. This quantity straightforwardly maps onto the static spin structure factor for spin-1/2,

$$n(\vec{k}) \rightarrow S(\vec{k}) = \frac{1}{N} \sum_{i \neq j} e^{-i\vec{k}(\vec{r}_i - \vec{r}_j)} \langle \hat{S}_i^x \hat{S}_j^x + \hat{S}_i^y \hat{S}_j^y \rangle, \qquad (5)$$

where the sum extends to all the lattice sites of the cluster and the expectation value is taken over the ground state of the system. From $S(\vec{k})$ can be extracted both the ordering vector $\vec{Q} = (Q_x, Q_y)$, which corresponds to the maxima of $S(\vec{k})$ and indicates classical order, and an order parameter,

$$M = \sqrt{S(\vec{Q})/N}, \qquad (6)$$

which signals LRO in ordered states. Before proceeding further it is instructive to review the classical phase diagram which is obtained by replacing at each lattice site the spin operator for a classical rotor $\vec{S}_i = S(Q_x^{\text{clas}} x_i, Q_y^{\text{clas}} y_i)$, up to a global phase factor. The classical ordering vector $\vec{Q}^{\text{clas}}$ lies in the XY plane and corresponds to the configurations that minimize the energy given by the Hamiltonian when the spin operators are replaced by spin vectors, $H = \sum t_{ij} \vec{S}_i \vec{S}_j$. In spin-wave theory, such classical ordering is the reference state to which quantum corrections are added and then the energy is minimized self-consistently. Minimization of the energy leads (at $Q_y = 0$) to the following conditions:

$$Q_x^{\text{clas}} = \pm\pi \quad \text{for } t_2 = 0,$$
$$Q_x^{\text{clas}} = \pm 2 \arccos\left(-\frac{t_2}{2t_1}\right) \quad \text{for } 0 \leqslant t_2/t_1 \leqslant 2,$$
$$Q_x^{\text{clas}} = \pm 2\pi \quad \text{for } t_2/t_1 > 2. \qquad (7)$$

The classical phase diagram of the model is sketched in Fig. 1, where the classical spin configurations together with their corresponding $S(\vec{k})$ are displayed. Notice that at $t_2 = 0$, the system reduces to AF uncoupled 1D chains that order classically in the Néel configuration. For such order, $S(\vec{k})$ has a maximum along $Q_x^{\text{clas}} = \pm\pi$ and is completely uncorrelated (disordered) along the y direction. At the isotropic point, $t_2/t_1 = 1$, the system has spiral order (Néel 120°). The maxima of $S(\vec{k})$ are given now at the vertex of the hexagon $(Q_x^{\text{clas}}, Q_y^{\text{clas}}) = \pm\vec{b}_1; \pm\vec{b}_2; (b_{2x}, -b_{2y}); (-b_{2x}, b_{2y})$, provided by the triangular lattice. Here, $\vec{b}_1 = (4\pi/3, 0)$ and $\vec{b}_2 = 2\pi(1/3, 1/\sqrt{3})$ are the inverse vectors of the lattice while the direct ones are given by $\vec{a}_1 = (1, 0)$ and $\vec{a}_2 = (1/2, \sqrt{3}/2)$ with unit lattice constant. Finally, for $t_2 \geqslant 2t_1$, classically the AF order is given by a Néel configuration along the diagonal chains, while horizontal chains display antiferromagnetic order, as schematically represented in Fig. 1. In this case, the triangular lattice becomes effectively a rhombic one and $S(\vec{k})$ displays the square order with maxima at $\vec{Q}^{\text{clas}} = (\pm 2\pi, 0), (0, \pm 2\pi/\sqrt{3})$.

We have also depicted in Fig. 1 the regions where there is presently not a clear consensus on the nature of the quantum phases. Lately, the possibility has been pointed out that quantum SL phases appear in the transition from commensurate to incommensurate (i.e., the spins order with a period which is irrationally related to the lattice space) order. No direct evidence of such phases and their extension has already been unambiguously provided. Numerical results for the XX model using PEPS [30] supports such claim. However, MSWT [22] only finds signatures of the SL phase between the spiral and the 2D-Néel phases. Recently, calculations for the Heisenberg model using ED with twisted boundary conditions [37] and 2D-DMRG [28] seem compatible with yet another ordering, the collinear antiferromagnetic (CAF) one.

III. METHOD: ED WITH RANDOM BOUNDARY CONDITIONS

Exact diagonalization is normally performed either on a cluster without considering links in the boundaries, the so-called open boundary conditions (OBC), or closing the plaquette with periodic boundary conditions (PBC). For clusters as small as the ones to which we are usually restricted for computational reasons, these boundary conditions have a strong influence on the results. That is so because both the cluster geometry and the boundary conditions act as a rigid box and the results obtained are conditioned by these two factors. Ideally, one should increase the size of the cluster used for ED until border effects become negligible, but this is usually not possible due to the fact that the corresponding Hilbert space grows exponentially imposing severe restrictions on computational resources. A way that we believe can substantially mitigate the effect of the boundaries and the geometry is imposing random boundary conditions. We define a set of random phases $\{\varphi_{ij}\}$ corresponding to complex tunneling elements hopping in/out from the cluster $t_{i,j} \rightarrow t_{i,j} e^{i\varphi_{ij}}$, $t_{j,i} \rightarrow t_{j,i} e^{-i\varphi_{ij}}$. Where (i, j) correspond to the links which can be associated with periodic boundary conditions. In the language of the Bose-Hubbard Hamiltonian this corresponds to hopping in and out of the cluster with a phase; in spin language this is equivalent to a spin twisting.

We have used two criteria to define the random boundary conditions. The first one, denoted by RBC, has been used previously in [37,38]. In RBC, for each realization i two different random phases are defined, $(\phi_1, \phi_2)_i$, as sketched in Fig. 2. The phase ϕ_1 (in Fig. 2 denoted by blue color) corresponds to tunneling in the cluster through the rightwards (leftwards) boundary links, $t_1 e^{\pm i\phi_1}$ along horizontal couplings and $t_2 e^{\pm i\phi_1}$ along diagonal ones. The phase ϕ_2 (denoted by red color) corresponds to the upwards (downwards) boundary links which always occur through diagonal couplings and the tunneling reads $t_2 e^{\pm i\phi_2}$. The link in the corner, since it can be interpreted as both a leftward and an upward, acquires a phase, $\phi_3 = \phi_1 + \phi_2$ (pink line). The rest of the boundary links are defined so as to keep the Hamiltonian Hermitian. Such set of boundary conditions can be interpreted as a twist of the lattice along the directions determined by the direct vector of the lattice.

We have also considered a less restrictive configuration, denoted by RRBC and also schematically shown in Fig. 2 by angles θ_i. These boundary conditions cannot be interpreted
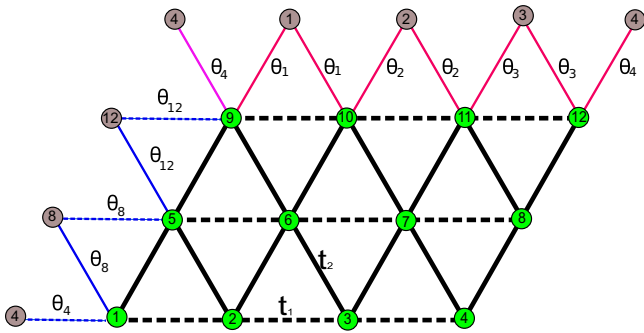
FIG. 2. Dashed lines indicate tunnelling along the horizontal links (t_1) while solid lines indicate tunnelling along diagonal links (t_2). Random Boundary Conditions (RBC) can be understood as the simultaneous twisting of the lattice along the horizontal direction with an angle ϕ_1 (blue lines) and along the diagonal direction with an angle ϕ_2 (red lines). The link in the corner gets a phase $\phi_1 + \phi_2$ (pink lines). We also consider RRBC, depicted in the figure by the θ_i. Here, all the boundary tunneling links depicted in the figure from site i acquire the same random phase θ_i. For instance, in the figure, if a boson in site 8 tunnels into sites 1 or 5, it acquires the same random phase θ_8. The phases of the boundary links which are not shown are defined so as to keep the Hamiltonian Hermitian.

as a twist of the lattice anymore. However, they provide a larger flexibility on searching for disordered quantum spin systems.

With the above constraints, we have performed ED on rectangular clusters of $N = L \times W = 12$, 16, and 24 sites, where L corresponds to the size of the chain and W the number of chains in the plaquette. Diagonalization is done by keeping only the sector $S_z = 0$ where the ground state lies. We generate a set of random phases for the boundary conditions, $\{\varphi_k\}_i$, and for each configurations i calculate the ground state energy $E_{0,i}$, the static spin structure factor $S_i(\vec{k})$, the ordering vector $\vec{Q}_i$, and the order parameter $M_i = \sqrt{S_i(\vec{Q}_i)/N}$. All the above quantities obviously depend on $\{\varphi_k\}_i$ and on the size and geometry of the lattice. Finally, we perform the average of the quantities of interest over the random configurations, which we denote with $\langle \ldots \rangle_d$. For each realization of RRBC, the set of random phases needed is sensibly larger than for RBC. For computational reasons we keep the number of realizations equal to 200 in both cases. Therefore, the results obtained from RRBC are less accurate. Nevertheless, as we shall see, our averaged results remain quite similar.

IV. RESULTS AND DISCUSSION

For simplicity, unless stated otherwise in what it follows we refer to the RBC method. The first thing which is worth noticing is the relative independence of the results on the geometry of the cluster. In Fig. 3, we show the averaged static spin structure factor, $\langle S(\vec{k}) \rangle_d$, at the isotropic point, $t_2/t_1 = 1$,
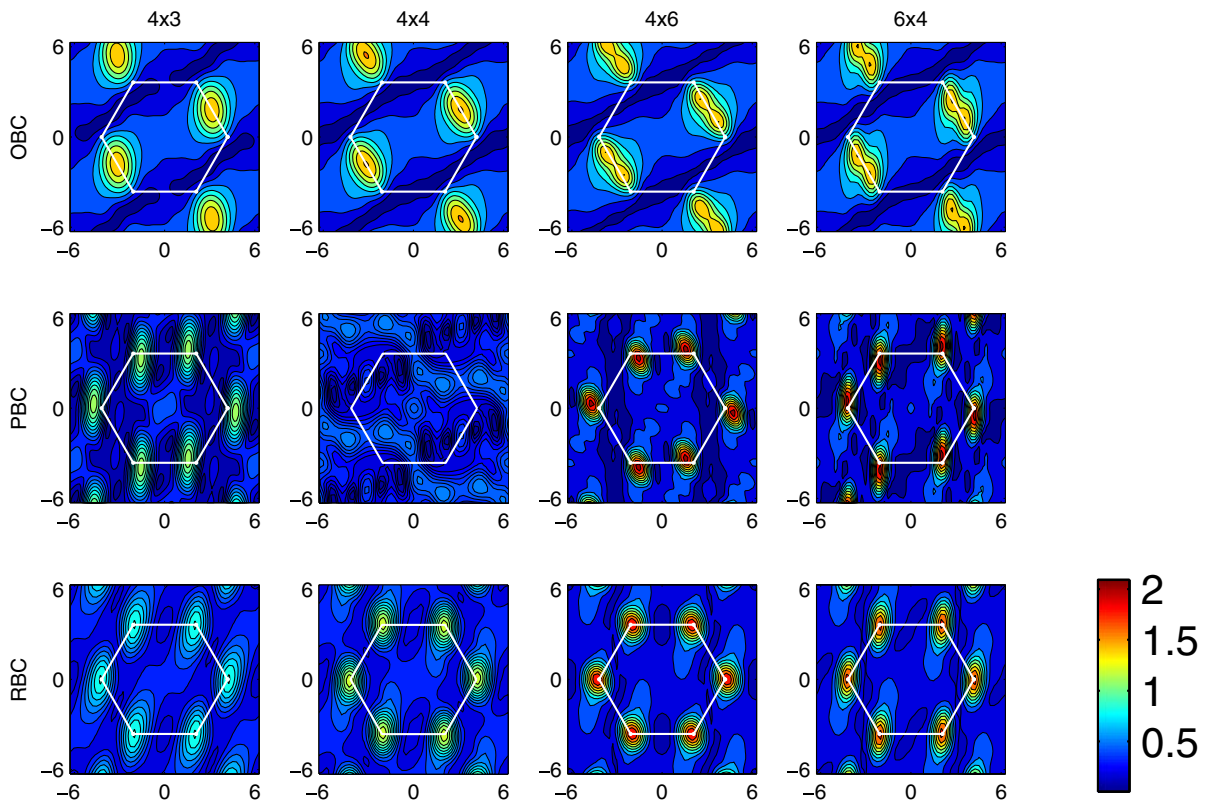

FIG. 3. Static spin structure factor $S(\vec{k})$ obtained from ED for different cluster geometries at the isotropic point, $t_2/t_1 = 1$. Upper panel: Open boundary conditions (OBC). Middle panel: Periodic boundary conditions (PBC). Lower panel: Random boundary conditions (RBC). For the RBC, the averaged value over all the random configurations, $\langle S(\vec{k}) \rangle_d$, is depicted. The limit of the first Brillouin zone is shown with a white line.
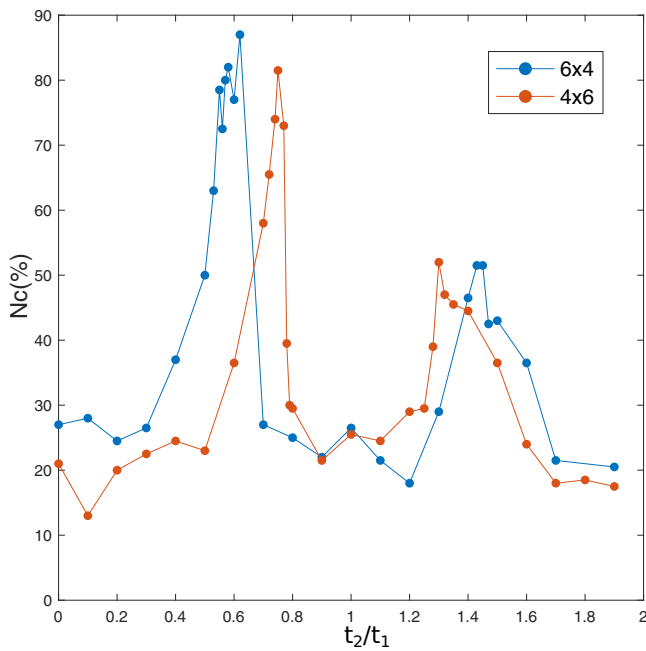
FIG. 4. Number of configurations, $N_c(\%)$, whose normalized ground state energy fulfills $\epsilon_i < 1$ (see text) for a fixed value of the anisotropy t_2/t_1 using RBC. The two maxima signal the predicted quantum SL phases.

for a cluster of 4×3, 4×4, and 6×4 sites and compare our results with the ones obtained imposing either OBC and PBC. On one hand, the rigidity of OBC reflects into a wrong CAF order for all lattices sites, whereas it forces PBC to dramatically fail for the 4×4 lattice since such geometry suppresses spiral order. On the other hand, RBC is the only case which gives the correct order for all geometries, signaled by maxima at the

corners of the hexagon in the first Brillouin zone that indicates the correct spiral order.

More interesting is to look into the conjectured disordered quantum phases. Notice that when sampling with random boundary conditions there can be configurations, $|\Psi_{0,i}\rangle$, whose corresponding ground state energy, $E_{0,i}$, substantially differs from the lowest achieved within the configurations, $E_{0,\min}$. We define a renormalized energy, $\epsilon_i = \frac{E_{0,i} - E_{0,\min}}{E_{0,\min}} \times 100$, and consider just those configurations with $\epsilon_i < 1$, i.e., with an energy not larger than 1% of $E_{0,\min}$. As a first proof of concept, we plot the number of configurations, N_c, which lie in such interval as a function of t_2/t_1. Our method shows that, independently of the geometry of the lattice, there are two regions around $t_2/t_1 \sim 0.6$ and ~ 1.5 where there exist many configurations whose energy is close to the minimal one as depicted in Fig. 4. These regions coincide with the conjectured SL phases predicted in the literature. For all other regions of the phase diagram—corresponding to the ordered phases—the number of compatible configurations decreases keeping a flat structure. It is also interesting to show that, in agreement with all previous calculations, the ordered 2D-Néel order seems to appear already for values of $t_2/t_1 \geqslant 1.7$ and stabilizes before its classical value, $t_2/t_1 \geqslant 2$, due to quantum fluctuations. From now on, all quantities averaged over the disorder, $\langle \ldots \rangle_d$, correspond to the average only over those configurations N_i whose ground state energy fulfills $\epsilon_i < 1$ for each value of t_2/t_1.

In order to infer the possible orders of the ground states for a given value of the anisotropy t_2/t_1, we examine the ordering vector Q_x at ($Q_y = 0$). In Fig. 5, we show both the distribution of Q_x (color map) as well as its averaged value over the random configurations (dashed black line). It is important to recall that ordered classical phases have a well-defined value of Q_x. Thus, $Q_x/\pi = 1$, 4/3, and 2 correspond to perfect 1D-Néel chains, to the isotropic lattice $t_2 = t_1$, and to the 2D-Néel in the square lattice. ED studies
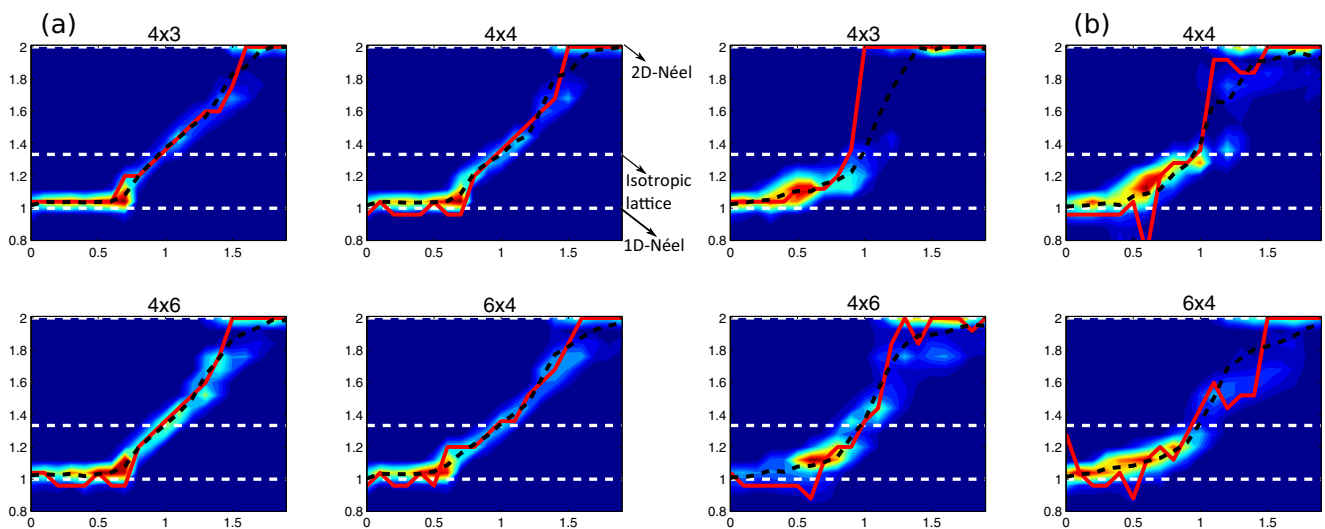

FIG. 5. Color map distribution of the ordering vector, Q_x/π, for a sample of 200 set of random phases $\{\varphi_{i,j}\}$ defined as RBC (RRBC) in panels (a) [(b)], as a function of the anisotropy t_2/t_1. Horizontal lines show the classical values for the ordered phases, $Q_x/\pi = 1, 4/3$, and 2, corresponding to 1D Néel, isotropic lattice, and 2D Néel, respectively. The black dashed line depicts $\langle Q_x \rangle_d$, i.e., the averaged value over the disorder, and the red solid line depicts $Q_x^{\min}$ corresponding to the ground state with minimum energy, $E_{o,\min}$.

with the usual boundary conditions show that Q_x/π presents a smooth dependence on the anisotropic parameter t_2/t_1. It increases from its lower value 1 (at $t_2/t_1 = 0$) until $t_2/t_1 \simeq 1.6$, where it abruptly jumps to the value 2 signaling the transition to the 2D-Néel order. Neither ED with periodic or open boundary conditions or MSWT show a signature of the presence of a SL around $t_2/t_1 \sim 0.5$. An inspection of Fig. 5 shows that, as expected for $t_2 > 0$, the ordering vector Q_x increases over its classical value 1 and the system is no longer in the uncoupled 1D chain limit. At values $t_2/t_1 \sim 0.5, 1.4$ we observe that the distribution of Q_x spreads significantly. This translates, as we will see later, into a broader filling of the first Brillouin zone, since a wide range of k vectors is, in these regions, allowed. At the isotropic point, $t_2/t_1 = 1$, and only there, $Q_x/\pi = 4/3$, while the ordering vector smoothly changes along the spiral phase. It is interesting to remark that the above features are reproduced in all the plaquette sizes and geometries. They are also quite independent on the way we choose the random boundary conditions as indicated in Fig. 5 by comparing panels (a) corresponding to RBC using the configurations fulfilling the bias $\epsilon < 1$ and panels (b) corresponding to RRBC considering, here, the bias $\epsilon < 5$. To complete the study, we also display $Q_x^{\min}$ (thick red line) corresponding to the ordering vector associated with the lowest ground state energy, $E_{0, \min}$, as in the study of Ref. [37]. As expected, such quantity has a more pronounced dependence on the lattice geometry and size.

In Fig. 6 we plot $\langle M \rangle_d$, i.e., the order parameter defined in Eq. (6) averaged over the N_c configurations fulfilling $\epsilon < 1$ for each t_2/t_1. The occurrence of a SL phase, in contrast to ordered phases, is characterized by the absence of LRO, and thus, the disappearance of the order parameter M. Notice that while this should occur strictly speaking in the thermodynamic limit, for finite-size lattices what it is expected is a decrease of M, i.e., a broader maxima in $S(\vec{k})$ as compared to the ordered phases. This is what we clearly observe around $t \sim 1.3$ for all the lattices sizes we have used. Another dip should appear also around $t \sim 0.6$, but we just vaguely detect it only for the 4×6 lattice. This is so because for $t_2 \lesssim 0.5$ the system is in the 1D weakly coupled AF chain limit meaning that it is completely disordered along the y direction. As depicted in Fig. 1 and Fig. 3, $S(\vec{k})$ in this limit corresponds to a constant value along k_y which in turn translates into a small value of M in this region. This fact masks the decrease of M around $t_2/t_1 = 0.6$ for small lattices. However, as we will show latter, the presence of a SL in this region can be unambiguously signaled by the lack of convergence on the order parameter, M, obtained from the different configurations that are compatible with the ground state of the system.

The effect of random boundary conditions to study disordered quantum spin phases can be summarized in Fig. 7 where we concentrate most of our results taking as a representative case a plaquette of 6×4 sites. In the first row we plot $|\langle \Psi_{0, \min} | \Psi_{0, i} (\phi_1^i, \phi_2^i) \rangle|$ as a function of the renormalized energy, ϵ, for some representative values of the anisotropy t_2/t_1. Note that when plotting as a function of ϵ, we are sorting the configurations by their ground state energy. The vertical dashed line indicates those configurations whose ground state energy differs by less than 1% of $E_{0, \min}$ (i.e., $\epsilon < 1$) and which are used to perform the averages. The first column
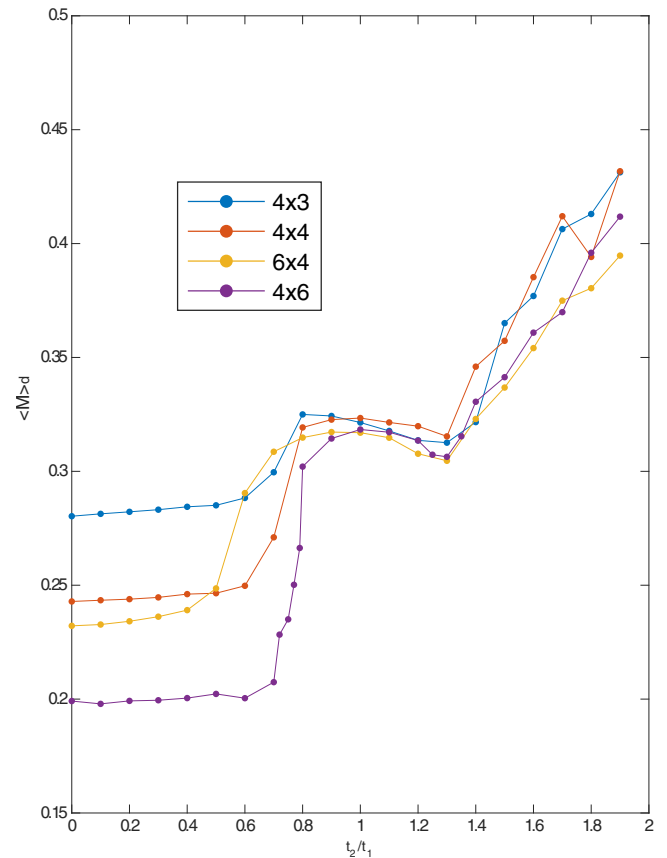

FIG. 6. Order parameter, $\langle M \rangle_d$, averaged over the disorder as a function of t_2/t_1 for different lattice sizes and geometries. The results are obtained using RBC.

displays for $t_2/t_1 = 0.1$ the generic behavior of the system for $0 < t_2/t_1 \leqslant 0.5$. The overlap with any configuration smoothly decreases as the ground state energy of the configurations increases. Nevertheless, all configurations close in energy to $E_{0, \min}$ have the same order parameter M and $\langle S(\vec{k}) \rangle_d$ corresponds to weakly coupled 1D Néel chains. As depicted in the second column, for $t_2/t_1 = 0.57$ a drastic change appears. Many different configurations are quasidegenerate in energy, but their corresponding ground states can be very different as indicated by all possible values of the overlap. The order parameter of these quasidegenerate configurations spans all possible values between the M associated with 1D Néel chains and the one associated with spiral ordering. Interestingly enough, the ground state energy of any random configuration does not deviate more than $\sim 3\%$ from the minimal one. These features are compatible with a quantum SL, a disordered system with a large variety of superposed ground states, as for instance is a resonating valence bond state (RVB). The associated $\langle S(\vec{k}) \rangle_d$ is depicted at the bottom. Our calculations show that this phenomenon can persist till $t_2/t_1 \sim 0.8$. The precise border depends on the size/geometry of the lattice. At the spiral phase, here depicted in the third column by its most representative case, $t_2/t_1 = 1$, two almost degenerate orthogonal ground states with minimal energy appear. They correspond to the two chiral ground states known to exist in the spiral phase. Two branches of ground state
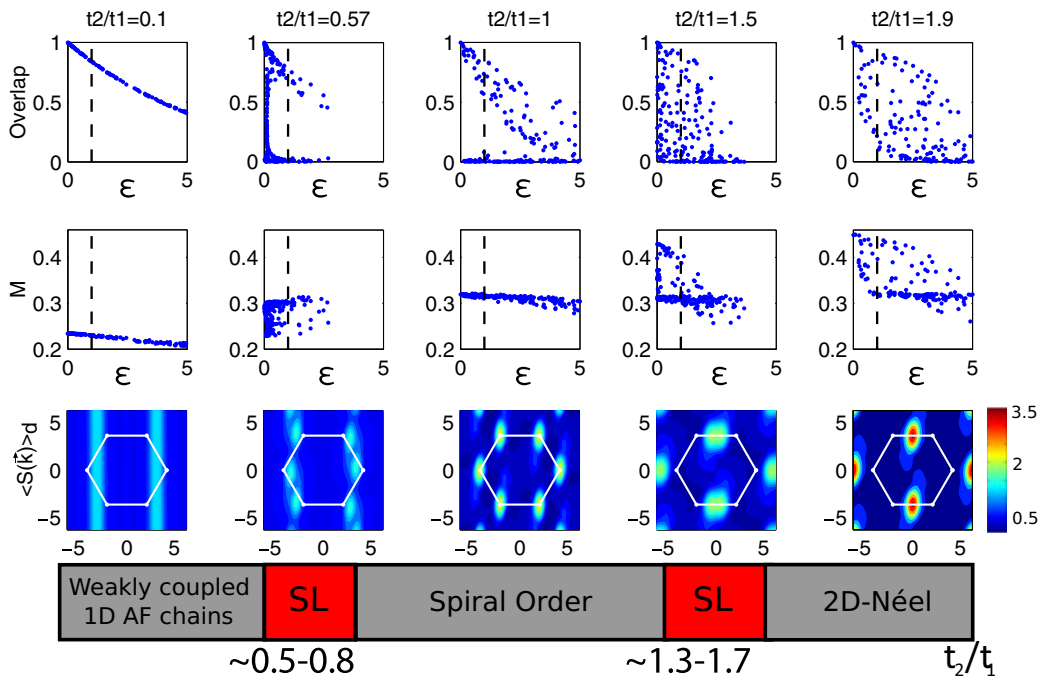
FIG. 7. First row: Overlap between the ground state which minimizes the energy for a fixed t_2/t_1, $|\Psi_{0,\min}\rangle$, and the ground states obtained for the other random configurations of the sample, $|\langle\Psi_{0,\min}|\Psi_{0,i}(\phi_1^i,\phi_2^i)\rangle|$, as a function of the renormalized energy, ϵ. The vertical dashed line indicates the bias on the energy set to select from the random sample of boundary conditions only those ground states which are energetically closed to the lowest one, with energies which are not larger than 1% of $E_{0,\min}$ ($\epsilon < 1$). Second row: Order parameter, M, as defined in the text. In the ordered phases, M remains the same for all energetically close configurations; for quantum disordered systems this is not the case showing that an order parameter can be defined on average but it is a meaningless quantity. Third row: Static spin structure factor, $\langle S(\vec{k})\rangle_d$, averaged over the configurations fulfilling $\epsilon < 1$. Notice that, for the ordered phases, $\langle S(\vec{k})\rangle_d$ is as expected and for the disordered ones the maxima are blurred. Fourth row: Quantum phase diagram obtained from RBC with two possible SL phases between the ordered ones.

configurations appear close in energy; the upper one has an overlap $|\langle\Psi_{0,\min}|\Psi_{0,i}(\phi_1^i,\phi_2^i)\rangle| \simeq 1$ if they share the same chirality and zero if they correspond to different chirality. The order parameter, M, attains the same value independently of the chirality, stressing thus the character of the ordered phase. For $t_2/t_1 \in [1.3, 1.7]$ similar features to those in $t_2/t_1 \sim 0.6$ appear. We depict the behavior of such phase at $t_2/t_1 = 1.5$ where again a large number of quasidegenerate configurations give an overlap which runs between 1 and 0. In a similar fashion to that which happens for $t_2/t_1 \sim 0.6$, there is not a defined value of M. In this way, the values in the SL regions in Fig. 6 are merely the averages of the sampling but are meaningless in the sense that M is not well defined in these regions. The corresponding averaged spin structure factor over the first Brillouin zone, $\langle S(\vec{k})\rangle_d$, shows indeed broad maxima in the predicted disorder phases as compared to the ordered phases. Finally, for $t_2/t_1 > 1.7$, we start to recover the results corresponding to the 2D-Néel ordered phase in the square lattice. There are very few configurations whose ground state energy is close to the lowest one. The order parameter for the lower energy configurations is quite similar, and the averaged spin structure factor shows the expected peaks in the first Brillouin zone corresponding to the 2D-Néel order as indicated by the 4th row of Fig. 7. At the bottom of the plot, we add the inferred phase diagram one can extract from our results. It shows the ordered phases together with the presence of two regions compatible with the existence of a gapped SL.

V. CONCLUSIONS

We have approached quantum AF spin systems using ED with random boundary conditions. In this work, we have concentrated our efforts in the spin-$1/2$ XX model in the SATL, aiming at obtaining a signature of the predicted quantum SL phases. Our results show that there are regions of the phase diagram where many different quasidegenerate ground states are compatible. In these regions, the associated observables (i.e., the static spin structure factor, ordering vector, and order parameter) are, however, very different.

The presence of these regions, which we identify as quantum SL, agrees quite closely with numerical predictions obtained for the same model with a variational method like PEPS [30]. Regarding finite-size effects, we would like to remark that our results are general, in the sense that the two regions characterized by a large number of quasidegenerate energy ground states persist in all cases. However, the precise location at which such degeneracy appears and how long it extends depend on the lattice geometry and size.

Our method not only provides significant signatures of the disordered quantum phases, but it is also robust in reproducing the features of the ordered phases, independently of the sample used to simulate random boundaries (if it is large enough), the size of the plaquette, and the energy bias used to select the compatible configurations. It seems reasonable to conclude that the ordered phases are robust in front of quantum fluctuations while the disordered ones are clearly enhanced

by them. Finally, it is worth mentioning that the method we propose is completely general and can be applied for any 2D quantum spin disordered system not only with ED but also with any numerical method relying on the specific choice of boundary conditions.

[1] G. Misguich and C. Lhuillier, Two-dimensional quantum antiferromagnets, in *Frustrated Spin Systems* (World Scientific, Singapore, 2004), pp. 229–306.

[2] A. Kitaev and J. Preskill, Phys. Rev. Lett. **96**, 110404 (2006).

[3] M. Levin and X.-G. Wen, Phys. Rev. Lett. **96**, 110405 (2006).

[4] S. V. Isakov, M. B. Hastings, and R. G. Melko, Nat. Phys. **7**, 772 (2011).

[5] X.-G. Wen, arXiv:1610.03911.

[6] L. Balents, Nature (London) **464**, 199 (2010).

[7] A. Kitaev, Ann. Phys. (Leipzig) **321**, 2 (2006).

[8] R. Moessner and S. L. Sondhi, Phys. Rev. Lett. **86**, 1881 (2001).

[9] M. Yamashita, N. Nakata, Y. Senshu, M. Nagata, H. M. Yamamoto, R. Kato, T. Shibauchi, and Y. Matsuda, Science **328**, 1246 (2010).

[10] S. Yamashita, Nat. Phys. **4**, 459 (2008).

[11] M. A. de Vries, J. R. Stewart, P. P. Deen, J. O. Piatek, G. J. Nilsen, H. M. Rønnow, and A. Harrison, Phys. Rev. Lett. **103**, 237201 (2009).

[12] Y. Shimizu, K. Miyagawa, K. Kanoda, M. Maesato, and G. Saito, Phys. Rev. Lett. **91**, 107001 (2003).

[13] P. Mendels, F. Bert, M. A. de Vries, A. Olariu, A. Harrison, F. Duc, J. C. Trombe, J. S. Lord, A. Amato, and C. Baines, Phys. Rev. Lett. **98**, 077204 (2007).

[14] Y. Kurosaki, Y. Shimizu, K. Miyagawa, K. Kanoda, and G. Saito, Phys. Rev. Lett. **95**, 177001 (2005).

[15] T. Itou, A. Oyamada, S. Maegawa, M. Tamura, and R. Kato, Phys. Rev. B **77**, 104413 (2008).

[16] J. S. Helton, K. Matan, M. P. Shores, E. A. Nytko, B. M. Bartlett, Y. Yoshida, Y. Takano, A. Suslov, Y. Qiu, J.-H. Chung, D. G. Nocera, and Y. S. Lee, Phys. Rev. Lett. **98**, 107204 (2007).

[17] T.-H. Han, J. S. Helton, S. Chu, D. G. Nocera, J. A. Rodriguez-Rivera, C. Broholm, and Y. S. Lee, Nature (London) **492**, 406 (2012).

[18] B. Fåk, E. Kermarrec, L. Messio, B. Bernu, C. Lhuillier, F. Bert, P. Mendels, B. Koteswararao, F. Bouquet, J. Ollivier, A. D. Hillier, A. Amato, R. H. Colman, and A. S. Wills, Phys. Rev. Lett. **109**, 037208 (2012).

[19] R. Coldea, D. A. Tennant, A. M. Tsvelik, and Z. Tylczynski, Phys. Rev. Lett. **86**, 1335 (2001).

[20] J. Struck, C. Ölschläger, R. Le Targat, P. Soltan-Panahi, A. Eckardt, M. Lewenstein, P. Windpassinger, and K. Sengstock, Science **333**, 996 (2011).

[21] P. Hauke, Phys. Rev. B **87**, 014415 (2013).

[22] P. H. Schmied, T. Roscilde, V. Murg, J. I. Cirac, and Roman, New J. Phys. **12**, 53036 (2010).

[23] A. Celi, T. Grass, A. J. Ferris, B. Padhi, D. Raventós, J. Simonet, K. Sengstock, and M. Lewenstein, Phys. Rev. B **94**, 075110 (2016).

[24] D. Yamamoto, G. Marmorini, and I. Danshita, Phys. Rev. Lett. **112**, 127203 (2014).

[25] M. Moreno-Cardoner, H. Perrin, S. Paganelli, G. De Chiara, and A. Sanpera, Phys. Rev. B **90**, 144409 (2014).

[26] M. Moreno-Cardoner, S. Paganelli, G. D. Chiara, and A. Sanpera, J. Stat. Mech.: Theory Exp. (2014) P10008.

[27] M. Q. Weng, D. N. Sheng, Z. Y. Weng, and R. J. Bursill, Phys. Rev. B **74**, 012407 (2006).

[28] A. Weichselbaum and S. R. White, Phys. Rev. B **84**, 245130 (2011).

[29] W.-J. Hu, S.-S. Gong, W. Zhu, and D. N. Sheng, Phys. Rev. B **92**, 140403 (2015).

[30] R. Schmied, T. Roscilde, V. Murg, D. Porras, and J. I. Cirac, New J. Phys. **10**, 045017 (2008).

[31] S. Yunoki and S. Sorella, Phys. Rev. B **74**, 014408 (2006).

[32] L. F. Tocchio, A. Parola, C. Gros, and F. Becca, Phys. Rev. B **80**, 064419 (2009).

[33] L. F. Tocchio, H. Feldner, F. Becca, R. Valentí, and C. Gros, Phys. Rev. B **87**, 035143 (2013).

[34] P. W. Leung and K. J. Runge, Phys. Rev. B **47**, 5861 (1993).

[35] B. Bernu, P. Lecheminant, C. Lhuillier, and L. Pierre, Phys. Rev. B **50**, 10048 (1994).

[36] D. Heidarian, S. Sorella, and F. Becca, Phys. Rev. B **80**, 012404 (2009).

[37] M. Thesberg and E. S. Sørensen, Phys. Rev. B **90**, 115117 (2014).

[38] T. Mendes-Santos, T. Paiva, and R. R. dos Santos, Phys. Rev. A **91**, 023632 (2015).

Signatures of quantum spin liquids in small lattices

Initial questions and motivations

This work is an extension of the previous article. The motivation was twofold. On the one hand, to apply our novel method to the study of other paradigmatic spin models to further check its truthfulness. On the other hand, to deepen into what we can and what we cannot observe using RBC. In concrete, we were concerned whether random boundary conditions could detect or not two of the main characteristics of a QSL, i.e., massive ground state degeneracy and long range entanglement. We focus in two models. The first one, the AF spatially completely anisotropic triangular lattice, has been previously studied just by means of MSWT and therefore there is a lack of knowledge on its phase diagram. The second one, the $J_1 - J_2$ model, has been recently studied in several works which point towards a phase diagram with a QSL with a well defined location.

Main results

We successfully show that we can find signatures of QSL phases in both studied models using small lattices (up to 24 sites). The first signature corresponds to a massive ground state degeneracy which in our framework means that many different random boundary configurations lead to a ground state which minimizes the energy. These degenerate or compatible ground states differ a lot among each other giving a picture which resembles a resonating

valence bound solid. Furthermore, in the areas where the putative QSL is located, we can detect an increase of geometric entanglement. For both models under study, the areas of the phase diagram where the QSL signatures are found are in accordance with the present literature. However, strong finite size effects avoid us to make a precise estimation of their extension and location. In conclusion, this work provides a sharpened interpretation of the RBC presented in the previous one with a clear description of the signatures of QSL which can be obtained.

Signatures of quantum spin liquids in small lattices

A. Yuste,[1] D. Castells-Graells,[1] and A. Sanpera[1,2,*]

[1]*Departament de Física, Grup d'Informació Quantica, Universitat Autònoma de Barcelona, 08193, Bellaterra, Spain.*
[2]*ICREA, Psg. Lluís Companys 23, 08010, Barcelona, Spain.*

Quantum spin liquids remain one of the most challenging subjects of quantum magnetism. Characterized by massive degenerate ground states that have long range entanglement and are locally indistinguishable, highly demanding numerical techniques are often needed to describe them. Here we propose an easy computational method based on exact diagonalization with engineered boundary conditions to unveil their most significant features in small lattices. We derive the quantum phase diagram of diverse antiferromagnetic Heisenberg models in the triangular lattice. For all studied cases, our results are in accordance with the previous results obtained by means of sophisticated variational methods.

I. INTRODUCTION

Some entangled ground states of spin systems do not order even at zero temperature. The lack of order, which is originated by strong quantum fluctuations on the spin orientations, prevents their characterization by means of local order parameters. Such quantum disordered states, termed generically quantum spin liquids (QSL), are linked to a highly degenerated ground state and contain long range entanglement. Moreover, they are locally indistinguishable [1–3], meaning that they cannot be detected or distinguished using local measurements.

QSL are often caricatured as a liquid of singlets, where the singlets formed between nearby spins strongly fluctuate from one configuration to another. Due to such fluctuations, the ground state of the system is far from a product state, implying that entanglement in QSL plays a crucial role. Ground states of local spin Hamiltonians are normally short range entangled, as evidenced by the fact that the entanglement entropy, $\mathcal{S}$, of any bipartite cut of the system follows an area law: $\mathcal{S}(L) \sim L^{D-1}$, where D is the dimension of the system and L the linear size of the boundary separating both regions. Corrections to this law appear, for instance, in critical gapless quantum phases or in topologically ordered states. In 2D, the later fulfill $\mathcal{S}(L) \sim L + b_0\gamma$, where γ is a universal correction, independent of the lattice size that signals topological order [4–6].

The combination of the above features makes unfeasible the description of QSL in terms of effective mean field approaches with fluctuation corrections over the mean field ansatz. Hence, finding the eigenstates of the corresponding Hamiltonians mostly relies, for the time being, in numerical approaches and/or complex variational ansatzes in very large lattice systems. The numerical methods are, of course, severely hindered by the requirement of large lattices.

Here we show, however, that the relevant signatures of QSL in frustrated disordered 2D systems can be correctly obtained in surprisingly small lattices by properly engineering the boundary conditions.

With this aim, we analyze several anisotropic spin $1/2$ antiferromagnetic (AF) Heisenberg models in the triangular lattice, where quantum fluctuations and frustration compete. The effect of frustration, which is, the impossibility to simultaneously minimize the Hamiltonian locally, can be further tunned by introducing different spin couplings along all lattice directions. This model, sometimes denoted as the spatially completely anisotropic triangular lattice (SCATL) has been scarcerly addressed in the literature. It is a generalization of the model with anisotropy just between horizontal and diagonal bonds (SATL), which has been extensively addressed in the literature using different methods such as tensor networks, quantum Monte Carlo, 2D DMRG, exact diagonalization (ED) or modified spin wave theory (MSWT) [7–19]. We also investigate here the $J_1 - J_2$ model, with anisotropy between nearest-neighbor (NN) and next-to-nearest neighbor (NNN) couplings, also addressed recently in [20–25]. The above models give room to both, gapless and highly nontrivial gapped QSL.

Before proceeding further we summarize here our main results. We derive the quantum phase diagram of the above models using ED with engineered boundary conditions in lattices of only $N = 12$, 16 or 24 spins. Our results reproduce both, the ordered and disordered quantum phases previously reported for such models and show explicitly that massive superpositions of almost quasi-degenerate ground states are at the heart of QSL. Despite we cannot calculate the topological entanglement entropy in such small lattices, geometric entanglement –quantifying how far an entangled state is from its closest separable one–, shows that the predicted gapped QSL have a large entanglement as compared to their surrounding ordered phases. Remarkably enough our method puts at reach the study and detection of new QSL in complex systems with a simple numerical approach.

The paper is organized as follows: in Sec. II, we explain the main features of our numerical method together with the relevant figures of merit used along. In Sec. III, we derive the quantum phase diagram of the SCATL model, with anisotropic couplings along all lat-

*Electronic address: anna.sanpera@uab.cat

tice directions. For this model, to the best of our knowledge, only a study based in a MSWT exist [14]. Therefore, alternative methods are clearly needed to settle the presence of conjectured QSL. In Sec. IV, we move onto another paradigmatic frustrated model, the so-called $J_1 - J_2$. We analyze it also in the presence of chiral interactions which helps to elucidate the nature of the predicted QSL and compare our results with the quantum phase diagram obtained recently in [25] using 2D DMRG. Finally, in Sec. V, we conclude and present some open questions.

II. RANDOM TWISTED BOUNDARY CONDITIONS

Twisted boundary conditions (TBC) were introduced in the seminal contributions of [26, 27], and can be thought of as periodic boundary conditions (PBC) under a twist. Since then, they have been often used to calculate properties of quantum magnets, as they provide better access to momentum space and help to mitigate finite size effects, see e.g. [17, 28–31]. However, here we use TBC in a conceptually different approach. In Fig. 1, we sketch our philosophy. Consider a generic AF Heisenberg model in the triangular lattice. For the ordered phases of the Hamiltonian, the relative orientation of the spins is fixed due to a broken symmetry, as depicted for example in the cartoon of a 2D Néel phase in Fig. 1 (top left). If the lattice is large, the bulk spins dominate over the boundary ones imposing the order expected in the thermodynamical limit, independently of the chosen boundaries. However, for small lattices this is not anymore the case. The boundaries must be properly chosen –in accordance to the lattice geometry– to recover the underlying symmetries of the ordered phase , Fig. 1 (bottom left). For quantum disordered phases that are not associated to a symmetry breaking, we expect the ground state of the system to be spanned over a large superposition of states, as schematically shown in Fig. 1. Presumible, for small lattices different boundary configurations should be compatible with the ground states of the system in the thermodynamic limit. We cannot predict a priori which are the right boundaries configurations since there is not an underlying local symmetry in the phase. This feature is illustrated with the symbols "?" in Fig. 1 (bottom right). Nevertheless, we can count how many random TBC lead to the same ground state energy and post-select only those to calculate physical quantities of interest. This post-selection is the key point to engineer our boundary conditions [19].

Specifically, for 2D spin 1/2 AF Heisenberg models, the spins lay in the XY plane and TBC correspond to adding a phase in the spins i, j interacting through the boundaries:

$$S_i^+ S_j^- \rightarrow S_i^+ S_j^- e^{-i\phi}, \quad (1)$$
$$S_i^- S_j^+ \rightarrow S_i^- S_j^+ e^{+i\phi}. \quad (2)$$

To twist the lattice simultaneously in two directions requires two different phases ϕ_1 (ϕ_2), for left-right (top-bottom) boundaries, as depicted in the bottom panels of Fig. 1. The spins of the lattice laying at both boundaries acquire a phase $\phi = \phi_1 + \phi_2$. Notice that conventional PBC favor order commensurate with the lattice dimensions, $N = L \times W$, since in the reciprocal lattice, momentum is selected at $k_1 = 2\pi n_1/L$ and $k_2 = 2\pi n_2/W$ for $n_i \in \mathbb{N}$. In contrast, TBC allow to test all possible momenta in the first Brillouin zone [17, 26, 27]

$$
\begin{aligned}
k_1 &= \frac{2\pi n_1}{L} \pm \frac{\phi_1}{L}, \\
k_2 &= \frac{2\pi n_2}{W} \pm \frac{\phi_2}{W}.
\end{aligned} \quad (3)
$$

Let us briefly review our approach [19]. First, we fix the lattice size, N, and geometry. Here, we use $N = 4 \times 3$ or $N = 4 \times 4$, but to ensure convergence, some of the results are also calculated for $N = 6 \times 4$ and 4×6 . Then, we generate a set p of two randomly chosen phases, $\{\phi_1, \phi_2\}_p$, with $\phi_i \in [0, 2\pi)$ and $p = 1, 2, \ldots, 200$. For each configuration, we diagonalize the Hamiltonian, generating a ground state $|\psi_p\rangle$ with energy E_p, and denote by $|\psi_0\rangle$ the ground state with the lowest energy, E_0. We post-select those configurations whose ground state energy fulfills: $\epsilon_p = (E_p - E_0)/E_0 < \alpha$. The election of the energy bias, α, is somehow arbitrary as it depends on the lattice size and the ratio between bulk and boundary interactions. Nevertheless, our results are independent of it, if the set p is sufficiently large. Notice, however, that for small lattices the bias cannot be vanishingly small.

Consequently, one relevant figure of merit is the number of configurations, N_c, laying in the interval $0 \leq \epsilon_p < \alpha$. Typically, we choose $\alpha = 0.01$ meaning that only configurations whose ground state energies are less than 1% than E_0 are retained. Actually, for ordered phases just very few random TBC accommodate the symmetry of the phase, and the ones which do not, correspond to large E_p and are automatically discarded in our approach. In contrast, we find regions in the Hamiltonian parameters where N_c increases dramatically. The corresponding ground states, $|\psi_p\rangle$, strongly differ one from each, as observed by computing the overlap $O_p = |\langle \psi_p | \psi_0 \rangle|$. Finally, as it is standard in disordered systems, we calculate the quantities of interest for each post-selected configuration and perform afterwards the corresponding average which we denote by $\langle \ldots \rangle_d$. The average washes out the spurious symmetries introduced by TBC. In ED, one quantity which can be easily obtained is the static spin structure factor

$$S(\vec{k}) = \frac{1}{N} \sum_{i \neq j} e^{-i\vec{k} \cdot (\vec{r}_i - \vec{r}_j)} \langle S_i S_j \rangle, \quad (4)$$

where the expectation value is taken over the corresponding ground state $|\psi_p\rangle$. From the spin structure factor, one can extract the following order parameter

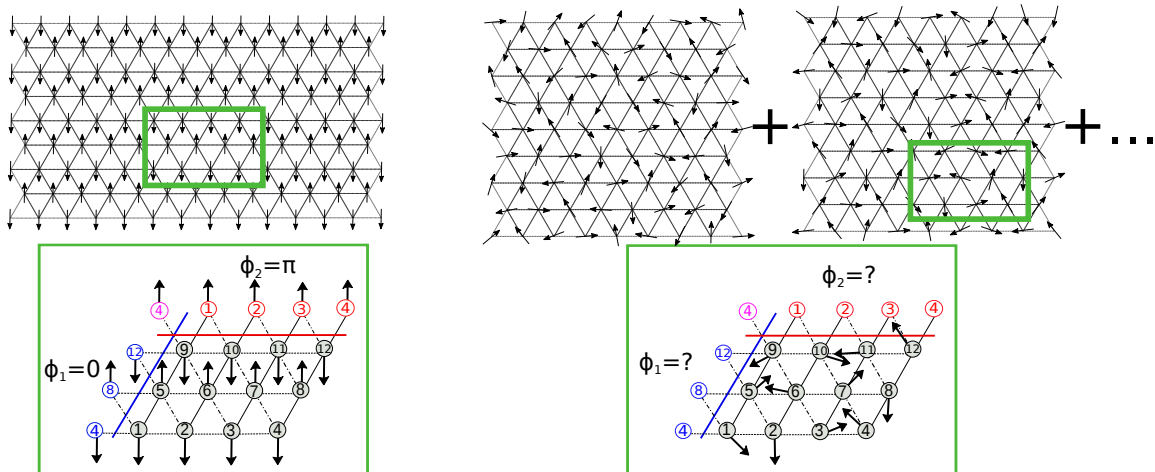$$M = \sqrt{S(\vec{Q}_{\max})/N} , \quad (5)$$

FIG. 1: Upper panels: sketch representation of a quantum ordered Néel phase (left) and a QSL phase (right) in a large lattice. Lower panels: sketch of twisted boundary conditions in a 4×3 triangular lattice with anisotropic nearest-neighbor interactions. Boundary spins in blue are twisted in the XY plane by an angle ϕ_1, while red colored boundary spins are twisted by a phase ϕ_2. The pink colored boundary spin (top-left corner) is twisted by an angle $\phi = \phi_1 + \phi_2$. For the Néel phase (bottom left) the phases which reproduce the order are $\phi_1 = 0$ and $\phi_2 = \pi$. For the QSL (bottom right) such a set of phases cannot be defined. The anisotropy of the SCATL model is depicted by the three different line styles in the bottom panels.

where $\vec{Q}_{max}$ are the k-vectors corresponding to the maxima of the spin structure factor in the first Brillouin zone. This parameter signals long range order (LRO), and helps to identify possible QSL. Regarding entanglement, it is well known that local entanglement measures cannot detect QSL, but they help to identify the underlying ordering of the phases. We choose the concurrence, C, as a measure of bipartite entanglement between any two spins i, j in the mixed state $\rho_{ij} = \text{Tr}_{k \neq ij}(|\psi_p\rangle \langle \psi_p|)$ which can be easly computed in ED methods [32]. For local Hamiltonians, the concurrence cannot capture long range entanglement. To go beyond NN entanglement, we calculate the geometrical entanglement. It "measures" the distance of a state to its closest separable one

$$\Lambda_{\text{max}} = \max_{|\phi_{\text{prod}}\rangle} |\langle \psi_p | \phi_{\text{prod}} \rangle| \qquad (6)$$

where $|\phi_{\text{prod}}\rangle = \otimes_{i=1}^{N} |\phi_i\rangle$ and we maximize over the set of all separable (non entangled) states. The larger Λ_{max} is, the lower the entanglement of $|\psi_p\rangle$ is since it is closer to a product state. It makes sense to define the geometric entanglement [33] as:

$$E_G = 1 - \Lambda_{\text{max}}, \qquad (7)$$

which clearly goes beyond bipartite entanglement.

III. SPATIALLY COMPLETELY ANISOTROPIC TRIANGULAR LATTICE (SCATL)

Our staring point is AF Heisenberg spin $1/2$ model in a triangular lattice whose Hamiltonian reads:

$$H = \sum_{<i,j>} t_{ij} \left(S_i^x S_j^x + S_i^y S_j^y + \lambda S_i^z S_j^z \right), \qquad (8)$$

where S_i^α are the spin 1/2 Pauli matrices for site i, the sum runs over all NN pairs, and all coupling constants $t_{ij} > 0$. We restrict ourselves to the cases $\lambda = 0$ ($\lambda = 1$) which correspond to XY (Heisenberg) interactions. The anisotropy of the model is given by the different interaction strengths (t_1, t_2, t_3) along the lattice directions (see Fig. 1 (bottom)). Without loosing generality, we consider $t_1 = 1$ and leave as free parameters t_2 and t_3. The case $t_2 = t_3$ has been extensively studied [9, 11, 14, 19]. For the sake of completeness, it is instructive to reproduce first its classical phase diagram. The reader familiar with it can skip this part.

Classical Phase Diagram.

The classical phase diagram provides an estimate on the location and nature of the ordered phases. Order is signaled by the points in the reciprocal space that maximize correlations or, equivalently, the ones that minimize the Hamiltonian energy. The classical ordering vector, $\vec{Q}^{\text{cl}}$, is obtained replacing the spin operators in Eq.(8) by a classical rotor laying in the XY plane, $S_i = S \cdot \left(\cos \left(\vec{Q}^{\text{cl}} \cdot \vec{r}_i \right), \sin \left(\vec{Q}^{\text{cl}} \cdot \vec{r}_i \right) \right)$, up to a global phase. Energy minimization yields a region in the phase diagram with continuously varying ordering vector, described by the following equations:

$$Q_x^{\text{cl}} = \pm \arccos \left[\frac{t_2 t_3}{2} - \frac{t_2^2 + t_3^2}{2 t_2 t_3} \right] \quad \text{if} \quad \frac{t_2 t_3}{2} - \frac{t_2^2 + t_3^2}{2 t_2 t_3} \leq 1$$

$$Q_y^{\text{cl}} = \pm \frac{2}{\sqrt{3}} \arccos \left[\mp \left(\frac{t_2 + t_3}{2 t_2 t_3} \right) \sqrt{t_2 t_3 + 2 - \frac{t_2^2 + t_3^2}{t_2 t_3}} \right], \quad (9)$$

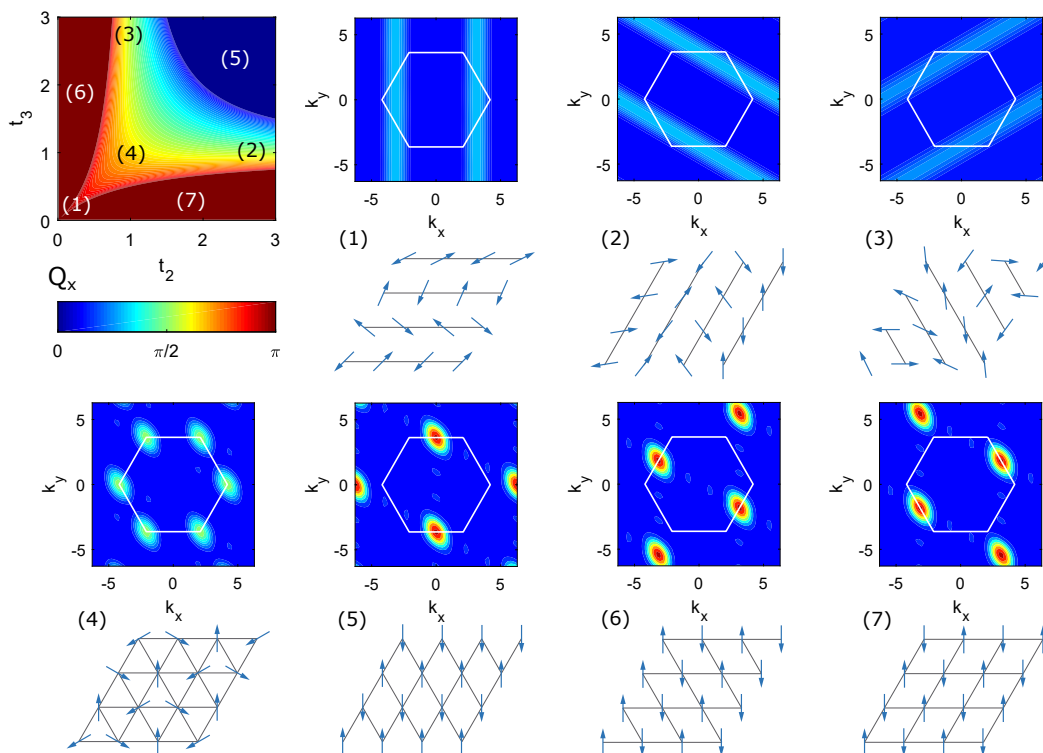where the argument of Q_y^{cl} is negative if the correspond-

FIG. 2: Classical phase diagram for the SCATL for both XY ($\lambda = 0$) and Heisenberg ($\lambda = 1$) interactions, obtained by plotting Q_x in Eq. (9) as a function of the anisotropy (top left). The other panels show the spin structure factor and a sketch of the spin order for each classical phase.

ing Q_x^{cl} satisfies $|Q_x^{cl}| \leq \pi$, and positive otherwise. The classical phase diagram is depicted in Fig. 2, together with the representative spin structure factor of each phase. First, we describe the 1D lattice limit corresponding to (1) $t_2 = t_3 = 0$; (2) $t_2 \to \infty, t_3 = 1$; and (3) $t_3 \to \infty, t_2 = 1$ as shown in Fig. 2. For these cases, the lattice becomes a system of uncorrelated chains and the corresponding phases are 1D Néel ordered along the dominant lattice coupling and uncorrelated along the other two. This is clearly shown in the corresponding spin structure factors. At the isotropic point, $t_2 = t_3 = 1$, indicated by (4) in Fig. 2, the system has spiral order (Néel 120°) with maxima in the structure factor at all the vertices of the reciprocal lattice cell. This phase extends as an incommensurate spiral phase merging smoothly with the classical 2D Néel phases corresponding to $t_i = t_j \gg t_k$, and the lattice deforms into diamond lattices along the two dominant directions, indicated in Fig. 2 by (5,6,7). This completes the classical phase diagram. Finally, we also add a symbolic sketch of the spin orientations for each phase.

Quantum phase diagram.

Our first main result for both, XY and Heisenberg interactions, is summarized in the schematic phase diagram of Fig. 3 (column 1 and 2). Our figure of merit

there is N_c, i.e., the number of configurations such that $\epsilon_p < 0.01$ for a lattice of size $N = 4 \times 3$ and $N = 4 \times 4$. For the sake of comparison, we also plot in the last column of this figure, the quantum phase diagram obtained with MSWT from [34]. The dependence of our results on the lattice size prevents a precise localication of the phase boundaries but not, as we shall see, on their characterization.

In accordance to the classical phase diagram, spiral ordering (labelled by (4) in Fig. 3) occurs around the isotropic point $t_3 = t_2 = 1$ and its extension is much reduced as compared to the classical case, in particular in the Heisenberg model. Surrounding the spiral phase, we observe a region, absent in the classical phase diagram, with a massive number of energetically compatible ground states (labelled by (8) in Fig. 3). This is a signature of a disordered quantum phase and it is reconcilable with the conjectured gapped QSL reported in [9, 11, 14, 18, 34] for the isotropic line $t_2 = t_3$. Continuously connected to this "gapped QSL" phase, there are three regions labeled by (1,2,3) in Fig. 3. These regions lay between two 2D Néel ordered phases (5,6,7) that span around $t_i = t_j \gg t_k$, and are connected to the respective classical 1D limit of uncoupled chains: $t_i \to \infty, t_j = t_k$. The regions (1,2,3) are commonly referred in the literature as gapless QSL, and are not particularly enhanced
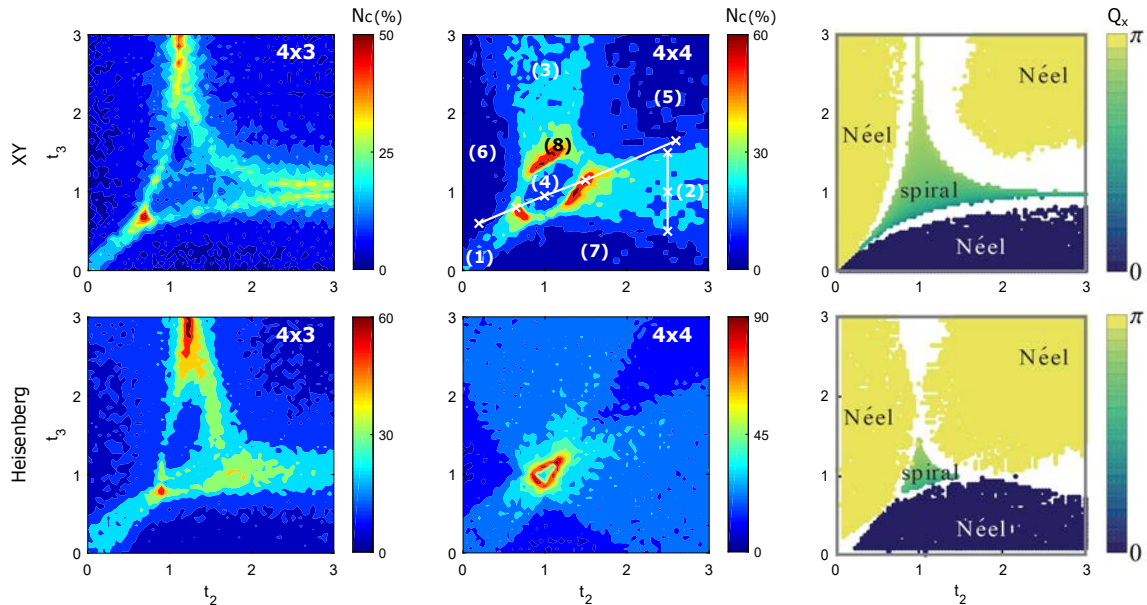
FIG. 3: Quantum phase diagram of the SCATL model as obtained through the number of quasi degenerate configuration, N_c, for a 4×3 and 4×4 lattice. Upper (lower) panels, XY (Heisenberg) interactions. In the 4×4 XY diagram, the different quantum phases are labeled 1 to 8 (see text for details). The right panels correspondon to the quantum phase diagram obtained with MSWT from Ref. [34], where the white regions correspond to the breakdown of the MSWT calculations and are indiguishably associated to gapless or gapped QSL.
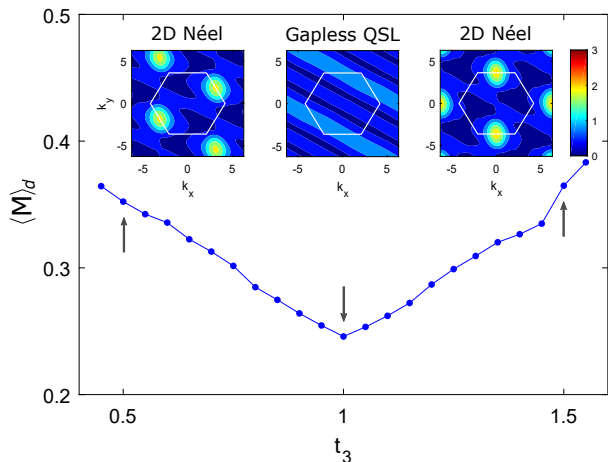
FIG. 4: Study of the SCATL quantum phase diagram in the region between two 2D Néel phases. The averaged order parameter, as defined in (5), is plotted along the vertical white line in Fig. 3 for the 4x4 lattice with XY interactions. The three arrows depict the points where the three representative spin structure factors are plotted.

in Fig. 3, because in them, the spins are ordered along the corresponding dominant direction and totally disordered along the other two. This constrain strongly restricts the number of random TBC which are quasi degenerate in energy. However, an inspection on the corre-

sponding ground states shows that indeed they are 1D disordered quantum phases. All our results apply both for the XY and the Heisenberg model, but for the sake of concreteness we refer from now on the XY model.

In Fig. 4, we depict the averaged order parameter $\langle M \rangle_d$ for the parameters along the vertical line displayed in Fig. 3 which goes from the 2D Néel (5) to the 2D Néel (7). We observe that between the two 2D Néel ordered phases – faithfully identified by the average spin structure factor– , there is a region with lower LRO, signaled by the decrease of $\langle M \rangle_d$. The corresponding spin structure shows 1D Néel order. We identify this region as a trivial gapless QSL. The same features are observed in the two other limiting cases (1) and (3).

To further explore the nature of the truly quantum disordered phase, we restrict now our analysis to the quantum phase diagram along the diagonal line depicted in Fig. 3 which crosses several quantum phases including the putative QSL (8). In the top row of Fig. 5, we display $\langle S(\vec{k}) \rangle_d$ for some selected points along this line. Its inspection allows for an easy identification of two 2D Néel phases at the extrems of this quantum phase diagram, the first one examplarized at $t_2 = 0.2$, $t_3 = 0.6$ and the second one at $t_2 = 2.6$, $t_3 = 1.65$. Between them, we find the expected spiral phase at $t_2 = 1$, $t_3 = 0.95$. Finally, between the 2D Néel phases and the spiral one, there are two regions (circa $t_2 = 0.65$, $t_3 = 0.8$ and $t_2 = 1.5$, $t_3 = 1.15$) whose spin structure factor does not correspond to any order. In the middle row of the same figure, we plot the corresponding overlap $O_p = |\langle \psi_p | \psi_0 \rangle|$ for all config-
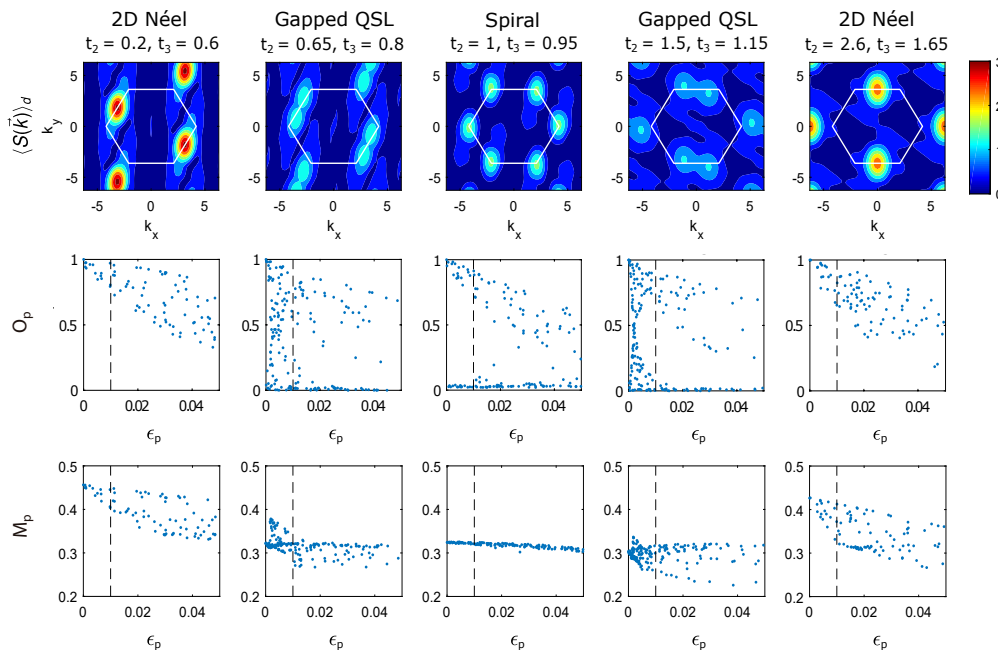
FIG. 5: Quantum phase diagram along the diagonal white line in Fig. 3 for the 4×4 lattice with XY interactions. Top: averaged structure factor $\langle S(\vec{k}) \rangle_d$. Center: overlap, O_p, versus normalized energy ϵ_p. Bottom: order parameter, M_p (see text). The dashed vertical lines limit the region $\epsilon_p < 0.01$, where the average is done.

urations p, sorted by energy. The energy bias for post-selection is there indicated by a dashed vertical line. For the 2D Néel order, O_p slowly decreases as ϵ_p increases meaning that quasi degenerate states correspond to alike ground states. A similar behaviour is observed for the spiral phase though O_p has two branches around $O_p = 1$ and 0. They correspond to the two orthogonal chiralities of the spiral ground state. In contrast, the "gapped QSL" phase, shows a radically different behaviour. All set of post-selected configurations (i.e., $\epsilon_p < 0.01$), might correspond to very different ground states. This feature reconciles with the description of a gapped QSL as a massive superposition of very different states, as could be a resonating valence bond solid [35]. Finally, in the last row of Fig. 5 we display the value of the order parameter M_p (as defined in 4) for all configurations. While ordered quantum phases have a very small dispersion of the order parameter, the dispersion becomes much more significant for the putative gapped QSL making its average value meaningless.

We conclude our study by calculating entanglement properties for the same parameters of the previous figure. In Fig. 6 (top panel), we show the averaged concurrence, C_{ij}, between NN along the three lattice directions (t_1, t_2, t_3) as well as its dispersion. The vertical arrows in the figures point out the location of the different quantum phases (2D Néel–QSL–spiral–QSL–2D Néel) under study in Fig. 5. As expected, the spiral phase has an isotropic concurrence along all directions. The concurrence also signals the two preferred directions in the 2D

Néel phases. Though C_{ij} cannot detect long range entanglement, in the putative QSL phases the dispersion is larger than in the ordered phases meaning that the NN entanglement can be different in energy compatible configurations. Again, this merges with the idea of a ground state which is a superposition of very different states. In the bottom panel, we display the geometrical entanglement. In the same figure, we also plot the overlap of the post-selected states with the classical product state ansatz corresponding to a 2D Néel and spiral phases. QSL have small classical order and a larger entanglement as compared with ordered phases, displaying yet another characteristic feature of QSL beside their massive ground state superpositions.

IV.   J1-J2 MODEL

In this section, we extend our work to the AF Heisenberg model with nearest (NN) and next-nearest-neighbours (NNN) interactions,

$$H_{J_1-J_2} = J_1 \sum_{\langle i,j \rangle} \vec{S}_i \vec{S}_j + J_2 \sum_{\langle\langle i,j \rangle\rangle} \vec{S}_i \vec{S}_j, \qquad (10)$$

where we fix $J_1 = 1$ leaving J_2 as the free parameter and the sums run over all NN and NNN pairs respectively.

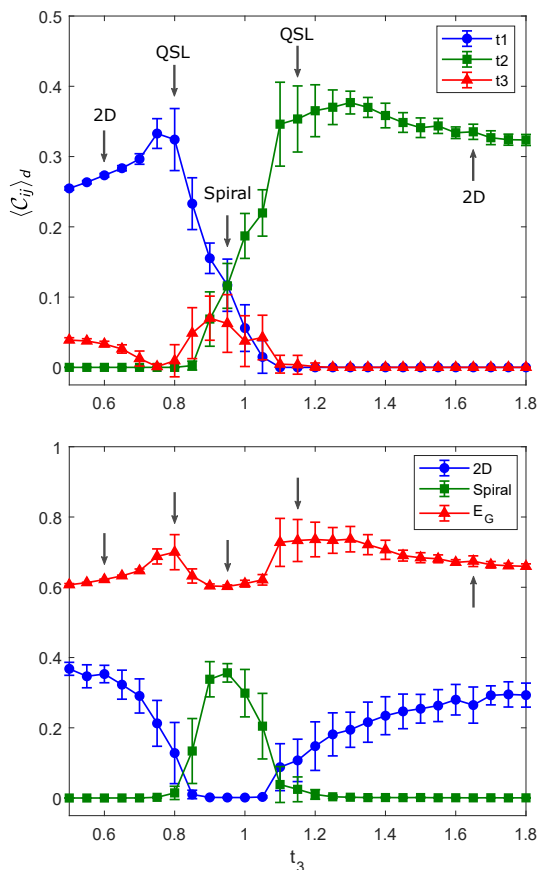Before proceeding further, let us mention that finite size effects are now further enhanced by the presence of

FIG. 6: Top: averaged concurrence between NN sites along the three lattice directions. Bottom: geometrical entanglement, E_G (Eq. (7)), and projections to separable states (see text). All quantities are averaged over the configurations with $\epsilon_p < 0.01$, and the dispersion of the values is represented by error bars. The plotted region correspons to the while diagonal line in Fig.3, where the values of t_2 are choosen accordingly. The arrows indicate the values used in Fig. 5 which are representative of each quantum phase explored.

NNN terms. However, in consonance with Sec.III, our aim here is to find the signatures of the ground states which are compatible with QSL rather than to provide the precise location of the quantum phase boundaries. It is important also to stress that implementing random TBC for a Hamiltonian hosting both NNN and chiral interactions, as we will later introduce, demands some subtleties which are explained in the Appendix.

Classical phase diagram.

The classical phase diagram of this system is well known [36]. For $J_2 < 1/8$, there is a three-sublattice 120 Néel ordered ground state (spiral order). For $1/8 < J_2 < 1$ the classical phase diagram is degenerate with the three different collinear 2D Néel order and a tetrahedral noncoplanar state. However, an order-by-disorder mechanism selects the 2D Néel order when

quantum fluctuations are taken into account [36, 37]. For $J_2 > 1$, there is non-commensurate spiral order.

Quantum phase diagram.

Recent studies have analyzed the quantum phase diagram of the model with special attention in the surroundings of the classical phase transition point, at $J_2 = 1/8$, with 2D DMRG [20, 21], variational quantum Montecarlo [22], exact diagonalization [24] and Schwinger-boson mean-field [38]. A consensus has been reached in identifying a QSL phase for $0.08 \lesssim J_2 \lesssim 0.15$. The nature of this phase, though, is still under debate. To shed more light in the issue, an extra chiral term in the Hamiltonian has been proposed [23–25, 39, 40],

$$H_\chi = H_{J_1-J_2} + J_\chi \sum_{i,j,k \in \triangle} \vec{S}_i(\vec{S}_j \times \vec{S}_k), \qquad (11)$$

where the sum runs to all the up and down triangles of the lattice clock-wisely.

In Fig. 7 (left panel), we show an sketch of the quantum phase diagram taken from Refs. [23–25]. For $J_\chi = 0$, we recover the $J_1 - J_2$ model. As J_χ is turned on, there is a phase transition from the QSL under debate into a chiral spin liquid (CSL) which lies between the ordered spiral, the 2D Néel collinear and the tetrahedral phase. In Fig. 7 (right panel), we show our schematic quantum phase diagram obtained by counting the number of post-selected configurations, N_c, for $\epsilon_p < 0.005$, as a function of the parameters of the model, J_2 and J_χ for a lattice of just $N = 4 \times 4$ spins. For this model, in contrast with the analysis of previous models (Sec. III), we choose a smaller energy bias, ϵ_p, for post-selection of quasi-degenerate states, because the number of inner bonds is much increased as compared to the Heisenberg model. For $J_\chi = 0$, we observe a region with a large number of quasi degenerate ground states that extends approximately from $0.05 \lesssim J_2 \lesssim 0.10$. As J_χ incrases, this region is continuously enlarged and at, $J_2 = 0$, it expands aproximately between $0.1 \lesssim J_\chi \lesssim 0.40$. It is interesting to compare both figures. Despite that the boundaries we obtain are clearly different from those sketched in Fig. 7 (left panel), our results show a large increase of compatible configurations in a region reconciliable with the location of both, the CSL present in the model described above (Eq.11) and the QSL of the J1-J2 model (Eq. 10).

Finite size effects can be spotted by calculating the quantum phase diagram in larger lattices. In Fig. 8 (top), we display, N_c as function of J_2 ($J_\chi = 0$) for different lattice sizes and geometries; $N = 4 \times 4; 4 \times 6; 6 \times 4$. As expected, by increasing the lattice size, the localization of the maximum of N_c shifts to larger values of J_2 in accordance to the quantum phase diagram of the system. To deepen further in the nature of the possible phases observed in Fig. 7 (right panel), we explore other physical quantities, like the averaged spin structure factor to determine the corresponding orders for a lattice of $N = 6 \times 4$. Our results are depicted in Fig.8 and agree quite closely
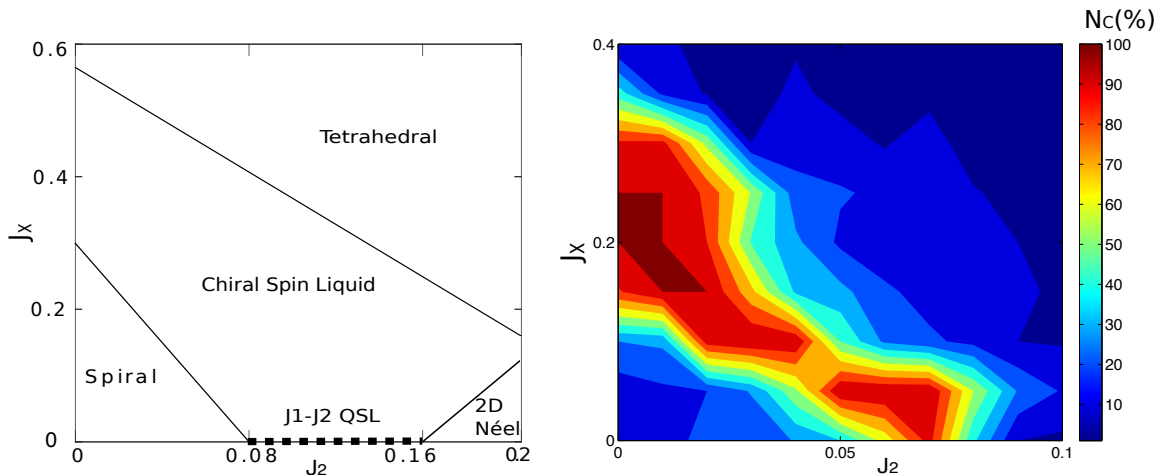
FIG. 7: Left, sketched quantum phase diagram of the $J_1 - J_2$ model with chiral interactions obtained from Refs.[24, 25]. Right, N_c for the same model using a 4×4 lattice. The area with large N_c is a signature of putative gapped QSL phase.

with the expected orders. For $0 \leq J_2 \lesssim 0.05$, spiral order is dominant. As J_2 further increases, there is a region with large number of random configurations, N_c, which lead to a ground state energy E_p quasi degenerate with the smallest one E_0. These configurations correspond to different ground states, as demonstrated by all possible values the overlap O_p takes. In this region, the averaged structure factor, $\langle S(\vec{k}) \rangle_d$, is blurred, showing that there are not clear preferable k-vectors. This indicates disorder and, consequently, a decrease of LRO. Again, it is instructive to compare our results with the results of the quantum phase diagram obtained with more sophisticated methods for larger lattices. In the bottom row of Fig. 8, we attach for comparison, $S(\vec{k})$ obtained with 2D DMRG from Ref.[21]. For the values where the putative QSL is predicted, both $S(\vec{k})$ obtained from the 2D DMRG simulations and our $\langle S(\vec{k}) \rangle_d$ are impressively similar. For $J_2 = 0.2$, the 2D DMRG shows collinear order corresponding the a 2D Néel order along two lattice directions (see Fig. 2) while our results shows a superposition of two of the 2D Néel collinear orders. This is not relevant, as all collinear orders are degenerate and of course any superposition of them as well. Finally, let us remark that in the same spirit, we have also analyzed the nature the quantum phases that appear when the chiral term is included for a lattice of $N = 4 \times 4$. The results in this case suffer from strongly finite size effects but ordered phases can be easily identified by $\langle S(\vec{k}) \rangle_d$.

V. CONCLUSIONS

We have shown that with a simple numerical method, based in exact diagonalization with engineered random twisted boundary conditions, it is possible to find clear signatures of QSL phases in small lattice sizes. In particular, we have analyzed with this method the anisotropic
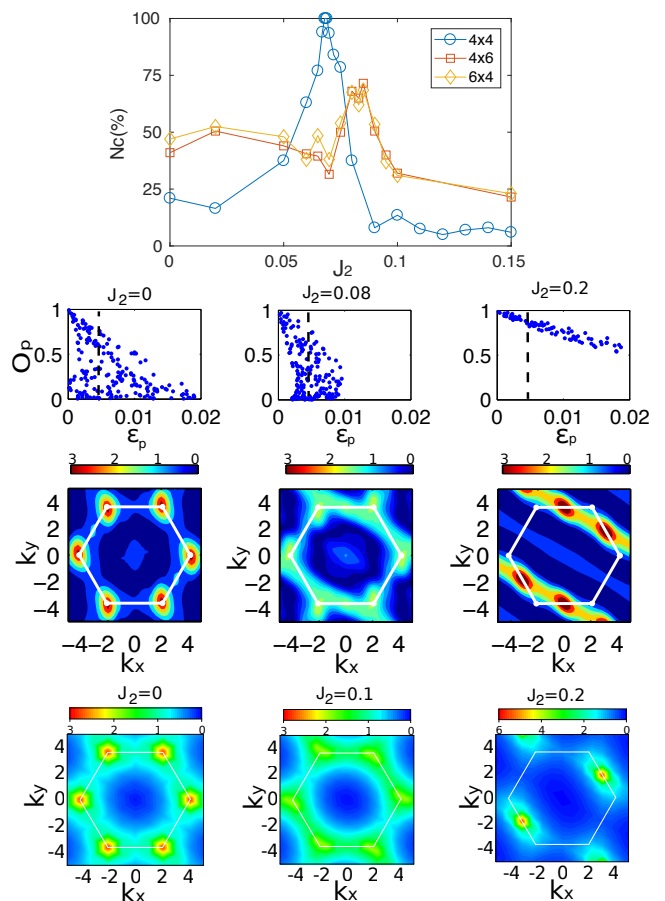

FIG. 8: $J_1 - J_2$ model without chiral interactions ($J_\chi = 0$). Top panel, number of configurations, N_c, with $\epsilon_p < 0.05$ for different lattice sizes and geometries. First row O_p and energy bias ϵ_p for a 6×4 lattice. Bottom rows, our averaged spin structure factor, $\langle S(\vec{k}) \rangle_d$ and $S(\vec{k})$ obtained with 2D DMRG taken from Ref.[21].

spin 1/2 triangular lattice with AF Heisenberg interactions and the J1-J2 model. Our results closely reproduce in both cases the quantum phase diagram obtained with other methods. We have found regions which display massive ground state degeneracy, large entanglement and ill defined spin structure factors. We have identified these regions as QSL. Our method provides a feasible tool for the study and detection of novel quantum disordered phases in frustrated systems, as it unveils explicitly the underlying properties of quantum spin liquids.

[1] X.-G. Wen, Phys. Rev. B **65**, 165113 (2002).
[2] L. Balents, Nature **464**, 199 (2010).
[3] L. Savary and L. Balents, Reports on Progress in Physics **80**, 016502 (2017).
[4] A. Kitaev and J. Preskill, Phys. Rev. Lett. **96**, 110404 (2006).
[5] M. Levin and X.-G. Wen, Phys. Rev. Lett. **96**, 110405 (2006).
[6] S. V. Isakov, M. B. Hastings, and R. G. Melko, Nature Phys. **7**, 772 (2011).
[7] P. W. Leung and K. J. Runge, Phys. Rev. B **47**, 5861 (1993).
[8] B. Bernu, P. Lecheminant, C. Lhuillier, and L. Pierre, Phys. Rev. B **50**, 10048 (1994).
[9] S. Yunoki and S. Sorella, Phys. Rev. B **74**, 1 (2006).
[10] M. Q. Weng, D. N. Sheng, Z. Y. Weng, and R. J. Bursill, Phys. Rev. B **74**, 772 (2006).
[11] R. Schmied, T. Roscilde, V. Murg, D. Porras, and J. I. Cirac, New Journal of Physics **10**, 045017 (2008).
[12] L. F. Tocchio, A. Parola, C. Gros, and F. Becca, Phys. Rev. B **80**, 064419 (2009).
[13] D. Heidarian, S. Sorella, and F. Becca, Phys. Rev. B **80**, 012404 (2009).
[14] P. H. Schmied, T. Roscilde, V. Murg, J. I. Cirac, and Roman, New J. Phys. **12**, 53036 (2010).
[15] A. Weichselbaum and S. R. White, Phys. Rev. B **84**, 245130 (2011).
[16] L. F. Tocchio, H. Feldner, F. Becca, R. Valentí, and C. Gros, Phys. Rev. B **87**, 035143 (2013).
[17] M. Thesberg and E. S. Sørensen, Phys. Rev. B **90**, 115117 (2014).
[18] A. Celi, T. Grass, A. J. Ferris, B. Padhi, D. Raventós, J. Simonet, K. Sengstock, and M. Lewenstein, Phys. Rev. B **94**, 075110 (2016).
[19] A. Yuste, M. Moreno-Cardoner, and A. Sanpera, Phys. Rev. B **95**, 195167 (2017).
[20] Z. Zhu and S. R. White, Phys. Rev. B **92**, 041105 (2015).
[21] W.-J. Hu, S.-S. Gong, W. Zhu, and D. N. Sheng, Phys. Rev. B **92**, 140403 (2015).
[22] Y. Iqbal, W.-J. Hu, R. Thomale, D. Poilblanc, and F. Becca, Phys. Rev. B **93**, 144411 (2016).
[23] W.-J. Hu, S.-S. Gong, and D. N. Sheng, Phys. Rev. B **94**, 075131 (2016).
[24] A. Wietek and A. M. Läuchli, Phys. Rev. B **95**, 035141 (2017).
[25] S.-S. Gong, W. Zhu, J.-X. Zhu, D. N. Sheng, and K. Yang, Phys. Rev. B **96**, 075116 (2017).
[26] D. Poilblanc, Phys. Rev. B **44**, 9562 (1991).
[27] C. Gros, Zeitschrift für Physik B Condensed Matter **86**, 359 (1992).
[28] M. A. de Vries, J. R. Stewart, P. P. Deen, J. O. Piatek, G. J. Nilsen, H. M. Rønnow, and A. Harrison, Phys. Rev. Lett. **103**, 237201 (2009).
[29] C. N. Varney, K. Sun, V. Galitski, and M. Rigol, Phys. Rev. Lett. **107**, 077201 (2011).
[30] C. N. Varney, K. Sun, V. Galitski, and M. Rigol, New Journal of Physics **14**, 115028 (2012).
[31] T. Mendes-Santos, T. Paiva, and R. R. dos Santos, Phys. Rev. A **91**, 023632 (2015).
[32] S. Hill and W. K. Wootters, Phys. Rev. Lett. **78**, 5022 (1997).
[33] T.-C. Wei and P. M. Goldbart, Phys. Rev. A **68**, 042307 (2003).
[34] P. Hauke, Phys. Rev. B **87**, 014415 (2013).
[35] P. Anderson, Materials Research Bulletin **8**, 153 (1973).
[36] T. Jolicoeur, E. Dagotto, E. Gagliano, and S. Bacci, Phys. Rev. B **42**, 4800 (1990).
[37] P. Lecheminant, B. Bernu, C. Lhuillier, and L. Pierre, Phys. Rev. B **52**, 6647 (1995).
[38] D.-V. Bauer and J. O. Fjærestad, Phys. Rev. B **96**, 165141 (2017).
[39] S. N. Saadatmand and I. P. McCulloch, Phys. Rev. B **96**, 075117 (2017).
[40] C. Hickey, L. Cincio, Z. Papić, and A. Paramekanti, Phys. Rev. B **96**, 115115 (2017).

Appendix

In this Appendix we show how TBC are implemented for the next-nearest-neighbours and chirality terms present in the model studied in sect IV. We show the scheme for both cases in Fig. A.1. In the same way than in the next neighbours interactions (Fig. 1) when a interaction term crosses the left-right (up-down) boundary the external spin gets twisted by a phase ϕ_1, blue colour (ϕ_2, red color). The external spins in the top-left corner of the figures, are twisted by $\phi_3 = \phi_1 + \phi_2$ (pink color) because the interaction crosses both boundaries. In the next-nearest-neighbours case, there is, as well, an external spin in the bottom-left corner which crosses the left-right down-up border. Note that crossing the down-up border is the opposite as crossing the up-down one. Therefore, the spin in the bottom-left corner gets twisted by a phase $\phi_4 = \phi_1 - \phi_2$ (green colour).
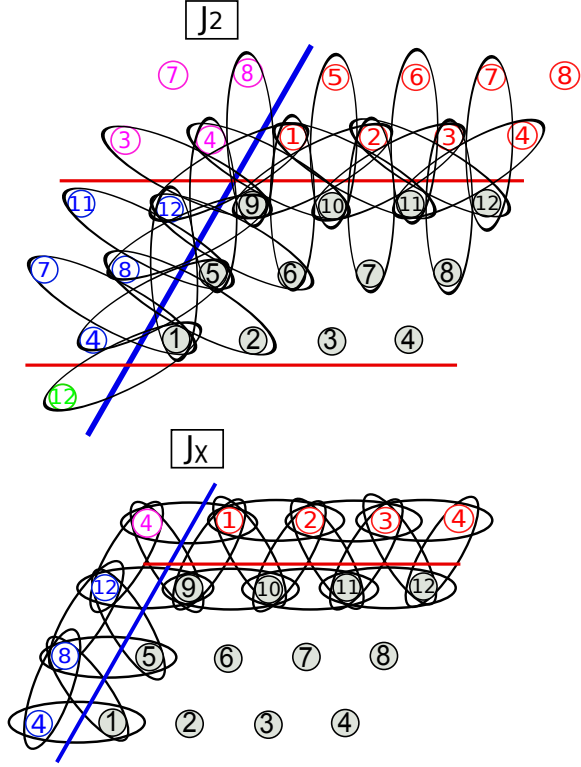
FIG. A.1: Scheme of twisted boundary conditions in a 4×3 triangular lattice with next-nearest-neighbours interactions (top panel) and chiral interactions (bottom panel). In every interaction term in the periodic boundary, depicted by a black oval, the coloured spin is twisted by an angle ϕ_1 (blue), ϕ_2 (red) for the left-right and top-bottom boundaries respectively. Interaction terms which cross two boundaries get twisted by both phases, $\phi_3 = \phi_1 + \phi_2$ (pink) for the left-top boundary, and $\phi_4 = \phi_1 - \phi_2$ (green) for the left-bottom one. The inner bounds are not depicted for clarity.

Appendixes

APPENDIX A

MSWT in the triangular lattice: comparison of the existent derivations

In this Appendix, different derivations of the MSWT formalism in the triangular lattice are compared. The seminal work by Xu and Ting [10] considers Heisenberg interactions. The works by Hauke and collaborators [6, 8, 179], generalize Xu's work by using a parameter λ in the Hamiltonian allowing to consider both Heisenberg ($\lambda = 1$) and XY ($\lambda = 0$) interactions. Both derivations, although they lead to sound results, are not fully comprehended. Paralelly, a MSWT for XY interactions has been rigurously derived by Celi and collaborators [9]. Their final equations, though they resemble Hauke's for $\lambda = 0$, are not in fully agreement.

Initially motivated by deriving, in a similar riguorous way as [9], a MSWT for Heisenberg interactions, I provide in Sec. 5.4 a derivation which considers both Heisenberg and XY interactions following Hauke's works. However, the expression obtained for $E = \langle H \rangle$ (Eq. 5.25) differs from the ones of Xu/Hauke and coincides with the one of Celi, when settling $\lambda = 0$. At the moment of the thesis handing, the discrepancies between the proposed derivation and Xu/Hauke's are still not comprehended.

This Appendix has its grounds in some fruitful discussions maintained with P.Hauke and A.Celi. It provides some technical details of the mentioned derivations pointing out the mismatches among them. It is aimed for readers which are already familiar with the MSWT formalism presented in the reported works. Therefore, most of the the steps, definitions and subtleties of the approach are taken as known. It remains an open issue, to

fully understand the discrepancies between the derivations and to provide a general MSWT for both XY and Heisenberg interactions.

Takahashi's MSWT in the square lattice with Heisenberg interactions

In Takahashi's seminal work [7], MSWT is derived for a square (bipartite) lattice with AF Heisenberg interactions. Even though this Appendix focuses on the triangular lattice formalism, some paradigmatic steps of Takahashi's derivation are detailed.

Two Dyson-Malev transformations, one for each sublattice, are performed. In the different works here reported, the definition of the DM transformation has some differences which are detailed here [1]. Using Wick's theorem, the expected values obtained are,

$$\langle S_l S_m \rangle = -[X + g(r)]^2 \tag{A.1}$$
$$\langle S_l S_l \rangle = [X + f(r)]^2, \tag{A.2}$$

where the first (second) equation is for spins in different (same) sublattices. Note that the energy, as obtained with $\langle H \rangle$, just includes the $\langle S_l S_m \rangle$ for NN interactions. Here, it is defined,

$$X \equiv S + 1/2 - f(0). \tag{A.3}$$

This quantity is forced to be 0 (Takahashi's constrain), but has to be kept during the energy minimization. It is important to stress that in the square lattice, by construction, there are no 6-bosons terms and that $g(0) = 0$.

---

[1] The DM transformations in the works considered are,

Takahashi sublattice A, $S_l^- = a_l^\dagger$, $\quad S_l^+ = (2S - a_l^\dagger a_l)a_l$, $\quad S_l^z = S - a_l^\dagger a_l$

Takahasi sublattice B, $S_m^- - = -b_m$, $\quad S_l^+ = -b_m^\dagger(2S - b_n^\dagger b_m)$, $\quad S_m^z = -S + b_m^\dagger b_m$

Xu: $S_i^- = (2S - a_i^\dagger a_i)a_i$, $\quad S_i^+ =, a_i^\dagger$, $\quad, S_i^z = -S + a_i^\dagger a_i$

Celi/Hauke: $S_i^- = \sqrt{2S}(1 - a_i^\dagger a_i/(2S))a_i$, $\quad S_i^+ = \sqrt{2S}a_i$, $\quad S_i^z = -S + a_i^\dagger a_i$

Xu and Ting: triangular lattice with Heisenberg interactions

Xu and Ting [10] extend the work of Takahashi to the triangular lattice. First of all, twisted coordinates are defined,

$$
\begin{aligned}
S_i^\xi &= - S_i^z \\
S_i^\eta &= - S_i^x \sin Q \cdot r_i + S_i^y \cos Q \cdot r_i \\
S_i^\zeta &= S_i^x \cos Q \cdot r_i + S_i^y \sin Q \cdot r_i
\end{aligned}
\tag{A.4}
$$

and a DM transformation is performed. Then, it is literally written,:

It should be pointed out that DM transformation violates the Hermitian conjugate relationship, which is different from the HP transformation. It is expected that this will not affect the ground-state propierties. In fact, this Hermitian can be recovered by an additional nonunitary transformation, $\alpha_k = cosh\theta_k a_k - sinh\theta_k a_{-k}^\dagger$. Using Wick's theorem for the interaction terms we can compute $\langle H \rangle$. We require that $\langle S_i^\zeta \rangle = 0$. Minimising the free energy of the system...

After this quote, the final of A_k and B_k are presented,

$$
A_k^{Xu} = 1/2 \sum_{\langle ij \rangle} t_{ij}(1 - \cos(Q \cdot r_{ij}))g(r_{ij})e^{-ik \cdot r_{ij}}
\tag{A.5}
$$

$$
\begin{aligned}
B_k^{Xu} = 1/2 \sum_{\langle ij \rangle} t_{ij}[&(1 - \cos(Q \cdot r_{ij}))g(r_{ij}) \\
&- (1 + \cos(Q \cdot r_{ij}))f(r_{ij})(1 - e^{-ik \cdot r_{ij}})] + \mu,
\end{aligned}
\tag{A.6}
$$

together with the energy,

$$
E = -1/2 \sum_{\langle ij \rangle} t_{ij}[-(1 + \cos Q \cdot r_{ij})f^2(r_{ij}) + (1 - \cos Q \cdot r_{ij})]g^2(r_{ij})].
\tag{A.7}
$$

In the following, some aspects of Xu and Ting's work are pointed out:

1. Xu and Ting do not specifically write down the extensive derivation. Nevertheless, the steps mentioned in the above quote are in accordance with the ones followed in Sec. 5.4.

2. The presence of the 6 bosons-terms is not mentioned. This is puzzling since the 6-bosons terms need to be explicity dropped in the other reported derivations.

3. The quantity $g(0)$ does not appear anywhere in the derivation, (though it is not specifically stated that $g(0) = 0$, as in the square lattice).

4. The expression for the energy, Eq. A.7, can be obtained from Takahashi expected values (Eq.(A.1) and (A.2) taking $X \to 0$),

$$E = 1/2 \sum_{i,j} t_{ij}[(1 + \cos(Q \cdot r_{ij})) \times Eq.A1$$
$$+ (1 - \cos(Q \cdot r_{ij})) \times Eq.A2] \tag{A.8}$$

5. A_k and B_k equations do recover the LSWT limit when $S \to \infty$, $(G(r), F(r) \to S)$, (setting $\mu = 0$).

$$A_k^{LSW} = S/2 \sum_{ij} t_{ij}[(\lambda - \cos(Q^{cl} \cdot r_{ij})) \cos(k \cdot r_{ij})] \tag{A.9}$$

$$B_k^{LSW} = S/2 \sum_{ij} t_{ij}[(\lambda + \cos(Q^{cl} \cdot r_{ij})) \cos(k \cdot r_{ij}) - 2\cos(Q^{cl} \cdot r_{ij})]. \tag{A.10}$$

All the points mentioned above, seem to indicate that there is a subtler connection between Takahashi's and Xu's works. Yet, to follow the scrupulous derivation performed by Xu is still a pending issue. Nevertheless, the above equations lead to sound results which have been succesfully contrasted, with QMC calculations in the square lattice limit [173].

Hauke's derivation for XY and Heisenberg interactions

Hauke's and collaborators extend Xu's work to a Hamiltonian which can have both Heisenberg and XY interactions (see for instance the Apendix in Ref. [6]). Twisting the coordinates and performing a DM transformation, the following Hamiltonian is obtained,

$$H = 1/4 \sum_{\langle i,j \rangle} t_{ij}\{[2S(a_i^\dagger a_j + a_i a_j^\dagger) - a_i^\dagger a_j^\dagger a_j a_j - a_i^\dagger a_i a_i a_j^\dagger](\lambda + \cos(Q \cdot r_{ij})))$$
$$+ [2S(a_i^\dagger a_j^\dagger + a_i a_j) - a_i a_j^\dagger a_j a_j - a_i^\dagger a_i a_i a_j](\lambda - \cos(Q \cdot r_{ij}))$$
$$+ 4[S^2 - S(a_i^\dagger a_i + a_j^\dagger a_j) + a_i^\dagger a_i a_j^\dagger a_j] \cos(Q \cdot r_{ij})\}, \tag{A.11}$$

where here, 6-bosons terms have been dropped. Then, using Wicks' theorem, the following expected value of the energy is provided,

$$
\begin{aligned}
\langle H \rangle_{Hauke} = 1/2 \sum_{\langle ij \rangle} t_{ij}[(\lambda + \cos Q \cdot r_{ij})(X + f(r_{ij}))^2 \\
- (\lambda - \cos Q \cdot r_{ij})](X + g(r_{ij}))^2],
\end{aligned} \tag{A.12}
$$

using the following definitions,

$$
\begin{aligned}
\langle a_i^\dagger a_j \rangle = \langle a_i a_j^\dagger \rangle = f(r_{ij}); \quad \langle a_i^\dagger a_i \rangle = f(0) - 1/2; \quad \langle a_i a_i^\dagger \rangle = f(0) + 1/2; \\
\langle a_i a_j \rangle = \langle a_i^\dagger a_j^\dagger \rangle = g(r_{ij}) \quad \langle a_i a_i \rangle = \langle a_j^\dagger a_j^\dagger \rangle = g(0).
\end{aligned} \tag{A.13}
$$

The above expression of the energy does **not** follow from the Hamiltonian above, it is a misleading step. Notice that it has been obtained by replacing in Xu's Energy (Eq.(A.7)) $1 \to \lambda$. This expression also resembles Takahashi's for the square lattice,

$$
\sum_{i,j} t_{ij}[(\lambda + \cos(Q \cdot r_{ij})) \times Eq.A.2 + (\lambda - \cos(Q \cdot r_{ij})) \times Eq.A.1].
$$

The following A_k and B_k are obtained,

$$
A_k^{Hauke} = 1/N \sum_{\langle ij \rangle} t_{ij}[\lambda - \cos(Q \cdot r_{ij})]g(r_{ij})e^{ik \cdot r_{ij}}, \tag{A.14}
$$

$$
\begin{aligned}
B_k^{Hauke} = 1/N \sum_{\langle ij \rangle} t_{ij}\{[\lambda - \cos(Q \cdot r_{ij})]g(r_{ij}) \\
- [\lambda + \cos(Q \cdot r_{ij})]f(r_{ij})(1 - e^{ik \cdot r_{ij}})\} - \mu.
\end{aligned} \tag{A.15}
$$

Note that, for $\lambda = 1$, these expressions are equivalent to Xu's.

Celi's derivation for XY interactions

Celi and collaborators [9] derive the formalism from scratch for XY interactions in an inhomogeneous triangular lattice. Along this Appendix, just the case without inhomogeneity is considered. After dropping the 6 bosons terms, the following expected value of the energy obtained,

$$
\begin{aligned}
\langle H \rangle_{Celi} = 1/2 \sum_{ij} t_{ij} cos(Q \cdot r_{ij})[(X + f(r_{ij}))^2 + (X - g(r_{ij}))^2 \\
+ g(0)[f(r_{ij}) - g(r_{ij})] + f^2(r_{ij}) + g^2(r_{ij})],
\end{aligned} \tag{A.16}
$$

which, in order to be the same as Hauke's ($\lambda = 0$) should be,

$$\langle H \rangle_{Celi} = 1/2 \sum_{ij} t_{ij} cos(Q \cdot r_{ij})[(X + f(r_{ij}))^2 + (X \cancel{+}^{+} g(r_{ij}))^2$$

$$+ \cancel{g(0)[f(r_{ij}) - g(r_{ij})] + f^2(r_{ij}) + g^2(r_{ij})]}. \tag{A.17}$$

Immediately after this equation (Eq.17 in Ref. [9]), it is stated that the discrepancies with Hauke's simply come from the omission of the $g(0)$ term. Certainly, if Takahashi's constraint is taken, $X \to 0$, Eq.(A.16) resembles Eq.(A.12) ($\lambda = 0$) except for the $g(0)$ term and a global factor $1/2$ in front. However, it is not clear that in Hauke's work such term is dropped. Moreover, both the change of sign in front of $g(r_{ij})$ and the term $g(0)[f(r_{ij}) - g(r_{ij})]$ are clearly relevant when computing A_k and B_k. At the present moment, the discrepancies between Hauke's and Celi's works are still not fully understood. The final expressions for A_k and Bk obtained are,

$$A_k^{Celi} = 1/2 \sum_{ij} t_{ij} \cos{(Q \cdot r_{ij})}[g(r_{ij}) - f(r_{ij})$$

$$+ \cos{(k \cdot r_{ij})}(g(0) - 4g(r_{ij}))] \tag{A.18}$$

$$B_k^{Celi} = \sum_{ij} t_{ij} \cos{(Q \cdot r_{ij})}[\frac{-3}{2}g(r_{i,j}) - \frac{5}{2}f(r_{ij})$$

$$+ \cos{(k \cdot r_{ij})}(g(0)/2 + 2f(r_{ij}))]. \tag{A.19}$$

They are clearly different to Hauke's ($\lambda = 0$), Eq. (A.14) and (A.15). However, they lead to similar, though not equal, results.

Comparision with the presented derivation

In Sec. 5.4, the derivation leads to the Hamiltonian derived by Hauke, Eq. (A.11). Using Wicks' theorem, it follows,

$$\langle H \rangle_{Yuste} = \sum_{\langle ij \rangle} t_{ij}\{(f(r_{ij})X - \frac{g(r_{ij})g(0)}{2})[\lambda + \cos{(Q \cdot r_{ij})}]$$

$$+ (g(r_{ij})X - \frac{f(r_{ij})g(0)}{2})[\lambda - \cos{(Q \cdot r_{ij})}]$$

$$+ (X^2 + g^2(r_{ij}) + f^2(r_{ij})) \cos{(Q \cdot r_{ij})}\}, \tag{A.20}$$

which corresponds to Celi's expresion Eq.(A.16),

$$\langle H \rangle_{Yuste,\lambda=0} = \sum_{\langle ij \rangle} t_{ij} \cos\left(Q \cdot r_{ij}\right)[X(f(r_{ij}) - g(r_{ij})) + \frac{g(0)}{2}(f(r_{ij}) - g(r_{ij}))$$
$$+ X^2 + f(r_{ij})^2 + g(r_{ij})^2] = \langle H \rangle_{Celi}, \tag{A.21}$$

but which clearly differs from Hauke's,

$$\langle H \rangle_{Hauke} = \frac{1}{2} \sum_{\langle ij \rangle} t_{ij}\{\cos\left(Q \cdot r_{ij}\right)[2X^2 + f^2(r_{ij}) + g^2(r_{ij}) + X(f(r_{ij}) + g(r_{ij}))]$$
$$+ \lambda[+f^2(r_{ij}) - g^2(r_{ij}) + X(f(r_{ij}) - g(r_{ij}))]\}, \tag{A.22}$$

$$\frac{1}{2}\langle H \rangle_{Yuste} = \frac{1}{2} \sum_{\langle ij \rangle} t_{ij}\{\cos\left(Q \cdot r_{ij}\right)[\overset{2}{f}X^2 + f^2(r_{ij}) + g^2(r_{ij})$$
$$+ X(f(r_{ij})\overset{+}{\diagup} g(r_{ij})) + \frac{g(0)}{2}\cancel{(f(r_{ij}) - g(r_{ij}))}]$$
$$f^2(r_{i,j}) - g^2(r_{ij})$$
$$+ \lambda[\frac{-g(0)}{2}\cancel{(g(r_{ij}) + f(r_{i,j}))}$$
$$+ X(f(r_{ij})\overset{-}{\nearrow} g(r_{ij})]\}. \tag{A.23}$$

Apart from a factor 1/2, the discrepancies between the obtained expression and Hauke's are pointed out. Notice that in the terms with $\cos\left(Q \cdot r_{ij}\right)$, (i.e., present in the XY interactions derivation), the changes are all small in energy since we will set $X \to 0$ and $f(r_{ij}) - g(r_{ij}) \sim 0$. However, this is not anymore the case for the terms with λ which clear differ from Hauke's expression.

The following A_k and B_k are obtained,

$$A_k^{Yuste} = A_k^{Celi} + \lambda/2 \sum_{ij} t_{ij}[g(0)\cos\left(k \cdot r_{ij}\right) + g(r_{ij}) + f(r_{ij})]$$
$$B_k^{Yuste} = B_k^{Celi}$$
$$+ \lambda/2 \sum_{ij} t_{ij}[-g(0)\cos\left(k \cdot r_{ij}\right) + 2g(0) + g(r_{ij}) + f(r_{ij})]. \tag{A.24}$$

The numerical implementation of such expressions with $\lambda = 1$ lead to inconsistent results.

Addition of the six-bosons terms

As pointed out before, in Xu's work the presence or neglection of 6-boson terms is not even mentioned. Therefore, it could be a priori a possible origin of the discrepancies between derivations. Using Wicks' theorem with the same definitions as in Eq.(A.13), the 6-boson terms leads to,

$$\langle H \rangle_{6bosons} = \frac{1}{2S} \sum_{ij} t_{ij} [\lambda - \cos{(Q \cdot r_{ij})}] \{ f(r_{ij}) g(0)(f(0) - 1/2)$$
$$+ g(r_{ij})(f(0) - 1/2)^2 + f^2(r_{ij}) g(r_{ij}) + g(r)^3/2 + g(r_{ij}) g^2(0)/4 \}.$$
(A.25)

Thus, they only contribute in the $[\lambda - \cos{(Q \cdot r_{ij})}]$ term. Notice that in this expression Takahashi's constraint implies: $(f(0) - 1/2) = S$. It is clear that the six-bosons terms cannot fix the mismatches signaled in Eq.(A.23).

Conclusions

A fully comprehension of the MSWT in the triangular lattice for both Heisenberg and XY interactions is still pending. In the XY case, a rigorous study by Celi leads to similar, though not equal, results as the works by Hauke which are obtained generalizing Xu's equations to XY interactions. What is the origin of these small discrepancies between both approaches? Is there a subtle connection between Xu's/Hauke's works and Takahashi's expressions for the square lattice? The answer to these questions might provide a new insight to formulate a rigorous derivation for Heisenberg interactions. This complete MSWT formalism in the triangular lattice might provide the possibility to study other frustrated models and to elucidate the two conjectures formulated in Chapter 6.

APPENDIX B

MATLAB codes

In this Appendix, I provide some of the MATLAB codes I have written along my Ph.D. The first 5 codes are the ones which implement exact diagonalization in spin models in the 2D triangular lattice with random boundary conditions. The 6th code implements modified spin wave theory on the same models. Along my thesis I have also used 1D DMRG calculations but the code is taken from an open source [164] and therefore I do not provide the details here.

The codes are explained by steps and provide a helpful guide to implement them from the scratch. The reader who actually desires to use the codes should comment the section titles.

Basis in subblocks of constant Sz

This code computes the basis of a many body quantum system with L particles and d internal degrees of freedom. It splits the basis in the different constant Sz sectors.

Input

- L---> System size (must be even!)

- d---> internal degrees of freedoom,e.g., d=2 for spin 1/2

Output

- basis_sz---> basis for each sector sz (each sector stored in one cell).

- order_sz---> position of each element of a subblock in the whole basis.

Whole basis computation

```matlab
basis_spin=zeros(d^L,L);
for i1=1:1:L
    ba=0;
    for i2=1:1:d^L
        basis_spin(i2,i1)=ba;
        if mod(i2,d^(L-i1))==0
            ba=mod(ba+1,d);
        end
    end
end
```

Splitting the basis according to Sz

```matlab
basis_sz=cell(L/2+1,1);
 M=L;
   for i1=L/2+1:-1:1
     val=1;
     for i2=1:d^L
if sum(basis_spin(i2,:))==M
     basis_sz{i1}(val,:)=basis_spin(i2,:);
     order_sz{i1}(1,val)=i2;
     val=val+1;
end
     end
 M=M-1;
   end
```

Published with MATLAB® R2017a

Hamiltonian terms: SxSx+SySy

This code computes the terms of the Hamiltonian given a list of interacting pairs de ning the lattice geometry

Input

- sz---> total magnetization subspace

- basis_sz, order_sz---> basis in the subblock and position of the elements in the whole basis

- L---> Number of sites

- z---> list of interacting pairs i,j

Output

- Two matrices containing the terms S_i^xS_j^x+S_y^xS_j^y of a given list of interacting pairs and their complex conjugate. Stored in hard drive.

De nitions

```
basis=basis_sz{sz+1};
order=order_sz{sz+1};
dimensio=size(basis,1);
cont1=1;
cont2=1;
```

Loop over interacting pairs. Can be paralelized

```
     ppp=parpool(6); % e.g, calculations with 6 cores
parfor  i1 = 1:size(z,1)

  cont1=1;cont2=1;
       n = z(i1,1); m = z(i1,2); %interacting pair
        value=2^(L-n)-2^(L-m); % Jump in the "binary" basis when
 destroying in m and creating in n
```

Loop over the basis elements

```
       for i2=1:dimensio
       if basis(i2,m)==1 && basis(i2,n)==0

           aux=order(i2)+value; %Output vector in the whole basis
           out= nd(order==aux); %Output vector position in the
 subblock
```

We construct the matrix and the complex conjugate

```
v1{i1}(cont1)=out;
vc1{i1}(cont1)=i2;
w1{i1}(cont1)=i2;
wc1{i1}(cont1)=out;
cont1=cont1+1;

       end
```

```
end

end
 delete(ppp)
```

End of the loops and parallel computing

Merging the sparse matrices which are obtained in di erent paralel computations

```
vv1=[];ww1=[];
vv2=[];ww2=[];

vvc1=[];wwc1=[];
vvc2=[];wwc2=[];


for i1=1:size(z,1)
vv1=[vv1 v1{i1}];ww1=[ww1 w1{i1}];
vvc1=[vvc1 vc1{i1}];wwc1=[wwc1 wc1{i1}];
end
```

Store both matrices in hard drive memory

```
Hamiltonian=sparse(vv1,ww1,1,dimensio,dimensio);
Hamiltonian_com=sparse(vvc1,wwc1,1,dimensio,dimensio);

  lename = ['Hamiltonian_test.mat'];
  save( lename,'Hamiltonian','Hamiltonian_com');
```

Published with MATLAB® R2017a

Hamiltonian terms: SzSz

Computation of the SzSz terms of the Hamiltonian given a list of interacting pairs.

Input

- sz---> total magnetization subspace

- d---> local dimension

- basis_sz, order_sz---> basis in the subblock and position of the elements in the whole basis

- L---> Number of sites

- z---> list of interacting pairs i,j

Output

- A matrix containing the terms $S_i^z S_j^z$ of a given list of interacting pairs and its complex conjugate. It gets stored in hard drive memory.

De nitions

```
basis=basis_sz{sz+1};
order=order_sz{sz+1};
dimensio=size(basis,1);
Sigmaz=cell(L,1);
```

Sz operator for each site

```
for i1=1:L
     Sigmaz{i1}=sparse(1:1:dimensio,1:1:dimensio,(basis(:,i1)+1-(d
+1)/2));
end
```

Interacting Hamiltonian

```
  Hamiltonian_SzSz=sparse(dimensio,dimensio);
for 1:size(z,1)
 Hamiltonian_SzSz=Hamiltonian_SzSz+Sigmaz{z(i1,1)}*Sigmaz{z(i1,2)};

end
```

Hard drive saving

```
  lename=['Hamiltonian_SzSz'.mat']

  save( lename,'Hamiltonian_SzSz');
```

Published with MATLAB® R2017a

ED with random boundary conditions

Computes and diagonalizes the Hamiltonian with RBC for a given anisotropy. The code changes as a function of the model used.

As example: SATL (anisotropy t1=1 and t2)

Input

- lambda---> =0 XY interactions =1 Heisenberg interaction

- rasize---> Size of the random sampling

- tt2---> vector with the anisotropy values of t2

- lattice---> string with lattice used,e.g., '6x4'

Output

- Ground state and energy stored with a ag depicting the anisotropy and random sampling value.

De nitions

```matlab
pbc=1;  % pbc=1 ==>  PBC, pbc=0 RBC
sz=0;   %Subblock of sz for the computations
if(pbc==1)
        rasize=1;
end
dimensio=size(Ham_t1,1);
Ham=sparse(dimensio,dimensio);
```

Loading the stored matrices

```matlab
load(['data/data_' lattice '.mat'])
%
% *Ham_t1, Ham_t2 NN in the bulk with anisotropy t1 and t2
% *Ham_tunt1 NN Tunneling with phase 1 and t1
% *Ham_tunt2 NN Tunneling with phase 2 and t2
% *Ham_tunt3 NN Tunneling with phase 1 and t2
% *Ham_tunt4 NN Tunneling with phase1+phase2 and t2
% *Ham_tun*_com Complex conjugate of the above matrices
% *Ham_SzSz_t1 NN SzSz terms with anisotropy t1
% *Ham_SzSz_t2 NN SzSz terms with anisotropy t2
```

Loops and computation

```matlab
 parpool('local',2) %e.g, 2 cores
parfor i1=1:size(tt2,2) % Anisotropy loop, can be done in parallel
    t2=tt2(i1); %anisotropy value of the loop
    for i2=1:rasize    %  Random sampling Loop

     phase1=rand*2*pi; %random phase 1
     phase2=rand*2*pi; % random phase 2
      if(pbc==1)
```

```
    phase1=0;
      phase2=0;
      end
phase3=phase1+phase2; % random phase 3
    Ham=Ham_t1+t2*Ham_t2;      % Bulk Hamiltonian
    Ham=Ham+2*lambda*(Ham_SSz_t1+t2*Ham_SzSz_t2);  % SzSz terms
    Ham=Ham
+exp(1i*phase1)*(Ham_tunt1+t2*Ham_tunt3)+exp(-1i*phase1)*(Ham_tunt1_com
+t2*Ham_tunt3_com); %Left-Right Boundaries
    Ham=Ham
+exp(1i*phase2)*(t2*Ham_tunt2)+exp(-1i*phase2)*(t2*Ham_tunt2_com); %Up-
Down Boundary
    Ham=Ham
+exp(1i*phase3)*(t2*Ham_tunt4)+exp(-1i*phase3)*(t2*Ham_tunt4); %
 Corner Boundary

    [vep,vap]=eigs(Ham,1,'SR'); %Lanczos diagonalization
vep_ground(:)=vep(:,1); % Ground state
e0=vap(1,1); %energy
```

Storing the ground state and energy. File name with anisotropy and sampling value

```
  lename=['out/output_' lattice '_t2_' num2str(t2) '_rand_'
 num2str(i2) '.mat'] %example of output name
 save( lename,'vep_ground','eo')

    end
end
```

Published with MATLAB® R2017a

Computing the overlap and Nc

The code computes the overlap of a con guration with the con guration that minimizes the energy. It sorts the output by encreasing normalized energy epsilon. It also computes the number of con gurations below the energy bias Nc. (go to Sec. ED with RBC for details)

Example:SATL model

Input

- rasize ---> Random sample size

- tt2 ---> Vector with the anisotropy values

- lattice---> Lattice used

- out le--->Flag in the name of the output les

- bias---> Energy bias to do the post selection and compute Nc

Output

- overlap---> Overlap of each con guration with the con guration that minimizes the energy. Results sorted by increasing epsilon

- epsilon--> Energy of each con guration normalized by the minimal one

- Nc---> Number of con gurations with an energy below the bias

```matlab
%%%%%%%%
%%%%%%%%%
for i1=1:size(tt2,2) % Anisotropy loop

t2=tt2(i1);
```

Computing epsilon

```matlab
for i2=1:rasize % Random sampling loop
  lename=['out/output_' lattice '_t2_' num2str(t2) '_rand_'
 num2str(i2) '.mat'] %example of input  le
load( lename,'vep_ground','e0') % it loads ground state and energy
energies{i1}(i2)=e0;
end

[Y,I]=sort(energies{i1}(:));
out2{i1}=energies{i1}(I);
epsilon(:,i1)=abs(100*(out2{i1}(:)-out2{i1}(1))/out2{i1}(1)); %Epsilon
Nc(i1)=sum(epsilon(:,i1)<bias); %Number of con gurations with
 normalized energy below the bias.
```

Computing the overlap

```matlab
  lename=['out/output_' lattice '_t2_' num2str(t2) '_rand_'
  num2str(I(1)) '.mat'] %con gurations with minimal energy
  load( lename);
```

```
vep_min=vep_ground;
overlap{i1}(:,1)=epsilon(:,i1);
for i2=1:rasize
  lename=['out/output_' lattice '_t2_' num2str(t2) '_rand_'
 num2str(I(i1)) '.mat'] %con gurations sorted by increasing energy
 load( lename)
overlap{i1}(i2,2)=abs(ctranspose(vep_min)*vep_ground); %Overlap sorted
 by increasing energy
end

end
```

Published with MATLAB® R2017a

Structure factor

This code computes the structure factor given an input state and a lattice geometry.

Input

- knum---> Discretization of kx and ky (odd!), typically 51

- SxSx_SySy_pairs, SzSz_pairs ---> For all interacting pairs. Obtained similarly as in the Hamiltonian_XXX code.

- vep---> input vector

- position----> coordinates of each site (x_i,y_i)

- L system size

- lambda---> =0 XY interactions =1 Heisenberg interactions

Output

*skk---> structure factor

```matlab
%*De nitions*
npairs=(size(SxSx_SySy_pairs,1));
distance=cell(npairs,1);
expect=cell(npairs,1);
cont=1;

%*Computation of the structure factor
for i1=1:L

for i2=1:i1-1
    l=i1;m=i2;
distance{cont}=transpose((position(m,:)-position(l,:)));
%Expected value of SiSj
expect{cont}=vep(:,1)'*(SxSx_SySy_pairs{cont})*vep(:,1)/2;
expect{cont}=expect{cont}+vep(:,1)'*(SxSx_SySy_pairs{cont}')*vep(:,1)/2;

expect{cont}=expect{cont}+lambda*vep(:,1)'*SzSz_pairs{cont}*vep(:,1);
        cont=cont+1;
end

end


kx=[-2*pi:4*pi/(knum-1):2*pi]; %momentum discretization
ky=[-2*pi:4*pi/(knum-1):2*pi];
skk=zeros(knum,knum);

        for j1=1:knum
        for j2=1:knum;
         k=[kx(j1) ky(j2)];
            Sk=0;
```

```
 for i1=1:npairs;
Sk=Sk+exp(1i*k*distance{i1})*expect{i1}; %Fourier transform
 end

skk(j2,j1)=2*Sk/L; % Factor 2 to include j,i terms.
end
end
```

Published with MATLAB® R2017a

MSWT for the anisotropic J1-J2

Modi ed spin wave theory on the SATL model with NNN interactions in the in nite lattice limit (sums to integrals).

Input

- lambda---> =0 XY interactions =1 Heisenberg interactions

- NextNext ----> =1 J1-J2 model with anisotropy. =0 SATL

- S=1/2 ---> Spin

- backwards---> =0(1) Computes forwards (backwards) the anisotropy values (could change convergence)

- j2 ---> Next-to-nearest neighbors interactions (Vector)

- anisotropia---> SATL anisotropy (Vector)

Output

- Files with Energy, Q, M (both LSWT and MSWT) and number of iterations.

De nitions

```
nitera=100; %Maxim number of iterations if  convergence is not
 reached.
previous_msw=2; %  % if=1 self iterating equations just with LSW
 values if 2 uses previous MSWT result as well
tolerance=10^(-3); % ;tolerance in Mzero to stop iterations.
z=3; %number of  rst neighbors
Delta=[1,0;1/2,sqrt(3)/2;-1/2,sqrt(3)/2]; % r vectors between next
 neigbhors
if (NextNext==1)
z=6;
    Delta=[Delta; 0, sqrt(3); 3/2 , sqrt(3)/2;-3/2 ,
 sqrt(3)/2]; %second neighbors
end
if(backwards==1)
j2=abs(sort(-j2));
end
both_initial=1; %both initial conditions (LSWT and previous MSWT)
%%%%%%%%%%%%%%%%%%%%%%%%
```

Loop over anisotropy, can be done in parallel

```
parfor it3=1:size(anisotropia,2)

    extra_ani=anisotropia(it3)
% Quantities de ned for the parfor loop to work, and initialize the
 j2 loop.
Qcl=zeros(size(j2,2),2);
Ecl=zeros(size(j2,2));
A_k=@(x)0;B_k=@(x)0;
```

```
A_lsw=@(x)0;B_lsw=@(x)0;
A_k_hauke=@(x)0;B_k_hauke=@(x)0;
cos2theta_lsw=@(x)0;omega_lsw=@(x)0;sin2theta_lsw=@(x)0;
omega=@(x)0;cos2theta=@(x)0;sin2theta=@(x)0;
Mzero_lsw=zeros(size(j2,2),2);
Q=zeros(2,1);Q_opt=zeros(2,1); Ene_msw=0;
A=zeros(2,1); B=zeros(2,1);
sin_initial=cell(2,1);cos_initial=cell(2,1);Q_initial=cell(2,1);
t_aft=0;t_bef=0;havent_converge=0;
output_iteration=0;
cosQ=zeros(z,1);
%%%%%%%%%
```

Quantities which are rede ned in every step of the loop

```
 output_MSW=zeros(1,7);
%%%%%%%%%%%%%%%%%%%%%%%%%%%%%%%
sin2theta_msw_prev=@(x,y)0;
cos2theta_msw_prev=@(x,y)0; % values computed with MSWT of the
 previous iterations. We set them to zero to start the  rst iteration
 with a value.
Q_msw_prev=[0 0];
if (NextNext==0)
Qcl_before=2*acos(-extra_ani/2); % As initial value for the
 minimization we take Qcl analytic from the SATL
end
if (NextNext==1)
Qcl_before=2*pi; % As initial value for the minimization we take 2*pi
 (collinear)
end
havent_converge=0;   contador_aft=1; contador_bef=1;
converged_points=0; no_convergence=0;
%%%%%%%%%%%%%
```

Loop over second neighbours interactions

```
for it2=1:size(j2,2)

    t2=j2(it2);
    aniso=[1 j2 j2]; %Anisotropy SATL
    if (NextNext==1)
    aniso=[1 extra_ani extra_ani t2 t2 t2]; %AnisotropyNN+IsotropicNNN
    end
     converged_points(it2)=0;
```

Classical Energy and ordering vector

```
      E_clas=@(x)0;
    for iJ=1:z
        E_clas=@(x)E_clas(x)+aniso(iJ)*cos(x(1)*Delta(iJ,1));

    end

% Qy=0 is  xed in the classical order parameter
   if(NextNext==1)  % Analytic for the J1-J2
```

```matlab
        if(extra_ani==1) %comensurate spiral to 2D Neel
            if(t2<1/8)
                Qcl(it2,:)=[4/3*pi 0];
            end
            if(t2>1/8)
                Qcl(it2,:)=[2*pi 0];
            end
    if(t2==1/8)
                Qcl(it2,:)=[2*pi 0];
    end
    Ecl(it2)=E_clas(Qcl(it2,1));
    end
        if(extra_ani<1)
% Region not considered in the MSWT calculations
            'Error, no extra_ani<1 allowed'
        end
    if(extra_ani>1)
  opt = optimset('Display','o ');
  %Energy minimization with di erent initial values of iteration to
  nd
  %the global minimum.
[A(1) B(1)]=fmincon(E_clas,Qcl_before,[],[],[],[],[4/3*pi-0.1],[2*pi
+0.01],[],opt);
[A(2) B(2)]=fmincon(E_clas,2*pi,[],[],[],[],[4/3*pi-0.1],[2*pi+0.01],
[],opt);
[A(3) B(3)]=fmincon(E_clas,4/3*pi,[],[],[],[],[4/3*pi-0.1],[2*pi
+0.01],[],opt);

   %Global minimum .
   [a b]=min([B]);
   Qcl(it2,1)=A(b);
   Ecl(it2)=B(b);


Qcl_before=Qcl(it2); %Set Qcl_before for next iterations
  Qcl(it2,2)=0;
    end

  end

   % Clasical Order parameter SATL (Analytic)
   if(NextNext~=1)
   Qcl(it2,1)=2*acos(-t2/2); Qcl(it2,2)=0;
   if(t2>2)
    Qcl(it2,1)=2*pi; Qcl(it2,2)=0;
   end
     Ecl(it2)=E_clas([Qcl(it2,1)]);
   end
```

LSWT: Obtaining Ak and Bk

```matlab
cont=1;
        A_lsw=@(x,y)0;
        B_lsw=@(x,y)0;
```

```matlab
    for iJ=1:z
 cosQ(iJ)=cos(dot(Qcl(it2,:),Delta(iJ,:)));
 A_lsw=@(x,y)A_lsw(x,y)+S/2*aniso(iJ)*(lambda-
cosQ(iJ))*cos(x*Delta(iJ,1)+y*Delta(iJ,2));
B_lsw=@(x,y)B_lsw(x,y)+S/2*aniso(iJ)*((lambda
+cosQ(iJ))*cos(x*Delta(iJ,1)+y*Delta(iJ,2))-2*cosQ(iJ));
    end


omega_lsw=@(x,y)sqrt(B_lsw(x,y).^2-A_lsw(x,y).^2);
cos2theta_lsw=@(x,y)sqrt(B_lsw(x,y).^2./(B_lsw(x,y).^2-
A_lsw(x,y).^2));
sin2theta_lsw=@(x,y)A_lsw(x,y)./B_lsw(x,y).*cos2theta_lsw(x,y);
integrand_lsw=@(x,y)B_lsw(x,y)./omega_lsw(x,y);
Mzero_lsw(it2,1)=t2;
```

Self iterative equations till convergence is reached

```matlab
% Previous MSWT values
 sin_initial{1}=sin2theta_lsw; cos_initial{1}=cos2theta_lsw;
 sin_initial{2}=sin2theta_msw_prev; cos_initial{2}=cos2theta_msw_prev;
 Q_initial{1}=Qcl(it2,:); Q_initial{2}=Q_msw_prev;

 for starting_value=1:previous_msw  % This loop is over the starting
 value of costheta and sintheta, (LSWT and previous MSWT)

 cos2theta=cos_initial{starting_value};
 sin2theta=sin_initial{starting_value};
 Q_msw_before=Q_initial{starting_value}; %Starting value for the Q
 Mzero_old=0; Mzero=1; %Allows the  rst iteration to start
 cont=1;

 for iteration=1:nitera  %Loop for self iteracting equations

fprintf(1,'%s\n',['Computing for t2=' num2str(t2) ' and anisotropy='
 num2str(extra_ani) ' . Iteration' num2str(iteration) '. M_zero='
 num2str(Mzero) ])

if(abs(Mzero-Mzero_old)<tolerance)      %Condition for convergence

    fprintf(2,'%s\n',['Convergence reached for t2=' num2str(t2) '
 and anisotropy=' num2str(extra_ani) '. Number of iterations'
 num2str(iteration)])
 %  Save output just when convergence
    output_MSW(it2,:)=[t2 Q(1) Q(2)  Mzero Ene_msw iteration
 starting_value];
       cos2theta_msw_prev=cos2theta; % Keep the values for next
 iteration
   sin2theta_msw_prev=sin2theta;
   Q_msw_prev=Q;
     converged_points(it2)=1;

   break
 end
```

```matlab
    % Takahashi constraint for the zero mode
    if(iteration>1)
    Mzero_old=Mzero;   %M_old is M_zero of previous interaction.
 end
      Mzero=S+1/2;
 [result] = integral(cos2theta);
Mzero=-result+S+1/2; %New Mzero

 if(abs(imag(Mzero))>0) %If Mzero imaginary breaks loop
    fprintf(2,'%s\n',['Error of convergence for t2=' num2str(t2) ' and
 anisotropy=' num2str(extra_ani) '., iteration=' num2str(iteration)])
       no_convergence(it2)=iteration;
               output_MSW(it2,:)=[t2 0 0  0 0 0 0];

    break
 end
  if(is nite(Mzero)==0) %If Mzero in nite or NAN breaks
    fprintf(2,'%s\n',['Error of convergence (divergence of integral)
 for t2=' num2str(t2) ' and anisotropy=' num2str(extra_ani) '.,
 iteration=' num2str(iteration)])
       no_convergence(it2)=iteration;
               output_MSW(it2,:)=[t2 0 0  0 0 0 0];

    break
  end
```

Fr and Gr computation

```matlab
for iJ=1:2
integrand=@(x,y)cos2theta(x,y).*cos(x*Delta(iJ,1)+y*Delta(iJ,2));
[Fr(iJ)] = integral(integrand);
integrand=@(x,y)sin2theta(x,y).*cos(x*Delta(iJ,1)+y*Delta(iJ,2));
[Gr(iJ)] = integral(integrand);
Fr(iJ)=+Fr(iJ)+Mzero;
Gr(iJ)=+Gr(iJ)+Mzero;
end
Fr(3)=Fr(2);Gr(3)=Gr(2); %equal bounds equal values of Fr Gr
if(NextNext==1)
for iJ=4:6   %%%integral in the Brillouin zone for second neighbours
integrand=@(x,y)cos2theta(x,y).*cos(x*Delta(iJ,1)+y*Delta(iJ,2));
[Fr(iJ)] = integral_second(integrand);
integrand=@(x,y)sin2theta(x,y).*cos(x*Delta(iJ,1)+y*Delta(iJ,2));
[Gr(iJ)] = integral_second(integrand);
Fr(iJ)=+Fr(iJ)+Mzero;
Gr(iJ)=+Gr(iJ)+Mzero;
end
end
Fzero=S+1/2;
[result] = integral(sin2theta);
 Gzero=Mzero+result;
%Check integral convergence
resultats_integral=[Gzero Fzero Fr Gr];
if(is nite(sum(resultats_integral))==0) %If Mzero in nite or NAN
 breaks
```

```
    fprintf(2,'%s\n',['Error of convergence (divergence of integral)
 for t2=' num2str(t2) ' and anisotropy=' num2str(extra_ani) '.,
 iteration=' num2str(iteration)])
        no_convergence(it2)=iteration;
                output_MSW(it2,:)=[t2 0 0  0 0 0 0];

    break
 end

%%%%%%% F(r) G(r) Gzero computed.
```

Computation of Q optimal

```
  E_msw=@(x)0;

   for iJ=1:z
 E_msw=@(x)E_msw(x)+1/2*aniso(iJ)*(Fr(iJ)^2*(lambda
+cos(x(1)*Delta(iJ,1)+x(2)*Delta(iJ,2)))-Gr(iJ)^2*(lambda-
cos(x(1)*Delta(iJ,1)+x(2)*Delta(iJ,2))));
   end

%%%%  SATL Q is analytic
if(NextNext==0)
argument=-t2/2*(Fr(2)^2+Gr(2)^2+Gzero/2*(Fr(2)-Gr(2)))/
(Fr(1)^2+Gr(1)^2+Gzero/2*(Fr(1)-Gr(1)));
if(argument>-1)
Q_opt(1)=2*acos(argument); Q_opt(2)=0;
end
if(argument<-1)
 Q_opt(1)=2*pi;  Q_opt(2)=0;
end
if(argument==-1)
 Q_opt(1)=2*pi;  Q_opt(2)=0;
end
if(t2==0) %1D limit
 Q_opt(1)=pi;  Q_opt(2)=0;
end
Ene_msw=E_msw(Q_opt);
end

if(NextNext==1)
%Energy minimization with di erent initial values
    opt = optimset('Display','o ');
  E_msw_qy0=@(x)E_msw([x 0]);
  [A(1) B(1)]=fmincon(E_msw_qy0,Q_msw_before(1),[],[],[],[],0,2*pi
+0.01,[],opt);
  [A(2) B(2)]=fmincon(E_msw_qy0,[4/3*pi],[],[],[],[],[0],[2*pi+0.01],
[],opt);
  [A(3) B(3)]=fmincon(E_msw_qy0,[2*pi],[],[],[],[],[0],[2*pi+0.01],
[],opt);
  [a b]=min(B); %absolut minimum
   Q_opt(1)=A(b);
   Q_opt(2)=0;
   Ene_msw=B(b);
```

```matlab
end

 Q_msw_before=Q_opt(:);    %Values used in next interaction
 minimization


Q=Q_opt; %Q which minimizes the energy
%%%%%%%%%%%%%%%%%%%
```

A_k B_k with MSWT

```matlab
A_k=@(x,y)0;B_k=@(x,y)0;
for iJ=1:z
cosQ(iJ)=cos(dot(Q,Delta(iJ,:)));
A_k=@(x,y)A_k(x,y)+aniso(iJ)*(lambda-
cosQ(iJ))*Gr(iJ)*cos(x*Delta(iJ,1)+y*Delta(iJ,2));
B_k=@(x,y)B_k(x,y)+aniso(iJ)*((lambda-cosQ(iJ))*Gr(iJ)-(lambda
+cosQ(iJ))*Fr(iJ)*(1-cos(x*Delta(iJ,1)+y*Delta(iJ,2))));
end
Ak=A_k;
Bk=B_k;
%New values for next iteration
 omega=@(x,y)sqrt(B_k(x,y).^2-A_k(x,y).^2);
 cos2theta=@(x,y)sqrt(B_k(x,y).^2./(B_k(x,y).^2-A_k(x,y).^2));
 sin2theta=@(x,y)+A_k(x,y)./B_k(x,y).*cos2theta(x,y);

%Outputs at every iteration (Energy Magnetization Qx Qy)
  output_iteration(it2,iteration,1)=Mzero;
  output_iteration(it2,iteration,2)=Ene_msw;
  output_iteration(it2,iteration,3:4)=Q_opt;

 end  %end of the self consistent equations

if(iteration==nitera)
 %   no convergence obtained in  niterations.
      output_MSW(it2,:)=[t2 0 0  0 0 0 3];
end
 if(both_initial~=1) %If both_initial=1 uses both initial conditions
 if(abs(Mzero-Mzero_old)<tolerance) % If convergence reached, skip
 loop.
  break
 end
 end
 %If converged not reached with LSWT initial values, tries it with
 MSWT of
 %the previous iteration (if converged was reached)
 if(it2>1)
 if(previous_msw==2) & starting_value==1 & converged_points(it2-1)==1
 fprintf(1,'Trying now with previous MSWT')
 continue
 end
 end
```

```
 end % end of the loop for the initial values of the self consisten
 equations

end % End of second neighbours loop

end

end %End extra  anisotropy loop

%Saving output
save(out le,'output_MSW','Mzero_lsw','Ecl','Qcl','no_convergence','j2')

end
```

Integral function over NN Brillouin zone

```
function [ result] = integral(fun)
warning('o ','all')
%Hexagon limit of the Brillouin zone
 Hexagon_y=[0 2/sqrt(3) 2/sqrt(3) 0 -2/sqrt(3) -2/sqrt(3) 0]*pi;
Hexagon_x=[4/3,2/3,-2/3,-4/3,-2/3,2/3 4/3]*pi;
% Integration limits
xx=[Hexagon_x(4) Hexagon_x(1) Hexagon_x(2) Hexagon_x(3)];
 yy=[Hexagon_y(4) Hexagon_y(1) Hexagon_y(2) Hexagon_y(3)];
 h = @(x,y) (inpolygon(x, y, xx, yy) .* fun(x,y));
integration = integral2(h, min(xx), max(xx), min(yy), max(yy));
area=4*pi^2/sqrt(3); % Area half hexagon
result=integration/(2*area); %factor 2 from the equations of MSWT
end
```

Integral function over NNN Brillouin zone

```
function [ result] = integral_second(fun)
warning('o ','all')
%Hexagon
 Hexagon_y=[0 2/sqrt(3) 2/sqrt(3) 0 -2/sqrt(3) -2/sqrt(3) 0]*pi;
Hexagon_x=[4/3,2/3,-2/3,-4/3,-2/3,2/3 4/3]*pi;
% integration limits
xx=[Hexagon_x(4) Hexagon_x(1) Hexagon_x(2) Hexagon_x(3)];
 yy=[Hexagon_y(4) Hexagon_y(1) Hexagon_y(2) Hexagon_y(3)];
 h = @(x,y) (inpolygon(x, y, xx, yy) .* fun(x,y));
integration = integral2(h, min(xx), max(xx), min(yy), max(yy));
area=2*pi^2/sqrt(3);
result=integration/(4*area); %factor 4 from the equations of MSWT
end
```

Published with MATLAB® R2017a

APPENDIX C

Previous articles

A Ph.D. thesis is also an opportunity for a young researcher to summarize his first steps in research in a compact work which will be a valuable memory for a lifetime. It is with this feeling in mind, that I provide in this appendix the two articles I did during my master in Universitat de Barcelona (UB) in collaboration with Artur Polls, Bruno Díaz-Júlia and Miguel Àngel García-March. Both works, which fall outside the scope of the rest of the thesis, are not intended to take part of the Ph.D. defense.

The first article describes a protocol to change the Hamiltonian parameters of a bosonic Josepshon junction, i.e., the tunneling and the on-site interactions, faster than an adiabatic protocol. In intermediate times of our protocol, we may not have the ground state of the system, but at the final time we end up with a state which is really close to the ground state of the system with fidelity ~ 1. Remarkable enough, this protocol provides a speed up in experimental production of spin-squeezed states.

In the second article we study a one-dimensional bosonic system in the limit of a contact interaction of infinite strength. Under such conditions, two bosons cannot simultaneously be at the same position. This feature mimics the effect of Pauli principle in fermionic systems. A 1D system of this "fermionized" bosons is called a Tonks-Girardeau gas and has been well studied for harmonic traps. In this work, we consider a Tonks-Girardeu gas in a double well potential and look into the fermionization process observing, for the first time, the creation of NOON Tonks-Girardeau states.

Shortcut to adiabaticity in internal bosonic Josephson junctions

A. Yuste,[1] B. Juliá-Díaz,[1,2] E. Torrontegui,[3] J. Martorell,[1] J. G. Muga,[3,4] and A. Polls[1]

[1]*Departament d'Estructura i Constituents de la Matèria, Facultat de Física, Universitat de Barcelona, 08028 Barcelona, Spain*
[2]*ICFO-Institut de Ciències Fotòniques, Parc Mediterrani de la Tecnologia, 08860 Barcelona, Spain*
[3]*Departamento de Química-Física, UPV-EHU, Apartado 644, 48080 Bilbao, Spain*
[4]*Department of Physics, Shanghai University, 200444 Shanghai, People's Republic of China*

We extend a recent method to shortcut the adiabatic following to internal bosonic Josephson junctions in which the control parameter is the linear coupling between the modes. The approach is based on the mapping between the two-site Bose-Hubbard Hamiltonian and a one-dimensional effective Schrödinger-like equation, valid in the large-N (number of particles) limit. Our method can be readily implemented in current internal bosonic Josephson junctions and it substantially improves the production of spin squeezing with respect to the usually employed linear rampings.

I. INTRODUCTION

Practical applications of quantum technologies will require the controlled production of many-body correlated quantum states, in particular ground states. It is thus desirable to find efficient mechanisms for their fast production. Bosonic Josephson junctions (BJJs) are among the simplest systems whose ground states already contain many-body correlations beyond the mean field. Schematically, BJJs are ultracold bosonic vapors in which, to a good approximation, the atoms populate only two mutually interacting single-particle levels. Recently, BJJs have been studied experimentally by several groups [1–7]. Current nomenclature calls external Josephson junctions those in which the two levels are spatially separated, usually by means of a potential barrier [1,4,7,8]. In internal Josephson junctions, instead, the two levels are internal to the same atom [5]. The two-site Bose-Hubbard Hamiltonian provides a suitable theoretical description of both internal and external junctions [8–11]. A notable feature of this simple Hamiltonian is that, within subspaces of fixed number of particles, it can be mapped into an SU(2) spin model. This makes these systems suitable to study very squeezed spin states [12,13], as proven experimentally in Refs. [2,4].

In previous work [14], we described how a method to shortcut the adiabatic following in elementary quantum-mechanical systems could be applied to produce spin-squeezed states in BJJs. In particular, we adapted a simple method developed for harmonic oscillators in which the frequency could be varied in time [15,16]. In [14], we described the most straightforward application, where the interatomic interaction strength was the control parameter. This is nowadays a parameter that can be varied experimentally, but it is difficult to control with good accuracy on the time scales considered. To overcome this problem, here we will extend the earlier protocol by varying instead the linear coupling between the states (atomic levels) in internal junctions.[1] This variation can be done with fantastic accuracy [5,17,18], so we shall focus on this case.

The protocols to shortcut adiabatic evolution are generally designed to drive, in a finite time, a system from some initial state to a final state that could be reached adiabatically. An important advantage of these protocols is that they can, in addition, aim to control other properties during the evolution, e.g., reducing transient energy excitation, noise sensitivity, or optimizing other quantities of interest [19–21]. In addition, formulas to achieve shortcuts to adiabatic following are analytic for harmonic-oscillator Hamiltonians [15]. From the experimental point of view, the methods are capable of producing a stationary eigenstate of the Hamiltonian at the final time, making it unnecessary to stop or freeze the dynamics.

The paper is organized as follows. First, in Sec. II, we describe the theoretical framework. Next, in Sec. III, we present our numerical results, including a specific subsection with parameter values within reach with current experiments. Finally, in Sec. IV, we summarize the results and provide some concluding remarks.

II. THEORETICAL FRAMEWORK

The dynamics of a BJJ can be well described by a quantized two-mode model [8,10,11], the Bose-Hubbard Hamiltonian $H = \hbar \mathcal{H}_{\mathrm{BH}}$,

$$\mathcal{H}_{\mathrm{BH}} = -2J\hat{J}_x + U\hat{J}_z^2 , \tag{1}$$

where the pseudoangular momentum operator $\hat{\mathbf{J}} \equiv \{\hat{J}_x, \hat{J}_y, \hat{J}_z\}$ is defined as

$$\begin{aligned}
\hat{J}_x &= \tfrac{1}{2}(\hat{a}_1^\dagger \hat{a}_2 + \hat{a}_2^\dagger \hat{a}_1), \\
\hat{J}_y &= \tfrac{1}{2i}(\hat{a}_1^\dagger \hat{a}_2 - \hat{a}_2^\dagger \hat{a}_1), \\
\hat{J}_z &= \tfrac{1}{2}(\hat{a}_1^\dagger \hat{a}_1 - \hat{a}_2^\dagger \hat{a}_2),
\end{aligned} \tag{2}$$

and $\hat{a}_j^\dagger$ ($\hat{a}_j$) creates (annihilates) a boson at site j. For bosons, $[\hat{a}_i, \hat{a}_j^\dagger] = \delta_{i,j}$. J is the hopping strength and U is the nonlinear coupling strength proportional to the atom-atom s-wave scattering length. In internal BJJs, U is proportional to $a_{1,1} + a_{2,2} - 2a_{1,2}$, with $a_{1,1}$ and $a_{2,2}$ the intraspecies scattering lengths and $a_{1,2}$ the interspecies one [5]. In this

---

[1]In external junctions, this can be done by increasing the barrier height between the two wells.

work, we consider repulsive interactions, $U > 0$. For internal BJJs, the interspecies s-wave scattering length in ^{87}Rb atoms can be varied by applying an external magnetic field, thanks to a well-characterized Feshbach resonance at $B = 9.1$ G, as done in Ref. [5] for the setup that we are considering. In this work, instead, we assume a time-dependent hopping strength $J(t)$, keeping U and N fixed during the time evolution, which should be simpler and more accurate from an experimental point of view.

The time-dependent Schrödinger equation (TDSE) is written as

$$i\partial_t |\Psi\rangle = \mathcal{H}_{\mathrm{BH}} |\Psi\rangle. \tag{3}$$

For a given N, an appropriate many-body basis is the Fock basis, $\{|m_z = (N_1 - N_2)/2\rangle\}$, with $m_z = -N/2, \ldots, N/2$. A general many-body state $|\Psi\rangle$ can then be written as

$$|\Psi\rangle = \sum_{m_z=-N/2}^{N/2} c_{m_z} |m_z\rangle. \tag{4}$$

It is useful to define the population imbalance of the state as $z \equiv m_z/(N/2)$.

For a given state, the Kitagawa-Ueda spin-squeezing parameter [13], termed also the number-squeezing parameter [2], is defined as $\xi_N^2(t) = \Delta \hat{J}_z^2/(\Delta \hat{J}_z^2)_{\mathrm{ref}}$, where $\Delta \hat{J}_z^2 \equiv \langle \hat{J}_z^2 \rangle - \langle \hat{J}_z \rangle^2$ and $(\Delta \hat{J}_z^2)_{\mathrm{ref}} = N/4$ is the value for a coherent state with $\langle \hat{J}_y \rangle = \langle \hat{J}_z \rangle = 0$. The many-body state is said to be number squeezed when $\xi_N < 1$ [13]. The Wineland spin-squeezing parameter [12], also referred to as the coherent spin-squeezing parameter [3], is defined as [12,22] $\xi_S^2 = N(\Delta \hat{J}_z^2)/\langle \hat{J}_x \rangle^2 = \xi_N^2/\alpha^2$, where the phase coherence of the many-body state is $\alpha(t) = \langle \Psi(t)|2\hat{J}_x/N|\Psi(t)\rangle$. ξ_S takes into account the delicate compromise between improvements in number squeezing and loss of coherence. States with $\xi_S < 1$ have been proposed to be the basis of a new Ramsey-type atom interferometer with increased phase precision (compared to that of the coherent spin states). This gain in precision can be directly related to entanglement in the system [22].

Since we take J as the control parameter, we slightly detour from the derivation in Refs. [23–25]. Following similar steps as described in those references, one can obtain, in the semiclassical $\eta \equiv 1/N \ll 1$ limit, a Schrödinger-like equation,

$$i\eta\partial_t \psi(z,t) = \mathcal{H}_N \psi(z,t), \tag{5}$$

for the continuous extrapolation of z, where

$$\mathcal{H}_N(z)\psi(z) \equiv -2\eta^2 J \partial_z \sqrt{1-z^2} \partial_z \psi(z) + \mathcal{V}(z)\psi(z), \tag{6}$$

$\mathcal{H}_N \equiv \eta \mathcal{H}_{\mathrm{BH}}$, and $\mathcal{V}(z) = -J\sqrt{1-z^2} + (1/2)(NU/2)z^2$. Here, $\psi(z) = \sqrt{N/2}\, c_{m_z}$ is normalized as $\int_{-1}^{1} dz |\psi(z)|^2 = 1$.

For repulsive atom-atom interactions, the potential in Fock space, $\mathcal{V}(z)$, is, to a very good approximation, a harmonic oscillator. Neglecting the z dependence of the effective mass term, and expanding $\sqrt{1-z^2} \simeq 1 - z^2/2$ in $\mathcal{V}(z)$, the Hamiltonian in Eq. (6) reduces to [24,25]

$$\mathcal{H}_N \simeq -2J\eta^2 \partial_z^2 + \frac{1}{2}(J + NU/2)z^2, \tag{7}$$

an approximation which we have previously used [24,25] and numerically verified. A difference with respect to Ref. [14]

and to previous applications of shortcuts-to-adiabaticity to harmonic-oscillator expansions is that now the control parameter $J(t)$ shows up both as a formal time-dependent (inverse of) mass and as an additive term in the force constant. In Appendix A, we provide the extension of the shortcut technique for this type of time dependence when $NU/2 \gg |J|$, so that we can approximate $(J + NU/2) \simeq NU/2$. Defining $\gamma = NU/(2J)$, this limit corresponds to $\gamma \gg 1$, which is easily attainable in current experiments. It is also relevant as it corresponds to very spin-squeezed ground states of the bosonic Josephson junction. In Appendix B, we verify that the method is not applicable when $|\gamma| < 1$.

For the case at hand, the inverse engineering described in Appendix A translates into solving for $J(t)$ in the following Ermakov equation:

$$\ddot{b} - 2\frac{(\dot{b})^2}{b} = \frac{4k}{J(t)}b - \frac{k^2}{\eta^2}b^5, \tag{8}$$

where the dots indicate time derivatives, and $k = NU/2$ and $b(t)$ must satisfy the boundary conditions

$$b_i \equiv b(0) = \left[\frac{8\eta^2 J(0)}{NU}\right]^{1/4}, \tag{9}$$

$$b_f \equiv b(t_f) = \left[\frac{8\eta^2 J(t_f)}{NU}\right]^{1/4},$$

$$\dot{b}(0) = \ddot{b}(0) = \dot{b}(t_f) = \ddot{b}(t_f) = 0. \tag{10}$$

For simplicity, we apply the polynomial [15]

$$b_{\mathrm{poly}}(t) = b_i + 10(b_f - b_i)s^3 - 15(b_f - b_i)s^4 + 6(b_f - b_i)s^5, \tag{11}$$

with $s = t/t_f$. We also consider a nonpolynomial form in some comparisons,

$$b_{\mathrm{nonpoly}}(t) = b_i \left(\frac{b_f}{b_i}\right)^{6s^5 - 15s^4 + 10s^3}. \tag{12}$$

III. NUMERICAL SIMULATIONS OF THE SHORTCUT PROTOCOL

In all cases, we will consider the evolution from an initial ground state corresponding to $\gamma = \gamma_i$ to a final one with $\gamma = \gamma_f$. The control parameter $J(t)$ will go from $J(0) = J_i$ to $J(t_f) = J_f$ in a time t_f with a fixed value of U. In our first application, we will measure the time in units of the initial Rabi time, $t_{\mathrm{Rabi}}^{(i)} = \pi/J_i$. Later, we will consider realistic values of U and t taken from recent experiments. Let us emphasize that the large-N limit discussed in the previous section leading to the harmonic-oscillator approximation is used to design the protocol. In what follows, all results are obtained by directly solving the original many-body problem, given by Eq. (3), using the function $J(t)$ given by the shortcut protocol as detailed above.

In Fig. 1, we consider a factor 2 change in γ, from $\gamma_i = 10$ to $\gamma_f = 20$ in a time $t_f = 0.08 t_{\mathrm{Rabi}}^{(i)}$, with $N = 100$ and $NU/2 = 1/t_{\mathrm{Rabi}}^{(i)}$. We compare the shortcut protocol using the polynomial ansatz for $b(t)$ to a linear ramping: $J(t) = J_i + (J_f - J_i)(t/t_f)$. The shortcut method is shown to work almost perfectly, and we obtain a final fidelity $\simeq 1$ (despite the process
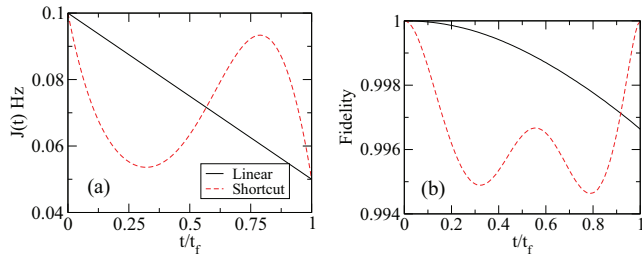
FIG. 1. (Color online) (a) $J(t)$ used in the shortcut protocol compared to the corresponding linear ramping. The initial and final values of γ are $\gamma_i = 10$, $\gamma_f = 20$, and $t_f = 0.08 t_{\text{Rabi}}^{(i)}$. (b) The fidelity (overlap) between the evolved state and the instantaneous ground state. The number of particles and nonlinearity are $N = 100$ and $U = 1/(50 t_{\text{Rabi}}^{(i)})$, respectively.

being diabatic during the intermediate evolution). For this case, the linear ramping produces a final fidelity of $\simeq 0.9965$. As it occurred with the harmonic oscillator [15] or in Ref. [14], for more stringent processes, i.e., shorter final times or larger changes in γ, the method requires negative values of the control parameter. For instance, if we require a factor of 10 change, from $\gamma_i = 10$ to $\gamma_f = 100$ under the same conditions, then $J(t)$ becomes negative during part of the evolution. Although for usual tunneling phenomena the hopping term is always positive, e.g., in external Josephson junctions, there are several proposals to implement negative or even complex hopping terms in optical lattices [26,27]. For the internal Josephson junctions achieved in Oberthaler's group, negative tunneling presents no obstacle as they are able to engineer a tunneling term of the form (see Sec. 3.5 of Ref. [17])

$$J(t)[\hat{J}_x \cos \phi_c(t) + \hat{J}_y \sin \phi_c(t)], \qquad (13)$$

with $\phi_c(t)$ a phase which can be controlled externally.

Our results are shown in Fig. 2. First we see that for both polynomial and nonpolynomial choices of $b(t)$ described above, J changes its sign at intermediate times; see Fig. 2(a). This implies a transient loss of fidelity (overlap) between the evolved state and the instantaneous ground state of the system, as shown in Fig. 2(d). With the shortcut protocol, both the coherence [Fig. 2(b)] and number squeezing [Fig. 2(c)] evolve smoothly towards their adiabatic value. In contrast, the linear ramping fails to provide the adiabatic values at the final time. The instantaneous ground-state coherence [dotted red line in Fig. 2(b)] is rather involved as it follows the $J(t)$ path. As seen in Fig. 2(c), the linear squeezing is $\simeq -6$ dB, while the adiabatic one, accurately reproduced by the shortcut protocol, is $\simeq -10$ dB. This is a notable feature which should be experimentally accessible. The linear ramp gives a final fidelity of 0.95, well below those of the polynomial and nonpolynomial shortcut protocols which get final fidelities of nearly 1. It is also worth stressing that the many-body state produced by the shortcut method at $t = t_f$ is almost an eigenstate of the system, which implies constant coherence and squeezing for $t > t_f$; see Figs. 2(b) and 2(c).

It is also possible to engineer fidelity-one processes where the control $J(t)$ is constrained from below and above by predetermined values (in particular, we could make both bounds positive). Prominent examples are the bang-bang protocols,
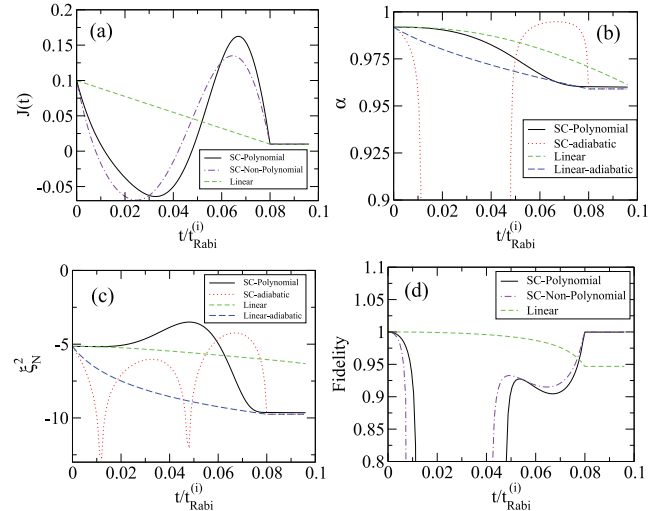

FIG. 2. (Color online) (a) Evolution of $J(t)$, (b) coherence of the state, (c) its number squeezing, and (d) the instantaneous fidelity. $N = 100$ atoms, $\gamma_i = 10$, $\gamma_f = 100$, and $t_f = 0.08 t_{\text{Rabi}}^{(i)}$. For $t > t_f$, we fix $\gamma(t) = \gamma(t_f)$.

with stepwise constant J, which solve the time-minimization variational problem for given bounds and boundary conditions [16,19,28,29].

A. Simulations using experimental values for the parameters

As explained above, the variation of J with time can be readily implemented experimentally. In this section, we will consider realistic values of the parameters. Following Refs. [4,17], we take a value of the nonlinearity $U = 0.49$ Hz, with $N = 100$ atoms, and make variations of γ during typical experimental values of time: $t_f = 10, 15, 30, 50,$ and 100 ms. At $t = t_f$, we fix $\gamma(t) = \gamma_f$ and evolve the system during an additional small time to check whether or not the state remains close to the desired final ground state.

In Fig. 3, we depict the final value of the fidelity [Fig. 3(c)], number squeezing [Fig. 3(b)], and coherence of the many-body state [Fig. 3(a)] as a function of the final time imposed t_f. The shortcut method (with polynomial ansatz) is compared to the linear ramping. The first observation is that for $t_f > 40$ ms, the shortcut protocol produces a fidelity $\simeq 1$, while the linear ramp stays always below 0.95; see Fig. 3(c). Similarly, for $t_f > 40$ ms, the final coherence and number squeezing are essentially those of the corresponding ground state [Figs. 3(a) and 3(b)]. This is an important finding, as for instance the linear ramping produces roughly half of the number squeezing as compared to the adiabatic or shortcut protocol. For $t_f < 40$ ms, the shortcut protocol is seen to fail and, in particular, the achieved final fidelities drop to 0.7 for $t_f = 10$ ms, which is smaller than the linear ramping ones. As explained above, our shortcut protocol has been derived assuming the validity of a parabolic approximation for the potential in Fock space. Therefore, we expect the method to fail when the intermediate wave packet spreads far from the central region in Fock space. In Fig. 4, we have plotted the spectral decomposition of the
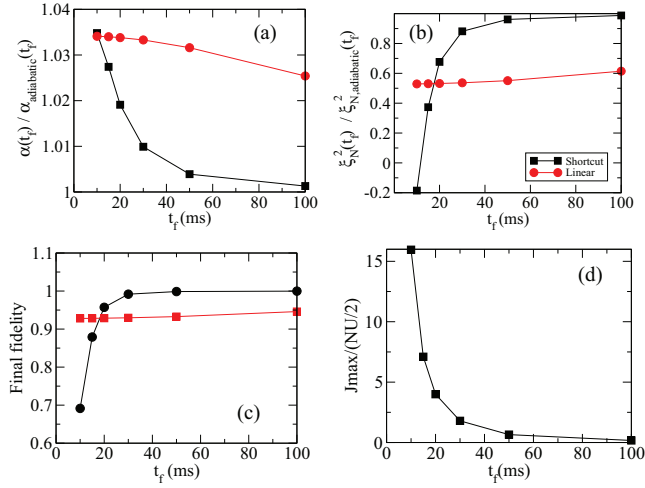
FIG. 3. (Color online) Properties of the state of the system at t_f after a shortcut protocol (black) and a linear ramp (red), for different values of t_f. (a) The relative coherence, $\alpha/\alpha_{\text{adiabatic}}$. (b) The relative number squeezing, $\xi_N^2/\xi_{N,\text{adiabatic}}^2$. (c) The value of the final fidelity. (d) The maximum value of $1/\gamma$ required for the shortcut process. In all simulations, $\gamma_i = 10$, $\gamma_f = 100$, $N = 100$, and $U = 0.49$ Hz.

many-body state $|c_z|^2$ as a function of time for the same final times t_f as above. When the final time is large, the process is smooth and the wave function does not spread considerably. When we use shorter final times, $J(t)$ takes large values (so γ is small at intermediate times) and the effective wave function spreads considerably in z space. A parameter that affects the $J(t)$ functional form is the number of atoms N. The larger N, the smoother the $J(t)$ path and the better are the results obtained. This is seen in Fig. 5, where we choose only two values of t_f, i.e., 10 and 20 ms, and consider $N = 50, 100, 150$, and 400 atoms. We also depict $J(t)$, which is on average smaller for larger N.
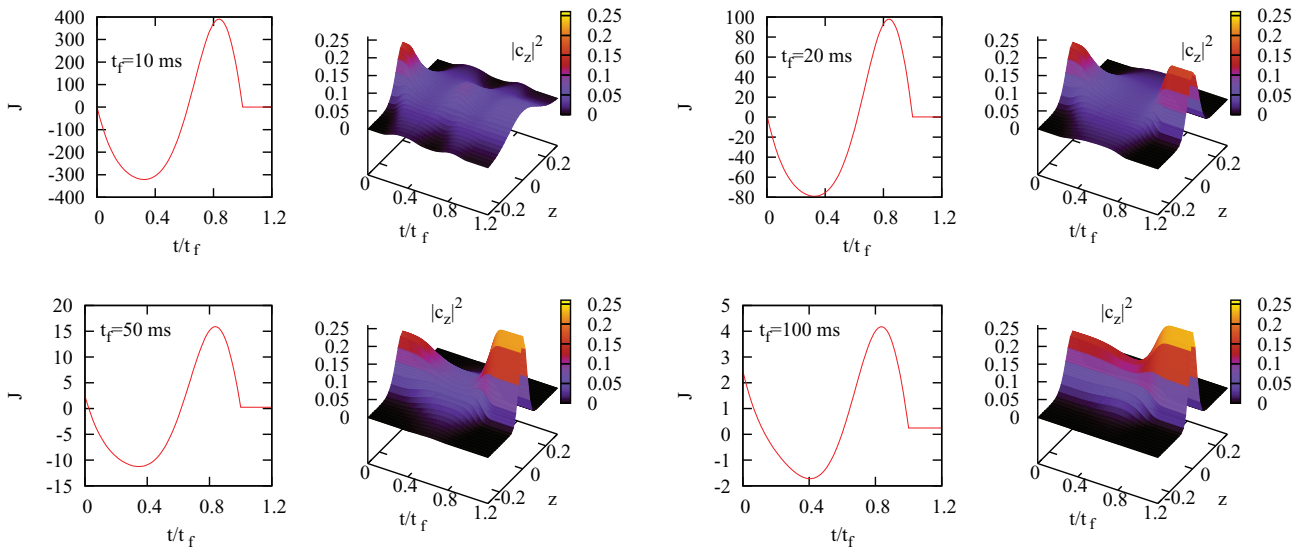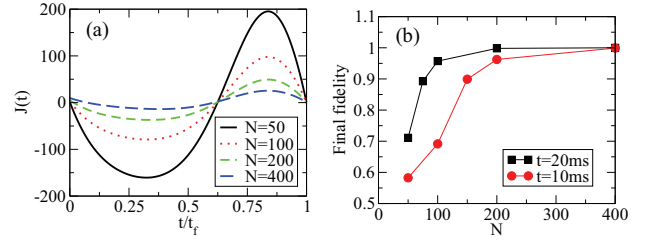

FIG. 5. (Color online) (a) Evolution of $J(t)$ required by the polynomial shortcut protocol for different values of N and $t_f = 20$ ms. (b) The final fidelities attained in the process for $t_f = 10$ and 20 ms. $U = 0.49$ Hz and $\gamma_i = 10$, $\gamma_f = 100$.

IV. SUMMARY AND CONCLUSIONS

We have presented a method to produce ground states of bosonic Josephson junctions for repulsive atom-atom interactions using protocols to shortcut the adiabatic following. We inverse engineer the accurately controllable linear coupling J by mapping a Schrödinger-like equation for the (imbalance) wave function of the Josephson junction onto an ordinary harmonic oscillator for which shortcut protocols can be set easily. The original equation is *a priori* more involved for that end, as the kineticlike term includes a time-dependent formal mass. As detailed in Appendix A, the mapping requires a reinterpretation of kinetic and potential terms, which interchange their roles in a representation conjugate to the imbalance. The time dependence of the formal mass of the original equation (inversely proportional to J) implies the time dependence of the frequency of the ordinary (constant mass) harmonic oscillator, and J plays finally the role of the squared frequency. This mapping is different and should be distinguished from the ones used to treat harmonic systems with a time-dependent mass both in the kinetic and the potential terms [30]. From the experimental point of view, our protocol should help the production of spin-squeezed states,

FIG. 4. (Color online) Left: Evolution of $J(t)$ required by the polynomial shortcut protocol for different final times $t_f = 10, 20, 50, 100$ ms. Right: Spectral decomposition of the many-body state $|c_z|^2$ for the same t_f as a function of time. In all simulations, $\gamma_i = 10$, $\gamma_f = 100$, $N = 100$, and $U = 0.49$ Hz.

increasing the maximum squeezing attainable in short times. In particular, an important shortcoming of recent experimental setups [17] is that they have sizable particle loss on time scales of the order of $\simeq 50$ ms for atom numbers on the order of a few hundred. For these systems, our methods could be targeted at shorter times, as in the examples presented, providing an important improvement with respect to linear rampings.

APPENDIX A: SHORTCUT EQUATIONS FOR THE JOSEPHSON JUNCTION WITH CONTROLLABLE LINEAR COUPLING

In this Appendix, we shall transform the Schrödinger-like Eq. (5) so that the invariant-based engineering technique for time-dependent harmonic oscillators developed in [15,16] may be applied. The structure of the Hamiltonian (7) is peculiar as it involves a time-dependent (formal) mass factor in the kineticlike term. The first step is to transform this Hamiltonian according to

$$\eta \to \hbar, \quad 4J(t) \to \frac{1}{m(t)}, \quad \frac{NU}{2} \to k, \qquad \text{(A1)}$$

to rewrite Eq. (7) as

$$H = \frac{1}{2m(t)}p^2 + \frac{1}{2}kz^2, \qquad \text{(A2)}$$

where $p = -i\hbar\partial_z$ is the "momentum" conjugate to z.[2] These and other transformations performed below are formal so that the dimensions do not necessarily correspond to the ones suggested by the symbols and terminology used. For example, neither p, $m(t)$, nor z have dimensions of momentum, mass, and length, respectively.

Multiplying the time-dependent Schrödinger equation corresponding to Eq. (A2) from the left by momentum eigenstates $\langle p|$, we get

$$i\hbar\partial_t\Psi(p,t) = -\frac{\hbar^2 k}{2}\frac{\partial^2}{\partial p^2}\Psi(p,t) + \frac{p^2}{2m(t)}\Psi(p,t). \quad \text{(A3)}$$

Finally, with the new mapping,

$$k \to \frac{1}{m_x},$$
$$\frac{1}{m(t)} \to m_x\omega_x^2(t), \qquad \text{(A4)}$$
$$p \to x,$$

---

[2]We shall use the symbol p also for the momentum eigenvalues since the context makes its meaning clear.

the Hamiltonian takes the standard time-dependent harmonic oscillator form

$$H = -\frac{\hbar^2}{2m_x}\frac{\partial^2}{\partial x^2} + \frac{1}{2}m_x\omega_x^2(t)x^2. \qquad \text{(A5)}$$

Note that thanks to the above transformations and basis change, the kineticlike and potential-like terms in the Hamiltonian (7) have interchanged their roles so that the time dependence of the formal mass has become a time dependence of the formal frequency in Eq. (A5), whereas m_x is constant. Fast dynamics between $t = 0$ and t_f, from $\omega_x(0)$ to $\omega_x(t_f)$ without final excitations for this Hamiltonian may be inverse engineered by solving for $\omega_x(t)$ in the Ermakov equation [15,16],

$$\ddot{\rho} + \omega_x^2(t)\rho = \frac{\omega_0^2}{\rho^3}, \qquad \text{(A6)}$$

where ω_0 is, in principle, an arbitrary constant, and $\rho(t)$ is a scale factor for the state that we may design, e.g., with a polynomial, so that it satisfies the boundary conditions

$$\rho(0) = \left(\frac{\omega_0}{\omega_x(0)}\right)^{1/2}, \quad \rho(t_f) = \left(\frac{\omega_0}{\omega_x(t_f)}\right)^{1/2},$$
$$\dot{\rho}(0) = \dot{\rho}(t_f) = \ddot{\rho}(0) = \ddot{\rho}(t_f) = 0. \qquad \text{(A7)}$$

Defining $b = \hbar/\rho$, choosing $\omega_0 = k\hbar$, and undoing the changes (A4) and (A1), we rewrite the Ermakov equation as Eq. (8) and the boundary conditions become those in Eq. (9).

APPENDIX B: LIMITATIONS OF THE METHOD

As explained in the main text, to perform the mapping between the results in Appendix A and the Bose-Hubbard Hamiltonian, we have assumed $NU/2 \gg J$ ($\gamma \gg 1$). Thus our mapping should not be valid for small values of γ. Figure 6 demonstrates that this is indeed the case. It shows the fidelity of the shortcut protocol for $\gamma_i = 0.1$ and $\gamma_f = 1$ when $t_f = t_{\text{Rabi}}^{(i)}$. In this special case, one finds a better fidelity with the linear ramping than with the shortcut path.
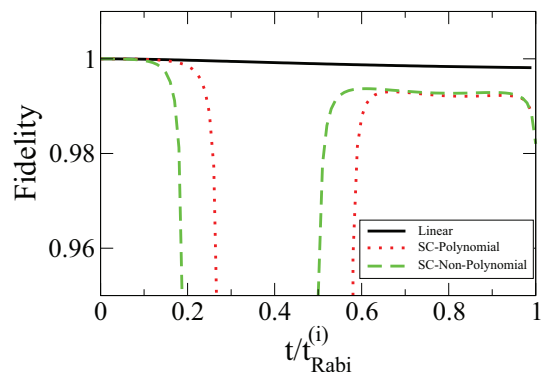

FIG. 6. (Color online) Instantaneous fidelity as a function of time. $\gamma_i = 0.1$ and $\gamma_f = 1$ with $t_f = t_{\text{Rabi}}^{(i)}$ for the shortcut and a linear path.

[1] M. Albiez, R. Gati, J. Fölling, S. Hunsmann, M. Cristiani, and M. K. Oberthaler, Phys. Rev. Lett. **95**, 010402 (2005).

[2] J. Esteve, C. Gross, A. Weller, S. Giovanazzi, and M. K. Oberthaler, Nature (London) **455**, 1216 (2008).

[3] C. Gross, T. Zibold, E. Nicklas, J. Estève, and M. K. Oberthaler, Nature (London) **464**, 1165 (2010).

[4] M. F. Riedel, P. Bohi, Y. Li, T. W. Hansch, A. Sinatra, and P. Treutlein, Nature (London) **464**, 1170 (2010).

[5] T. Zibold, E. Nicklas, C. Gross, and M. K. Oberthaler, Phys. Rev. Lett. **105**, 204101 (2010).

[6] M. Abbarchi, A. Amo, V. G. Sala, D. D. Solnyshkov, H. Flayac, L. Ferrier, I. Sagnes, E. Galopin, A. Lemaître, G. Malpuech, and J. Bloch, Nat. Phys. **9**, 275 (2013).

[7] T. Berrada, S. van Frank, R. Bücker, T. Schumm, J.-F. Schaff, and J. Schmiedmayer, Nat. Commun. **4**, 2077 (2013).

[8] R. Gati and M. K. Oberthaler, J. Phys. B **40**, R61 (2007).

[9] H. J. Lipkin, N. Meshkov, and A. J. Glick, Nucl. Phys. **62**, 188 (1965).

[10] G. J. Milburn, J. Corney, E. M. Wright, and D. F. Walls, Phys. Rev. A **55**, 4318 (1997).

[11] A. J. Leggett, Rev. Mod. Phys. **73**, 307 (2001).

[12] D. J. Wineland, J. J. Bollinger, W. M. Itano, and F. L. Moore, and D. J. Heinzen, Phys. Rev. A **46**, R6797 (1992).

[13] M. Kitagawa and M. Ueda, Phys. Rev. A **47**, 5138 (1993).

[14] B. Julia-Diaz, E. Torrontegui, J. Martorell, J. G. Muga, and A. Polls, Phys. Rev. A **86**, 063623 (2012).

[15] X. Chen, A. Ruschhaupt, S. Schmidt, A. del Campo, D. Guéry-Odelin, and J. G. Muga, Phys. Rev. Lett. **104**, 063002 (2010); A. del Campo, Europhys. Lett. **96**, 60005 (2011); Phys. Rev. A **84**, 031606(R) (2011).

[16] X. Chen and J. G. Muga, Phys. Rev. A **82**, 053403 (2010); X. Chen, E. Torrontegui, and J. G. Muga, *ibid.* **83**, 062116 (2011);

E. Torrontegui, S. Ibañez, X. Chen, A. Ruschhaupt, D. Guéry-Odelin, and J. G. Muga, *ibid.* **83**, 013415 (2011).

[17] T. Zibold, Ph.D. thesis, University of Heidelberg, 2012.

[18] E. Nicklas, Ph.D. thesis, University of Heidelberg, 2013.

[19] X. Chen, E. Torrontegui, D. Stefanatos, Jr-Shin Li, and J. G. Muga, Phys. Rev. A **84**, 043415 (2011); E. Torrontegui, X. Chen, M. Modugno, S. Schmidt, A. Ruschhaupt, and J. G. Muga, New J. Phys. **14**, 013031 (2012).

[20] A. Ruschhaupt, X. Chen, D. Alonso, and J. G. Muga, New J. Phys. **14**, 093040 (2012).

[21] X.-J. Lu, X. Chen, A. Ruschhaupt, D. Alonso, S. Guérin, and J. G. Muga, Phys. Rev. A **88**, 033406 (2013).

[22] A. Sørensen, L.-M. Duan, I. Cirac, and P. Zoller, Nature (London) **409**, 603 (2001).

[23] V. S. Shchesnovich and M. Trippenbach, Phys. Rev. A **78**, 023611 (2008).

[24] B. Juliá-Díaz, J. Martorell, and A. Polls, Phys. Rev. A **81**, 063625 (2010).

[25] B. Juliá-Díaz, T. Zibold, M. K. Oberthaler, M. Melé-Messeguer, J. Martorell, and A. Polls, Phys. Rev. A **86**, 023615 (2012).

[26] D. Jaksch and P. Zoller, New J. Phys. **5**, 56 (2003).

[27] A. Eckardt, C. Weiss, and M. Holthaus, Phys. Rev. Lett. **95**, 260404 (2005).

[28] P. Salamon, K. H. Hoffmann, Y. Rezek, and R. Kosloff, Phys. Chem. Chem. Phys. **11**, 1027 (2009).

[29] D. Stefanatos, J. Ruths, and Jr-Shin Li, Phys. Rev. A **82**, 063422 (2010).

[30] I. A. Pedrosa, J. Math. Phys. **28**, 2662 (1987); C. M. A. Dantas, I. A. Pedrosa, and B. Baseia, Phys. Rev. A **45**, 1320 (1992); I. A. Pedrosa, G. P. Serra, and I. Guedes, *ibid.* **56**, 4300 (1997).

Mesoscopic superpositions of Tonks-Girardeau states and the Bose-Fermi mapping

M. A. García-March,[1,2] A. Yuste,[1,3] B. Juliá-Díaz,[1,2] and A. Polls[1]

[1]*Departament d'Estructura i Constituents de la Matèria, Universitat de Barcelona, 08028 Barcelona, Spain*

[2]*ICFO–Institut de Ciències Fotòniques, Parc Mediterrani de la Tecnologia, 08860 Barcelona, Spain*

[3]*Física Teòrica: Informació i Fenòmens Quàntics, Departament de Física, Universitat Autònoma de Barcelona,*
08193 Bellaterra (Barcelona), Spain

We study a one-dimensional gas of repulsively interacting ultracold bosons trapped in a double-well potential as the atom-atom interactions are tuned from zero to infinity. We concentrate on the properties of the excited states which evolve from the so-called NOON states to the NOON Tonks-Girardeau states. The relation between the latter and the Bose-Fermi mapping limit is explored. We state under which conditions NOON Tonks-Girardeau states, which are not predicted by the Bose-Fermi mapping, will appear in the spectrum.

I. INTRODUCTION

The ground state of an ultracold bosonic gas confined in one dimension in which the atoms interact through a contact potential of infinite strength is known to be the so-called Tonks-Girardeau (TG) gas [1,2]. More generally, in this regime, the Bose-Fermi (BF) mapping theorem allows one to build bosonic wave functions from symmetrized versions of the free-fermion ones, establishing a deep connection between the infinite contact strength and the Pauli principle [3]. This fermionization mechanism takes place for any number of atoms in both trapped and untrapped systems, the only difference being the single-particle wave functions needed to build the free fermionic states prior to symmetrization [4]. Interestingly, for a finite number of trapped atoms one can reach strongly correlated states of the TG type for finite, albeit large, interaction strengths [5–8]. Two experimental groups have confirmed the latter, producing TG gases of $\simeq 50$ [9] and 15 [10] ultracold atoms, respectively, and many more are expected to explore the strong interacting limit following the ground-breaking experiments with few trapped atoms [11–18].

Simultaneously, double-well experiments with ultracold bosons [19,20] have already produced correlated many-body states [21] and should sooner rather than later allow one to produce macroscopic superpositions [22,23]. So combining the two may allow one to produce macroscopic superpositions of strongly interacting TG gases. In this article we settle under which conditions the superpositions in the Fock regime, so-called NOON (Schrödinger-cat-like) states [24–27], evolve into superpositions of TG gases, denoted NOON TG, as the interactions are tuned from small to infinity.

This article is organized as follows. First, in Sec. II we present the model Hamiltonian and revise the case of spinless fermions. Then, in Sec. III we concentrate on the case of bosons trapped in the double well, going from the small to large interactions and discussing the effect of a finite range of the atom-atom interaction. Finally, in Sec. IV we discuss further implications and give an outlook for our article.

II. MODEL HAMILTONIAN

Let us consider N atoms trapped in a one-dimensional double-well potential, described by the first-quantized

Hamiltonian $\hat{H} = \sum_{j=1}^{N} [-(1/2)\partial_{z_j}^2 + V_{\mathrm{DW}}(z_j)] + V_{\mathrm{int}}$, with contact interactions $V_{\mathrm{int}} = g \sum_{i<j} \delta(z_i - z_j)$, where $\hbar = m = 1$. We model the double well with a Duffing potential, $V_{\mathrm{DW}}(z) = V_0[-8(z/V_0)^2 + 16(z/V_0)^4 + 1]$, with minima at $z = \pm V_0/2$ and a local maximum at $z = 0$ (thus V_0 is the barrier height and the distance between the wells). Let ϕ_n be the nth eigenstate of the single-particle Hamiltonian $H_{\mathrm{sp}} = (1/2)\partial_{z^2}^2 + V_{\mathrm{DW}}(z)$ with energy ε_n. As V_0 is increased, quasidegeneracies between the single-particle energies are introduced [see Fig. 1(a)].

Spinless fermions

For N spinless fermions, the ground and all excited states Ψ_k^{f} of $\hat{H}$ are the Slater determinants of N single-particle eigenstates ϕ_n. Their eigenenergies are the summation of the energies of the N states ϕ_n used in the corresponding Slater determinant. The states Ψ_k^{f} fulfill the Pauli exclusion principle, i.e., are zero whenever $z_i = z_j$, and therefore do not feel the contact interaction.

For $N = 2$ fermions the ground state is $\Psi_0^{\mathrm{f}}(z_1,z_2) = 1/\sqrt{2}\, \mathrm{Slater}(\phi_0,\phi_1) = 1/\sqrt{2}[\phi_0(z_1)\phi_1(z_2) - \phi_1(z_1)\phi_0(z_2)]$ and has energy $E_0 = \varepsilon_0 + \varepsilon_1$ for all V_0. For large V_0, the first two single-particle states are quasidegenerate, $\varepsilon_1 = \varepsilon_0 + \varepsilon_{01}$, with $\varepsilon_{01} \ll \varepsilon_0$. The next four excited states are $\Psi_1^{\mathrm{f}} \sim \mathrm{Slater}(\phi_0,\phi_2)$, $\Psi_2^{\mathrm{f}} \sim \mathrm{Slater}(\phi_1,\phi_2)$, $\Psi_3^{\mathrm{f}} \sim \mathrm{Slater}(\phi_0,\phi_3)$, and $\Psi_4^{\mathrm{f}} \sim \mathrm{Slater}(\phi_1,\phi_3)$. For $V_0 \gtrsim 4.5$, the second and third single-particle states are also quasidegenerate (see Fig. 1), and then $\varepsilon_3 = \varepsilon_2 + \varepsilon_{23}$, with $\varepsilon_{23} \ll \varepsilon_2$. Thus, for $V_0 \gtrsim 4.5$ the first four excited states are quasidegenerate and have energies $E_1 = \varepsilon_0 + \varepsilon_2$, $E_2 = E_1 + \varepsilon_{01}$, $E_3 = E_1 + \varepsilon_{23}$, and $E_4 = E_1 + \varepsilon_{01} + \varepsilon_{23}$. For two atoms, the next excited state has a finite energy gap with this manifold (see gap between ε_3 and ε_4 for large V_0 in Fig. 1).

Let us define the following single-particle wave functions:

$$\phi_n^j = \begin{cases} \phi_n^L = \frac{1}{\sqrt{2}}(\phi_{2n} + \phi_{2n+1}), \\ \phi_n^R = \frac{1}{\sqrt{2}}(\phi_{2n} - \phi_{2n+1}), \quad n = 0,1,\ldots. \end{cases} \quad (1)$$

Here $j = L$ (R) stands for left (right). These ϕ_n^j functions are mostly localized either in the left or right well when the
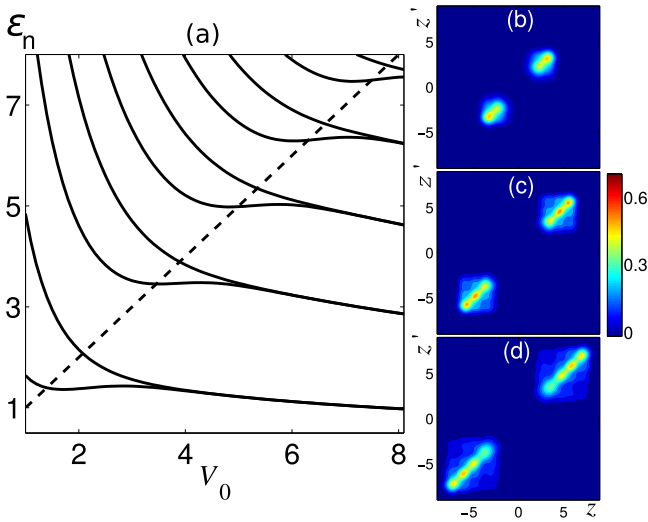
FIG. 1. (Color online) (a) The first ten eigenvalues of the single-particle Hamiltonian as a function of V_0. The dashed line represents the condition $E = V_0$. (b)–(d) One-body density matrix for NOON Tonks-Girardeau states of $N = 2, 3$, and 4 obtained with $g = 20$ and $V_0 = 6, 10$, and 12, respectively.

pair of delocalized functions ϕ_n used to construct them is quasidegenerate.

III. INTERACTING BOSONS IN A DOUBLE WELL

Using the single-particle eigenfunctions to build the Fock basis, the many-body Hamiltonian for bosons reads

$$\hat{\mathcal{H}} = \sum_{i=1}^{M} \varepsilon_i \hat{a}_i^\dagger \hat{a}_i + \frac{g}{2} \sum_{k,l,m,n}^{M} I_{k,l,m,n} \hat{a}_k^\dagger \hat{a}_l^\dagger \hat{a}_m \hat{a}_n, \quad (2)$$

with $I_{k,l,m,n} = \int dz \phi_k(z) \phi_l(z) \phi_m(z) \phi_n(z)$, where $[\hat{a}_k^\dagger, \hat{a}_i] = \delta_{ik}$ and $[\hat{a}_k^\dagger, \hat{a}_i^\dagger] = [\hat{a}_k, \hat{a}_i] = 0$. A Fock vector is written as $|n_0, n_1, \ldots, n_M\rangle = \mathcal{N}(\hat{a}_0^\dagger)^{n_0}, \ldots, (\hat{a}_M^\dagger)^{n_M} |\text{vac}\rangle$, where $|\text{vac}\rangle$ is the vacuum, n_i is the number of atoms in mode i, and $\mathcal{N}^{-1} = \sqrt{n_0! \cdots n_M!}$.

A. Beyond the Fock regime

For a barrier high enough to have a number of quasidegenerate single-particle doublets, the simplest picture is provided using the *localized* single-particle basis defined in Eq. (1). Using this basis, the Fock vectors can be written as $|n_0^L, n_0^R, n_1^L, n_1^R, \ldots\rangle_{\text{lo}} = \mathcal{N}(a_0^{L\dagger})^{n_0^L}(a_0^{R\dagger})^{n_0^R} \cdots (a_{M/2}^{L\dagger})^{n_{M/2}^L}(a_{M/2}^{R\dagger})^{n_{M/2}^R} |\text{vac}\rangle$, with $\mathcal{N}^{-1} = \sqrt{n_0^R! n_0^L! \cdots n_{M/2}^L! n_{M/2}^R!}$. For small interactions the system remains bimodal, allowing us to explore with a two-mode model from the Josephson to the Fock regimes [28,29]. As interactions are increased, the system approaches the strongly correlated regime [5–7]. Let us explore in detail this transition, using as driving examples the $N = 2$ and $N = 3$ cases.

For instance, when $N = 2$ and for interactions larger than the first gap, the ground state is well approximated by $|1,1,0,\ldots\rangle_{\text{lo}}$. This state has one atom in each well and is thus unaffected by the interaction. Its energy remains
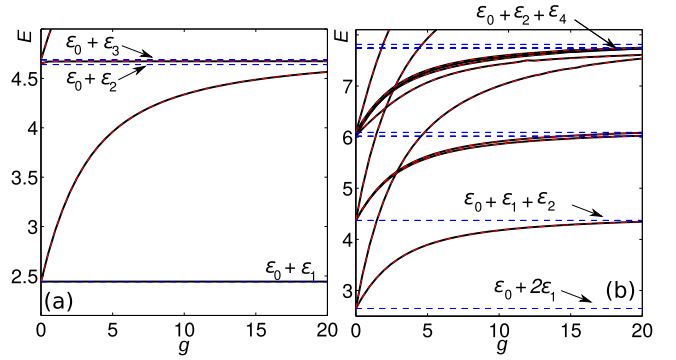

FIG. 2. (Color online) Energy spectra for (a) $N = 2$ with $V_0 = 5$ and (b) $N = 3$ with $V_0 = 10$. The blue dashed lines represent the energies expected in the fermionized limit, $g \to \infty$ (we explicitly label a few of them). We extrapolate these energies from the ones calculated with an increasing number of modes, with a maximum of 30 (24) modes for $N = 2$ (3).

constant as g is increased [see Fig. 2(a)]. The first two excited states, quasidegenerated with the ground state in the noninteracting case, are the NOON states, $|\text{NOON}_2\rangle = (|0,2,0,\ldots\rangle_{\text{lo}} \pm |2,0,0,\ldots\rangle_{\text{lo}})/\sqrt{2}$, which contain a delocalized pair of interacting atoms (two atoms in the same well). Their energy grows linearly with g for small g [see Fig. 2(a)]. The next excited states involve more than two modes and are clearly gapped in the absence of interactions [30–32]. They read $(|0,1,1,0,\ldots\rangle_{\text{lo}} \pm |1,0,0,1,0,\ldots\rangle_{\text{lo}})/\sqrt{2}$ and $(|0,1,0,1,0,\ldots\rangle_{\text{lo}} \pm |1,0,1,0,\ldots\rangle_{\text{lo}})/\sqrt{2}$. As before, the first two are mostly noninteracting, and thus, their energies remain constant as g is increased. The latter, however, have one pair of interacting atoms; their energy grows linearly with a slope similar to that of the $|\text{NOON}_2\rangle$ states [see Fig. 2(a)].

For $N > 2$ there are no noninteracting states. For $N = 3$ the lowest-energy manifold at small interactions is $(|1,2,0,\ldots\rangle_{\text{lo}} \pm |2,1,0,\ldots\rangle_{\text{lo}})/\sqrt{2}$ and the NOON states, $|\text{NOON}_3\rangle = (|3,0,0,\ldots\rangle_{\text{lo}} \pm |0,3,0,\ldots\rangle_{\text{lo}})/\sqrt{2}$. For the first two, the energy increases linearly with g, with the same slope as for $N = 2$ discussed above, due to the pair of atoms in the same well. In contrast, the NOON states have three interacting pairs, with a correspondingly larger slope [see Fig. 2(b)].

In general, the lowest-energy manifold at small g is $|N,0,0,\ldots\rangle_{\text{lo}} \pm |0,N,0,\ldots\rangle_{\text{lo}}$, $|1,N-1,0\ldots\rangle_{\text{lo}} \pm |N-1,1,0\ldots\rangle_{\text{lo}}$, etc. Our interest at this point is to disentangle the fate of these states as the interaction is varied from the Fock regime into the strongly interacting regime, in particular what happens with the states in which more than one atom populates each well in the Fock regime. The driving intuition is twofold. First, we know that for bosons in a single well, the system evolves into a TG gas; that is, the NOON would directly evolve into a NOON TG gas. Second, the BF mapping theorem can be directly applied to the system [3], providing exact solutions in the infinitely interacting case, which will be shown to be in contradiction with the first intuition.

B. From NOON to the NOON Tonks-Girardeau

The $N = 2$ and $N = 3$ cases are again very illustrative. We note that, energetically, the fate of the NOON states in
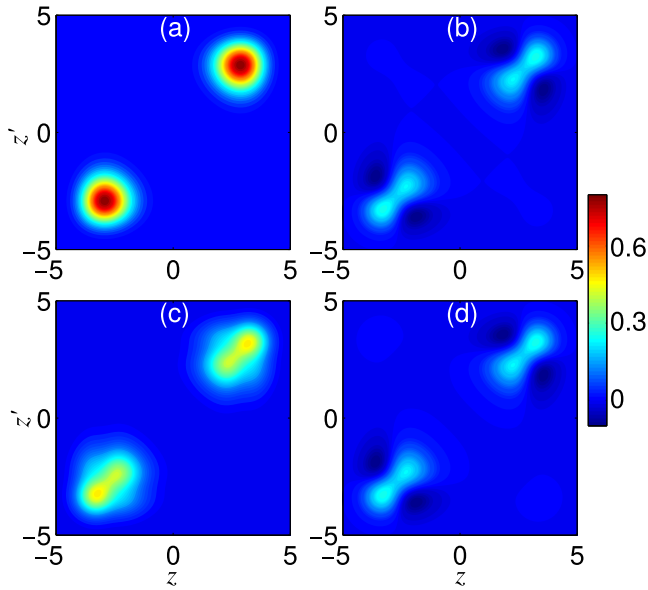
FIG. 3. (Color online) One-body density matrices of the first and third excited states for two bosons and $V_0 = 5$. The top (bottom) row is computed with $g = 0.5$ ($g = 20$). The NOON state in (a) evolves into the NOON TG in (c). The noninteracting state in (b) remains mostly unchanged in (d).

FIG. 4. (Color online) Comparison of two of the four excited numerical wave functions for $g = 20$ (top row) and the analytic ones Ψ_1^b [(e) and (g)] and Ψ_3^b [(f) and (h)] obtained through the BF mapping (bottom row). (a), (b), (e), and (f) are obtained with $V_0 = 4$, and (c), (d), (g), and (h) are obtained with $V_0 = 5$. $N = 2$.

$N = 2$ is very similar to what happens to the $(|1,2,0, \ldots \rangle_{\mathrm{lo}} \pm |2,1,0, \ldots \rangle_{\mathrm{lo}})/\sqrt{2}$ states in $N = 3$ (see Fig. 2); that is, the third particle in the $N = 3$ case plays a spectator role as g is increased. The latter takes place also in the general $N > 2$ case, in which none of the eigenstates are noninteracting and in which, upon increasing g, the system is expected to increase correlations to avoid the interaction. Thus, let us first disentangle the fate of the NOON states at $N = 2$. From Fig. 2(a) we see that as g is further increased, their energies saturate to a constant value which actually approaches $\varepsilon_0 + \varepsilon_2$. This is also essentially the energy of the states evolved from $(|0,1,1,0, \ldots \rangle_{\mathrm{lo}} \pm |1,0,0,1,0, \ldots \rangle_{\mathrm{lo}})/\sqrt{2}$, which are noninteracting. Thus, in the strongly interacting regime, there are four quasidegenerate states.

The evolution with increasing g of their one-body density matrices (OBDM) is very telling. The NOON states evolve from the $|\mathrm{NOON}_2\rangle$ states at $g = 0.5$ [see Fig. 3(a)] to distributions with two peaks per well [or three and four peaks per well for $N = 3$ and $N = 4$, respectively; see Figs. 1(c) and 1(c)], resembling the OBDM for two TG gases [Fig. 3(c)] at $g = 20$. The OBDM for the noninteracting states similarly shows two peaks per well, which would correspond to populating the single-particle states $\phi_{2,3}$, which have one node in each well.

The rigorous BF mapping theorem is established by noting that the bosonic problem in the $g \to \infty$ case is equivalent to the bosonic problem when imposing the boundary condition that the wave functions have to vanish if $z_j = z_{j'}$. This boundary condition is automatically obeyed by the fermions due to the Pauli exclusion principle. Then, the bosonic wave functions Ψ^b can be obtained from the fermionic ones Ψ^f after symmetrizing them, $\Psi^b = A \Psi^f$ with $A = \prod_{j>j'} \mathrm{sgn}(z_j - z_{j'})$, with $\mathrm{sgn}(z)$ being the sign function. The analytic form of the wave functions for the case of fermions was discussed above. The
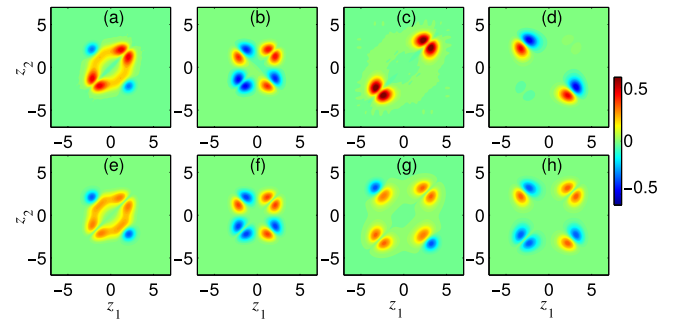
BF mapping theorem applies equally regardless of the value of V_0.

In Fig. 4 we compare the predictions of the BF mapping to the actual numerical results for $N = 2$ and for $V_0 = 4$ and $V_0 \gtrsim 4.5$. For $V_0 = 4$, the BF mapping [Figs. 4(e) and 4(f)] provides an accurate representation of the numerically obtained results [Figs. 4(a) and 4(b)]. Both the NOON and the noninteracting states evolve at $g = 20$ to the states predicted by the BF mapping. Note that in this case, the barrier is not high enough to produce two pairs of quasidegenerate single-particle states (see Fig. 1). None of the states is, however, a NOON TG state.

A surprising result appears, however, as we increase the barrier height, going from $V_0 = 4$ to $V_0 = 5$ in Fig. 4. In this case, the prediction of the BF mapping [Figs. 4(g) and 4(h)] and the numerical results [Figs. 4(c) and 4(d)] clearly disagree. The numerical results show less left-right coherence than the BF mapping prediction. That is, there is essentially zero probability of finding two bosons in the same well, as seen in Fig. 4(d), while in the BF mapping, the probability is clearly non-negligible in all four states. It is worth mentioning that these differences, which involve pair correlations, are not reflected in the density profiles, i.e., the diagonal of the one-body density matrices [Figs. 1(b), 1(c), 1(d), 3(c), and 3(d)]. What causes such a discrepancy? And, more important, what would an experiment find? Let us note that in all cases, the left-right symmetry is fully respected; that is, it is not a consequence of spurious numerical biases in the numerics.

C. Finite-range effects

The BF mapping applies for contact interaction potentials in the strict infinite interaction case. To understand what happens with finite interaction we can build a perturbation theory on the BF mapped states. Let us consider a finite-range perturbation on the four states predicted by the BF mapping, e.g., $V_{\mathrm{pert}}(z_j - z_{j'}) = \eta / \sqrt{2\pi\sigma^2} \exp[-(z_j - z_{j'})^2/(2\sigma^2)]$, and diagonalize it in the restricted space spanned by $\{\Psi_1^b, \Psi_2^b, \Psi_3^b, \Psi_4^b\}$. The new eigenstates are the dressed states $\{\bar{\Psi}_1^b, \bar{\Psi}_2^b, \bar{\Psi}_3^b, \bar{\Psi}_4^b\}$. The perturbative calculation predicts an avoided crossing (see Fig. 5). For $\eta < 0$, thus removing repulsion from the $g \to \infty$ limit, we have the NOON TG as the lowest state of the manifold, $\bar{\Psi}_1^b \simeq (\Psi_1^b + \Psi_4^b)/\sqrt{2}$ (see Fig. 5) and $\bar{\Psi}_2^b \simeq$
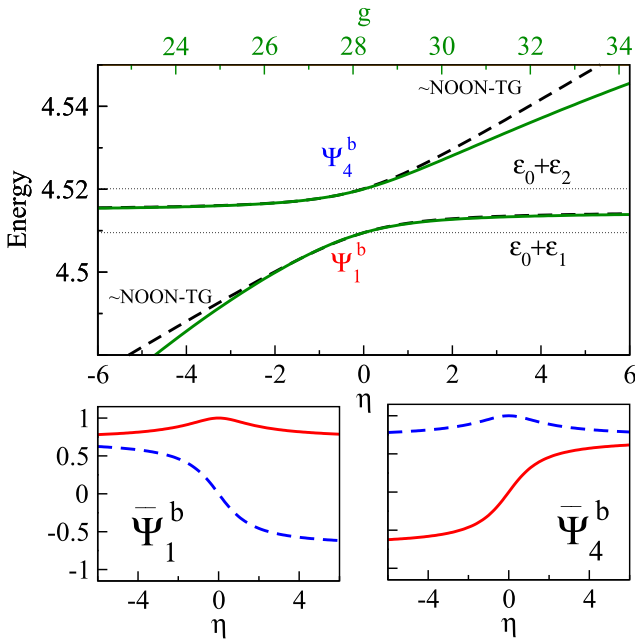
FIG. 5. (Color online) Detailed analysis of the $g \to \infty$ limit for $V_0 = 5.5$ and $N = 2$ (top panel). Two of the first excited states computed numerically (solid lines) are compared to the results of the perturbation theory when the width of the perturbation is $\sigma \simeq 0.07$ (dashed lines). The bottom panels depict the composition of the dressed states, $\bar{\Psi}_1^b$ and $\bar{\Psi}_4^b$: $\langle \bar{\Psi}_k^b | \Psi_1^b \rangle$ (solid red line) and $\langle \bar{\Psi}_k^b | \Psi_4^b \rangle$ (dashed blue line). A similar qualitative picture is obtained for states $\bar{\Psi}_2^b$ and $\bar{\Psi}_3^b$.

IV. DISCUSSION AND OUTLOOK

These results have been checked for $N = 2, 3$, and 4. For arbitrary N, at least N quasidegenerate doublets are needed, like in the fermionic case experimentally proven recently [12,13,17]. The corresponding quasidegenerate manifold predicted by the BF mapping in the $g \to \infty$ limit has 2^N many-body states. Finite-range interactions mix the states, producing again the avoided crossing at g_c between the two NOON TG states and less interacting states (less localized) in the manifold. Notice that in an actual experiment aiming to realize the infinitely interacting limit, this residual interaction will be present. These findings, which require two-body correlations to be explicitly measured, will be of relevance in future experimental efforts to build strongly correlated states with intersite spatial entanglement. As an outlook, we foresee that for a general trapping potential with an associated single-particle eigenspectrum showing quasidegeneracies, the effect of the finite range of the contact interactions may involve discrepancies between the result predicted by the BF mapping and the actual solution.

$(\Psi_2^b + \Psi_3^b)/\sqrt{2}$. For $\eta > 0$, the repulsive finite-size correction sets the noninteracting states $\bar{\Psi}_1^b \simeq (\Psi_1^b - \Psi_4^b)/\sqrt{2}$ and $\bar{\Psi}_2^b \simeq (\Psi_2^b - \Psi_3^b)/\sqrt{2}$ as the lowest in the manifold. Note that $\eta = 0$ corresponds to the strength of the perturbation at which the BF mapping is fulfilled.

These predictions are actually in good agreement with our full direct diagonalization results. To compare the two let us first define g_c as the value at which the eigenenergies of the system coincide with the BF mapping prediction. With a strict contact potential, $g_c = \infty$. If the interaction has a finite range (which effectively happens when using a finite number of modes), g_c becomes finite. For instance, in Fig. 5 we compare the perturbation theory with the results using $M = 28$ modes. In that case, the agreement is fairly good if $\sigma \simeq 0.07$. Further increasing M, g_c is found to increase, and as expected, the effective σ decreases.

To clarify the role played by the range of the interaction, we have replaced the contact V_{int} by a finite-range, σ, Gaussian atom-atom interaction (see the Appendix). By increasing the number of modes used in Eq. (2) we can obtain converged results and get g_c as a function of σ. We find $g_c \propto 1/\sigma$, diverging in the $\sigma \to 0$ limit, as expected from the BF mapping prediction. In a realistic experimental setup with two ^{87}Rb atoms confined to 1 μm, the critical value g_c can be attained by combining a Feshbach resonance and the confinement-induced one-dimensional resonance predicted in Ref. [33], as done experimentally in Ref. [34].

APPENDIX: ESTIMATE OF THE CRITICAL COUPLING STRENGTH

We provide the details to estimate the value of the critical coupling strength for a realistic value of the atom-atom interaction strength. To do so we have performed extensive numerical simulations for different values of the range of the atom-atom interaction σ,

$$V(z_j - z_{j'}) = \frac{g}{\sqrt{2\pi\sigma^2}} \exp[-(z_j - z_{j'})^2/(2\sigma^2)]. \quad \text{(A1)}$$

In all cases we have considered as the external potential the Duffing potential with $V_0 = 5.5$. In our numerical method, which builds the Fock space on a finite number M of single-particle modes, we can converge by considering a large enough M up to $\sigma = 0.1$. The critical value g_c is defined as the one for which the energy of the numerically computed states coincides with the prediction of the Bose-Fermi mapping theorem. Let us recall that for $\sigma \to 0$, we have $g_c \to \infty$; this limit cannot be obtained numerically as any truncation of the single-particle basis imposes an effective finite range of the contact interaction. As we increase σ, the value of g_c decreases.
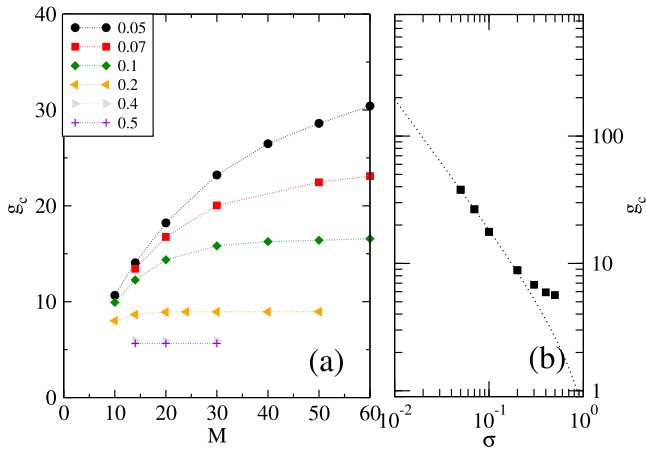
FIG. 6. (Color online) (a) Critical interaction strength g_c for different values of σ and different numbers of modes M. (b) Critical interaction strength for different values of σ. The dotted line is a fit of the form $g_c = b_0 + b_1/\sigma$ to the four lower values of $\sigma = 0.05, 0.07, 0.1$, and 0.15.

In Fig. 6(a) we show the value of g_c obtained for different values of σ and for different M. As expected, the convergence is much faster for larger values of σ. For $\sigma \geqslant 0.3$ convergence is achieved with $M \simeq 14$. For $\sigma = 0.1$ a large number of modes, 50, is required to get an essentially converged result. For smaller values, $\sigma = 0.05$ and $\sigma = 0.07$, we have

performed an extrapolation to larger M by fitting the computed points with the form $g_c = g_c^0 - a_1/M - a_2/M^2$.

The obtained values of g_c are compiled in Fig. 6(b) as a function of σ. The computed values are well approximated by $g_c = b_0 + b_1/\sigma$, which indeed diverges for $\sigma \rightarrow 0$ as expected.

In a realistic experiment we could consider a cloud of ^{87}Rb atoms globally trapped by a harmonic oscillator (h.o.) with $\omega_z = 2\pi 500$ Hz. The associated distance would then be $a_z = \sqrt{\hbar/(M_{\text{Rb}}\omega_z)} \simeq 5 \times 10^{-7}$ m. The size of the atom-atom interaction can be taken roughly as the bare scattering length, $\sigma \simeq 100 a_B$ (a_B is the Bohr radius), and thus, in h.o. units $\sigma/a_z \simeq 0.01$. In our numerics we have been able to go down to $\sigma/a_z \simeq 0.05$, but we can use an extrapolation to get g_c at $\sigma/a_z = 0.01$, which turns out to be $g_c \simeq 200$.

As described in Ref. [33], in one-dimensional systems, g_{1D} can be written in terms of the three-dimensional scattering length a_{3D} and transverse confining $a_\perp$ as

$$g_{1D} = \frac{2\hbar^2 a_{3D}}{M_{\text{Rb}} a_\perp^2} \frac{1}{1 - B \frac{a_{3D}}{a_\perp}}, \qquad \text{(A2)}$$

with $B = |\zeta(1/2)|/\sqrt{2} = 1.0326$. Following a procedure similar to the one in the experiment in Ref. [34], we can combine the effect of a Feshbach resonance to increase a_{3D} to the size of the transversal confinement to achieve the desired g_{1D} profiting from the resonant behavior of Eq. (A2).

[1] M. Girardeau, J. Math. Phys. **1**, 516 (1960).

[2] M. A. Cazalilla, R. Citro, T. Giamarchi, E. Orignac, and M. Rigol, Rev. Mod. Phys. **83**, 1405 (2011).

[3] V. I. Yukalov and M. D. Girardeau, Laser Phys. Lett. **2**, 375 (2005).

[4] M. D. Girardeau, E. M. Wright, and J. M. Triscari, Phys. Rev. A **63**, 033601 (2001).

[5] A. I. Streltsov, L. S. Cederbaum, and N. Moiseyev, Phys. Rev. A **70**, 053607 (2004); S. Zöllner, H.-D. Meyer, and P. Schmelcher, *ibid.* **75**, 043608 (2007).

[6] D. S. Murphy and J. F. McCann, Phys. Rev. A **77**, 063413 (2008).

[7] T. Ernst, D. W. Hallwood, J. Gulliksen, H.-D. Meyer, and J. Brand, Phys. Rev. A **84**, 023623 (2011).

[8] F. Deuretzbacher, K. Bongs, K. Sengstock, and D. Pfannkuche, Phys. Rev. A **75**, 013614 (2007); F. Deuretzbacher, K. Fredenhagen, D. Becker, K. Bongs, K. Sengstock, and D. Pfannkuche, Phys. Rev. Lett. **100**, 160405 (2008).

[9] T. Kinoshita, T. Wenger, and D. S. Weiss, Nature (London) **440**, 900 (2006).

[10] B. Paredes, A. Widera, V. Murg, O. Mandel, S. Fölling, I. Cirac, G. V. Shlyapnikov, T. W. Hänsch, and I. Bloch, Nature (London) **429**, 277 (2004).

[11] X. He, P. Xu, J. Wang, and M. Zhan, Opt. Express **18**, 13586 (2010).

[12] F. Serwane, G. Zürn, T. Lompe, T. B. Ottenstein, A. N. Wenz, and S. Jochim, Science **332**, 336 (2011).

[13] G. Zürn, F. Serwane, T. Lompe, A. N. Wenz, M. G. Ries, J. E. Bohn, and S. Jochim, Phys. Rev. Lett. **108**, 075303 (2012).

[14] A. N. Wenz, G. Zürn, S. Murmann, I. Brouzos, T. Lompe, and S. Jochim, Science **342**, 457 (2013).

[15] R. Bourgain, J. Pellegrino, A. Fuhrmanek, Y. R. P. Sortais, and A. Browaeys, Phys. Rev. A **88**, 023428 (2013).

[16] G. Pagano, M. Mancini, G. Cappellini, P. Lombardi, F. Schäfer, H. Hu, X.-J. Liu, J. Catani, C. Sias, M. Inguscio, and L. Fallani, Nat. Phys. **10**, 198 (2014).

[17] S. Murmann, A. Bergschneider, V. M. Klinkhamer, G. Zürn, T. Lompe, and S. Jochim, Phys. Rev. Lett. **114**, 080402 (2015).

[18] A. M. Kaufman, B. J. Lester, C. M. Reynolds, M. L. Wall, M. Foss-Feig, K. R. A. Hazzard, A. M. Rey, and C. A. Regal, Science **345**, 306 (2014).

[19] M. Albiez, R. Gati, J. Fölling, S. Hunsmann, M. Cristiani, and M. K. Oberthaler, Phys. Rev. Lett. **95**, 010402 (2005).

[20] S. Levy, E. Lahoud, I. Shomroni, and J. Steinhauer, Nature (London) **449**, 579 (2007).

[21] C. Gross, T. Zibold, E. Nicklas, J. Estéve, and M. K. Oberthaler, Nature (London) **464**, 1165 (2010).

[22] J. I. Cirac, M. Lewenstein, K. Molmer, and P. Zoller, Phys. Rev. A **57**, 1208 (1998).

[23] H. Strobel, W. Muessel, D. Linnemann, T. Zibold, D. B. Hume, L. Pezzé, A. Smerzi, and M. K. Oberthaler, Science **345**, 424 (2014).

[24] C. Weiss and Y. Castin, Phys. Rev. Lett. **102**, 010403 (2009).

[25] A. I. Streltsov, O. E. Alon, and L. S. Cederbaum, Phys. Rev. A **80**, 043616 (2009).

[26] L. D. Carr, D. Dounas-Frazer, and M. A. Garcia-March, Europhys. Lett. **90**, 10005 (2010).

[27] T. Fogarty, A. Kiely, S. Campbell, and Th. Busch, Phys. Rev. A **87**, 043630 (2013).

[28] A. J. Leggett, Rev. Mod. Phys. **73**, 307 (2001).

[29] B. J. Dalton and S. Ghanbari, J. Mod. Opt. **59**, 287 (2012).

[30] D. R. Dounas-Frazer, A. M. Hermundstad, and L. D. Carr, Phys. Rev. Lett. **99**, 200402 (2007).

[31] M. A. Garcia-March, D. R. Dounas-Frazer, and L. D. Carr, Phys. Rev. A **83**, 043612 (2011).

[32] M. A. Garcia-March, D. R. Dounas-Frazer, and L. D. Carr, Front. Phys. **7**, 131 (2012).

[33] M. Olshanii, Phys. Rev. Lett. **81**, 938 (1998).

[34] E. Haller, M. J. Mark, R. Hart, J. G. Danzl, L. Reichsöllner, V. Melezhik, P. Schmelcher, and H.-C. Nägerl, Phys. Rev. Lett. **104**, 153203 (2010).

Bibliography

[1] A. Osterloh, L. Amico, G. Falci, and R. Fazio, Nature **416**, 608 (2002).

[2] T. J. Osborne and M. A. Nielsen, Phys. Rev. A **66**, 032110 (2002).

[3] L.-A. Wu, M. S. Sarandy, and D. A. Lidar, Phys. Rev. Lett. **93**, 250404 (2004).

[4] M. Campostrini, J. Nespolo, A. Pelissetto, and E. Vicari, Phys. Rev. Lett. **113**, 070402 (2014).

[5] T. Mendes-Santos, T. Paiva, and R. R. dos Santos, Phys. Rev. A **91**, 023632 (2015).

[6] P. Hauke, Phys. Rev. B **87**, 014415 (2013).

[7] M. Takahashi, Phys. Rev. B **40**, 2494 (1989).

[8] P. Hauke, T. Roscilde, V. Murg, J. I. Cirac, and R. Schmied, New Journal of Physics **12**, 053036 (2010).

[9] A. Celi, T. Grass, A. J. Ferris, B. Padhi, D. Raventós, J. Simonet, K. Sengstock, and M. Lewenstein, Phys. Rev. B **94**, 075110 (2016).

[10] J. H. Xu and C. S. Ting, Phys. Rev. B **43**, 6177 (1991).

[11] R. Pathria and P. D. Beale, in *Statistical Mechanics (Third Edition)* (Academic Press, Boston, 2011) third edition ed., pp. 401 – 469.

[12] K. Huang, *Statistical mechanics*, 2nd ed. (John Wiley & Sons, Inc., 1987).

[13] H. Stanley and Eugene, *Introduction to Phase Transitions and Critical Phenomena* (OUP USA, 1973).

[14] M. E. Fisher, Reports on Progress in Physics **30**, 615 (1967).

[15] M. E. Fisher and M. N. Barber, Phys. Rev. Lett. **28**, 1516 (1972).

[16] Y. Imry, Phys. Rev. B **21**, 2042 (1980).

[17] M. E. Fisher and A. N. Berker, Phys. Rev. B **26**, 2507 (1982).

[18] K. Binder and D. P. Landau, Phys. Rev. B **30**, 1477 (1984).

[19] S. Sachdev, *Quantum Phase Transitions* (Cambridge University Press, 2001).

[20] X.-G. Wen, ISRN Condensed Matter Physics, vol. 2013, 198710 .

[21] X.-G. Wen, Rev. Mod. Phys. **89**, 041004 (2017).

[22] L. Amico, R. Fazio, A. Osterloh, and V. Vedral, Rev. Mod. Phys. **80**, 517 (2008).

[23] I. Bose and E. Chattopadhyay, Phys. Rev. A **66**, 062320 (2002).

[24] G. Vidal, J. I. Latorre, E. Rico, and A. Kitaev, Phys. Rev. Lett. **90**, 227902 (2003).

[25] J. I. Latorre, E. Rico, and G. Vidal, Quantum Info. Comput. **4**, 48 (2004).

[26] J. Vidal, G. Palacios, and R. Mosseri, Phys. Rev. A **69**, 022107 (2004).

[27] F. C. Alcaraz, A. Saguia, and M. S. Sarandy, Phys. Rev. A **70**, 032333 (2004).

[28] J. Vidal, R. Mosseri, and J. Dukelsky, Phys. Rev. A **69**, 054101 (2004).

[29] H. Barnum, E. Knill, G. Ortiz, R. Somma, and L. Viola, Phys. Rev. Lett. **92**, 107902 (2004).

[30] R. Orús and T.-C. Wei, Phys. Rev. B **82**, 155120 (2010).

[31] S.-J. Gu, H.-Q. Lin, and Y.-Q. Li, Phys. Rev. A **68**, 042330 (2003).

[32] J. Stasińska, B. Rogers, M. Paternostro, G. De Chiara, and A. Sanpera, Phys. Rev. A **89**, 032330 (2014).

[33] M. Hofmann, A. Osterloh, and O. Gühne, Phys. Rev. B **89**, 134101 (2014).

[34] J. Gemmer, M. Michel, and G. Mahler, *Quantum Thermodynamics* (Springer, Berlin, Heidelberg, 2019).

[35] C. Gogolin and J. Eisert, Reports on Progress in Physics **79**, 056001 (2016).

[36] M. Lewenstein, A. Sanpera, and V. Ahufinger, Advances in Physics Vol. 56 Nos. 1-2, January-April 2007, 243-379 .

[37] B. Zeng, X. Chen, D. Zhou, and X. Wen, arxiV:1508.02595 (2015).

[38] S. Sachdev, *Quantum Antiferromagnets in Two Dimensions* (World Scientific, Singapore, 1995).

[39] R. Moessner and S. L. Sondhi, Phys. Rev. B **63**, 224401 (2001).

[40] G. Misguich and C. Lhuillier, "Two-dimensional quantum antiferro-magnets," in *Frustrated Spin Systems* (World Scientific, 2004) pp. 229–306.

[41] M. Rasolt and Z. Tesanović, Rev. Mod. Phys. **64**, 709 (1992).

[42] M. Sigrist and T. M. Rice, Rev. Mod. Phys. **67**, 503 (1995).

[43] M. Mezard, G. Parisi, and M. Virasoro, *Spin Glass Theory and Beyond* (World Scientific, 1986).

[44] F. Alet, A. M. Walczak, and M. P. Fisher, Physica A: Statistical Mechanics and its Applications **369**, 122 (2006).

[45] X.-G. Wen, Phys. Rev. B **65**, 165113 (2002).

[46] L. Balents, Nature **464**, 199 (2010).

[47] L. Savary and L. Balents, Reports on Progress in Physics **80**, 016502 (2017).

[48] X.-G. Wen, Int. J. Mod. Phys **B4**, 239 (1990).

[49] X.-G. Wen, *Quantum Field Theory of Many-Body Systems* (Oxford University Press, 2004).

[50] A. Kitaev, Ann. Phys. (Leipz.) **321**, 2 (2006).

[51] M. Yamashita, N. Nakata, Y. Senshu, M. Nagata, H. M. Yamamoto, R. Kato, T. Shibauchi, and Y. Matsuda, Science **328**, 1246 (2010).

[52] S. Yamashita, Nature Phys. **4**, 459 (2008).

[53] M. A. de Vries, J. R. Stewart, P. P. Deen, J. O. Piatek, G. J. Nilsen, H. M. Rønnow, and A. Harrison, Phys. Rev. Lett. **103**, 237201 (2009).

[54] Y. Shimizu, K. Miyagawa, K. Kanoda, M. Maesato, and G. Saito, Phys. Rev. Lett. **91**, 107001 (2003).

[55] P. Mendels, F. Bert, M. A. de Vries, A. Olariu, A. Harrison, F. Duc, J. C. Trombe, J. S. Lord, A. Amato, and C. Baines, Phys. Rev. Lett. **98**, 077204 (2007).

[56] Y. Kurosaki, Y. Shimizu, K. Miyagawa, K. Kanoda, and G. Saito, Phys. Rev. Lett. **95**, 177001 (2005).

[57] T. Itou, A. Oyamada, S. Maegawa, M. Tamura, and R. Kato, Phys. Rev. B **77**, 104413 (2008).

[58] J. S. Helton, K. Matan, M. P. Shores, E. A. Nytko, B. M. Bartlett, Y. Yoshida, Y. Takano, A. Suslov, Y. Qiu, J.-H. Chung, D. G. Nocera, and Y. S. Lee, Phys. Rev. Lett. **98**, 107204 (2007).

[59] T.-H. Han, J. S. Helton, S. Chu, D. G. Nocera, J. a. Rodriguez-Rivera, C. Broholm, and Y. S. Lee, Nature **492**, 406 (2012).

[60] B. Fåk, E. Kermarrec, L. Messio, B. Bernu, C. Lhuillier, F. Bert, P. Mendels, B. Koteswararao, F. Bouquet, J. Ollivier, A. D. Hillier, A. Amato, R. H. Colman, and A. S. Wills, Phys. Rev. Lett. **109**, 037208 (2012).

[61] R. Coldea, D. A. Tennant, A. M. Tsvelik, and Z. Tylczynski, Phys. Rev. Lett. **86**, 1335 (2001).

[62] A. Kitaev and J. Preskill, Phys. Rev. Lett. **96**, 110404 (2006).

[63] M. Levin and X.-G. Wen, Phys. Rev. Lett. **96**, 110405 (2006).

[64] S. V. Isakov, M. B. Hastings, and R. G. Melko, Nature Phys. **7**, 772 (2011).

[65] C. Nayak, S. H. Simon, A. Stern, M. Freedman, and S. Das Sarma, Rev. Mod. Phys. **80**, 1083 (2008).

[66] H. Bethe, Zeitschrift für Physik **71**, 205 (1931).

[67] E. Schrödinger, Naturwissenschaften, 23:807 (1935).

[68] A. Einstein, B. Podolsky, and N. Rosen, Phys. Rev. **47**, 777 (1935).

[69] J. S. Bell, Rev. Mod. Phys. **38**, 447 (1966).

[70] J. Bell, *Speakable and Unspeakable in Quantum Mechanics* (Cambridge University Press, Cambdrige, England, 1987).

[71] A. Aspect, J. Dalibard, and G. Roger, Phys. Rev. Lett. **49**, 1804 (1982).

[72] M. Nielsen and I. Chuang, *Quantum Computation and Quantum Communication* (Cambridge University Press, Cambdrige, England, 2000).

[73] C. H. Bennett, G. Brassard, C. Crépeau, R. Jozsa, A. Peres, and W. K. Wootters, Phys. Rev. Lett. **70**, 1895 (1993).

[74] A. K. Ekert, Phys. Rev. Lett. **67**, 661 (1991).

[75] R. Horodecki, P. Horodecki, M. Horodecki, and K. Horodecki, Rev. Mod. Phys. **81**, 865 (2009).

[76] L. Amico, R. Fazio, A. Osterloh, and V. Vedral, Rev. Mod. Phys. **80**, 517 (2008).

[77] N. Laflorencie, Physics Reports **646**, 1 (2016).

[78] G. D. Chiara and A. Sanpera, Reports on Progress in Physics **81**, 074002 (2018).

[79] F. Verstraete, D. Porras, and J. I. Cirac, Phys. Rev. Lett. **93**, 227205 (2004).

[80] G. Vidal, Phys. Rev. Lett. **93**, 040502 (2004).

[81] F. Verstraete, V. Murg, and J. Cirac, Advances in Physics **57**, 143 (2008).

[82] R. Orús, Annals of Physics **349**, 117 (2014).

[83] O. Gühne and G. Tóth, Physics Reports **474**, 1 (2009).

[84] M. Plenio and S. Virmani, Quant.Inf.Comput **7**, 1 (2005).

[85] V. Vedral and M. B. Plenio, Phys. Rev. A **57**, 1619 (1998).

[86] M. J. Donald, M. Horodecki, and O. Rudolph, Journal of Mathematical Physics **43**, 4252 (2002).

[87] C. H. Bennett, H. J. Bernstein, S. Popescu, and B. Schumacher, Phys. Rev. A **53**, 2046 (1996).

[88] G. Vidal and R. F. Werner, Phys. Rev. A **65**, 032314 (2002).

[89] S. Hill and W. K. Wootters, Phys. Rev. Lett. **78**, 5022 (1997).

[90] K. Życzkowski, P. Horodecki, A. Sanpera, and M. Lewenstein, Phys. Rev. A **58**, 883 (1998).

[91] G. Vidal and R. F. Werner, Phys. Rev. A **65**, 032314 (2002).

[92] T.-C. Wei and P. M. Goldbart, Phys. Rev. A **68**, 042307 (2003).

[93] L. Bombelli, R. K. Koul, J. Lee, and R. D. Sorkin, Phys. Rev. D **34**, 373 (1986).

[94] M. Srednicki, Phys. Rev. Lett. **71**, 666 (1993).

[95] P. Calabrese and J. Cardy, Journal of Statistical Mechanics: Theory and Experiment **2004**, P06002 (2004).

[96] M. B. Hastings, Journal of Statistical Mechanics: Theory and Experiment **2007**, P08024 (2007).

[97] J. Eisert, M. Cramer, and M. B. Plenio, Rev. Mod. Phys. **82**, 277 (2010).

[98] U. Schollwöck, Rev. Mod. Phys. **77**, 259 (2005).

[99] S. Östlund and S. Rommer, Phys. Rev. Lett. **75**, 3537 (1995).

[100] F. Verstraete and J. I. Cirac, Phys. Rev. B **73**, 094423 (2006).

[101] F. Verstraete, M. M. Wolf, D. Perez-Garcia, and J. I. Cirac, Phys. Rev. Lett. **96**, 220601 (2006).

[102] G. Vidal, Phys. Rev. Lett. **99**, 220405 (2007).

[103] W. Chen, K. Hida, and B. C. Sanctuary, Phys. Rev. B **67**, 104401 (2003).

[104] P. Anderson, Materials Research Bulletin **8**, 153 (1973).

[105] D. A. Huse and V. Elser, Phys. Rev. Lett. **60**, 2531 (1988).

[106] T. Jolicoeur and J. C. Le Guillou, Phys. Rev. B **40**, 2727 (1989).

[107] B. Bernu, C. Lhuillier, and L. Pierre, Phys. Rev. Lett. **69**, 2590 (1992).

[108] L. Capriotti, a. Trumper, and S. Sorella, Phys. Rev. Lett. **82**, 3899 (1999).

[109] S. R. White and A. L. Chernyshev, Phys. Rev. Lett. **99**, 127004 (2007).

[110] S. Yunoki and S. Sorella, Phys. Rev. B **74**, 014408 (2006).

[111] M. Q. Weng, D. N. Sheng, Z. Y. Weng, and R. J. Bursill, Phys. Rev. B **74**, 012407 (2006).

[112] R. Schmied, T. Roscilde, V. Murg, D. Porras, and J. I. Cirac, New Journal of Physics **10**, 045017 (2008).

[113] D. Heidarian, S. Sorella, and F. Becca, Phys. Rev. B **80**, 012404 (2009).

[114] A. Yuste, M. Moreno-Cardoner, and A. Sanpera, Phys. Rev. B **95**, 195167 (2017).

[115] R. V. Mishmash, J. R. Garrison, S. Bieri, and C. Xu, Phys. Rev. Lett. **111**, 157203 (2013).

[116] Z. Zhu and S. R. White, Phys. Rev. B **92**, 041105 (2015).

[117] W.-J. Hu, S.-S. Gong, W. Zhu, and D. N. Sheng, Phys. Rev. B **92**, 140403 (2015).

[118] Y. Iqbal, W.-J. Hu, R. Thomale, D. Poilblanc, and F. Becca, Phys. Rev. B **93**, 144411 (2016).

[119] A. Wietek and A. M. Läuchli, Phys. Rev. B **95**, 035141 (2017).

[120] D.-V. Bauer and J. O. Fjærestad, Phys. Rev. B **96**, 165141 (2017).

[121] T. Jolicoeur, E. Dagotto, E. Gagliano, and S. Bacci, Phys. Rev. B **42**, 4800 (1990).

[122] P. Lecheminant, B. Bernu, C. Lhuillier, and L. Pierre, Phys. Rev. B **52**, 6647 (1995).

[123] S.-S. Gong, W. Zhu, J.-X. Zhu, D. N. Sheng, and K. Yang, Phys. Rev. B **96**, 075116 (2017).

[124] S. N. Saadatmand and I. P. McCulloch, Phys. Rev. B **96**, 075117 (2017).

[125] C. Hickey, L. Cincio, Z. Papić, and A. Paramekanti, Phys. Rev. B **96**, 115115 (2017).

[126] W.-J. Hu, S.-S. Gong, and D. N. Sheng, Phys. Rev. B **94**, 075131 (2016).

[127] J. K. Cullum and R. A Willoughby, *Lanczos Algorithms for Large Symmetric Eigenvalue Computations, Vol. I: Theory.*, Vol. 2 (2002).

[128] A. F. Albuquerque, D. Schwandt, B. Hetényi, S. Capponi, M. Mambrini, and A. M. Läuchli, Phys. Rev. B **84**, 024406 (2011).

[129] A. Läuchli, G. Schmid, and S. Trebst, Phys. Rev. B **74**, 144426 (2006).

[130] P. W. Leung and K. J. Runge, Phys. Rev. B **47**, 5861 (1993).

[131] B. Bernu, P. Lecheminant, C. Lhuillier, and L. Pierre, Phys. Rev. B **50**, 10048 (1994).

[132] I. Rousochatzakis, A. M. Läuchli, and F. Mila, Phys. Rev. B **77**, 094420 (2008).

[133] D. Poilblanc, Phys. Rev. B **44**, 9562 (1991).

[134] C. Gros, Zeitschrift für Physik B Condensed Matter **86**, 359 (1992).

[135] C. N. Varney, K. Sun, V. Galitski, and M. Rigol, Phys. Rev. Lett. **107**, 077201 (2011).

[136] C. N. Varney, K. Sun, V. Galitski, and M. Rigol, New Journal of Physics **14**, 115028 (2012).

[137] M. Thesberg and E. S. Sørensen, Phys. Rev. B **90**, 115117 (2014).

[138] *For most of the calculations of the thesis, the computer used is a Mac Pro with 64GB RAM and the Processor 3.5 Ghz 6-core Intel Xeon.*

[139] G. Vidal, J. I. Latorre, E. Rico, and A. Kitaev, Phys. Rev. Lett. **90**, 227902 (2003).

[140] J. I. Latorre, E. Rico, and G. Vidal, Quantum Info. Comput. **4**, 48 (2004).

[141] S. R. White, Phys. Rev. Lett. **69**, 2863 (1992).

[142] S. R. White, Phys. Rev. B **48**, 10345 (1993).

[143] K. G. Wilson, Rev. Mod. Phys. **47**, 773 (1975).

[144] R. M. Noack, S. R. White, and D. J. Scalapino, Phys. Rev. Lett. **73**, 882 (1994).

[145] S. Liang and H. Pang, Phys. Rev. B **49**, 9214 (1994).

[146] S. R. White and D. J. Scalapino, Phys. Rev. Lett. **80**, 1272 (1998).

[147] T. Xiang, J. Lou, and Z. Su, Phys. Rev. B **64**, 104414 (2001).

[148] E. Stoudenmire and S. R. White, Annual Review of Condensed Matter Physics **3**, 111 (2012).

[149] S. N. Saadatmand and I. P. McCulloch, Phys. Rev. B **94**, 121111 (2016).

[150] H. C. Jiang, Z. Y. Weng, and D. N. Sheng, Phys. Rev. Lett. **101**, 117203 (2008).

[151] S. Yan, D. A. Huse, and S. R. White, Science **332**, 1173 (2011).

[152] H.-C. Jiang, Z. Wang, and L. Balents, *Nature Physics*, **8**, 902 (2012).

[153] S. Depenbrock, I. P. McCulloch, and U. Schollwöck, Phys. Rev. Lett. **109**, 067201 (2012).

[154] Y.-C. He, M. P. Zaletel, M. Oshikawa, and F. Pollmann, Phys. Rev. X **7**, 031020 (2017).

[155] S. Rommer and S. Östlund, Phys. Rev. B **55**, 2164 (1997).

[156] F. Verstraete, J. I. Cirac, and V. Murg, Adv. Phys. 57,143 (2008).

[157] S.-J. Ran, E. Tirrito, C. Peng, X. Chen, G. Su, and M. Lewenstein, arXiv:1708.09213 (2017).

[158] U. Schollwöck, Annals of Physics **326**, 96 (2011).

[159] G. Vidal, Phys. Rev. Lett. **91**, 147902 (2003).

[160] F. Verstraete and J. I. Cirac, arXiv:cond-mat/0407066v1 (2004).

[161] V. Murg, F. Verstraete, and J. I. Cirac, Phys. Rev. A **75**, 033605 (2007).

[162] M. K. I. Peschel, X. Wang and K. Hallberg, *Density-Matrix Renormalization* (1999).

[163] G. De Chiara, M. Rizzi, D. Rossini, and S. Montangero, Journal of Computational and Theoretical Nanoscience **5**, 1277 (2008).

[164] *http://qti.sns.it/dmrg/phome.html*.

[165] H. A. van der Vorst, *Computational methods for large eigenvalue problems*, Handbook of Numerical Analysis, Vol. 8 (Elsevier, 2002) pp. 3 – 179.

[166] F. Bloch, Zeitschrift für Physik, 61(3),206-219 (1930).

[167] P. W. Anderson, Phys. Rev. **86**, 694 (1952).

[168] R. Kubo, Phys. Rev. **87**, 568 (1952).

[169] N. Majlis, *The Quantum Theory of Magnetism* (World Scientific, Singapore, 2000).

[170] T. Holstein and H. Primakoff, Phys. Rev. **58**, 1098 (1940).

[171] M. Takahashi, Progress of Theoretical Physics Supplement **87**, 233 (1986).

[172] G. E. Castilla and S. Chakravarty, Phys. Rev. B **43**, 13687 (1991).

[173] P. Hauke, Master's thesis, Technishe Universität München (2009).

[174] S. Tang and J. E. Hirsch, Phys. Rev. B **39**, 4548 (1989).

[175] J. E. Hirsch and S. Tang, Phys. Rev. B **40**, 4769 (1989).

[176] S. Tang, M. E. Lazzouni, and J. E. Hirsch, Phys. Rev. B **40**, 5000 (1989).

[177] H. Nishimori and Y. Saika, Journal of the Physical Society of Japan **59**, 4454 (1990).

[178] M. Takahashi, Journal of Magnetism and Magnetic Materials **104-107**, 845 (1992).

[179] P. Hauke, T. Roscilde, V. Murg, J. I. Cirac, and R. Schmied, New Journal of Physics **13**, 075017 (2011).

[180] E. Ghorbani, F. Shahbazi, and H. Mosadeq, Journal of Physics: Condensed Matter **28**, 406001 (2016).

[181] F. J. Dyson, Phys. Rev. **102**, 1217 (1956).

[182] A.Fetter and J. Walecka, *Quantum Theory of Many-Particle Systems* (McGraw Hill, New York, 1971).

[183] M. Moreno-Cardoner, S. Paganelli, G. D. Chiara, and A. Sanpera, Journal of Statistical Mechanics: Theory and Experiment **2014**, P10008 (2014).